Interior-surface-atmosphere interactions of rocky planets: simulation of volcanic outgassing and volatile chemical speciation in the C-O-H system

Dissertation
Submission for the academic title
”Doctor rerum naturalium“
(Dr. rer. nat.)

Submitted by
Gianluigi Ortenzi

Submitted to the Department of Earth Sciences
Freie Universität Berlin

Berlin, 2021

Supervisor: Prof. Dr. Lena Noack

Freie Universität Berlin Institut für Geologische Wissenschaften
Malteserstraße 74-100, 12249 Berlin, Germany.

Second examiner: Prof. Dr. Doris Breuer

Institut de Physique du Globe de Paris - Department of Planetary and Space Sciences.
Université de Paris. 1 Rue Jussieu, 75005 Paris, France.

and

German Aerospace Center (DLR), Institute of Planetary Research.
Rutherfordstraße 2, 12489 Berlin. Germany.

Date of defense: 25 May 2021

Hiermit versichere ich, die vorliegende Arbeit selbstständig angefertigt und keine anderen als die angeführten Quellen und Hilfsmittel benutzt zu haben.

Berlin, 2021

Gianluigi Ortenzi

Contents

Abstract

The characterization of the volcanic volatile outgassing is central for investigating the composition and the development of rocky planet atmospheres. I have analysed the volcanic gas release via numerical simulations of the volatile pathway from the mantle to the atmosphere of a planet. The thesis has been carried out as a subproject within the Transregional Collaborative Research Center TRR 170 ”Late accretion onto terrestrial planets” which gave the opportunity to collaborate with other subprojects and research institutions. The aim of the thesis was to develop a numerical model for characterising the volcanic outgassed composition during the early Earth evolution. The core of this research is the volatile chemical speciation model which simulates the volcanic outgassing considering the C-O-H system. I designed the model following the ”Mass balance and equilibrium” method (French, 1966; Holloway, 1981; Holland, 1984; Huizenga, 2005; Fegley, 2013; Gaillard and Scaillet, 2014; Schaefer and Fegley, 2017) taking into consideration the principal factors that define the outgassed composition of a silicate melt namely: pressure, temperature and redox state. The volatile chemical speciation is calculated considering that the volatile species are in chemical equilibrium with the silicate melt and an ideal gas behaviour. The redox state of the system was reproduced by using some of the most common petrological mineral buffers (Holloway et al., 1992), for both reducing or oxidising conditions. The collected results demonstrate how the magma redox state is the driving parameter that affects the final outgassed composition. In reducing conditions (QIF and IW buffers) the principal outgassed species are H_2 and CO whereas, in oxidising states (NiNiO and QFM buffers) the dominant volatile species are H_2O and CO_2. In order to investigate the volatile outgassing at a global scale, the volatile chemical speciation model was coupled with different models that reproduce the mantle convection regime (Noack and Breuer, 2013; Noack et al., 2014, 2017) and the corresponding outgassed atmospheres (Dorn et al., 2018). The coupling of the models is employed to investigate the volatile outgassing at different conditions. In Guimond et al. (2021), we investigated the early Earth evolution outgassing during the magma ocean stage. Still considering a global Earth magma ocean, in Katyal et al. (2020) we simulated the degassed atmospheric composition, H_2 escape and the infrared emission/transmission. Ortenzi et al. (2020) analyses the degassing for rocky planets considering a stagnant lid regime and calculating the outgassed atmospheric compositions and radial extents. The volatile chemical speciation model was extended to include also the sulphur species (H_2S, S_2 and SO_2) and for simulating the real gas behaviour. At the moment the simulations of the C-O-H-S system are only for a limited range of temperature and pressure, and the model needs further improvements for being employed in global outgassing simulations. In conclusion, the thesis includes a detailed description of the developed volatile chemical speciation models showing both their points of weakness and their versatility for investigating the volatile composition of outgassed atmospheres at different planet evolutionary stages.

Zusammenfassung

Um die Entstehung und Entwicklung von Atmosphären terrestrischer Planeten zu verstehen, ist es von zentraler Bedeutung das Verhalten und die Charakteristiken freiwerdender volatiler Stoffe bei vulkanischen Ausgasungsprozessen zu untersuchen. In dieser Dissertation wird mittels numerischer Simulierung der Weg vulkanischer Gase von ihrer gebundenen Form im Mantel bis hin zu ihrer freien Form in der Atmosphäre zurückverfolgt und deren Zusammensetzung analysiert. Die Promotionsarbeit ist im Rahmen des Transregio Sonderforschungsbereiches 170 (SFB TRR 170) "Late accretion onto terrestrial planets" angefertigt worden, wodurch Möglichkeiten zu Kollaborationen mit weiteren Gruppen und Instituten innerhalb des Projektes genutzt werden konnten. Das Ziel dieser Arbeit ist die Entwicklung eines numerischen Modells zur Bestimmung der Gaszusammensetzung, die während der Frühgeschichte und Evolution der Erde durch vulkanische Prozesse ausgegast wurde. Im Zentrum steht dabei das Modell zur chemischen Speziierung von volatilen Elementen, das die Zusammensetzung des Gases innerhalb des C-O-H Systems simuliert. Es wurde mittels der Massenbilanzierungs- und Gleichgewichtsmethode entworfen (French, 1966; Holloway, 1981; Holland, 1984; Huizenga, 2005; Fegley, 2013; Gaillard and Scaillet, 2014; Schaefer and Fegley, 2017) und berücksichtigt die wichtigsten Faktoren, die die Ausgasungsprozesse silikatischer Schmelzen beeinflussen, nämlich Druck, Temperatur und Redox-Zustand. Die volatile chemische Speziierung wird unter Berücksichtigung des chemischen Gleichgewichts mit der silikatischen Schmelze unter der Annahme von idealem Gasverhalten berechnet. Der Redox-Zustands des Systems wird sowohl für reduzierende als auch oxidierende Bedingungen durch die in der Petrologie üblichen Mineralpuffer reproduziert (Holloway et al., 1992). Die Ergebnisse dieser Arbeit zeigen, dass die Zusammensetzung der ausgegasten Verbindungen hauptsächlich durch den Redox-Zustand des Magmas bestimmt wird. In reduzierenden Bedingungen (QIF und IW Puffer) wird hauptsächlich H_2 und CO frei, während in oxidierenden Bedingungen (NiNiO und QFM Puffer) überwiegend H_2O und CO_2 ausgast. Um die Ausgasungsprozesse global zu untersuchen, wurde das volatile Speziierungs-Modell mit weiteren Modellen zur Reproduktion verschiedener Mantelkonvektionsregime (Noack and Breuer, 2013; Noack et al., 2014, 2017) und deren zugehörigen ausgegasten Atmosphären (Dorn et al., 2018) kombiniert. Durch die Verbindung der Modelle lässt sich das Ausgasen unter verschiedenen Umwelteinflüssen und Bedingungen untersuchen. In Guimond et al. (2021) wurde die Entwicklung der Ausgasung während der Magma Ocean Phase der frühen Erdgeschichte untersucht. Katyal et al. (2020) haben weiterhin, unter der Berücksichtigung eines globalen Magma Ozeans, die Zusammensetzung der ausgegasten Atmosphäre, den H_2 Verlust und die infrarot Emission sowie Transmission simuliert. In Ortenzi et al. (2020) wurden hingegen die Ausgasungsprozesse für terrestrische Planeten im 'Stagnant Lid Regime' simuliert sowie die Zusammensetzung und die radiale Ausdehnung der Atmosphäre berechnet. Des Weiteren wurde das volatile Speziierungs-Modell um Schwefel Verbindungen (H_2S, S_2 und SO_2) und das Verhalten von realen Gasen erweitert. Zum gegenwärtigen Zeitpunkt sind die Simulationen des C-O-H-S Systems jedoch durch limitierte Druck- und Temperaturbereiche beschränkt und benötigen Verbesserungen, um für die globalen Ausgasungssimulationen verwendet werden zu können. Zusammengefasst beinhaltet diese Dissertation eine detaillierte Beschreibung des entwickelten Gas-Speziierungs-Modell, wobei sowohl die Schwächen als auch die Vielseitigkeit der Methode zur Untersuchung der Zusammensetzung ausgegaster Atmosphären während verschiedener planetarer Entwicklungsstufen aufgezeigt werden.

1 Introduction

Volcanic volatiles are central for investigating the volcanic activity of the Earth, together with the silicate melts they represent the link between the interior of the planet and the atmosphere. Nowadays, the most common volatiles outgassed from a volcanic complex are H_2O and CO_2 followed by sulphur species such as SO_2 and H_2S (Oppenheimer et al., 2014). The composition of the fluid species dissolved in the silicate melts reproduces the volatile content of the mantle, of the melt source rocks and of the redox state of the system. The latter is crucial for defining the volatile chemical speciation of outgassed species. The oxygen fugacity (f_{O_2}) can be defined as the partial pressure of oxygen which describes the redox state of a system. Mineral buffers are chemical equilibria that are employed in petrology as standard values to compare systems at different redox states. The reactions are useful because they buffer the oxidation state as a function of temperature and pressure. The most common mineral buffers are Iron-Wuestite (IW) and Quartz-Iron-Fayalite (QIF) for reproducing reducing conditions and Quartz-Fayalite-Magnetite (QFM) and Nickel-Nickel-Oxyde (NiNiO) for oxidising systems. Present days oxygen fugacities of different geodynamics regimes including hot spot, divergent and convergent plate boundaries are considered oxidised and comprised within few log units around the NiNiO buffer (Fegley and Schaefer, 2014). Nevertheless, during the early Earth evolution the redox state of the mantle was likely more reduced than at present (figure 1). According to Gaillard and Scaillet (2014); Frost et al. (2008), the redox state of the mantle was influenced by the core mantle segregation. During that period, due to the presence of metal iron in equilibrium with the mantle, the oxidation state of the mantle was most likely very reduced and the volcanic outgassing in the C-O-H system was mainly dominated by reducing species like H_2, CO and likely CH_4 at low temperatures (Fegley and Schaefer, 2014; Wood et al., 2006; Kasting et al., 1993). The outgassed atmosphere reflects the redox state of the interior. Reducing atmospheres are of interest also for investigating the role of the primordial atmosphere for habitability and the emergence of life (Miller et al., 1953; Hill, 1992; Kasting et al., 1993; Johnson et al., 2008). In order to simulate the volcanic outgassing, I designed a chemical speciation model which shows the strong link between the volcanic degassing and the interior of a planet. In the following sections, I describe the principle peculiarities of the Earth evolution and the implications for the volatile cycling and atmospheric formation. I include a detailed explanation of the speciation model and its applications for analysing the atmospheres of rocky planets.

The thesis in the TRR context. The TRR-170 ”Late accretion onto terrestrial planets” is a research program which includes researchers and PhD students at the Freie Universität Berlin, the Technical University of Berlin and the Westfälische Wilhelms Universität Münster and research institutions as the Deutsches Zentrum für Luft- und Raumfahrt Berlin (DLR) and the Museum für Naturkunde Berlin. The main goal of the project is to shed light on the late accretion of the Earth, the Moon and other rocky planets in the period

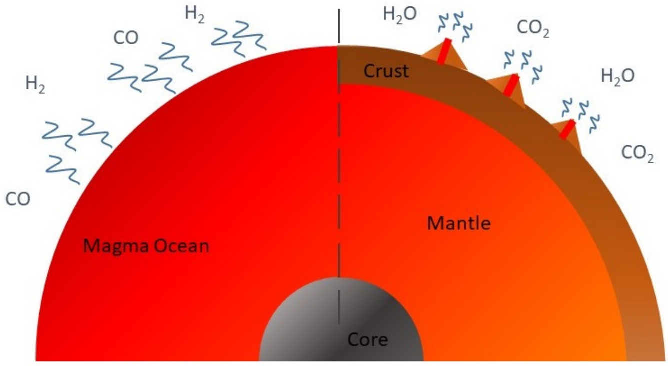

Figure 1: Representation of the volcanic outgassing of the C-O-H system not to scale. The left side of the cartoon shows the direct outgassing at surface during the magma ocean period. During the core mantle separation the magma ocean was likely in a more reduced state compared to present days value of mantle oxygen fugacity. Thus, the magma ocean outgassing was composed by reduced volatiles as H_2, CO and CH_4 at low temperatures. The right side of the figure displays present days volcanic outgassing which is characterized by oxidised gas phases as H_2O and CO_2.

between 4,5 and 3,8 billion years ago. The different aspects of the late accretion are analysed by applying a multidisciplinary approach. The project is divided in three main research areas: A) the timing and the rate of the late accretion, B) the chemical budget and C) the geodynamic implications. Area A is focused on the analyses of the Moon cratering record to investigate the timing of the late accretion of rocky planets. The projects of the area B) investigate the chemical composition of the accreted material during the late veneer. Area C) analyses through numerical modelling the Earth and Moon system. The different projects consider the geodynamic implications and interactions between the different layers of the planet namely the core, the mantle and the atmosphere. This thesis is part of the area C within the project C5. The goal of the project is to investigate the volcanic outgassing during the early Earth evolution and the development of the corresponding atmosphere. The volatiles gas chemical speciation was analysed by designing a numerical model which simulates the gas chemical speciation of the C-O-H system at different temperature, pressure and redox state. The research was performed within the C5 project in close collaboration with Nisha Katyal (see 3.1 and 3.3), and with the project C6 located at the Freie Universität Berlin with the P.I. Lena Noack and with Claire Guimond, Sara Vulpius and Julia Schmidt (see 3.1).

Motivation of the study. The main aims of the study are to analyse which are the factors that mostly affect the volcanic volatile degassing and the corresponding outgassed atmosphere during the early Earth evolution and to broaden the investigation also to rocky exoplanets. The study of the atmospheric composition and evolution is a key point for understanding both the conditions to develop an habitable planet and to analyse the link between the deep interior and atmosphere of a planet. In order to better characterise the volatiles outgassing, I have analysed the pathways of the volcanic gases from the interior to the atmosphere showing the strong connections between the interior of a planet and the corresponding atmosphere. I have investigated the volcanic outgassing by developing volatile chemical speciation models for the C-O-H and C-O-H-S systems. An important aspect was also to design a versatile outgassing model that was simple to couple with models for investigating the mantle convection and the atmospheric evolution. I have considered both stagnant lid and magma ocean planets to describe the atmospheric composition and evolution during the different phases of planetary evolution on a global scale. The results can be applied both to investigate the early Earth evolution and the present days signal from exoplanets.

Thesis outline. The thesis is divided in chapters in order to cover all the different aspects that were investigated during the PhD period, starting with an introduction on the volcanic volatile phases, a methods chapter which describes how the chemical speciation model was developed and two sections which collect the research papers. The introduction (1) is mostly focused on the role of the volatile phases in volcanology and in planetary science. There is a detailed characterisation of the volatile phases that are analysed for simulating the volcanic outgassing and a paragraph which includes the field work that was performed during the development of the PhD project. The methods section (2) is the central part of the thesis, it contains the theory that was necessary for developing the volatile chemical speciation model considering ideal or real gas behaviour and several step by step examples that describe the applications of the model. In section 3 are collected the research papers and the principal novelties introduced with the applications of the speciation model whereas, section 3.4 contains the research papers related to fieldwork analyses.

1.1 General description of volatile species and volcanic outgassing process

Volatiles are fundamental constituents of the magma and the driving force for determining the volcanic eruptive style (Wallace et al., 2015). The volcanic emissions have played a role during the entire Earth evolution and they have contributed to the development of both atmosphere and oceans generating the conditions for the emergence of life (Oppenheimer et al., 2014). The principal volatiles present in the magma are defined by the C-O-H-S system, which represents almost all the volcanic emission. Other important species, are the halogens (i.e. fluorine HF and chlorine HCl), nitrogen species (NH_3 and NH_2) and noble gases (e.g. Ar and He). For the investigation of this study and the atmospheric evolution the focus is on the C-O-H-S system, which represent roughly more than the 90% of present days volcanic emissions on Earth (Oppenheimer et al., 2014). The parameters which regulate the volatile flux and the composition from the interior to the atmosphere are temperature, the oxidation state of the system in terms of oxygen fugacity and pressure. Pressure and on a minor scale temperature regulate the ratio of dissolved/exsolved volatiles in the magma through the solubility of the gases. Temperature and redox state drive the chemical composition of the outgassed volatile species differentiating between oxidised (e.g. H_2O, CO_2 and SO_2) and reduced gas phases (e.g. H_2, CO, CH_4 and H_2S). Since volatiles have different solubility (see sections

1.1.1; 1.1.2; 1.1.3), the availability of volcanic gases released at different pressure (especially hydrogen and carbon species) is crucial for investigating the volcanic outgassing. The outgassing starts when the concentrations of gas phases exceed the solubility threshold (Shinohara, 2008). The volatiles exsolve from the magma, and start to aggregate in bubbles and then separate from the magma. The outgassing of a volcanic complex can be divided in passive or active outgassing. Passive outgassing is the most common expression of outgassing and it is not associated to any eruption. The exceed of volatiles is usually due to the crystallization of the magma chamber which produces an oversaturation in volatiles and consequently the outgassing (Burnham, 1967; Shinohara, 2008; Petrelli et al., 2018). This variety of outgassing is linked also to hydrothermal vents which can emit low-temperature species such as methane and H_2S (Parfitt and Wilson, 2008; Chiodini, 2009), that are of interest also for the emergence of life. Active degassing is associated to volcanic eruptions, and the different mode of outgassing produce different eruption styles. The nucleation of gas bubbles is the first step to produce volcanic outgassing. According to Parfitt and Wilson (2008) the bubbles nucleation can be divided into homogeneous or heterogeneous nucleation. The homogeneous nucleation occurs when the magma is saturated in a volatile species and the volatiles start to aggregate to exceed the superficial tension in order to generate a bubble. But, even if the magma is oversaturated in volatiles it is not simple to cross the superficial tension and to form a bubble. The heterogeneous nucleation takes place when there is an unconformity in the magma that assists to exceed the superficial tension. The crystals contained in the magma represent this discontinuity that helps the volatiles to aggregate and to form bubbles. Once the bubble is formed, it starts to rise up within the magma and begins to grow following three principles: the diffusion, the decompression and the coalescence (Parfitt and Wilson, 2008). The diffusion starts when the less soluble volatile in the melt dissolves and starts to nucleate a bubble. After that, any other volatiles species once reaches the saturation start to enter in the gas phase enlarging the bubble. During the rising of the bubble and of the magma, the decompression increases the volume of the bubble due to the lower surrounding pressure compared to the magma chamber. The consequent volume of the gas phase in the magma thus increases compared to the melt and the solid and the bubbles have an higher probability to collide and to merge generating larger bubbles. This last process is the coalescence which is important for some explosive eruptive styles such as Strombolian or Vulcanian. The main effect is that larger bubbles rise faster in the magma generating explosive eruptions (Parfitt and Wilson, 2008). The flow of the magma to the surface is characterised by the ratio of gas and liquid phase in the magma and can be divided in four flow regimes. According to Sigurdsson et al. (2015), at low volume of gas phase, the bubbles are carried by the liquid (bubble flow regime). This regime is typical of non explosive eruptions when vesicular lavas are extruded from a volcanic vent. When the amount of gas starts to be larger, the bubbles collide generating gas pockets (slug regime) and the typical Strombolian activity. Within the conduit the gas/liquid ratio can increase forming a central gas core surrounded by a thin layer of liquid (annular regime). This regime is not so common and associated still to Strombolian activity and lava fountaining. The last regime occurs when the gas is a continuous phase, which carries the magma (dispersed flow). This latter is typical of more viscous magmas causing Plinian eruptions or pyroclastic flow eruptions but, still can occur in lava fountains. Thus, according to the different volatile content, magma composition and geodynamic context the eruptive style of a volcano complex is divided in effusive or explosive volcanism. Effusive volcanism is mostly related to basaltic magmas which are characterized by a lower silica content and viscosity compared to silicic magmas. Some of the most interesting expressions of effusive volcanism for planetary science are the lava flows and the flood basalts. Lava flows are the extrusion of basaltic melts with low viscosity at temperature between 800 - 1200°C (Sigurdsson et al., 2015). They can produce lava tunnels which are of great interest also for astrobiology applications because on planets like Mars they can act as a shelter to preserve life from the extreme temperature and radiation (see section 1.3 for details). Flood basalts are the largest recorded volcanic episodes that occurred on Earth. They are characterised by upwelling mantle magma directly extruded within crust fissures to the surface (Sigurdsson et al., 2015). For this reason they can represent an analogue for magma ocean stages or of stagnant-lid planet volcanism. Basaltic magmas are divided in MORB (Midocean Ridge Basalt), OIB (Ocean Island Basalt), arc basalt, BABB (Back arc basin basalts). They are mostly generated in the mantle for partial melting and at divergent plate boundaries or hot spots. During the melt production the volatiles enter the melt phase because they behave as incompatible elements and thus, they represent the transfer from the Earth mantle (Wallace et al., 2015). According to Oppenheimer et al. (2014), the pre-eruptive volatile content in the C-O-H system of examples of MORB is up to 1.5 % for H_2O, 400 ppm for CO_2 and 800 - 1500 ppm for S. For the OIB the water content is up to 1% (Dixon et al., 1991), CO_2 to 6500 ppm and up to 3000 ppm for sulphur. For arc basalt and BABB are respectively up to 6% (Roggensack et al., 1997) (because of crustal contamination) and 3% for H_2O while CO_2 is approximately less than 1200 ppm for BABB. Silicic magmas can be highly enriched in volatiles, especially water. They are also the volcanic expression of convergent plate boundaries and the volatile content is influenced by crustal contamination. The explosive volcanism is divided in the less vigorous Hawaiian and Strombolian eruptions up to the catastrophic Plinian eruptions. Some examples of andesite have a water content of more than 3%, 10-1200 ppm of CO_2 and less than 1000 ppm of sulphur. Dacites and Rhyolites can contain up to 7% of water (Oppenheimer et al., 2014; Wallace, 2001; Wallace et al., 1995). The focus of the study is to analyse the global outgassing, which contribute to the formation of the atmosphere during and after the magma ocean stage of stagnant lid planets. As aforementioned, the basaltic magmas represent the best connection between the mantle and the corresponding outgassed volatiles and for this reason in the rest of the study all the simulations are performed considering basaltic compositions of the source rock.

1.1.1 Hydrogen species (H_2 and H_2O)

The two principal hydrogen species are H_2O and H_2. Water is the main volcanic outgassed species in present days and it is typical of an oxidised mantle, whereas H_2 is released in reducing scenarios. The solubility is a measure for the maximum amount of a volatile species that can be dissolved in a magma (Wallace et al., 2015). The solubility of H_2O is regulated by the pressure (Sigurdsson et al., 2015) whereas the H_2 is considered almost not soluble in silicate melts (Gaillard et al., 2003), or with a solubility comparable to that of noble gases (Oppenheimer et al., 2014) (see section 2.5 for details). As for other volatile species, the higher the pressure, the higher is the solubility of H_2O. Water dissolves in the melt as OH^- groups that react with aluminosilicate lowering the melt viscosity (Wallace et al., 2015; Oppenheimer et al., 2014; Giordano et al., 2008) or as H_2O. The proportion between the two species are regulated by the the total amount of water dissolved in the magma. At low water concentration water is dissolved as OH^-, whereas at around 3% of water in rhyolitic melts and 3,5% for basalts, OH^- and H_2O have the same proportion (Sigurdsson et al., 2015). The water solubility is influenced also by the melt composition and by the presence of other volatiles. At the same pressure, rhyolitic melts can dissolve more water compared to basaltic melts (Sigurdsson et al., 2015). The solubility of all the volatiles is influenced by the presence of other volatiles, thus upon that other species exsolved the water solubility gets increasingly lower.

1.1.2 Carbon species (CO_2, CO and CH_4)

The most diffuse volcanic outgassed carbon species are CO_2, CO and CH_4. Carbon dioxide is commonly outgassed as the oxidised carbon gas phase whereas CO and CH_4 are the reduced species. CH_4 is normally absent or present in very low quantity at high temperatures and is usually outgassed as hydrothermal gas phase (Chiodini, 2009). The solubility of CO and methane is considered very low (Morizet et al., 2010; Pawley et al., 1992; Oppenheimer et al., 2014) whereas CO_2 dissolves according to the melt composition and the silica content as CO_2 in rhyolitic composition and as ${CO_3}^{2-}$ in basalts (Oppenheimer et al., 2014; Wallace et al., 2015). At the same temperature and pressure, CO_2 solubility is 50-100 times less than of H_2O and increases with high alkali content (Wallace et al., 2015). Interesting to note is the dependence of the oxygen fugacity for partitioning of carbonate from the mantle source rock to the melt (Grott et al., 2011; Noack et al., 2017; Dorn et al., 2018). Thus, the volume of outgassed carbon species is influenced not only by the composition of the source rocks but also by the oxidation state during the melt production. In reducing scenarios the partitioning of carbonate in the melt is inhibited producing melt depleted in carbon species. Considered outgassing at a global planetary scale, interior redox state has a strong control on the atmospheric development and composition (Ortenzi et al., 2020).

1.1.3 Sulphur species

After hydrogen and carbon species, sulphur volatiles are the most abundant volatile phases of present days outgassing. Even if less abundant than carbon and hydrogen species, the sulphur species are central for investigating the volcanic hazard because they can potentially trigger eruptions and they have a strong climate and atmospheric impact (Oppenheimer et al., 2011). In the solar system, they are crucial for investigating the volcanic eruptions of Io (Zolotov and Fegley Jr, 1999; Lopes-Gautier et al., 2000). Sulphur solubility is characterised by the oxidation state of its different forms in the gas phase S_2, H_2S, SO_2 and SO_3 and of solid or liquid phases as pyrrotithe and anhydrite (Oppenheimer et al., 2011, 2014). In reducing conditions sulphur dissolves as S^{2-} whereas in oxidising conditions as S^{6+} (Wallace et al., 2015). The solubility of reduced species increase according to the Fe concentration in the melt. Both reducing and oxidising species increase their solubility at higher temperature. In contrast, the pressure has different effect on the solubility. In oxidising conditions the pressure increases the solubility whereas in reducing scenarios it decreases the sulphur solubility (Wallace et al., 2015).

1.1.4 Oxygen fugacity control on the gas chemical speciation

The redox state of the system is central for investigating the gas chemical speciation during the volcanic outgassing. Once the gas bubble is formed in the magma, the oxygen fugacity of the surrounding melt buffers the gas phases influencing the volatile chemical composition (Kadoya et al., 2020). As described in Symonds and Reed (1993), the volcanic gases behaviour is close to the chemical equilibrium and the results from chemical equilibria can be compared to direct measurements of volcanic degassing. Thus, the outgassing of the different species can be simulated following the ”Equilibrium and mass balance method” (French, 1966; Holloway, 1981; Holland, 1984; Gaillard and Scaillet, 2014; Fegley, 2013; Huizenga, 2005) (Figure 2). This method allows to quantify simultaneously which are the outgassed species at different redox states. The volcanic gas compositions can be simulated with several gas chemical equilibria. To give an example, here are summarized some equilibria that describe the C-O-H system (Gaillard and Scaillet, 2014):

$$\mathrm{CO} + \frac{1}{2}\mathrm{O_2} = \mathrm{CO_2}, \tag{1}$$

$$\mathrm{H_2} + \frac{1}{2}\mathrm{O_2} = \mathrm{H_2O}, \tag{2}$$

$$\mathrm{CH_4} + 2\mathrm{O_2} = \mathrm{CO_2} + 2\mathrm{H_2O}, \tag{3}$$

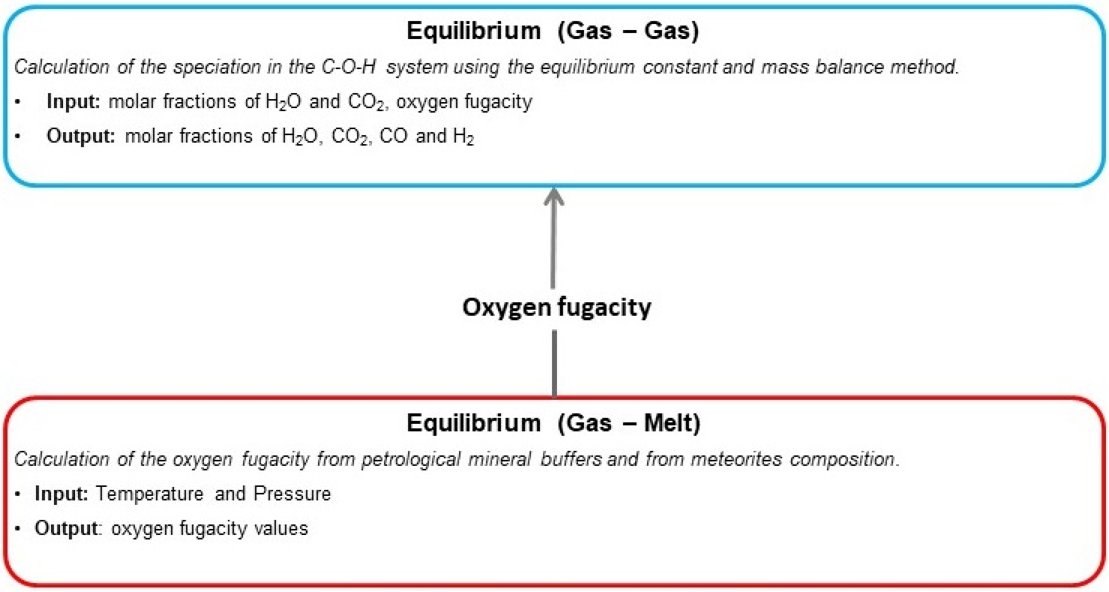

Figure 2: Schematic representation of the chemical speciation model employed to simulate the volcanic outgassing. The bottom red box describes the first phase of the simulation for calculating the composition of the outgassed volatile composition. The equilibrium between the gas phases and the melt which is used to simulate the oxygen fugacity of the system. The top light blue box includes the parameters which are used for simulating the equilibrium between the gas phases and thus, the final outgassed composition.

The system divides the C-O-H gas phases in reduced and oxidised species. Respectively, the reducing species (i.e. CO, CH_4, H_2) are present as reactants and as products there are the oxidised species which are the principal gas phases degassed at present days mantle oxidation (i.e. CO_2, H_2O) (Oppenheimer et al., 2014).

The O_2 is the oxygen partial pressure which represents the oxygen fugacity of the system. Thus, following ”Le Chatelier’s Principle”, a system at the equilibrium compensates a stress returning, if possible, to the equilibrium (Fegley, 2013). The role of the oxygen fugacity appears evident. An increase of the oxygen fugacity (i.e. an oxidising system) drives the equilibria towards the reactants producing more oxidising species. The opposite happens when the oxygen fugacity has low values (i.e. a reduced system) and the equilibria go in the directions of the products generating reducing species. In order to establish for which oxygen fugacity values a system has to be considered reduced or oxidised the petrologist introduced the concept and the reaction of ”Mineral Redox Buffers” (see section 2.4 for details). These reactions buffer the oxygen at different pressure and temperature and they describe the oxidation state of a system. Present days oxidation state values for different geodynamic context, including hot spots, divergent and convergent plates, are oxidised and within few log units around the NiNiO buffer (Fegley and Schaefer, 2014). But, during the early Earth evolution the redox state of the mantle was more reduced (Frost et al., 2008; Gaillard et al., 2011) influencing the corresponding atmospheric development and composition.

1.1.5 Volcanism across the solar system

Volcanism is a process which is spread in the rocky planets and moons of the Solar System (Wilson, 2009; Byrne, 2020; Spohn et al., 2014; Sigurdsson et al., 2015; Platz et al., 2015) and most likely in exoplanets. The volcanic activity played a role for the cooling and for the heat transfer from the interior to the surface of all the rocky planets of the Solar System (Wilson, 2009). On the planets and on the moons (i.e. the Moon and Io) the volcanism has started soon after the formation of the bodies (Byrne, 2020). On the Earth and on Io the volcanism is still active while on other bodies there is no more activity. Some possible explanations are that on the Earth the volcanism is controlled by the plate tectonics and on Io by the tidal deformation due to the presence of Jupiter. The other planets present no evidences of plate tectonic and the volcanism is driven only by radiogenic decay of heat producing elements in the interior. Another theory relates the planet size to the duration of volcanism. However, this is not always a direct connection. For instance, despite a marked difference in size, Mercury and the Moon present a similar eruptive history (Byrne, 2020). Effusive eruptions are the most common eruptive style in the Solar System. There is evidence that this style of eruption was present on Mercury, Venus, Earth, Mars, the Moon and Io (Wilson, 2009). Thus, in order to investigate volcanism of rocky planets, in the rest of the thesis the eruptions are assumed to be effusive and with a basaltic composition. Explosive eruptions are still taking place on the Earth and Io and most likely occurred on Mars (Wilson, 2009). Concerning the volatiles, the most common on the Earth and likely on Mars and Venus are water and CO_2. Due to its smaller size the Moon most probably had as major eruptive volatile CO and on Io the eruptions seem to be driven by the sulphur species (Wilson, 2009). But, during a planet evolution the principal outgassed species might change due to different redox state. Since, volcanism is/was present in all rocky bodies of the solar system in the thesis the volcanic outgassing is used as tool for investigating the composition of rocky planets and exoplanets atmospheres.

1.2 Accretion and differentiation of a planet: application to investigate the outgassed atmosphere

The composition and the origin of the mantle volatiles have influenced the evolution of the global volcanic outgassing. The formation of a planet consists of various and complex stages which are beyond the scope of this research. Nevertheless, two main processes, namely the accretion and the differentiation of a planet are strictly linked to the investigation of the global volcanic outgassing and of the atmospheric formation. The accretion process is characterised by a first phase where particles of centimetre size scales collide starting to generate the planetary embryos. When the dimension of the particles start to increase, the planetesimal growths up to reach planet sizes (Spohn et al., 2014). The provenance of the material that accreted forming the planets is still matter of debate. One possible scenario is the ”Grand Tack scenario” (Walsh et al., 2012). Numerical simulations show that likely the migration and the change of orbit of gas giant planets have influenced the composition of the material delivered on the planetary embryos producing a late heavy bombardment (Gomes et al., 2005). The accretion can be divided in two main theories of homogeneous or heterogeneous accretion. The homogeneous accretion considers that the Earth accreted from a mixture of homogeneous material and during the accretion it started to differentiate over a period characterised by a deep magma ocean (Kramers, 1998; Murthy, 1991; Righter and Drake, 2000). The heterogeneous accretion claims that the materials that accreted the Earth was delivered at different stages, starting with a reducing material to switch then to an oxidising composition (Wänke, 1981; Wänke and Dreibus, 1988; O'Neill, 1991). There are some evidences from experiments (Kegler et al., 2008; Mann et al., 2009; Righter, 2011; Rubie et al., 2011; Wade and Wood, 2005; Wood et al., 2006) and from the distribution and the abundances of the siderophile elements (Lodders and Fegley Jr, 1997; McDonough and Sun, 1995; Palme and O'Neill, 2003; Ringwood, 1979; Wänke and Dreibus, 1988) which support one or the other theory and for this reason the accretion process is still a matter of debate. The differentiation starts soon after or contemporary to the accretion. It is characterised by the segregation of the metallic core and its separation from the silicate mantle. The separation of the iron rich metal from the mantle needed high temperatures and most likely occurred during one or more magma ocean stages (Rubie et al., 2011; Stevenson, 1988; Rubie et al., 2007; Spohn et al., 2014). The accretion and the differentiation of the planet are strictly related to the outgassing history of the planet because the accretion scenario gives information about the budget of volatile phases in the mantle and the degree of differentiation about the mantle redox state. During the accretion, impacts of bodies with high volatile content can have produced a large uncertainty in the mantle (or magma ocean) volatile content of a planet (Rubie et al., 2011; Elkins-Tanton, 2008). The differentiation of the planet is characterised by the equilibrium between silicate (i.e. mantle) and liquid metallic iron rich phases (i.e. core) (Rubie et al., 2011; Stevenson, 1988; Rubie et al., 2007; Spohn et al., 2014). This equilibrium can reduce the redox state of the mantle even of 5 to 8 log units compared to after the core segregation (Scaillet and Gaillard, 2011). This produces a reducing scenario that strongly affect the outgassed volatile species and the corresponding atmospheric composition. According to Rubie et al. (2015) it is extremely hard to define the exact conditions of accretion and differentiation of a planet, thus in the rest of the thesis, I adopt a window of mantle volatile compositions and of redox states trying to cover various outgassing scenarios.

1.3 Activities and analysis in fieldtrips

The PhD project was characterised also by the participation in field trips, summer schools (e.g. Vulcano Robex international summer school, Etna International Training School of Geochemistry) and field campaign (ESA Pangaea-X Test Campaign). I took part in three editions from 2016 to 2019 of "The international Vulcano Summer school" held in Vulcano (Aeolian Islands, Italy). The Vulcano international

Summer school had the aim to bring together researchers and students with different backgrounds covering the geosciences, biology, marine geosciences and engineers. It was a great opportunity to test instruments with a multidisciplinary team on a perfect volcanic site. In the 2019 edition we tested handheld spectroscopic instruments on several outcrops in order to analyse the instruments response on different lithologies. The aim was to test the instruments with different conditions to compare the results with past and future spectroscopic data collected on extraterrestrial bodies. The results collected at the Vulcano International summer school are central for the recent published research paper entitled: ”Field investigation of volcanic deposits on Vulcano, Italy using a handheld laser-induced breakdown instrument” (section 3.4.3). The ”Etna International Training School of Geochemistry” was held at the Volcanological Observatory of Pizzi Deneri which is located on the Etna flank at an altitude of 2850 m a.s.l. The school was a great opportunity to perform in situ gas measurements on the Etna and to discover new analytical techniques applied to volcanic outgassing. This experience gave the perfect knowledge of the real volcanic outgassing process and new ideas for developing the volatile speciation model which is central for my PhD project. In 2017 I took part in the ESA campaign PANGAEA-X held in Lanzarote (Canary Islands, Spain). The campaign was composed of several research groups of different disciplines and it was designed as a training for the astronauts. I participated as part of the AGPA (Augmented field Geology and Geophysics for Planetary Analogues) group and my task was to perform seismics experiments on lava tubes. The goal was to identify the presence of lava tubes, which are of great interest for astrobiology, by using as less instrumentation as possible in order to simulate the equipment of an extraterrestrial mission. The field work was coordinated together with the groups from the Jacobs University Bremen, Julius-Maximilians-Universität Würzburg and the University of Pavia. In conclusions, the field activities gave a an opportunity to directly apply the theoretical knowledge on volcanic fluids to real cases and a better understanding of the volcanic outgassing process.

2 Methods

2.1 Introduction

This section touches several aspects of the thermodynamics of the gas phases, focusing on the volatile chemical speciation during the volcanic degassing process. All the processes are analysed considering chemical equilibrium and not the kinetics of the reactions. The following sections illustrate the principles and the thermodynamic parameters employed to investigate the volcanic outgassing including also step-by-step examples. Sections 2.2, 2.3 collect the principal parameters and the concept of the chemical equilibrium reaction. By applying the "Equilibrium and mass balance", I have developed chemical speciation models for investigating the volcanic outgassing respectively in the C-O-H and C-O-H-S system. Section 2.4 describes how the redox state affects the final volatile chemical composition. By simulating the volatile solubility, I analysed the availability of the volatile which exsolves from the magma to the gas phase (section 2.5). The volatile chemical speciation is analysed by assuming the ideal gas behaviour (section 2.6) and the real gas behaviour (sections 2.7, 2.8, 2.9), respectively. Section 2.10 shows a comparison between the numerical model used for investigating the gas chemical speciation of the C-O-H system considering ideal gas behaviour and the previous literature (i.e. the model described in Schaefer and Fegley (2017)). Every section of the methods chapter highlights the differences between the different models and for which context they are more representative. Considering the research interests of the PhD project, the chemical speciation model of the C-O-H system was the most stable and flexible for investigating the volcanic outgassing of rocky planets on a global scale. Due to these reasons, I have selected it for being employed in the development of the research papers (see section 3).

2.2 Chemical equilibrium

The following section describes some of the principal parameters involved in the study of chemical reactions at the equilibrium. The numerical model simulates the volcanic outgassing considering the equilibrium between the different gas phases. The value of the Gibbs free energy (G) is essential for investigating the chemical reactions. The Gibbs free energy indicates the direction of the reaction, and the system always tends to proceed to the lower value of G and therefore, to a low chemical potential. It is comparable to the gravitational potential, where an object tends to fall to a lower altitude for reducing its gravitational potential (Pyle, 1998). A chemical equilibrium is a system where the variations of the Gibbs energy (ΔG) between the reactants and the products is zero hence, the reaction is stable at defined temperature and pressure.

According to Fegley (2013), the Gibbs energy is known also as free energy and is defined by the equation:

$$G = H - TS, \tag{4}$$

where T is the temperature, H is the enthalpy and S the entropy of the system. The differential of the Gibbs energy is then:

$$\Delta G = \Delta H - T\Delta S, \tag{5}$$

considering that the differential of enthalpy dH is:

$$dH = TdS + VdP, \tag{6}$$

substituting 6 in 5 the dG is then:

$$dG = VdP - SdT, \tag{7}$$

according to Fegley (2013), an isothermal change in the Gibbs free energy of an ideal gas between two pressures can be expressed as:

$$G_2 - G_1 = nRT \ln \frac{P_2}{P_1}, \tag{8}$$

considering P_1 as the standard state, the Gibbs free energy of an ideal gas as function of pressure, temperature and number of moles (n):

$$G = G^0 + nRT \ln P, \tag{9}$$

The equilibrium constant can be described using an example of an equilibrium:

$$\mathrm{CO} + \frac{1}{2}\mathrm{O_2} = \mathrm{CO_2}, \tag{10}$$

the variation of the Gibbs energy at the equilibrium is then:

$$\Delta G = G_{products} - G_{reactants} = 0, \tag{11}$$

$$\Delta G = (G^0_{\mathrm{CO_2}} - G^0_{\mathrm{CO}} - \frac{1}{2}G^0_{\mathrm{O_2}}) + RT(\ln P_{\mathrm{CO_2}} - \ln P_{\mathrm{CO}} - \ln P^{1/2}_{\mathrm{O_2}}) = 0, \tag{12}$$

the first part of the equation is the variation of the Gibbs energy of reaction ($\Delta_r G^0$):

$$\Delta_r G^0 = (G^0_{\mathrm{CO_2}} - G^0_{\mathrm{CO}} - \frac{1}{2} G^0_{\mathrm{O_2}}), \tag{13}$$

where the G^0 is equal to the $\Delta_f G^0$ of the constituents. Since only the variation of G can be measured, the factors are calculated to the standard Gibbs energy of formation $\Delta_f G^0$:

$$\Delta G^0_{\mathrm{CO_2}} = \Delta_f G^0_{\mathrm{CO_2}}, \tag{14}$$

$$\Delta G^0_{\mathrm{CO}} = \Delta_f G^0_{\mathrm{CO}}, \tag{15}$$

$$\Delta G^0_{\mathrm{O_2}} = \frac{1}{2} \Delta_f G^0_{\mathrm{O_2}} = 0, \tag{16}$$

The Gibbs free energy of formation of O_2 is zero, because O_2 is the reference state of the oxygen. The reference states of the chemical elements are collected in the Chase (1999). The second term of equation 12 can be expressed as:

$$RT(\ln P_{\mathrm{CO_2}} - \ln P_{\mathrm{CO}} - \ln P^{1/2}_{\mathrm{O_2}}) = RT \ln \left(\frac{P_{\mathrm{CO_2}}}{P_{\mathrm{CO}} P^{1/2}_{\mathrm{O_2}}} \right) \tag{17}$$

Equation 12 can be written as follows:

$$\Delta G = \Delta_r G^0 + RT \ln \left(\frac{P_{\mathrm{CO_2}}}{P_{\mathrm{CO}} P^{1/2}_{\mathrm{O_2}}} \right) \tag{18}$$

considering that ΔG at equilibrium is zero, equation 18 is arranged as:

$$\Delta_r G^0 = -RT \ln \left(\frac{P_{\mathrm{CO_2}}}{P_{\mathrm{CO}} P^{1/2}_{\mathrm{O_2}}} \right) = -RT \ln K_p \tag{19}$$

K_p is the equilibrium constant of the reaction that can be written also as:

$$K_p = \exp \left(-\frac{\Delta_r G^0}{RT} \right) \tag{20}$$

Equation 20 combined with equation 19 are employed in the gas speciation models for investigating the volcanic gas release at the equilibrium and for calculating the chemical speciation.

As specified, it is assumed that the gas species follow the ideal gas behaviour. The equation of state of ideal gases is expressed as follows:

$$PV = nRT, \tag{21}$$

where P is pressure, V is volume, n quantity of component(s) (moles), R the universal gas constant and T the temperature. According to Pyle (1998), the activity of a perfect gas is equal to the gas pressures because in the ideal behaviour there are no interactions between the gas molecules. Considering an ideal behaviour the fugacity of a gas is equal to the partial pressure of the gas:

$$f = \phi P, \tag{22}$$

where f is the fugacity, P the pressure and ϕ the fugacity coefficient that in the ideal case is equal to 1. In the cases analysed in this research, I have simulated the volcanic outgassing at surface conditions considering low pressures and high temperatures. Hence, for simplicity and according to several outgassing studies (French, 1966; Holland, 1984; Gaillard and Scaillet, 2014; Fegley, 2013; Schaefer and Fegley, 2017) I have assumed an ideal behaviour of the gas species. I have compared the gas fugacities in the P-T range of interest to an assumed ideal gas behaviour. The fugacity coefficients slightly differ from one indicating no significant differences from the ideal behaviour. I have employed The Redlich-Kwong equation of state (Redlich and Kwong, 1949) (details in section 2.7) to investigate the deviations from the ideal behavior in the temperature and pressure range applied to the system.

2.3 Gibbs free energy of formation and of reaction

The first step for simulating the gas chemical speciation at the equilibrium is to evaluate which is the Gibbs energy of formation ($\Delta_f G^0$) of the molecules involved in the degassing process. For investigating the gas chemical equilibrium, I started from the calculation of the Gibbs Free Energy of formation of the molecules involved in the system from the gas reactions related to their formation. Bearing in mind that the Gibbs Free energy of formation of an element at its reference state is equal to zero (e.g. the $\Delta_f G^0$ for O_2 is zero because O_2 is the reference state of oxygen) (Fegley, 2013). For calculating the Gibbs Energy of Formation (J mol^{-1}) I used the parameterization from (Fegley, 2013) as follows:

$$\Delta_f G^0 = A + BTlogT + CT, \tag{23}$$

equation 23 is valid from 298 K to 2500 K, where T is the temperature (K), A B and C are different parameters for the gas reactions:

$$2\,H_2 + O_2 \rightleftharpoons 2\,H_2O, \tag{24}$$

Reactions for calculating the $\Delta_f G^0$ of H_2O, CO_2 and CO.	A	B	C
$2\,H_2 + O_2 \rightleftharpoons 2\,H_2O$, (25)	-483095	25.3687	21.9563
$2\,C(graphite) + O_2 \rightleftharpoons 2\,CO$, (26)	-214104	25.2183	-262.1545
$C(graphite) + O_2 \rightleftharpoons CO_2$, (27)	-392647	4.5855	-16.9762

Table 1: Standard Gibbs Energy of formation. Parameters A, B and C are collected from Fegley (2013)

Equation 23 is valid for 1 mole of products therefore, it is important to check the stoichiometry of the reaction. For instance, the reaction 24 considers 2 moles of H_2O and the $\Delta_f G^0$ is therefore 1/2 of the calculated value:

$$\Delta_f G^0_T(H_2O) = (-483095 + 25.3687 \cdot T \cdot logT + 21.9563T)/2 \tag{28}$$

the $\Delta_f G^0$ of water at 1200 K is:

$$\Delta_f G^0_{1200}(H_2O) = -1.815^{(5)}(Jmol^{-1}) \tag{29}$$

The Gibbs free energy of reaction ($\Delta_r G^0$) is another parameter for analysing the gas reactions. $\Delta_r G^0$ reflects the change of the standard Gibbs energy in a reaction and it is calculated as follows:

$$\Delta_r G^0 = \Delta_f G^0_{products} - \Delta_f G^0_{reagents} \tag{30}$$

here is an example for the equilibrium:

$$CO + 3\,H_2 \rightleftharpoons CH_4 + H_2O, \tag{31}$$

$$\Delta_r G^0_{(31)} = (\Delta_f G^0_{CH4} + \Delta_f G^0_{H2O}) - \Delta_f G^0_{\mathrm{CO}} \tag{32}$$

in the equilibrium 31 the $\Delta_f G^0_{\mathrm{H_2}}$ is zero because H_2 is the reference state of hydrogen.

2.4 Redox state and the importance of the oxygen fugacity

The oxygen fugacity ($f_{\mathrm{O_2}}$) is the partial pressure of the oxygen in a reaction and it defines the redox state of the system. It is one of the most important parameters for investigating the gas chemical reactions. For

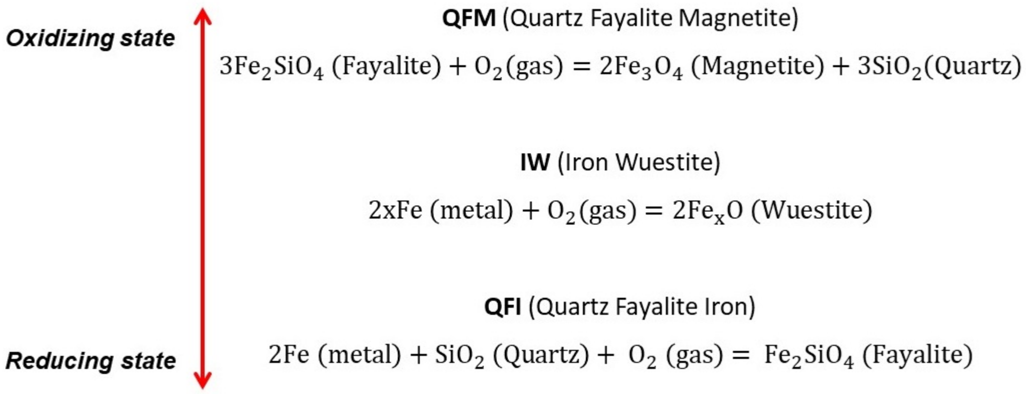

Figure 3: QFM, IW and QFI are three of the most commonly used mineral petrological buffers. The three buffers are ordered according to the oxidation state. The oxidation level and Fe oxidation number increase starting from the bottom (QFI) with Fe metal and Fe^{+2} to the top buffer (QFM) with Fe^{+2} and Fe^{+3}.

simulating different redox scenarios are employed different mineral petrological buffers. The mineral petrological buffers are an advantageous tool to simulate and to compare experiments in petrology considering different redox states. From more reducing Quartz Iron Fayalite (QIF) and Iron-Wuestite (IW) to more oxidising Quartz Fayalite Magnetite (QFM) and Nickel-Nickel-Oxide (NiNiO) states (figure 8), we assume the following buffers:

$$2\,\mathrm{Fe} + \mathrm{SiO_2} + \mathrm{O_2} \rightleftharpoons \mathrm{Fe_2SiO_4}, (\mathrm{QIF}) \tag{33}$$

$$2\,\mathrm{Fe} + \mathrm{O_2} \rightleftharpoons 2\,\mathrm{FeO}, (\mathrm{IW}) \tag{34}$$

$$3\,\mathrm{Fe_2SiO_4} + \mathrm{O_2} \rightleftharpoons 2\,\mathrm{Fe_3O_4} + 3\,\mathrm{SiO_2}, (\mathrm{QFM}) \tag{35}$$

$$\mathrm{Ni} + \frac{1}{2}\mathrm{O_2} \rightleftharpoons \mathrm{NiO}, (\mathrm{NiNiO}) \tag{36}$$

For instance, a tool for evaluating the oxygen fugacity is the ratio between the ferric (Fe^{+3}) and ferrous iron (Fe^{+2}) (Kress and Carmichael, 1991). The iron oxidation reaction in the magma is:

$$2\,\mathrm{FeO}^{\mathrm{melt}} + \frac{1}{2}\mathrm{O_2^{gas}} \rightleftharpoons \mathrm{Fe_2O_3^{melt}}, \tag{37}$$

On the reactants is present ferrous iron (oxidation number +2) while in the products there is the more oxidised ferric iron (oxidation number +3). The ratio (Fe^{3+}/Fe^{2+}) gives an indication on the oxygen fugacity of the system (Figure 3).

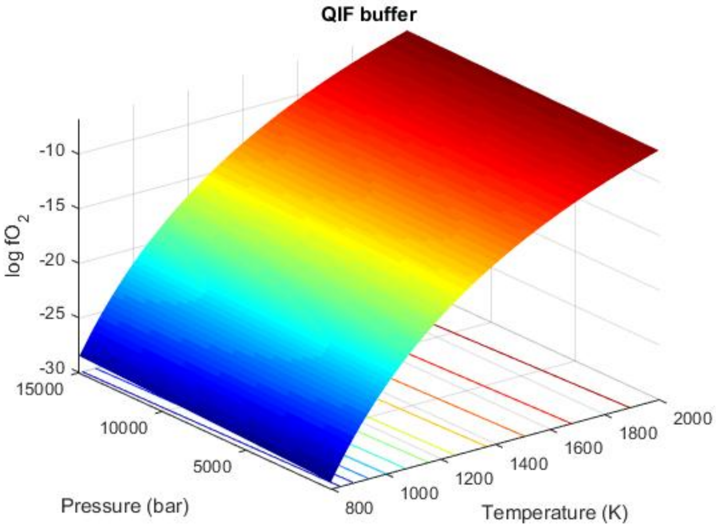

Figure 4: The 3D plot shows the influence of pressure and temperature on the QIF mineral buffers. The oxygen fugacity is affected by the temperature variation whereas pressure has a smaller effect in the investigated pressure range.

Increasing the oxygen fugacity the equilibrium is shifted to the products (i.e more oxidising state) while decreasing the oxygen fugacity produces more reducing conditions. The oxidation states in the gas speciation model is defined by selecting different mineral buffers using the following parametrization from Holloway et al. (1992) for the QIF, IW and NiNiO buffers:

$$\log_{10} f_{O_2} = A - B/T + C(P-1)/T \tag{38}$$

and the following one for the QFM buffer (Fegley, 2013):

$$\log_{10} f_{O_2} = A - B/T + C\log_{10} T + D(P-1)/T \tag{39}$$

with pressure (P) in bars, temperature (T) in Kelvin and A, B, C and D are parameters defined in table 2. The calculated mineral buffers determine the oxidation state of the system in the P-T range of interest (Figure 4).

Buffer	A	B	C	D
QIF	7.679	29673	0.05	-
IW	6.899	27714	0.05	-
QFM	5.5976	24505	0.8099	0.0937
NiNiO	8.951	24556	0.046	-

Table 2: The parameters are collected from Holloway et al. (1992) for: QIF from O'Neill (1987b), IW from O'Neill (1988) and NiNiO O'Neill (1987a). For QFM the parameters are from Fegley (2013).

2.5 Volatile solubility

The natural silicate melts are characterised by the presence of dissolved volatile species. The gas phases influence several factors of the magma from the rheology to different volcanic eruptive styles. Here, the focus is on the ratio between dissolved and exsolved volatiles and their chemical speciation. The solubility of the gas phases depends on pressure, chemical composition of the melts, and it varies according to the different gas phases. The principal interest is to analyse the role of the more common gas phases and their role in the development of rocky planet atmospheres. According to direct measurements of volatile release from worldwide volcanic emissions (Oppenheimer et al., 2014), H_2O and CO_2 represent about 90% of outgassed volatiles in different geodynamic regimes. The gas-melt in the magma are regulated by the equilibria:

$$H_2O^{(\text{fluid})} + O^{2-(\text{melt})} \rightleftharpoons 2\,OH^{-(\text{melt})} \tag{40}$$

$$CO_2^{(\text{fluid})} + O^{2-(\text{melt})} \rightleftharpoons CO_3^{2-(\text{melt})} \tag{41}$$

$$H_2^{(\text{fluid})} \rightleftharpoons H_2^{(\text{melt})} \tag{42}$$

The volatile content in the silicate melts can be simulated by applying several solubility models (e.g.: Parfitt and Wilson (2008); Iacono-Marziano et al. (2012); Newman and Lowenstern (2002); Dixon et al. (1995); Papale et al. (2006); Ghiorso and Gualda (2015)). Following the approach of Parfitt and Wilson (2008) the solubility of H_2O and CO_2 is:

$$H_2O(wt.\%) = 0.1078P^{(0.7)} \tag{43}$$

$$CO_2(wt.\%) = 0.0023P \tag{44}$$

where H_2O (wt.%) and CO_2 (wt.%) are the volatiles dissolved and P is the pressure in units of MPa. Water is more soluble than CO_2 in silicate melts, and this produces a different ratio of outgassed volatiles at different pressure. It is assumed that the H-bearing species are dissolved as H_2O and the C-bearing species as CO_2. The solubility of H_2 and CO are not considered in the simulations because their solubility in the magma is very low and they can be approximated to be not soluble in silicate melts (Oppenheimer et al., 2014; Gaillard et al., 2003; Gaillard and Scaillet, 2014).

The solubility calculations give the availability of outgassed gas phases from a silicate melt. Following

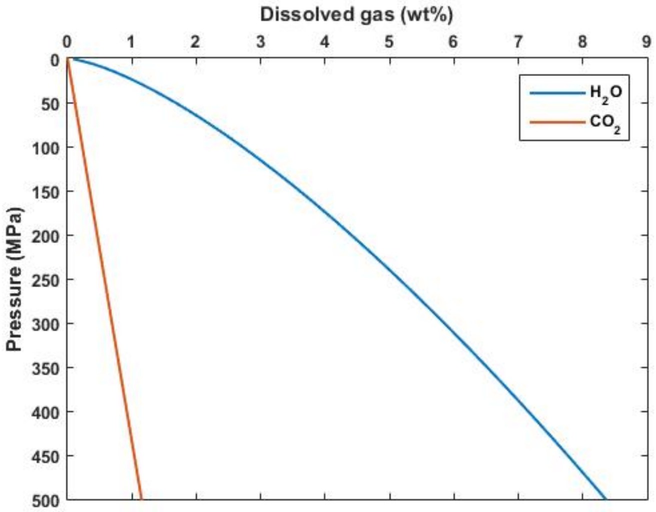

Figure 5: Solubility of H_2O and CO_2 in a basaltic melt. At low pressure both water and carbon species are outgassed whereas, at increasing pressures water is more soluble than CO_2. This produces a different ratio between the outgassed volatile species.

Parfitt and Wilson (2008) and applying equations 43 and 44 the inputs for the simulations are: the pressure interval (MPa) and the volatile content of H_2O and CO_2 in the magma in units of wt. %. The outputs are then the dissolved and the outgassed volatiles at different pressures. In the example, the selected pressure range is between 1 and 500 MPa, and the initial volatile contents for the different cases are 6, 3 and 1.5 wt. % for water and 1, 0.5 and 0.25 wt. % for CO_2. The resulting dissolved and outgassed gas phases are shown in figures 5, 6 and 7. Figure 5 shows the higher solubility of water compared to CO_2 at different pressures. The gas phases exsolve and outgas from the silicate melt when their concentrations in the magma exceed the solubility thresholds. Figures 6 and 7 show this process, where the cases with the highest volatile contents (green lines) outgas at higher pressures compared to silicate melts with a lower volatile contents (red and blue lines).

2.6 Gas chemical speciation: ideal gas behaviour

The section presents the theory and the calculations included in the gas speciation model. The gas chemical speciation of the C-O-H system is calculated considering the gas species H_2O, H_2, CO_2 and CO. These volatiles represent about 90% of the total volcanic gas release at present time on the Earth (Oppenheimer et al., 2014), and they are the more representative for investigating the atmosphere development during the early Earth history. Since the volatile chemical speciation is calculated at low pressures and high temperatures, I assumed an ideal gas behaviour. Methane is not considered in this model because it is not stable at high temperatures and low pressure (Ramirez et al., 2007; Oppenheimer et al., 2014; Chiodini, 2009; Wetzel et al., 2013) but, it will be considered in sections (2.8, 2.9). The gas speciation model simulates

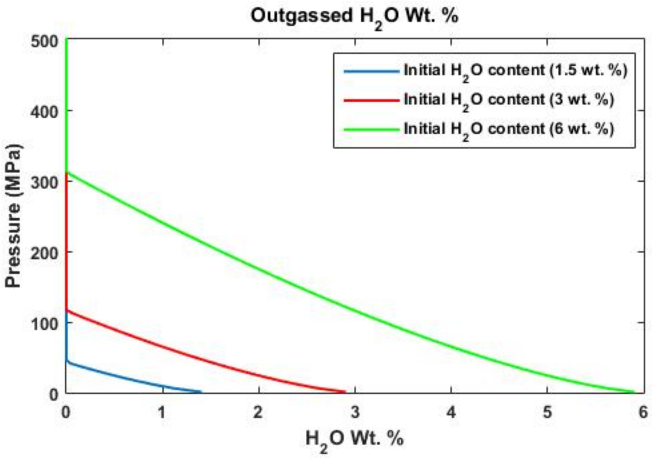

Figure 6: Outgassed H_2O at different pressures of a silicate melt with three initial water contents. The initial volatile contents are: 6 wt.% of water (green line), 3 wt.% of water (red line) and 1.5 wt.% of water (blue line). The silicate melt with the highest water content (green line) outgasses at higher pressure compared to silicate melts with lower volatile contents (red and blue lines).

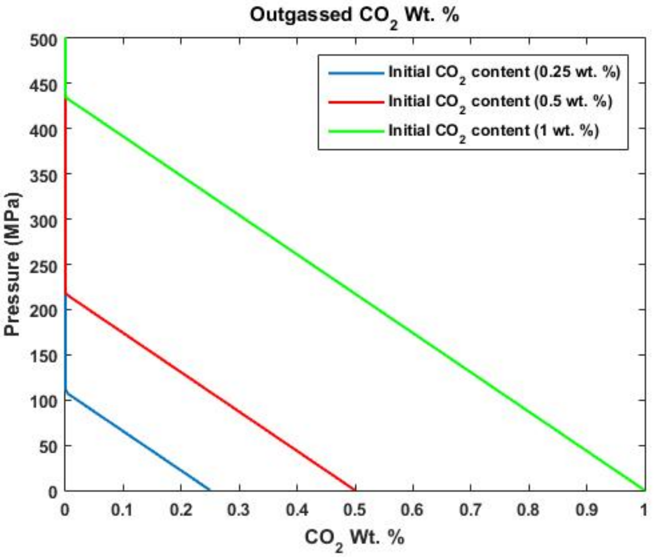

Figure 7: Outgassed CO_2 at different pressures of a silicate melt with three initial CO_2 contents. The initial volatile contents are: 1 wt.% of CO_2 (green line), 0.5 wt.% of CO_2 (red line) and 0.25 wt.% of CO_2 (blue line). The silicate melt with the highest CO_2 content (green line) outgasses at higher pressure compared to silicate melts with lower volatile contents (red and blue lines).

the volcanic outgassing via the ”Equilibrium and mass balance method” (French, 1966; Holloway, 1981; Holland, 1984; Fegley, 2013; Gaillard and Scaillet, 2014; Schaefer and Fegley, 2017) at different pressure, temperature, initial volatile content and redox state of the system. The values of oxygen fugacity calculated following Holloway et al. (1992) and Fegley (2013) are then employed to evaluate the molar fractions of the gas species in the equilibria as follows:

$$2\,H_2^{(\mathrm{fluid})} + O_2 \rightleftharpoons 2\,H_2O^{(\mathrm{fluid})}. \tag{45}$$

Considering equation 20, for estimating the proportion of H_2 and H_2O, the constant of equilibrium $K_{(eq:45)}$ is:

$$K_{(eq:45)} = \exp\left(\frac{-\Delta_r G^0_{(eq:45)}}{R \cdot T}\right) = \left(\frac{X^2_{H_2O}}{X^2_{H_2} f_{O_2}}\right), \tag{46}$$

where T is temperature in K, R is the universal gas constant (8.314 J K^{-1} mol^{-1}) and $\Delta_r G^0_{(eq:45)}$ indicates the Gibbs free energy of the reaction 45. Employing the relation expressed in equation 30:

$$\Delta_r G^0_{(eq:45)} = 2\Delta_f G^0_{H_2O}. \tag{47}$$

substituting $K_{(eq:45)}$ and the f_{O_2} calculated following the parametrization 38 and 39, the ratio between H_2 and H_2O is:

$$\left(\frac{X_{H_2O}}{X_{H_2}}\right)^2 = K_{(eq:45)} f_{O_2}, \tag{48}$$

Equation 48 shows the direct effect of the redox state on the volatile chemical speciation. The same approach is applied for simulating the gas chemical speciation of the other volatile species. For carbon species the equilibrium is:

$$CO^{(\mathrm{fluid})} + \frac{1}{2} O_2 \rightleftharpoons CO_2^{(\mathrm{fluid})}, \tag{49}$$

$$K_{(eq:49)} = \exp\left(\frac{-\Delta_r G^0_{(eq:49)}}{RT}\right) = \frac{X_{CO_2}}{X_{CO}} \frac{1}{f^{1/2}_{O_2}}, \tag{50}$$

$$\Delta_r G^0_{(eq:49)} = \Delta_f G^0_{CO_2} - \Delta_f G^0_{CO}. \tag{51}$$

As expressed at the beginning of this section, the speciation model simulates simultaneously the volatile outgassing of H_2O, H_2, CO_2 and CO. Nevertheless, I have developed also a numerical model for calculating the gas speciation of sulphur species and methane. Since it is necessary to introduce the real gas behaviour, the numerical models which includes also sulphur species and methane are described in sections 2.8 and 2.9.

Gas speciation model in the C-O-H system: a step by step example. The example shows how the model simulates the gas chemical speciation, including the different steps of the volatiles path from the mantle to the atmosphere. According to French (1966); Gaillard and Scaillet (2014); Fegley (2013); Kasting et al. (1993); Holloway (1981); Schaefer and Fegley (2017); Holland (1984) the gas speciation model of the C-O-H system simulates the volatile outgassing as a function of: temperature, pressure, redox state and volatile content of the magma. The model´s input are the melt temperature, the pressure related to the gas release and the volatile content, in terms of H_2O and CO_2 mole fractions in the magma. The outputs are the redox state of system and the outgassed mole fractions of H_2O, H_2, CO_2 and CO. The model does not calculate the outgassing of methane since the outgassing is simulated at surface. Methane is not stable in the low pressure range of investigation but for high pressure within the mantle (Zhang and Duan, 2009; Wetzel et al., 2013). The input values of the model for the step-by-step example are: pressure 200 bar, temperature interval 800-1200 K, magma volatile content of H_2O 3.0 wt.% and CO_2 0.5 wt.%. The chemical speciation is coupled with the volatile solubility. The first step is to determine the outgassed molar fraction of volatiles comparing the difference between the dissolved volatiles calculated with the equations 43 and 44 and the initial volatile content of the silicate melt as follows:

$$\text{dissolved H}_2\text{O }(wt.\%) = 0.1078P^{(0.7)} = 0.1078 \cdot (200/10)^{(0.7)} = 0.877(wt.\%) \tag{52}$$

$$\text{dissolved CO}_2\text{ }(wt.\%) = 0.0023P = 0.0023 \cdot 200/10 = 0.046(wt.\%) \tag{53}$$

$$\begin{gathered}\text{outgassed H}_2\text{O }(wt\%) = \text{initial H}_2\text{O (wt\%)} - \text{dissolved H}_2\text{O (wt\%)} = \\ 3(wt\%) - 0.877(wt\%) = 2.123(wt\%),\end{gathered} \tag{54}$$

$$\begin{gathered}\text{outgassed CO}_2\text{ }(wt\%) = \text{initial CO}_2\text{ (wt\%)} - \text{dissolved CO}_2\text{ (wt\%)} = \\ 0.5(wt\%) - 0.046(wt\%) = 0.454(wt\%),\end{gathered} \tag{55}$$

the outgassed volatiles are then 2.123 (wt%) for H_2O and for 0.454 (wt%) CO_2. H_2 and CO are assumed to be not soluble in silicate melt. At this point the outgassed values are arranged for expressing the mole

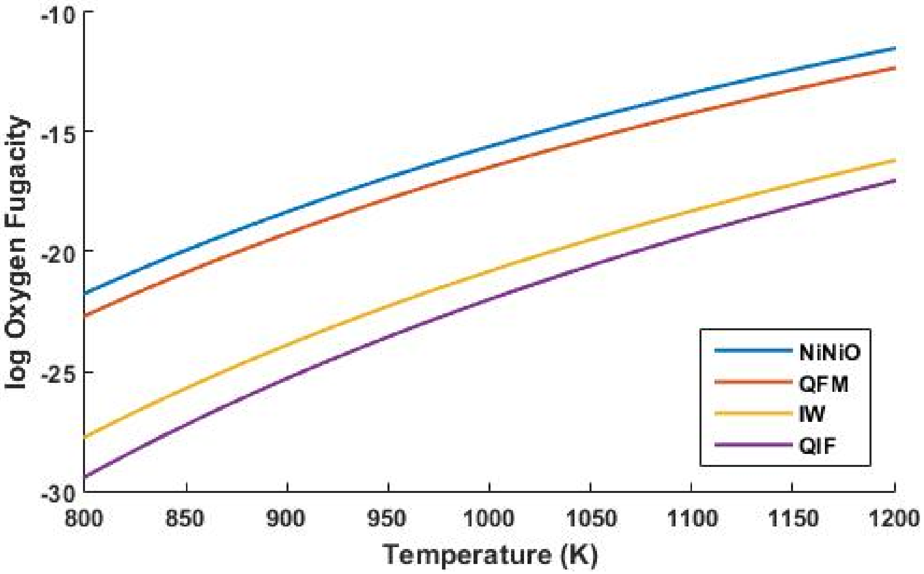

Figure 8: Petrological mineral buffers as function of temperature (Holloway et al., 1992; Fegley, 2013).

fraction of the volatiles:

$$\text{molar fraction } H_2O = \frac{H_2O\ (\text{wt\%})\ /\ \text{Molecular weight } H_2O}{\left(\frac{H_2O\ (\text{wt\%})}{\text{Molecular weight } H_2O}\right) + \left(\frac{CO_2\ (\text{wt\%})}{\text{Molecular weight } CO_2}\right)} = \frac{2.123/18}{(2.123/18) + (0.454/44)} = 0.9195 \tag{56}$$

$$\text{molar fraction } CO_2 = \frac{CO_2\ (\text{wt\%})\ /\ \text{Molecular weight } CO_2}{\left(\frac{H_2O\ (\text{wt\%})}{\text{Molecular weight } H_2O}\right) + \left(\frac{CO_2\ (\text{wt\%})}{\text{Molecular weight } CO_2}\right)} = \frac{0.454/44}{(2.123/18) + (0.454/44)} = 0.0805 \tag{57}$$

The molar fractions are used for simulating the gas chemical speciation at different redox states. The different mineral buffers are calculated by using equations 38 and 39 (figure 8).

The next step is to calculate the $\Delta_f G^0$ of H_2O, CO_2 and CO considering the parametrization 23, where $\Delta_f G^0$ of H_2 and O_2 are zero because H_2 and O_2 are the standard state of hydrogen and oxygen. The equilibria involved are:

$$2\,H_2 + O_2 \rightleftharpoons 2\,H_2O, \tag{58}$$

$$CO + \frac{1}{2}\,O_2 \rightleftharpoons CO_2, \tag{59}$$

and the $\Delta_r G^0$ of equilibrium 58 and 59 are:

$$\Delta_r G^0_{(eq:58)} = 2 \cdot \Delta_f G^0_{\mathrm{H_2O}} = -3.63 \cdot 10^5, \tag{60}$$

$$\Delta_r G^0_{(eq:59)} = \Delta_f G^0_{\mathrm{CO_2}} - \Delta_f G^0_{\mathrm{CO}} = -1.78 \cdot 10^5, \tag{61}$$

At this stage, the model includes all the necessary parameters for simulating the gas chemical speciation at 200 bar and within the temperature interval 800 - 1200 K. The molar fraction of the species involved for 1200 K and 200 bar are associated to the chemical equilibrium constant (K) as:

$$K_{(eq:58)} = \exp\left(\frac{-\Delta_r G^0_{(eq:58)}}{R{\cdot}T}\right) = \left(\frac{X^2_{\mathrm{H_2O}}}{X^2_{\mathrm{H_2}} f_{\mathrm{O_2}}}\right), \tag{62}$$

where:

$$\left(\frac{X_{\mathrm{H_2O}}}{X_{\mathrm{H_2}}}\right) = (K_{(eq:58)} f_{\mathrm{O_2}})^{1/2}, \tag{63}$$

and for carbon species:

$$K_{(eq:59)} = \exp\left(\frac{-\Delta_r G^0_{(eq:59)}}{RT}\right) = \frac{X_{\mathrm{CO_2}}}{X_{\mathrm{CO}}} \frac{1}{f^{1/2}_{\mathrm{O_2}}}, \tag{64}$$

where:

$$\frac{X_{\mathrm{CO_2}}}{X_{\mathrm{CO}}} = K_{(eq:59)} f^{1/2}_{\mathrm{O_2}}, \tag{65}$$

$K_{(eq:58)}$ and $K_{(eq:59)}$ are calculated as follows:

$$K_{(eq:58)} = \exp\left(\frac{-\Delta_r G^0_{(eq:58)}}{R \cdot T}\right) = \exp\left(\frac{-2\Delta_f G^0_{\mathrm{H_2O}}}{R \cdot T}\right) = \exp\left(\frac{-2 \cdot (-1.8150 \cdot 10^5)}{8.314 \cdot 1200}\right) = 6.338 \cdot 10^{15}, \tag{66}$$

$$\begin{gathered} K_{(eq:59)} = \exp\left(\frac{-\Delta_r G^0_{(eq:59)}}{R \cdot T}\right) = \exp\left(\frac{-(\Delta_f G^0_{\mathrm{CO_2}} - \Delta_f G^0_{\mathrm{CO}})}{R \cdot T}\right) = \\ \exp\left(\frac{-(-3.9607 \cdot 10^5 + 2.1775 \cdot 10^5)}{8.314 \cdot 1200}\right) = 5.7863 \cdot 10^7, \end{gathered} \tag{67}$$

knowing $K_{(eq:58)}$ and $K_{(eq:59)}$ and the $f_{\mathrm{O_2}}$ for the different mineral buffers, the ratio of hydrogen and carbon species for the QIF are:

$$\left(\frac{X_{H_2O}}{X_{H_2}}\right) = (K_{(eq:58)} f_{O_2})^{1/2} = [(6.338 \cdot 10^{15}) \cdot (9.116 \cdot 10^{-18})]^{1/2} = 0.2404, \tag{68}$$

following the approach of Fegley (2013), the outgassed hydrogen volatiles is a mixture of H_2 and H_2O, the O_2 is not considered since it is several orders of magnitude smaller compared to H_2 and H_2O. Considering that the total molar fraction of hydrogen species is 0.9195 (from equation 56), the molar fractions are:

$$X_{H_2O} + X_{H_2} = 0.2404 X_{H_2} + X_{H_2} = 0.9195, \tag{69}$$

$$X_{H_2} = \frac{0.9195}{0.2404 + 1} = 0.7413, \tag{70}$$

$$X_{H_2O} = 0.9195 - 0.7413 = 0.1782, \tag{71}$$

The same calculations are performed for the carbon species, where the total outgassed molar fraction is 0.0805 (from equation 57):

$$\frac{X_{CO_2}}{X_{CO}} = K_{(eq:59)} f_{O_2}^{1/2} = (5.786 \cdot 10^{7}) \cdot (9.116 \cdot 10^{18})^{1/2} = 0.1747, \tag{72}$$

$$X_{CO_2} + X_{CO} = 0.1747 X_{CO} + X_{CO} = 0.0805, \tag{73}$$

$$X_{CO} = \frac{0.0805}{0.1747 + 1} = 0.0685, \tag{74}$$

$$X_{CO_2} = 0.0805 - 0.0685 = 0.0120. \tag{75}$$

The resulting gas composition, outgassed from a melt with an initial volatile content of 3 wt.% of H_2O and 0.5 wt.% of CO_2, at 1200 K, 200 bar and in equilibrium with the QFI mineral buffer is: 74.13% H_2, 17.82% H_2O, 1.12% CO_2 and 6.85% CO (expressed in % in vol.). Since the QFI mineral buffer reproduces a reducing state, the dominant outgassed phases are H_2 and CO instead of the oxidising species H_2O and CO_2. Figure 9 and 10 display the gas chemical speciation considering the same input as the example above but, for various mineral buffers and within the temperature interval 800 - 1200 K. Figure 9 shows the molar fractions of outgassed volatiles. As expected, in oxidising conditions (QFM and NiNiO buffers) the

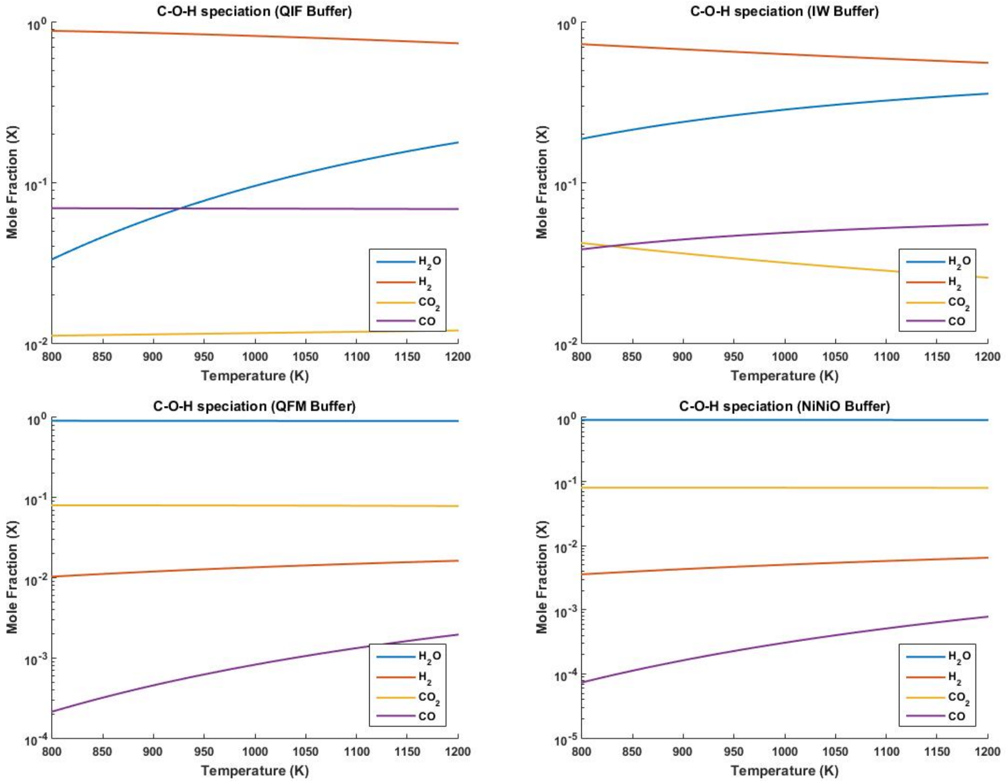

Figure 9: Gas chemical speciation at oxidising (QFM and NiNiO buffers) and reducing states (IW and QIF buffers).

principal species are H_2O and CO_2 whereas H_2 and CO govern the outgassing in reduced states (QIF and IW buffers). Figure 10 highlights the differences in outgassed species comparing the ratios of H_2/H_2O and CO/CO_2.

The same simulations can be run even by combining other solubility models to the chemical speciation model. For instance, the aforementioned example was simulated also following the Iacono-Marziano et al. (2012) solubility approach. Considering the same starting conditions, the input for the simulation are: pressure 200 bar, temperature interval 800-1200 K, magma volatile content of H_2O 3.0 wt.% and CO_2 0.5 wt.%. Considering the Iacono-Marziano et al. (2012) solubility model, the outgassed volatiles are 1.766 wt.% of H_2O and 0.499 wt.% of CO_2 (The solubility data were collected by using the simulations from Sara Vulpius at the Freie Universitaet Berlin). The different values of outgassed species compared to the results collected with the parametrization of Parfitt and Wilson (2008) will affect also the final outgassed composition. At the same outgassing conditions (i.e. 1200 K and 200 bar) the final volatile composition for the QIF buffer is: 72.27 % H_2, 17.37 % H_2O, 1.54 % CO_2 and 8.82 % CO. The principal difference of the results collected with the solubility model of Parfitt and Wilson (2008) and Iacono-Marziano et al. (2012) is the outgassed wt.% of H_2O, which is slightly higher for the Parfitt and Wilson (2008) (2.123 wt. % H_2O) simulations compared to Iacono-Marziano et al. (2012) (1.766 wt. % H_2O). This affects the ratio of

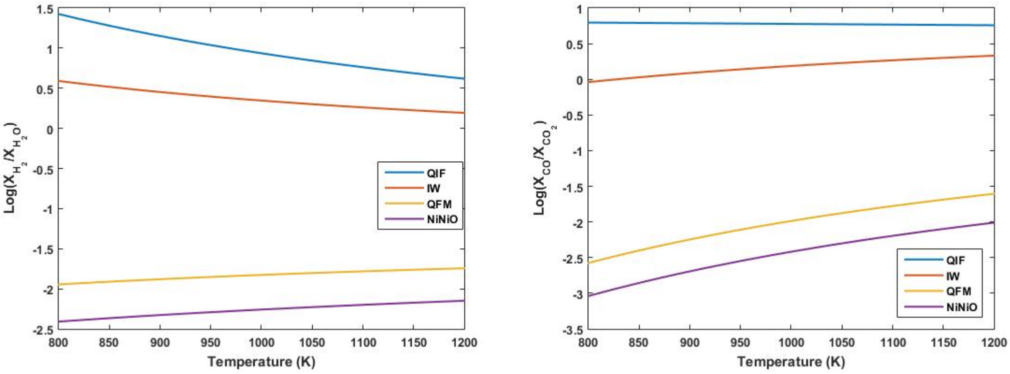

Figure 10: CO/CO_2 and H_2/H_2O ratios at different redox states.

outgassed hydrogen (H_2 and H_2O) and carbon (CO and CO_2) species producing an higher outgassing of CO in the results collected with the Iacono-Marziano et al. (2012) solubility parametrization. The difference between the two simulations demonstrates that the outgassed composition is affected also by the solubility model employed in the degassing simulations. Thus, the possibility to select between different solubility models shows the versatility of the chemical speciation model. Moreover, the chemical speciation model can be coupled also with mantle convection and atmospheric models. Sections 3.1, 3.2 and 3.3 collect some of its applications in research papers.

2.7 Gas chemical speciation: real gas behaviour

The paragraph includes the theory and the Redlich-Kwong (Redlich and Kwong, 1949) equation of state which are employed to simulate the chemical equilibrium reactions assuming a real gas behaviour. Here are considered also methane and sulphur species (SO_2, H_2S and S_2) as outgassed volatiles. The real gas behaviour has to be assumed for calculating the outgassing at low temperatures and high pressures. The ideal behaviour of the gas phases follows the equation 21 and it is assumed that there are no interactions between the gas species. This is not the case in the real behaviour where at high pressure and low temperatures the gases have interactions with each other. Following Redlich and Kwong (1949) and Fegley (2013) I have developed a numerical model to calculate the fugacity of: H_2O, H_2, CO_2, CO, CH_4, SO_2 and H_2S. The compression factor (Z) is a parameter can be expressed as:

$$Z = \frac{PV_m}{RT}, \tag{76}$$

where P is the pressure (in bar), V_M is the molar volume (in cm^3/mol). In the ideal case the compression factor is always unity but not for the real case. The compression factor is a necessary parameter for investigating the fugacity coefficient. There are different equations for studying the real behaviour and one of the most used is the Redlich-Kwong (Redlich and Kwong, 1949) equation which is a modifications of the van der Waals equation and can be expressed as:

$$P = \frac{RT}{V_m - b} - \frac{a}{\sqrt{T}(V_m(V_m + b))}, \tag{77}$$

The a and b are the van der Waals parameters. a is associated to the attractive forces between the molecules (in: $10^{-}4$ cm^6 bar K$^{0.5}$ mol^{-2}) and b is the co-volume (in: cm^3 mol^{-1}). A list of the a and b parameters for the van der Waals or Redlich Kwong equation can be found in Fegley (2013). The Redlich Kwong equation can be arranged as:

$$Z = 1/(1 - h) - (A^2/B)h/(1 + h), \tag{78}$$

$$A^2 = a/R^2T^{2.5} = 0.42748T_c^{2.5}/P_cT^{2.5}, \tag{79}$$

$$B = b/RT = 0.08664T_c/P_cT, \tag{80}$$

$$h = BP/Z = b/V, \tag{81}$$

where T_c (in K) and P_c (in bar) are respectively the critical temperature and the critical pressure of the gas species that are the T and P at the critical point which is the point where there is no distinction for gas and liquid phase (e.g. the critical point of water is 647.14 K and 220.5 bar (Fegley, 2013)).

Equation 77 can be expressed as:

$$(P + \frac{a}{\sqrt{T}(V_m(V_m + b))})(V_m - b) = RT, \tag{82}$$

$$\frac{P(T^{1/2}(V_m(V_m + b)) + a}{\sqrt{T}(V_m(V_m + b))}(V_m - b) = RT, \tag{83}$$

$$\frac{P(T^{1/2}(V_m(V_m + b)(V_m - b)) + a(V_m - b)}{\sqrt{T}(V_m(V_m + b))} = RT, \tag{84}$$

$$P(T^{1/2}((V_m(V_m + b)(V_m - b))) + a(V_m - b) = RT(T^{1/2}(V_m(V_m + b)), \tag{85}$$

$$P(T^{1/2}V_m^3 - V_m^2RT(T^{1/2}) + V_m(a - PT^{1/2}b^2 - RTbT^{1/2}) - ab = 0, \tag{86}$$

$$V_m^3 - V_m^2(RT/P) + V_m(\frac{a}{PT^{1/2}} - b^2 - \frac{RTb}{P})\frac{ab}{PT^{1/2}} = 0, \tag{87}$$

$$V_m^3 - V_m^2(RT/P) + V_m\frac{1}{P}(\frac{a}{PT^{1/2}} - b^2 - \frac{RTb}{P}) - \frac{ab}{PT^{1/2}} = 0, \tag{88}$$

Considering that from equations 79 and 80 a and b are:

$$a = 0.4278\frac{T_c^{2.5}R^2}{P_c}, \tag{89}$$

$$b = 0.08664\frac{T_cR}{P_c}, \tag{90}$$

Substituting a and b equation 77 can be expressed also as:

$$V_m^3 - (RT/P)V_m^2 + (1/P)\cdot(A/T^{0.5} - BRT - PB^2)V_m - AB/PT^{0.5} = 0, \tag{91}$$

substituting the V_m considering the equation 76 and assuming as A' and B' the equation is:

$$A' = \frac{aP}{T^{2.5}R^2}, \tag{92}$$

$$B' = \frac{bP}{RT}, \tag{93}$$

$$Z^3 - Z^2 + Z(A' - B'^{(2)} - B') - A'B' = 0, \tag{94}$$

For facilitating the simulations equation 94 can be expressed also as:

$$Z^3 - Z^2 + Z(P_r/T_r)\cdot(0.42748/T_r^{1.5} - 0.08664 - 0.007506\cdot(P_r/T_r)) - 0.03704(P_r^2/T_r^{3.5}) = 0, \tag{95}$$

where T_r and P_r are respectively temperature and pressure reduced ($T_r = T/T_c$ and $P_r = P/P_c$). The numerical model solves the cubic equation 95 using the parameters expressed in table 3. According to Redlich and Kwong (1949), the fugacity coefficient (ϕ) is associated to Z as follows:

$$\ln\phi = Z - 1 - \ln(Z - BP) - (A^2/B)\ln(1 + BP/Z), \tag{96}$$

the fugacity is then calculated as follows:

$$f = \phi P, \tag{97}$$

The fugacity describes the volatile behaviour in a high pressure context such as the volatile solubility in a silicate melt or in the passive outgassing within the lithosphere.

Gas	T_c (K)	P_c (bar)	V_c	V_m
H_2O	674.14	220.5	56	12
H_2	33.2	12.97	65	15.2
CO_2	304.1	73.75	0.274	23
CO	132.91	34.99	93	27.3
CH_4	190.58	46.04	99	29.7
SO_2	430.8	78.48	122	34.7
H_2S	373.2	89.4	98	20

Table 3: T_c is the critical temperature in K, P_c the critical pressure, V_c is critical volume (in cm^3/mol) and V_m the molar volume used in the model . T_c, P_c, V_c are from Fegley (2013). V_m of H_2O and CO_2 are from Dixon et al. (1995) and all the others V_m are from Fegley (2013).

2.8 Gas chemical speciation model C-O-H including CH_4

The section includes the theory behind the volatile chemical speciation model for the C-O-H system with a real gas behaviour considering as outgassed species: H_2O, H_2, CO_2, CO and CH_4. Methane is a gas of particular interest concerning the volatile outgassing at low temperature and also in hydrothermal ambient and it is considered a volatile with implication for the emergence of live in extreme environment. For simulating the volatile outgassing of the system, I applied the same approach described in section 2.6 but including different chemical equilibria. According to Huizenga (2001, 2005), the equilibria involved in the system are the following:

$$CO + \frac{1}{2}O_2 = CO_2, \tag{98}$$

$$H_2 + \frac{1}{2}O_2 = H_2O, \tag{99}$$

$$CH_4 + 2O_2 = CO_2 + H_2O, \tag{100}$$

$$C + O_2 = CO_2, \tag{101}$$

the equilibrium constants K are:

$$K_{(eq:98)} = \frac{X_{\mathrm{CO_2}}\phi_{\mathrm{CO_2}}}{X_{\mathrm{CO}}\phi_{\mathrm{CO}}f_{\mathrm{O_2}}^{1/2}}, \tag{102}$$

$$K_{(eq:99)} = \frac{X_{\mathrm{H_2O}}\phi_{\mathrm{H_2O}}}{X_{\mathrm{H_2}}\phi_{\mathrm{H_2}}f_{\mathrm{O_2}}^{1/2}}, \tag{103}$$

$$K_{(eq:100)} = \frac{X_{\mathrm{CO_2}}\phi_{\mathrm{CO_2}}X_{\mathrm{H_2O}}^2\phi_{\mathrm{H_2O}}^2P_{fluid}^2}{X_{\mathrm{CH_4}}\phi_{\mathrm{CH_4}}f_{\mathrm{O_2}}^2}, \tag{104}$$

$$K_{(eq:101)} = \frac{X_{\mathrm{CO_2}}\phi_{\mathrm{CO_2}}P_{fluid}}{a_{carbon}f_{\mathrm{O_2}}}, \tag{105}$$

where X_i is the molar fraction of the i species, ϕ_i is the fugacity of the i species, P_{fluid} is the pressure where the volatile chemical speciation and a_{carbon} is the carbon activity. If the system is graphite saturated the a_{carbon} is 1, if the system is undersaturated in graphite the carbon activity is in between $0 < a_{carbon} < 1$. Following Huizenga (2005), for estimating the molar fractions the system can be arranged as:

$$X_{\mathrm{H_2O}} + X_{\mathrm{CO_2}} + X_{\mathrm{H_2}} + X_{\mathrm{CO}} + X_{\mathrm{CH_4}} = 1, \tag{106}$$

$$X_{\mathrm{CO_2}} = \left[\frac{K_{(eq:101)}a_{\mathrm{carbon}}}{\phi_{\mathrm{CO_2}}P_{fluid}}\right]_{C_{107}} f_{\mathrm{O_2}} \tag{107}$$

$$X_{\mathrm{CO}} = \left[\frac{\phi_{\mathrm{CO_2}}}{K_{(eq:98)}\phi_{\mathrm{CO}}}\right]_{C_{108}} 1/f_{\mathrm{O_2}}^{1/2}X_{\mathrm{CO_2}} \tag{108}$$

$$X_{\mathrm{H_2}} = \left[\frac{\phi_{\mathrm{H_2O}}}{K_{(eq:99)}\phi_{\mathrm{H_2}}}\right]_{C_{109}} 1/f_{\mathrm{O_2}}^{1/2}X_{\mathrm{H_2O}} \tag{109}$$

$$X_{\mathrm{CH_4}} = \left[\frac{\phi_{\mathrm{CO_2}}\phi_{\mathrm{H_2O}^2}P_{fluid}^2}{K_{(eq:100)}\phi_{\mathrm{CH_4}}}\right]_{C_{110}} 1/f_{\mathrm{O_2}}^2X_{\mathrm{H_2O}}^2X_{\mathrm{CO_2}} \tag{110}$$

the system now is composed of 5 equations and 5 unknowns. Substituting $X_{\mathrm{CO_2}}$ from equation 107 in equation 110 and then substituting the molar fractions from equations 107 to 110 the system is now expressed only as a function of $X_{\mathrm{H_2O}}$ as:

$$C_{107}C_{110}f_{\mathrm{O_2}}^{-1}X_{\mathrm{H_2O}}^2 + (C_{109}f_{\mathrm{O_2}}^{1/2} + 1)X_{\mathrm{H_2O}} + C_{107}f_{\mathrm{O_2}}(1 + C_{108}f_{\mathrm{O_2}}^{-1/2}) = 1 \tag{111}$$

The positive root of equation 111 gives the molar fraction of H_2O that can be susbituted in equations 107

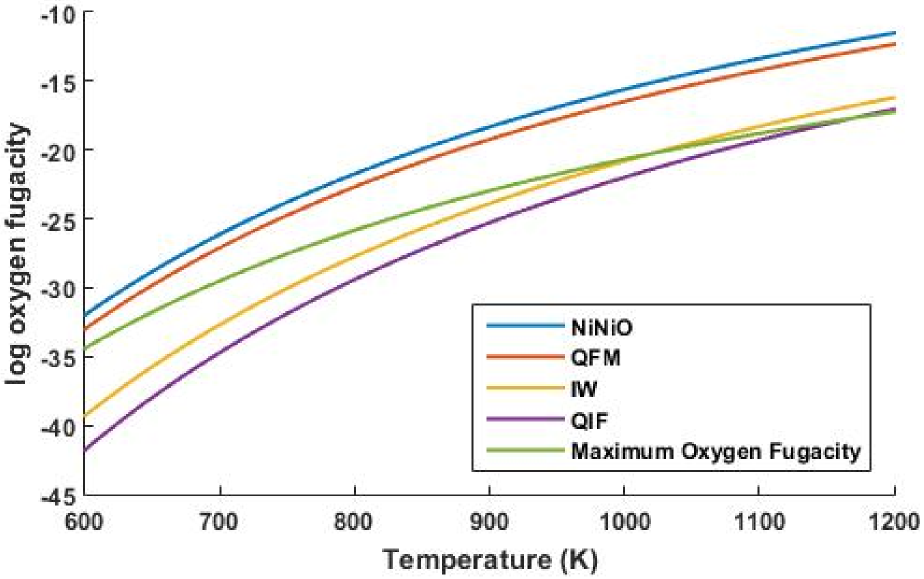

Figure 11: Petrological mineral buffers as a function of temperature (NiNiO, QFM, IW, QIF) (Holloway et al., 1992; Fegley, 2013) and maximum level of oxygen fugacity where the system is stable (Huizenga, 2005).

to 110 to obtain the molar fractions of CO, H_2, CO_2 and CH_4. The system is stable and valid at temperature below the one at which the CO_2 is consumed by the reaction:

$$f_{O_2} = \frac{\phi_{CO_2} P_{fluid}}{a_{carbon} K_{(eq:101)}} \tag{112}$$

The following example shows the effect of the temperature on the system and particularly on the oxygen fugacity, where the volatile chemical speciation is simulated at different mineral buffers in the temperature interval $600 < T < 1200K$ and at 1 bar of pressure. Figure 11 shows the maximum level of oxygen fugacity compared to the mineral buffers. The NiNiO and QFM buffers reproduce scenarios too oxidised for the stability of methane while the IW and QIF simulate stable conditions below around 900 K and 1000 K, respectively. Figure 12 displays the molar fractions of the volatiles species where the more reduced species including CH_4 and H_2 are the principal outgassed volatile. The outgassing of carbon species is dominated by methane because it is the most stable phase at low temperature and in reducing oxidation states.

2.9 Gas chemical speciation model C-O-H-S

Following French (1966); Holloway (1981); Huizenga (2001), the numerical model for investigating the ougassing of the C-O-H-S system considers a real gas behaviour. In terms of temperature and pressure, the simulations present a smaller range of investigation compared to a system without sulphur species (e.g.

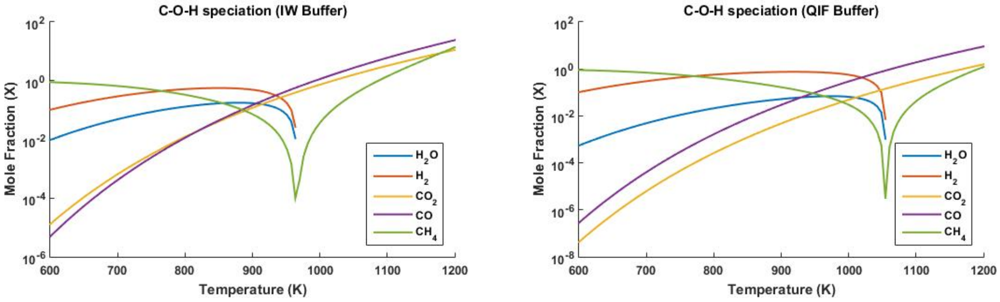

Figure 12: Volatile chemical speciation at different mineral redox buffers as a function of temperature. The range of validity is up to 900 K for the IW buffer and up to 1000 K for the QIF buffer.

sections 2.6 and 2.8) . The limitations depend on the real gas behaviour and on the stability of the selected sulphur fugacity buffer (i.e. 576 K $<$ Temperature $<$ 1016 K). Also the selection of the equation of state and of the carbon activity influence the outgassed composition. The model employs the Redlich-Kwong equation of state (Redlich and Kwong, 1949). The carbon activity is fixed to the value of 1 because the simulated system is considered graphite saturated. The equilibria involved in the simulations are:

$$\mathrm{C} + \frac{1}{2}\mathrm{O_2} = \mathrm{CO}, \tag{113}$$

$$\mathrm{C} + \mathrm{O_2} = \mathrm{CO_2}, \tag{114}$$

$$\mathrm{C} + 2\mathrm{H_2} = \mathrm{CH_4}, \tag{115}$$

$$\mathrm{H_2} + \frac{1}{2}\mathrm{O_2} = \mathrm{H_2O}, \tag{116}$$

$$\mathrm{H_2} + \frac{1}{2}\mathrm{S_2} = \mathrm{H_2S}, \tag{117}$$

$$\frac{1}{2}\mathrm{S_2} + \mathrm{O_2} = \mathrm{SO_2}, \tag{118}$$

The chemical composition of the gas phases is then:

$$P_{tot} = \frac{f_{\mathrm{H_2}}}{\phi_{\mathrm{H_2}}} + \frac{f_{\mathrm{H_2O}}}{\phi_{\mathrm{H_2O}}} + \frac{f_{\mathrm{H_2S}}}{\phi_{\mathrm{H_2S}}} + \frac{f_{\mathrm{SO_2}}}{\phi_{\mathrm{SO_2}}} + \frac{f_{\mathrm{CH_4}}}{\phi_{\mathrm{CH_4}}} + \frac{f_{\mathrm{CO_2}}}{\phi_{\mathrm{CO_2}}} + \frac{f_{\mathrm{CO}}}{\phi_{\mathrm{CO}}}, \tag{119}$$

where P_{tot} is the selected pressure for investigating the speciation (e.g. 1 atm at surface outgassing), f_i and ϕ_i are respectively the fugacity and the fugacity coefficient of the species i. The oxygen fugacity is calculated for the mineral buffers according to equations 38 and 39 and the sulphur fugacity, for the Pyrite (FeS_2)-Pyrrhotite (Fe_7S_8) buffer:

$$7FeS_2 = 3S_2(gas) + Fe_7S_8 \tag{120}$$

The sulphur fugacity is valid in the interval 567 K to 1016 K which, is simulated following Lusk and Bray (2002) modified by Fegley (2013):

$$\log_{10} f_{S_2} = 19.41 - 21004/T + 2061770/T^2 \tag{121}$$

The fluid composition is calculated at specified P, T, f_{O_2}, f_{S_2} and considering graphite (C) saturation (i.e. carbon activity = 1). If the graphite is not saturated the carbon activity is between 0 and 1. The fugacity coefficients and the fugacities are calculated according to 96 and equation 97. Taking the equations from 113 to 119 there are 7 equations and 7 unknowns (P_{H_2}, P_{H_2O}, P_{H_2S}, P_{SO_2}, P_{CH_4}, P_{CO_2}, P_{CO}), the system can be expressed as:

$$K_{(eq:113)} = \frac{f_{CO}}{a_{(C)} f_{O_2}^{1/2}} = \frac{\phi_{CO} P_{CO}}{f_{O_2}^{1/2}}, \tag{122}$$

$$K_{(eq:114)} = \frac{f_{CO_2}}{a_{(C)} f_{O_2}} = \frac{\phi_{CO_2} P_{CO_2}}{f_{O_2}}, \tag{123}$$

$$K_{(eq:115)} = \frac{f_{CH_4}}{a_{(C)} f_{H_2}^2} = \frac{\phi_{CH_4} P_{CH_4}}{(\phi_{H_2} P_{H_2})^2}, \tag{124}$$

$$K_{(eq:116)} = \frac{f_{H_2O}}{f_{H_2} f_{O_2}^{1/2}} = \frac{\phi_{H_2O} P_{H_2O}}{\phi_{H_2} P_{H_2} f_{O_2}^{1/2}}, \tag{125}$$

$$K_{(eq:117)} = \frac{f_{H_2S}}{f_{H_2} f_{S_2}^{1/2}} = \frac{\phi_{H_2S} P_{H_2S}}{\phi_{H_2} P_{H_2} f_{S_2}^{1/2}}, \tag{126}$$

$$K_{(eq:118)} = \frac{f_{SO_2}}{f_{S}^{1/2} f_{O_2}} = \frac{\phi_{SO_2} P_{SO_2}}{f_{S_2}^{1/2} f_{O_2}}, \tag{127}$$

the partial pressures can be written isolating H_2 and H_2O and coupling some parameters (C_i) for the different equilibria :

$$P_{CO} = \left[\frac{K_{113} f_{O_2}^{1/2} a_C}{\phi_{CO}} \right]_{C_{122}} \tag{128}$$

$$P_{CO_2} = \left[\frac{K_{114} f_{O_2} a_C}{\phi_{CO_2}}\right]_{C_{123}} \tag{129}$$

$$P_{CH_4} = \left[\frac{K_{115} (\phi_{H_2})^2 a_C}{\phi_{CH_4}}\right]_{C_{124}} (P_{H_2})^2 \tag{130}$$

$$P_{H_2O} = \left[\frac{\phi_{H_2} K_{116} (f_{O_2})^{1/2}}{\phi_{H_2O}}\right]_{C_{125}} P_{H_2} \tag{131}$$

$$P_{H_2S} = \left[\frac{\phi_{H_2} K_{117} (f_{S_2})^{1/2}}{\phi_{H_2S}}\right]_{C_{126}} P_{H_2} \tag{132}$$

$$P_{SO_2} = \left[\frac{f_{O_2} K_{118} (f_{S_2})^{1/2}}{\phi_{SO_2}}\right]_{C_{127}} \tag{133}$$

arranging the equations from 128 to 133 as H_2 is the only variable, equation 119 can be expressed as a quadratic equation:

$$P_{tot} = C_{124}(P_{H_2})^2 + C_{125}P_{H_2} + C_{126}P_{H_2} + P_{H_2} + C_{127} + C_{123} + C_{122} \tag{134}$$

Taking only the positive root of equation 134 the partial pressure of H_2 is:

$$P_{H_2} = \frac{(-1 - C_{125} - C_{126})}{2(C_{124})} + \frac{[(1 + C_{125} + C_{126})^2 - 4(C_{124})(C_{122} + C_{123} + C_{127} - P_{tot})]^{1/2}}{2(C_{124})} \tag{135}$$

The calculated partial pressure of H_2 is then substituted in equation 130, 131 and 132. Considering that the P_{tot} is known, ϕ_i and f_i are calculated with equation 96 and 97, all the partial pressures at any specified temperature and pressure are known for the C-O-H-S system.

Gas speciation model C-O-H-S system: a step by step example. Following the approach of French (1966); Holloway (1981); Huizenga (2001), I propose a detailed step by step example of the volcanic outgassing of the C-O-H-S system. The model inputs are temperature (K) and pressure (bar) and it simulates the molar fractions of H_2O, H_2, CO_2, CO, CH_4, SO_2 and H_2S. The gas partial pressures are calculated at the equilibrium and considering an infinite reservoir of volatiles. The limitations of the model are principally due to the sulphur fugacity, the selected equation of state and the carbon activity. The correct selection of these parameters are crucial for simulating the gas chemical speciation. The temperature interval validity of the selected sulphur fugacity is $567<T<1016$ K (Lusk and Bray, 2002). The simulations outside the interval can generate problems with the mass balance of the volatile phases. When the system is graphite saturated, the graphite activity is 1 but, if the system is not saturated the carbon activity is between 0< a_C <1. In the example, I applied the Redlich-Kwong (Redlich and Kwong, 1949) equation of state. But, other equations of state might fit better different scenarios as some modified Redlich-Kwong equations (de Santis et al., 1974; Flowers, 1979) or the Shi-Saxena equation (Shi and Saxena, 1992).

In the following example, the volatile outgassing is calculated at 1000 K and 200 bar. Since the volatile outgassing is simulated for real gases, the first step is to calculate the fugacities of the volatile species with an EoS for real gases, in this case by applying the equation from (Redlich and Kwong, 1949). The fugacity is calculated starting from equation 95 where the compressibility factor (Z) is expressed as :

$$Z^3 - Z^2 + Z(P_r/T_r) \cdot (0.42748/T_r^{1.5} - 0.08664 - 0.007506 \cdot (P_r/T_r)) - 0.03704(P_r^2/T_r^{3.5}) = 0, \quad (136)$$

considering the parameters for water from table 3, the reduced pressure (P_c) and the reduced temperature (T_c) are:

$$P_r = \frac{P}{P_c} = \frac{200}{220.5} = 0.907, \quad (137)$$

$$T_r = \frac{T}{T_c} = \frac{1000}{674.14} = 1.4834, \quad (138)$$

$$Z^3 - Z^2 + Z\left(\frac{0.907}{1.4834}\right)\left(\frac{0.42748}{1.4834^{(1.5)}} - 0.08664 - 0.007506 \cdot \frac{0.907}{1.4834}\right) - 0.03704\left(\frac{0.907^{(2)}}{1.4834^{(3.5)}}\right) = 0, \quad (139)$$

the roots (Z) of 139 are 0.8905, 0.1625 and -0.0530. Only one value is correct for calculating the fugacity coefficient. If the cubic equation has 3 real solutions, it has to be selected the one which represent better the physical parameter of the fugacity hence, the negative solution is excluded and it is chosen the one closer to the value of 1 (the fugacity coefficient is commonly close to 1). The fugacity coefficient is calculated with the equation 96 where A and B are calculated following equations 79 and 80:

$$A^2 = \frac{0.42784 \cdot 674.14^{2.5}}{220.5 \cdot 1000^{2.5}}, A^2 = 7.2402 \cdot 10^{-4}, \quad (140)$$

$$B = 0.0867 \cdot \frac{674.14}{220.5 \cdot 1000}, B = 2.6507 \cdot 10^{-4} \quad (141)$$

substituing in equation 142 the fugacity coefficient of water ($\phi_{\mathrm{H_2O}}$) is then:

$$\ln \phi_{\mathrm{H_2O}} = 0.8905 - 1 - \ln\left(\frac{0.8905}{2.6507 \cdot 10^{-4} \cdot 200}\right) - \left(\frac{7.2402 \cdot 10^{-4}}{2.6507 \cdot 10^{-4}}\right) \ln\left(\frac{1 + 2.6507 \cdot 10^{-4} \cdot 200}{0.8905}\right), \tag{142}$$

$$\phi_{\mathrm{H_2O}} = 0.9138 \tag{143}$$

By applying the same approach, the fugacities for the volatiles involved are:

$$\ln \phi_{\mathrm{H_2}} = 1.0431 - 1 - \ln\left(\frac{1.0431}{2.2193 \cdot 10^{-4} \cdot 200}\right) - \left(\frac{6.6250 \cdot 10^{-6}}{2.2193 \cdot 10^{-4}}\right) \ln\left(\frac{1 + 2.2193 \cdot 10^{-4} \cdot 200}{1.0431}\right), \tag{144}$$

$$\phi_{\mathrm{H_2}} = 1.0441, \tag{145}$$

$$\ln \phi_{\mathrm{CO_2}} = 1.0131 - 1 - \ln\left(\frac{1.0131}{3.5750 \cdot 10^{-4} \cdot 200}\right) - \left(\frac{2.9584 \cdot 10^{-4}}{3.5750 \cdot 10^{-4}}\right) \ln\left(\frac{1 + 3.5750 \cdot 10^{-4} \cdot 200}{1.0131}\right), \tag{146}$$

$$\phi_{\mathrm{CO_2}} = 1.0170, \tag{147}$$

$$\ln \phi_{\mathrm{CO}} = 1.0508 - 1 - \ln\left(\frac{1.0508}{3.2933 \cdot 10^{-4} \cdot 200}\right) - \left(\frac{4.9920 \cdot 10^{-5}}{3.2933 \cdot 10^{-4}}\right) \ln\left(\frac{1 + 3.2933 \cdot 10^{-4} \cdot 200}{1.0508}\right), \tag{148}$$

$$\phi_{\mathrm{CO}} = 1.0528, \tag{149}$$

$$\ln \phi_{\mathrm{CH_4}} = 1.0435 - 1 - \ln\left(\frac{1.0435}{3.5889 \cdot 10^{-4} \cdot 200}\right) - \left(\frac{1.4735 \cdot 10^{-4}}{3.5889 \cdot 10^{-4}}\right) \ln\left(\frac{1 + 3.5889 \cdot 10^{-4} \cdot 200}{1.0435}\right), \tag{150}$$

$$\phi_{\mathrm{CH_4}} = 1.0459, \tag{151}$$

$$\ln \phi_{\mathrm{SO_2}} = 0.9564 - 1 - \ln\left(\frac{0.9564}{4.7592 \cdot 10^{-4} \cdot 200}\right) - \left(\frac{6.6407 \cdot 10^{-4}}{4.7592 \cdot 10^{-4}}\right) \ln\left(\frac{1 + 4.7592 \cdot 10^{-4} \cdot 200}{0.9564}\right), \tag{152}$$

$$\phi_{\mathrm{SO_2}} = 0.9738, \tag{153}$$

$$\ln \phi_{\mathrm{H_2S}} = 0.9902 - 1 - \ln\left(\frac{0.9902}{3.6193 \cdot 10^{-4} \cdot 200}\right) - \left(\frac{4.0719 \cdot 10^{-4}}{3.6193 \cdot 10^{-4}}\right) \ln\left(\frac{1 + 3.6193 \cdot 10^{-4} \cdot 200}{0.9902}\right), \tag{154}$$

$$\phi_{\mathrm{H_2S}} = 0.9966, \tag{155}$$

The next step is the calculation of the oxygen and sulphur fugacity. The example considers the QIF mineral buffer for the $f_{\mathrm{O_2}}$ (equation 38) and the Pyrite-Pyrrhorite buffer (equation 121) which is valid for the temperature interval 567<T<1016 K, resulting at 1000 K as:

$$f_{\mathrm{O_2}} = 10^{(7.679 - \frac{29673}{1000} + 0.05(200-1)/1000)} = 1.0374 \cdot 10^{-22}, \tag{156}$$

$$f_{\mathrm{S_2}} = 10^{(19.41 - \frac{21004}{1000} + \frac{2061770}{1000^2})} = 2.9361, \tag{157}$$

The system is considered to be graphite saturated hence, the carbon activity (a_{C}) is fixed to 1. The carbon activity, the sulphur fugacity ($f_{\mathrm{S_2}}$) and the oxygen fugacity are determined hence, there is a system of 7 equations and 7 unknowns that can be solved algebraically ($P_{\mathrm{H_2}}$, $P_{\mathrm{H_2O}}$, $P_{\mathrm{H_2S}}$, $P_{\mathrm{SO_2}}$, $P_{\mathrm{CH_4}}$, $P_{\mathrm{CO_2}}$, P_{CO}). The calculated fugacity coefficients are employed for estimating the chemical composition of the gas mixture considering that:

$$f_i = \phi_i P_i, \tag{158}$$

$$P_{tot} = \frac{f_{\mathrm{H_2}}}{\phi_{\mathrm{H_2}}} + \frac{f_{\mathrm{H_2O}}}{\phi_{\mathrm{H_2O}}} + \frac{f_{\mathrm{H_2S}}}{\phi_{\mathrm{H_2S}}} + \frac{f_{\mathrm{SO_2}}}{\phi_{\mathrm{SO_2}}} + \frac{f_{\mathrm{CH_4}}}{\phi_{\mathrm{CH_4}}} + \frac{f_{\mathrm{CO_2}}}{\phi_{\mathrm{CO_2}}} + \frac{f_{\mathrm{CO}}}{\phi_{\mathrm{CO}}} = 200 \text{ bar}, \tag{159}$$

considering the equations from 122 to 127 the partial pressure can be expressed as:

$$P_{\mathrm{CO}} = \left[\frac{K_{113} f_{\mathrm{O}_2}^{1/2} a_{\mathrm{C}}}{\phi_{\mathrm{CO}}}\right]_{C_{160}} \tag{160}$$

$$C_{160} = \left(\frac{K_{113} f_{\mathrm{O}_2}^{1/2} a_{\mathrm{C}}}{\phi_{\mathrm{CO}}}\right) = \left(\frac{2.9045 \cdot 10^{10} \cdot (1.0374 \cdot 10^{-22})^{1/2} \cdot 1}{1.0528}\right) = 1.4310 \cdot 10^{-12} \tag{161}$$

$$P_{\mathrm{CO}_2} = \left[\frac{K_{114} f_{\mathrm{O}_2} a_{\mathrm{C}}}{\phi_{\mathrm{CO}_2}}\right]_{C_{162}} \tag{162}$$

$$C_{162} = \left(\frac{K_{114} f_{\mathrm{O}_2}^{1/2} a_{\mathrm{C}}}{\phi_{\mathrm{CO}_2}}\right) = \left(\frac{4.7720 \cdot 10^{20} \cdot (1.0374 \cdot 10^{-22})^{1/2} \cdot 1}{1.0170}\right) = 0.0487 \tag{163}$$

$$P_{\mathrm{CH}_4} = \left[\frac{K_{115} (\phi_{\mathrm{H}_2})^2 a_{\mathrm{C}}}{\phi_{\mathrm{CH}_4}}\right]_{C_{164}} (P_{\mathrm{H}_2})^2 \tag{164}$$

$$C_{164} = \left(\frac{K_{115} f_{\mathrm{O}_2}^{1/2} a_{\mathrm{C}}}{\phi_{\mathrm{CH}_4}}\right) = \left(\frac{0.0937 \cdot (1.0374 \cdot 10^{-22})^{1/2} \cdot 1}{1.0459}\right) = 0.00976 \tag{165}$$

$$P_{\mathrm{H}_2\mathrm{O}} = \left[\frac{\phi_{\mathrm{H}_2} K_{116} (f_{\mathrm{O}_2})^{1/2}}{\phi_{\mathrm{H}_2\mathrm{O}}}\right]_{C_{166}} P_{\mathrm{H}_2} \tag{166}$$

$$C_{166} = \left(\frac{K_{116} f_{\mathrm{O}_2}^{1/2} \phi_{\mathrm{H}_2}}{\phi_{\mathrm{H}_2\mathrm{O}}}\right) = \left(\frac{1.1386 \cdot 10^{10} \cdot (1.0374 \cdot 10^{-22})^{1/2} \cdot 1.0441}{0.9138}\right) = 6.7479 \cdot 10^{-13} \tag{167}$$

$$P_{\mathrm{H}_2\mathrm{S}} = \left[\frac{\phi_{\mathrm{H}_2} K_{117} (f_{\mathrm{S}_2})^{1/2}}{\phi_{\mathrm{H}_2\mathrm{S}}}\right]_{C_{168}} P_{\mathrm{H}_2} \tag{168}$$

$$C_{168} = \left(\frac{K_{117} f_{\mathrm{S}_2}^{1/2} \phi_{\mathrm{H}_2}}{\phi_{\mathrm{H}_2\mathrm{S}}}\right) = \left(\frac{139.9848 \cdot (2.9361)^{1/2} \cdot 1.0441}{0.9966}\right) = 251.2960 \tag{169}$$

$$P_{\mathrm{SO}_2} = \left[\frac{f_{\mathrm{O}_2} K_{118} (f_{\mathrm{S}_2})^{1/2}}{\phi_{\mathrm{SO}_2}}\right]_{C_{170}} \tag{170}$$

$$C_{170} = \left(\frac{K_{118} f_{O_2}^{1/2} \phi_{H_2}}{\phi_{H_2S}} \right) = \left(\frac{1.1964 \cdot 10^{15} \cdot (1.0374 \cdot 10^{-22})^{1/2} \cdot 1.0441}{0.9738} \right) = 2.1840 \cdot 10^{7} \tag{171}$$

the total pressure is then:

$$P_{tot} = C_{164}(P_{H_2})^2 + C_{166} P_{H_2} + C_{168} P_{H_2} + P_{H_2} + C_{170} + C_{162} + C_{160} \tag{172}$$

the positive root of H_2 is:

$$\begin{gathered} P_{H_2} = \frac{(-1 - C_{166} - C_{168})}{2(C_{164})} + \\ \frac{[(1 + C_{166} + C_{168})^2 - 4(C_{164})(C_{160} + C_{162} + C_{170} - P_{tot})]^{1/2}}{2(C_{164})} = 0.7923 \text{ (bar)} \end{gathered} \tag{173}$$

the P_{H_2} can be substituted in equations 164, 166 and 168. The final partial pressures are:

$$P_{CO} = 1.4310 \cdot 10^{-12} \text{ (bar)} \tag{174}$$

$$P_{CO_2} = 0.0487 \text{ (bar)} \tag{175}$$

$$P_{CH_4} = 0.0613 \text{ (bar)} \tag{176}$$

$$P_{H_2O} = 5.3463 \cdot 10^{-13} \text{ (bar)} \tag{177}$$

$$P_{H_2S} = 199.0978 \text{ (bar)} \tag{178}$$

$$P_{SO_2} = 2.1840 \cdot 10^{-7} \text{ (bar)} \tag{179}$$

2.10 Comparison of the speciation model C-O-H with previous literature

In the following section, I compare the gas speciation model (described in details in section 2.6) with the model presented in Schaefer and Fegley (2017). In the example, the volatile outgassing is simulated at 1 bar of pressure and all the gas species are exsolved from the silicate melt. The input is therefore only the temperature range which is 500 - 2000 K. The outputs are the oxygen fugacity of the system the CO/CO_2

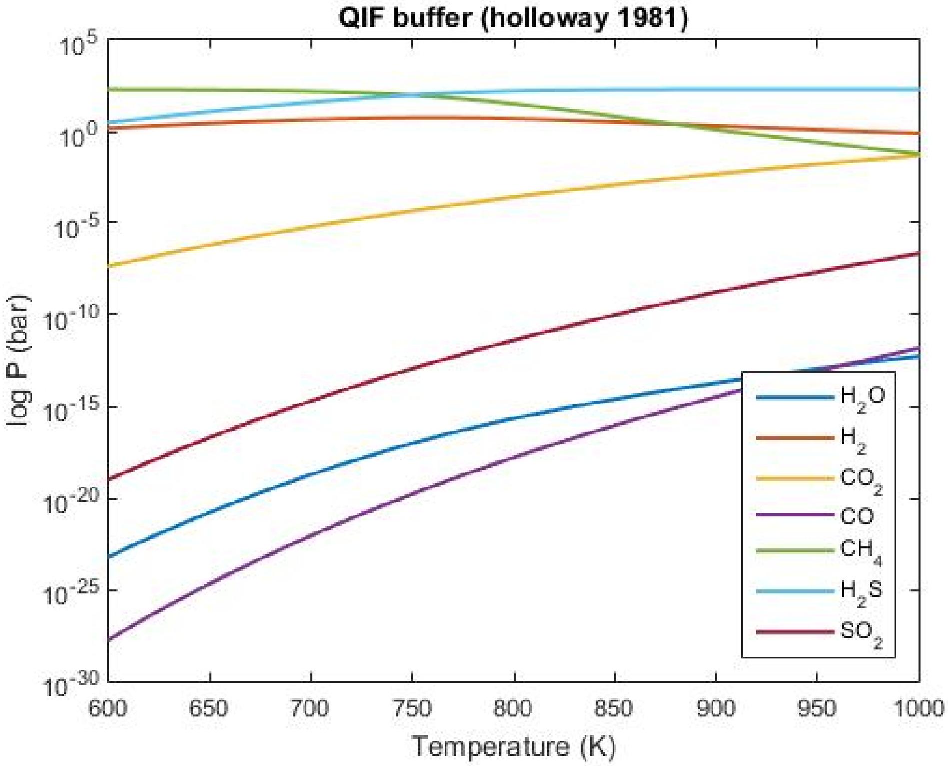

Figure 13: Gas chemical speciation of the C-O-H-S system simulated with the method described in section 2.9 (French, 1966; Holloway, 1981; Huizenga, 2001).

and H_2/H_2O ratios. The different oxidation state of the system is simulated following (Schaefer and Fegley, 2017), where the distribution of iron with different oxidation state leads to different oxygen fugacity of meteoritic composition. The iron oxidation states are: (0) metal iron $Fe^{(0)}$, ferrous iron $Fe^{(2+)}$ in olivine and pyroxene and ferric iron $Fe^{(3+)}$ in magnetite and hematite (Schaefer and Fegley, 2017; Krot et al., 2014; Rubin et al., 1988). By using this approach the oxidation states of the meteoritic compositions is calculated according to Schaefer and Fegley (2017) as follows:

$$\log_{10} f_{O_2} = a + b(10^3/T) + c(10^6/T^2) + d(10^9/T^3) + f(10^{12}/T^4) \tag{180}$$

where T is the temperature in Kelvin and a, b, c, d and f are the coefficients listed in table 4 and are valid for the temperature range 500 - 2000 K (figure 14).

Once the redox states of the meteoritic compositions are calculated, the following equilibria are solved in the Schaefer and Fegley (2017) approach:

$$H_2O \rightleftharpoons H_2 + \frac{1}{2}O_2, \tag{181}$$

Meteorites	a	b	c	d	f
CI	2.4976	-9.8605	-17.0701	7.5220	-1.0404
CV	9.0621	-31.193	5.1092	-1.8475	0.2000
H	5.0743	-22.906	-5.6610	2.0634	-0.2618
EH	4.9495	-24.024	-4.6236	1.7177	-0.2332
Eucrite	5.4856	-25.127	-3.6580	1.3014	-0.1650

Table 4: CI and CV are carbonaceous chondrites, H is a ordinary chondrite, EH is an enstatite chondrite and one achondrite the Eucrite. The parameters are taken from Schaefer and Fegley (2017).

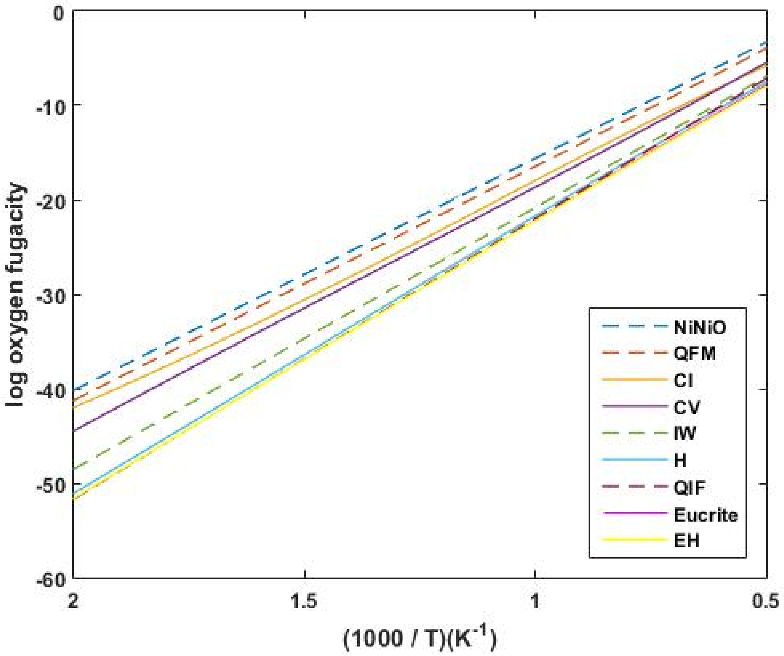

Figure 14: Petrological mineral buffers (NiNiO, QFM, IW and QIF) and meteoritic compositions as function of temperature (Holloway et al., 1992; Fegley, 2013; Schaefer and Fegley, 2017).

$$CO_2 \rightleftharpoons CO + \frac{1}{2} O_2, \tag{182}$$

the molar ratios of H_2/H_2O and CO/CO_2 are calculated via:

$$K_{(eq:181)} = \left(\frac{X_{H_2} f_{O_2}^{1/2}}{X_{H_2O}} \right), \tag{183}$$

$$\frac{K_{(eq:181)}}{f_{O_2}^{1/2}} = \frac{X_{H_2}}{X_{H_2O}}, \tag{184}$$

$$K_{(eq:182)} = \left(\frac{X_{CO} f_{O_2}^{1/2}}{X_{CO_2}} \right), \tag{185}$$

$$\frac{K_{(eq:182)}}{f_{O_2}^{1/2}} = \frac{X_{CO}}{X_{CO_2}}, \tag{186}$$

where $K_{(eq:181)}$ and $K_{(eq:182)}$ are respectively the equilibrium constants calculated as follows:

$$K_{(eq:181)} = \frac{-12794}{T} + 2.7768, \tag{187}$$

$$K_{(eq:182)} = \frac{-14787}{T} + 4.5472, \tag{188}$$

The equilibrium and mass balance method which is applied with the speciation model is described in detail at section 2.6, the equilibria involved are:

$$2\,H_2 + O_2 \rightleftharpoons 2\,H_2O, \tag{189}$$

$$\left(\frac{X_{H_2O}^2}{X_{H_2}^2}\right) = K_{189} f_{O_2}, \tag{190}$$

$$CO + \frac{1}{2}\,O_2 \rightleftharpoons CO_2, \tag{191}$$

$$\frac{X_{CO_2}}{X_{CO}} = K_{(eq:191)} f_{O_2}^{1/2}, \tag{192}$$

and the equilibrium constants are calculated as:

$$K_{(eq:189)} = \exp\left(\frac{-\Delta_r G^0_{(eq:189)}}{R \cdot T}\right) = \left(\frac{X_{H_2O}^2}{X_{H_2}^2 f_{O_2}}\right), \tag{193}$$

$$K_{(eq:191)} = \exp\left(\frac{-\Delta_r G^0_{(eq:191)}}{RT}\right) = \frac{X_{CO_2}}{X_{CO}} \frac{1}{f_{O_2}^{1/2}}, \tag{194}$$

where $\Delta_r G^0_{(eq:189)}$ and $\Delta_r G^0_{(eq:191)}$ are calculated with equation 30, and the H_2/H_2O and CO/CO_2 ratios are:

$$\frac{X_{H_2}}{X_{H_2O}} = \frac{1}{\sqrt{K_{(eq:189)} f_{O_2}}}, \tag{195}$$

$$\frac{X_{CO}}{X_{CO_2}} = \frac{1}{K_{(eq:191)} f_{O_2}^{1/2}}, \tag{196}$$

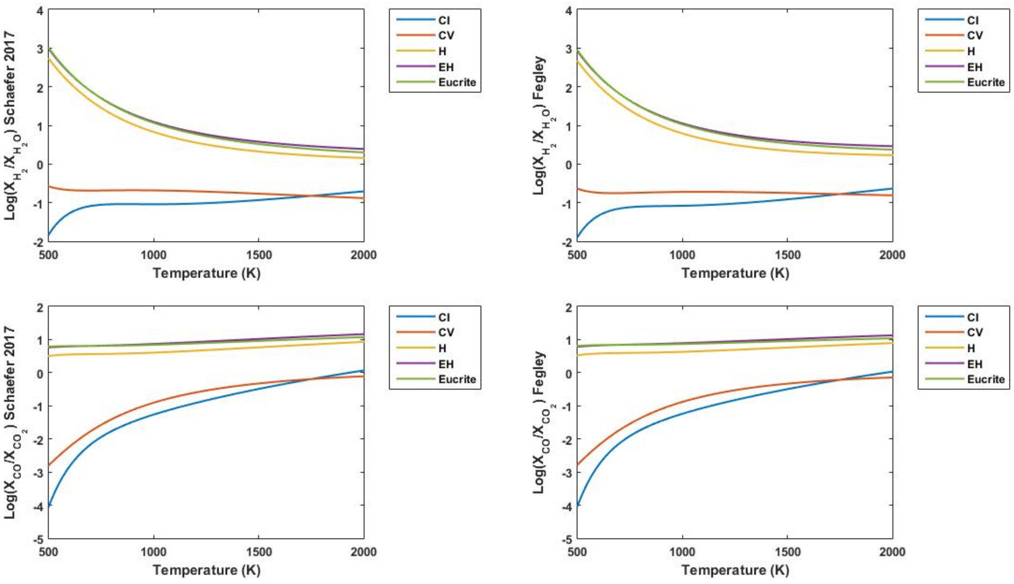

Figure 15: H_2/H_2O and CO/CO_2 ratio calculated according to Schaefer and Fegley (2017) (left column) and with the method described at section 2.6 (right column).

The outgassed composition for the temperature range 500 - 2000 K, at 1 bar of pressure and at different oxidation state is shown in figure 15. The ratios of the volatile species are almost the same even if are applied different techniques for calculating the equilibrium constants and different equilibria. The results confirm how the oxygen fugacity of the system is crucial for estimating the volatile chemical speciation.

2.11 Summary

In the chapter, I describe the theory and the thermodynamic principles for simulating the chemical equilibrium reactions of gas phases. Essentially, the main parameters that affect the volatile chemical speciation are temperature, pressure and redox state. The pressure regulates the volatile budget which is outgassed following the volatile solubility laws as described in section 2.5. Temperature and redox states drive the volatile chemical speciation between oxidised and reduced gas phases. I have developed different numerical models for simulating the outgassing under different scenarios. The chapter starts with the model which simulates the volcanic outgassing at surface for the C-O-H system considering as outgassed species H_2O, H_2, CO_2 and CO (section 2.6). This model is the most flexible and stable and for this reason it was the one that was employed in the development of three research papers (sections 3.1, 3.2 and 3.3). The numerical model simulates the majority of the natural volcanic outgassed volatiles and thus the most representative for simulating a cumulative outgassed atmosphere of a rocky planet. The range of stability in terms of temperature is very large (it covers the temperature interval for melt at low pressure $1000 < T < 2000$ K) and the pressure does not play a role since the outgassing occurs at surface. I have developed also other numerical models to investigate more specific scenarios and considering the real gas behaviour. In section

2.8, I added the methane to the numerical model of the C-O-H system. Methane is a very important gas species at high pressure or at low temperature and thus the model considers the real gas behaviour. The last model that was developed includes also the sulphur species (SO_2, H_2S and S_2) simulating the C-O-H-S system (section 2.9). Although the last model simulates the outgassing for the majority of volatile species, it simulates the outgassing for real gas behaviour and thus, it has limitations in terms of temperature and pressure range of investigation. It needs further development to extend the applicability to a wider range of outgassing scenarios.

3 Application of the chemical speciation model

The developed chemical speciation model has been applied for investigating the outgassing of the early Earth and of rocky planets. The chapter includes three research papers and here I specify my personal contribution to the articles:

- Section 3.1 has been published as ”Mantle redox state drives outgassing chemistry and atmospheric composition of rocky planets” Scientific reports, 2020, 10.1: 1-14.

  Author list: Ortenzi G., Noack L., Sohl F., Guimond C.M., Greenfell J.L., Dorn C., Schmidt J.M., Vulpius S., Katyal N., Kitzmann D. and Rauer H.

  In the research paper we have analysed the volcanic degassing and the corresponding outgassed atmospheres for rocky planets with different sizes. My personal contribution has started since the conceptualization of the research together with Noack L., Sohl F. and Rauer H. The first step was to couple the chemical speciation model to a mantle convective regime for obtaining the outgassing rate of stagnant lid planets of different sizes. Together with Noack L. and Guimond C., we coupled the chemical speciation model to a preexisting mantle convective model. By doing this, we obtained a degassing rate of stagnant lid planets as a function of: mantle volatile contents, temperature, pressure and mantle redox states. The collected results were combined with preexisting simulations of atmospheric thickness and partial pressure (Noack L., Dorn C. and Kitzmann D.). Thus, the model was able to simulate the complete volatile path from the interior to the atmosphere. I led the writing, the methodology (i.e combining the chemical speciation model with a mantle convection code), the interpretation of the results and the review process of the paper (in collaboration with all the co-authours). Specifically, Greenfell J.L., Katyal N. and Rauer H. contributed with the interpretation of the simulated rocky planet atmospheres. Guimond C., Noack L., Schmidt J.M. contributed with the graphical visualizations. Schmidt J.M., Vulpius S. and Noack L. performed the solubility calculations.

- Section 3.2 includes the submitted paper: ”The early Earth’s volcanic outgassing rates from mantle convection, melting, and volatile speciation”. Submitted to: ”Physics of the Earth and Planetary Interiors” (in revision).

  Author list: Guimond C.M., Noack L., Ortenzi G. and Sohl F.

  Claire Guimond spent one semester for an internship within the TRR-170 project at the Freie Universitaet Berlin. Thus, the research paper was developed within a collaboration in the TRR-170 project. In the research, we directly combined the chemical speciation model to outgassing simulations for obtaining values of local temperature, pressure and volatile content during the early Earth outgassing. My personal contribution was to share the chemical speciation model with Guimond

C.M. and Noack L. and to couple it with a mantle convection code (the latter designed by Noack L. and Guimond C.M.). I have actively participated in the writing, the methodology (i.e. the volatile chemical speciation model), the interpretation of the results and the review process. The paper is under the second round of the review process.

- Section 3.3 has been published as ”Effect of mantle oxidation state and escape upon the evolution of Earth’s magma ocean atmosphere”. Astronomy and Astrophysics 643, A81 (2020).

  Author list: Katyal N., Ortenzi G., Grenfell J.L., Noack L., Sohl F., Godolt M., Muñoz A.G., Schreier F., Wunderlich F. and Rauer H.

  Nisha Katyal was a post-doc at the ”Institute of Planetary Research” at the DLR Berlin in the TRR-170 project. We analysed the magma ocean volcanic outgassing by combining the volatile chemical speciation model with a line-by-line radiative transfer model for investigating the infrared emission and transmission at the top of the atmosphere. I participated to the conceptualization of the research with Katyal N. We started with combining the gas chemical speciation model and the line-by-line radiative transfer model. The aim was to simulate the outgassed atmosphere of a magma ocean planet considering different redox states of the mantle. With the combined model we simulated the H_2 escape and the infrared transmission at the top of the atmosphere. My contribution was in the writing, the conceptualization of the paper, the methodology (i.e. the chemical speciation model and its combination with the atmospheric model), the interpretation of the results and the revision of the last version of the paper.

3.1 Mantle redox state drives outgassing chemistry and atmospheric composition of rocky planets

Ortenzi G., Noack L., Sohl F., Guimond C.M., Greenfell J.L., Dorn C., Schmidt J.M., Vulpius S., Katyal N., Kitzmann D. and Rauer H. *Mantle redox state drives outgassing chemistry and atmospheric composition of rocky planets.* Scientific reports, 2020, 10.1: 1-14, DOI https://doi.org/10.1038/s41598-020-67751-7

3.1.1 Abstract

Volcanic degassing of planetary interiors has important implications for their corresponding atmospheres. The oxidation state of rocky interiors affects the volatile partitioning during mantle melting and subsequent volatile speciation near the surface. Here we show that the mantle redox state is central to the chemical composition of atmospheres while factors such as planetary mass, thermal state, and age mainly affect the degassing rate. We further demonstrate that mantle oxygen fugacity has an effect on atmospheric thickness and that volcanic degassing is most efficient for planets between 2 to 4 Earth masses. We show that outgassing of reduced systems is dominated by strongly reduced gases such as H_2, and only smaller fractions of moderately reduced/oxidised gases (CO, H_2O). Overall, a reducing scenario leads to a lower atmospheric pressure at the surface and to a larger atmospheric thickness compared to an oxidised system. Atmosphere predictions based on interior redox scenarios can be compared to observations of atmospheres of rocky exoplanets, potentially broadening our knowledge on the diversity of exoplanetary redox states.

3.1.2 Introduction

Atmospheric evolution on a rocky planet is affected by numerous fundamental processes. Generally, atmospheres can be accreted from the proto-planetary disk (primordial atmosphere), or outgassed from the interior either during the cooling of a magma ocean (primary atmosphere) or by volcanism during the planet's long-term geological history (secondary atmosphere). The total volume of volcanic outgassing is the sum of the contribution from the deeper magmatic emplacements, also called passive degassing, and from extrusive volcanism (discussed in detail in the supplementary materials). Furthermore, atmospheres can be lost via escape (driven by thermal or non-thermal processes or via large impacts) and enriched via delivery from smaller impacts (Van Hoolst et al., 2019). The interplay of these central processes determines the atmospheric evolution and observable gas species in the atmosphere. Gaseous species released from present-day volcanoes on Earth are dominated by H_2O and CO_2 which are strong greenhouse gases (Schaefer and Fegley, 2010). Consequently, a planet's potential to develop habitable conditions is linked to interior processes in a variety of ways (Shahar et al., 2019).

The oxidation state of the mantle at a given point in time depends on numerous factors such as the primordial disk composition, core-mantle processes and loss of atmospheric hydrogen to name but a few (Kasting et al., 1993). During the core segregation process, the co-existence of liquid iron and silicate led to a reduced mantle (Wood et al., 2006). The oxidation of the mantle is related to core differentiation and depends on factors such as the mantle pressure, temperature and stellar irradiation (Wordsworth et al., 2018; Righter and Ghiorso, 2012). The Earth's upper mantle is oxidized at present; geological evidence suggests that this transition from a reduced mantle to an oxidized one occurred during its earliest evolution, although the exact timing is still debated (Trail et al., 2011; Smart et al., 2016; Frost et al., 2008; Nicklas et al., 2018, 2019; Pahlevan et al., 2019). Whether rocky exoplanets are expected to follow an analogous pattern in redox state represents a major uncertainty in the understanding of their atmospheric evolutions. Previous model studies of rocky planets have suggested that the efficiency and the composition of volcanic outgassing depend on properties such as mass, thermal state, age, tectonic style and planetary bulk composition (Kite et al., 2009; Noack et al., 2014, 2017; Tosi et al., 2017; Dorn et al., 2018). Here, we simultaneously investigate the different phases of the volatile pathways from the interior to the atmosphere, combining processes that are usually analysed separately. We analyse planets operating in a stagnant lid tectonic regime. We do not consider whether any lingering gases from the primary atmosphere would affect the compositions of the secondary atmospheres we model. This assumes that the species degassed during a short magma ocean stage would be lost or replaced within billions of years of volcanic outgassing. A massive atmosphere during the magma ocean phase most likely implies a surface still molten and therefore, not a stagnant lid planet (Nikolaou et al., 2019; Katyal et al., 2019). In particular, we analyse how a planet's mantle redox state affects its outgassed atmospheric composition through the double influences of mantle-melt volatile partitioning and gas chemical speciation. Whether outgassing is dominated by reduced or oxidized species can regulate the atmospheric scale height (equation 223) via the mean molecular mass. The smaller molecular weights of CO, H_2O and H_2 as compared to CO_2 generate less dense atmospheres leading to a larger atmospheric thickness. In our work we consider the three main elements on Earth which together constitute the bulk of Earth's volatile molecular inventory and which are central for determining surface habitability conditions, namely C, H and O.

3.1.3 Results

To investigate the variations in atmospheric composition and surface pressure for rocky exoplanets of different masses, we consider the influence of the initial volatile content in the magma and the melt redox state. Our numerical model simulates the volatile flux from the mantle to the atmosphere, as detailed in the methods section. In section 3.1.5 we calculate the volatile solubility in the silicate melt and the gas chemical speciation of the C-O-H system. Finally, in section 3.1.5, we simulate the atmosphere evolution analysing the final volatile composition and the atmospheric radial extent. Dorn et al. (2018) modelled in total 2,340 different rocky planet evolutionary cases by varying initial conditions and major element compositions of hypothetical exoplanets, while assuming a fixed amount of CO_2 melt concentration and oxidised conditions in the melt. Here, we use the same cases as reported in Dorn et al. (2018) but consider that both H_2O and CO_2 are stored in the mantle subsequent to the solidification of the magma ocean (Elkins-Tanton, 2008; Hier-Majumder and Hirschmann, 2017), combined with variable redox scenarios. Table 5 lists different cases of volatile amounts in the melt, based on three volatile delivery cases investigated for Earth in Elkins-Tanton (2008). In our simulations, we employed as starting volatile contents of the mantle the H_2O and CO_2 stored after the magma ocean solidification (table 5). Whereas the first and second cases assume different relative amounts of CO_2 and H_2O, the third case considers a dry scenario where only CO_2 was delivered. To investigate the influence of H_2O degassing for a more carbon-rich mantle, we add a small amount of water to the third case. We consider different mantle redox states reproducing an oxidised (Iron-Wuestite buffer) and a reduced scenario (Quartz-Fayalite-Magnetite buffer) and their influence upon the amount and composition of the outgassed volatiles (see Section 3.1.5). This results in a total of 28,080 evolutionary scenarios.

Table 5: Initially delivered volatile concentrations in the magma ocean (weight percent) and resulting volatile fractions stored in the mantle after the magma ocean solidification, based on different initial delivery scenarios from Elkins-Tanton (2008). The CO_2 is stored as graphite in the mantle. [a] We consider here a small water fraction instead of the dry case investigated in Elkins-Tanton (2008).

	Delivered		Stored	
Case	H_2O	CO_2	H_2O	CO_2
Low	0.05	0.01	0.015	0.0022
High	0.5	0.1	0.045	0.005
Dry	0	0.6	0.005[a]	0.018

Given the initial volatile contents in the mantle, the corresponding concentrations in the melt are regulated by the partitioning between the mantle and the melt produced. For carbon species, this is directly influenced by the oxidation state of the system (equation 198). The main effect is that for reducing conditions, the dissolution of carbonates from the mantle rocks into the melt is suppressed, and therefore the volatile content in the magma will be dominated by water. On the other hand, an oxidising scenario favours an enrichment in carbonates in the melt. Hence, melts with different volatile contents can be generated even if they originate from source rocks with identical starting volatile concentrations but different redox states. Once the melt reaches the surface, we simulate the dissolved gas chemical speciation in the C-O-H system.

Figure 16 illustrates the combined effects of volatile melt partitioning and speciation on the ultimate outgassing chemistry. The upper panel isolates the redox-dependence of the surface (1 bar pressure) gas speciation for a constant volatile concentration in the melt; without calculating the melt partitioning. This essentially reproduces (Holland, 1984): H_2 and CO are the most abundant outgassed species in the more

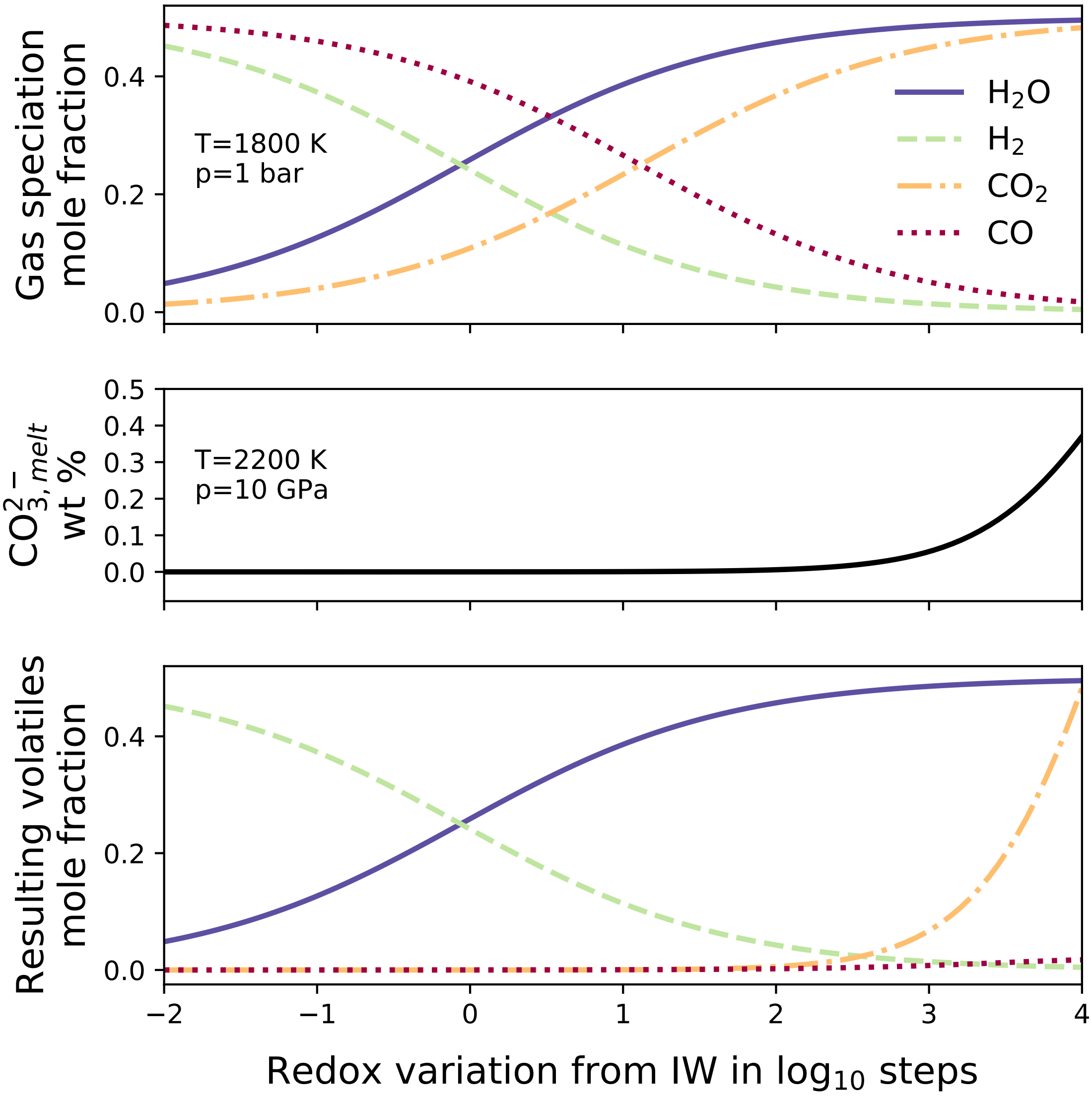

Figure 16: Composition of outgassed volatiles as a function of oxygen fugacity which is shown in logarithmic values relative to the Iron-Wuestite buffer, where the initial volatile composition is 50 mol% for both H_2O and CO_2. The most oxidised case shown here (IW+4) reflects a redox state similar to Earth's upper mantle at present day temperature. *Top:* Outgassed volatile composition without considering the mantle-melt composition (i.e. starting volatile composition is considered in the melt). *Middle:* Weight percent of carbonates dissolved in the melt as a function of oxygen fugacity at 2200 K and 10 GPa. *Bottom:* Outgassed volatile composition considering the mantle-melt volatile partitioning and the volatile chemical speciation.

reducing states (log $f_{O_2} < 0$), while in the more oxidised scenarios (log $f_{O_2} > 1$), the principal gas phases are H_2O and CO_2. However, as described above, the volatile concentrations in the melt depend on redox state as well (middle panel). If both of these effects are coupled (bottom panel), we get rather different results for the outgassed composition. Now in reducing scenarios, H_2 is the most outgassed species, while zero-to-little CO is degassed because the carbonate partitioning in the melt is inhibited. Upon increasing the oxidation state, carbonate starts to become present and the outgassing is dominated by CO_2 and H_2O.

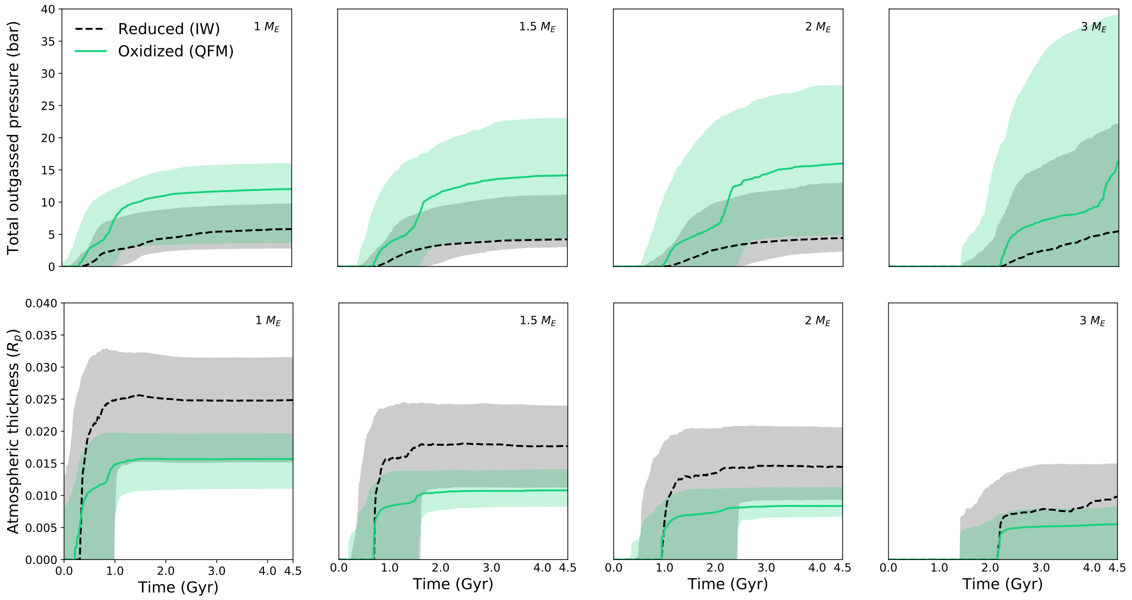

Figure 17: Shaded area is the 1σ variation while lines represent the median of the modelled evolution of atmospheric thickness bottom panel) and outgassed pressure (top panel) over 4.5 Gyr, where subplots group simulations by planet mass. Black dashed lines represent reduced mantles (IW buffer), while green solid lines represent oxidised cases (QMF buffer).

Atmospheric evolution is analysed considering melt fluxes over time in combination with the volatile solubility and the chemical equilibrium during the outgassing process. Therefore, the scenarios performed here are affected by the melt production, temperature, pressure, volatile content and oxidation state of the system. For simplicity, we select the atmospheric pressure at the surface as the outgassing pressure. The pressure has a direct influence on the volatile solubility in the melt and the outgassed composition. The bottom panel of figure 17 displays the median and 1σ variation (68% confidence interval) of modelled atmospheric thickness, expressed in units of planetary radius over time for the four different planetary masses investigated. Results suggest a general decrease in atmospheric thickness with increasing planetary mass, hence increased surface gravity in the scale height definition (see Equation 223), and larger radial atmospheric extent for reducing conditions. Figure 17 (top panel) shows the atmospheric pressure over time at different redox states and planet sizes. In the analysed cases, highest outgassing values occur for planets of several Earth masses, and oxidised mantles lead to higher atmospheric surface pressure as compared to

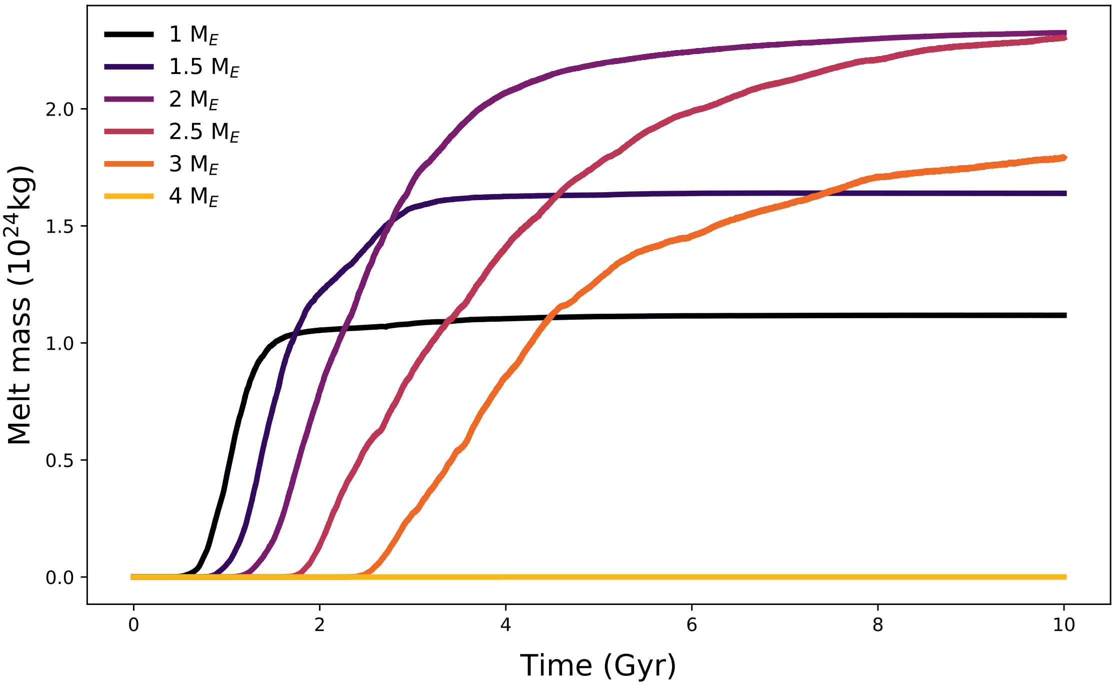

Figure 18: Melt production over time (Gyr) for different planet sizes considering an Earth-like interior structure and composition. With increasing planet size there is a delay in the production of melt and no further magma generation for massive planets above $4M_E$.

reduced mantles since the oxidised volatile species have a higher molecular weight than reduced gases (in the case of H_2O versus H_2 the weight varies by a factor of nine). After 4.5 Gyr of mantle convection, most degassing from the interior (if it occurred) had already taken place Dorn et al. (2018), although in general the more massive the planet, the later degassing occurs. The outgassing lag for increasing planetary mass is due to the larger internal pressure which produces a higher mantle viscosity. The rheology variation reduces the vigor of mantle convection so that outgassing starts later compared to planets with lower mass (Figure 17). An increasing planet mass leads to higher initial mantle temperatures and an increased inventory of volatiles and radioactive heat sources. This is reflected in a larger amount of volcanic activity and outgassing for planets with masses up to 2 to 4 M_E (depending on the specific simulation parameters). However, for planets of masses above this threshold, we can observe a negative trend in volcanic activity. This trend is directly related to the increasing planetary mass and surface gravitational acceleration and therefore increasing pressure gradient in the lithosphere. The pressure at the bottom of the lithosphere leads to a higher melting temperature than for Earth-mass planets, causing reduced or even no outgassing (see Figure 18 using longer, sample evolution scenarios up to 10 Gyr for planets of different masses but with the most Earth-like composition scenario in our data set).

Figure 19 compares atmospheric thickness and the resulting partial pressures obtained for all investigated cases as a function of the planetary mass. The degassing trend still reflects that under oxidising

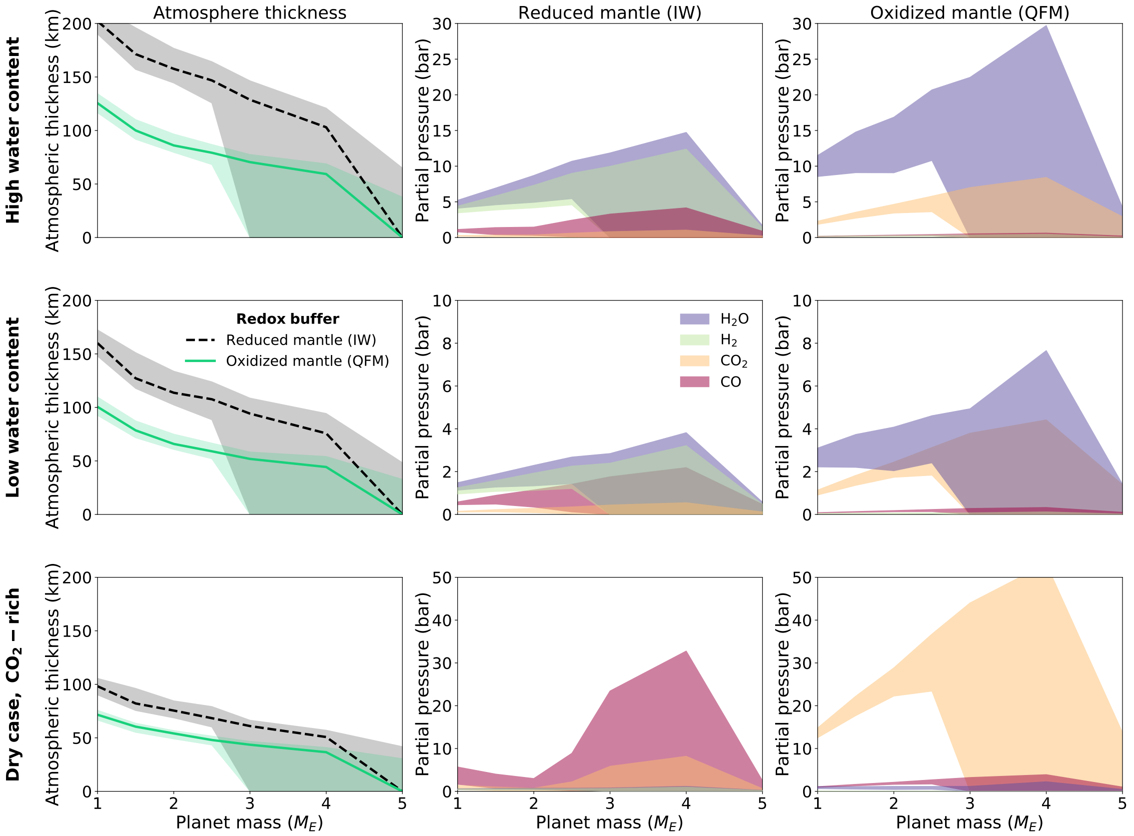

Figure 19: Change of atmospheric thickness and outgassed partial pressures with planetary mass after 4.5 Gyr of simulated mantle convection. Individual panels compare reduced mantles (IW buffer) with oxidised mantles (QFM buffer), and rows indicate different initial volatile cases (i.e. dry, low, high) from table 5. The left column of the panel shows the mass-dependence of modelled atmospheric thickness, comparing reduced mantles (black dashed line) with oxidised mantles (green solid line). Shaded areas show the 1σ variation across all simulations therein, while the lines denote the median. In the central and right column we examine the partial pressures of H_2O (purple swaths), H_2 (green swaths), CO_2 (orange swaths), and CO (red swaths). Shaded areas show the 1σ variation across all simulations therein, considering that for a given volatile and redox scenario, factors causing variation in atmospheric thickness include bulk Mg/Fe/Si ratios and initial mantle temperature profiles and heat sources.

conditions the atmospheric pressure will be larger and mainly composed of H_2O and CO_2. On the other hand, under reducing conditions the atmospheric pressure is lower because a part of the H_2O content is replaced by H_2 and CO outgassing is favoured over CO_2 though strongly limited due to the smaller carbonate content in the reduced melt. Concerning the influence of the planetary mass, for both reducing and oxidising cases, maximum degassing occurs between 2 and 4 Earth masses. A higher molecular weight of the atmosphere leads to a shallower atmospheric vertical extent. This can be seen in the left column of figure 19, which shows the median and 1σ variation of atmospheric thickness as a function of the planetary mass after 4.5 Gyr of mantle convection, for different initial volatile contents. For all the volatile scenarios, the oxidation level leads to strongest differences in atmospheric thicknesses for the low-mass planets. In the case of a more reduced mantle, the atmospheric thickness is generally larger compared to the oxidised case. However, this difference decreases as the planetary mass increases. In addition, results suggest either low or virtually zero outgassing rates for the more massive planets considered here, consistent with Noack et al. (2017) and Dorn et al. (2018).

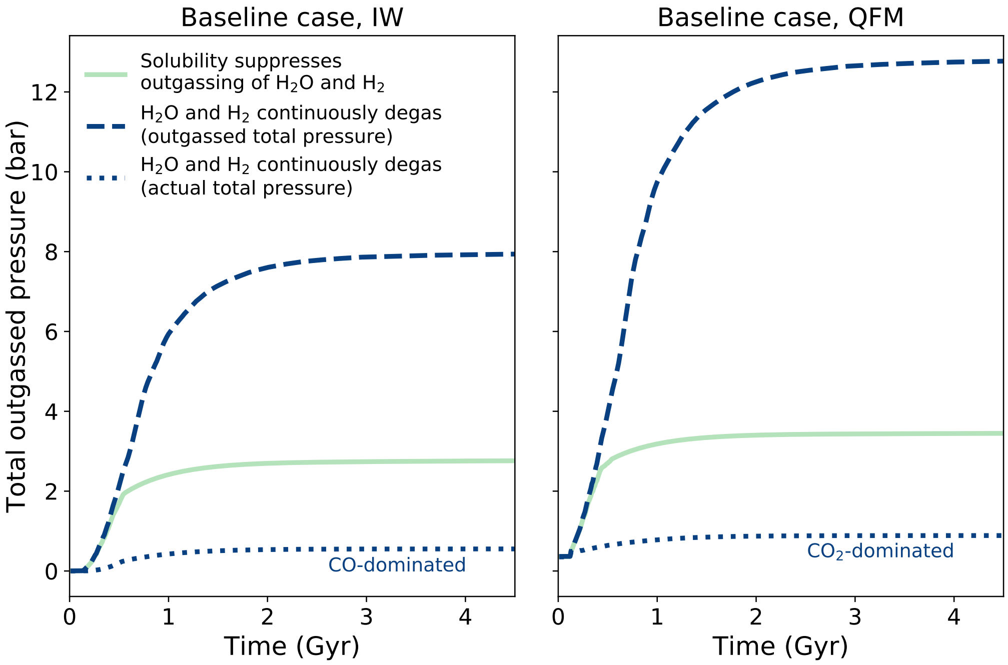

Figure 20: Evolution of an outgassed atmosphere's total pressure for different scenarios, showing a single case (mass = 1 $M_{\oplus}$, initial volatile concentrations X_{CO_2} = 22 ppm, X_{H_2O} = 150 ppm, Fe/Si = 0.5, Mg/Si = 1.0) as an example. The dashed blue line represents the atmospheric evolution without considering solubility, hydrogen escape, or water condensation. The solid green line shows the melt solubility effect on outgassing, but neither hydrogen escape nor water condensation are simulated. The dotted line shows the case where hydrogen escape and water condensation are simulated.

We performed simulations considering also the H_2 atmospheric escape and the H_2O condensation in an ocean layer. Figure 20 shows surface pressure as a function of time for an Earth mass planet assuming that all the hydrogen is lost to space via escape, and all of the water retained in oceans. These results suggest that the evolution of the atmospheric composition is strongly linked/coupled with the surface pressure. The dashed blue lines denote runs which assume no solubility limitations to the outgassing of H_2 and H_2O and resulting in a large atmospheric pressure at surface. For the reducing state (IW buffer), the surface pressure is lower compared to the oxidised case (QFM buffer), as expected. The green solid lines denotes runs which show the effect of solubility without hydrogen escape and water condensation (all gases remain in the atmosphere). Here, due to the solubility effect, there is a slight difference in the surface pressure between the IW and the QFM buffers. The dotted lines represent the scenario where all the hydrogen escapes and the water condenses. In this case, the pressures at the surface are lower compared to the other cases analysed. The chemistry of the atmosphere reflects the reducing or oxidizing nature of the mantle in terms of a CO- versus a CO_2-dominated atmosphere.

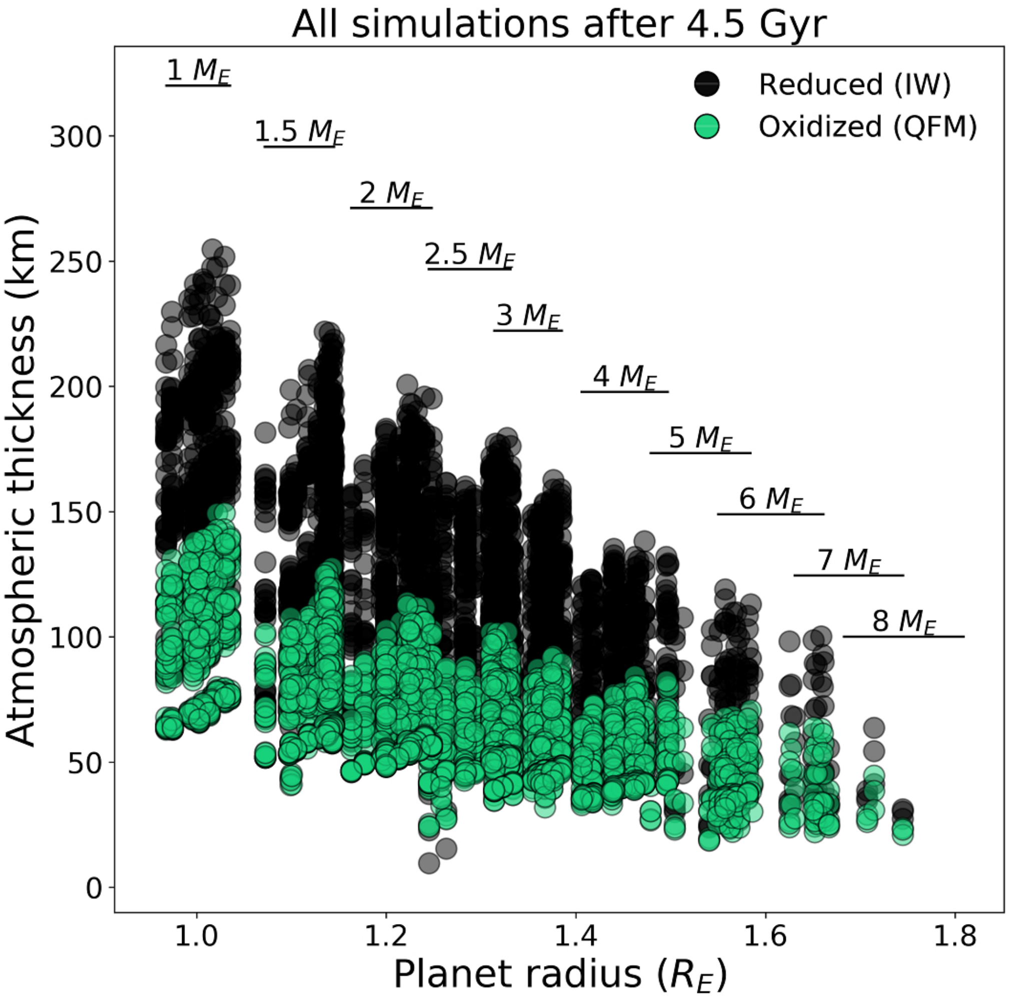

Figure 21: Scatter plot showing calculated atmospheric thicknesses versus planetary radii of all 7,650 scenarios which result in outgassing. Colours indicate mantle redox buffers (black is IW; green is QFM.) The range of planet radii corresponding to the individual input planetary masses are marked with horizontal lines.

To summarise the effect of the oxygen fugacity on the radial extent of the atmosphere, figure 21 compares the calculated atmospheric thicknesses for different planet radii considering the two different petrological mineral buffers assuming no atmosphere losses. There is a marked difference between the atmospheric thickness for the reducing (IW) compared to the oxidising (QFM) scenario. In all the cases analysed, the reduced states have larger atmospheric thicknesses than the oxidised scenarios. It is interesting to note, that even though the reducing scenario atmospheres have smaller masses and densities, in our simulations their atmospheric thicknesses are larger than in the oxidised cases. This is due to the different molecular weights of the outgassed species. In a reducing scenario the volatiles have a smaller molecular weight and this results in a larger atmospheric thickness.

3.1.4 Discussion

Our numerical simulations show that the mantle's redox state influences the volatile content of the melt as well as the volatile chemistry during degassing. On the other hand, planetary mass affects the total volume of melt that is produced and hence the volatile depletion of the mantle. Some authors (Wood et al., 2006; Ramirez et al., 2014) have suggested there is an influence of planet mass on the oxidation of the mantle. More massive planets are able to reach higher central pressures, which facilitate more effective disproportionation of ferrous iron and its segregation into the core. Further, (Elkins-Tanton and Seager, 2008) have hypothesized coreless super-Earths, which would not see any mantle oxidation from this mechanism. Since we consider multiple redox buffers for all planets, our analysis does not exclude the possibility of coreless super-Earths and the idea that Mars-sized planets may generally have more reduced mantles (Ramirez et al., 2007). Figure 16 (middle panel) shows that the CO_3^{2-} partitioning in the melt is suppressed in the reducing scenarios causing an enrichment in H_2O in the rising melt and favoring an outgassing of H_2O or H_2 over carbon-containing species. When the melt reaches the surface, the gas chemical speciation governs the partial pressure of the different outgassed volatile species (Figure 16, bottom panel) and the atmospheric composition. Figure 19 shows the variation of the gas species due to different melt oxidation states. Depending on the initial volatile composition, CO, H_2 and H_2O dominate the outgassing for the reduced mantle case whereas H_2O and CO_2 dominate for the oxidised case. Assessing the melt fluxes and the volatile outgassing, we analysed atmospheric growth and evolution over time. Masses from 2 to 4 Earth masses are the most efficient in depleting the mantle of volatiles and outgassing large volumes of gas. As shown in figure 19, the reducing scenarios produce a larger atmospheric thickness compared to the oxidised cases. This is due to the different atmospheric composition between the two analysed cases. In the reducing case, the smaller molecular weights of CO, H_2O and H_2 compared to CO_2 favour atmospheres which are less dense and which have a larger atmospheric scale height.

Considering atmosphere evolution, one aspect that affects the final composition is hydrogen escape, which was treated in a simplified way in figure 20. In general, transport (via eddy or molecular diffusion) together with photochemistry of H-containing species from the surface to the lower boundary of the homopause can result in the loss of atomic hydrogen from the atmosphere to space. Diffusion-limited escape depends on the atmosphere species, the hydrogen mixing ratio and the scale height of the atmosphere (equation 223). The diffusion of hydrogen to space is limited by the rate of transport of molecules from the atmosphere below. On the other hand, the loss of hydrogen dominated atmospheres due to the host star can be limited by the XUV energy which is dependent upon several factors such as stellar age, rotation and activity (Johnstone et al., 2015). For planets with strong hydrogen outgassing or/and Super-Earths which retain hydrogen envelopes, H_2 can modify climate by influencing the greenhouse affect (Pierrehumbert and

Gaidos, 2011). Regarding the loss of hydrogen from early Earth's atmosphere, a rapid steam collapse leading to the formation of a water ocean would likely result in enhanced hydrogen escape from the atmosphere due to the strong EUV radiation of the young Sun. Atmosphere sinks (e.g. erosion, condensation, carbonate formation) and chemical reactions in the atmosphere can change the redox state and composition of the atmosphere Wordsworth and Pierrehumbert (2014); Luger and Barnes (2015), but a reduced interior with strong, long-lasting volcanic activity would be expected to replenish reduced gases to the atmosphere, which might lead to detectable signatures.

The forthcoming PLATO mission (Rauer et al., 2014; Rauer et al., 2016) will observe planetary radii down to an accuracy of 3 percent. For an Earth-like (Venus-like) planet, making the (rather approximate) assumption that transit measurements will be made in the atmosphere above $\sim$70 km (200 km) depending on wavelength, suggests that the atmospheric contribution to the observed radius makes up $\sim$1.1 (3.3) percent overall. We showed that the redox state of the mantle is one of the main factors influencing the thickness of the atmosphere and its evolution, translating into a few percent change (all other things being equal) in the observed planetary radius. This range is indeed comparable with the detection accuracy of the PLATO mission. The interior redox state of rocky planets could therefore be constrained with PLATO data especially for the thicker, Venus-like terrestrial atmospheres orbiting quieter stars where atmospheric escape is kept to a modest level and where condensation of water is unlikely.

In conclusion, our simulations show that redox-dependent geophysical models can improve interpretation of observed atmosphere data and provide a first-order characterisation of the interior chemical state of rocky exoplanets. Future observations of the atmospheric composition could give further constraints on the interior. Knowledge about the reducing or oxidising state of an atmosphere can guide future selection of target candidates for follow-up missions to detect a potentially habitable or even inhabited planet.

3.1.5 Methods

Melting and volatile partitioning For investigating the transfer of volatiles from the interior to the atmosphere we use a 2D thermal evolution model to simulate mantle convection and melt production over time. In order to cover a wide range of different possible exoplanets, according to (Noack et al., 2017; Dorn et al., 2018) we vary the initial conditions of the system considering different planet masses (from 1 to 8 Earth masses), Mg/Si and Fe/Si ratios (0.5, 1 and 1.5 times solar values), distribution of iron between mantle and core (going from small cores with a high mantle iron content to the largest possible iron cores), the initial lithosphere thickness (50 to 100 km), initial upper mantle temperature (from 1600 to 2000 K beneath an initial lithosphere), temperature difference between core and mantle, initial amount of radiogenic heat sources (from 0.5 to 1.5 times Earth values), different mantle rheology and a wet compared to a dry mantle. For more details on the parameter cases we refer the reader to (Dorn et al., 2018). Melting occurs locally if the mantle temperature rises above the solidus melting temperature (Hirschmann, 2000; Katz et al., 2003) and we assume that 10% (Crisp, 1984) of the melt is immediately extracted to the surface and contributes to outgassing. The amount of melt depends on the rock composition that affects the solidus temperature, the internal thermal state and the size of the planet. The melting temperature is affected by variable initial iron and volatile content of the mantle (Noack et al., 2017; Dorn et al., 2018). The internal thermal state (i.e. the initial mantle temperature and the quantity of radioactivity heat sources) regulates the production of melt. Melting leads to the mantle being depleted in volatiles.

Our mantle and melt model is based on previous outgassing studies (Noack et al., 2017; Dorn et al., 2018) conducted with the convection code Crust, Habitability, and Interior Code (CHIC). CHIC is a 2D convection code which simulates the mantle convection in a stagnant lid tectonic regime solving the conservation equations of mass, momentum and energy in the rocky mantle (Noack et al., 2017). We use a regional 2D spherical annulus geometry (Hernlund and Tackley, 2008) with the mantle being divided into cells with height of 25 km each. Pressure dependent parameters such as mineral-dependent density, thermal expansion coefficient and heat capacity for an adiabatic temperature profile are employed as in Dorn et al. (2018). We model a compressible mantle by employing the truncated anelastic liquid approximation (TALA). In Dorn et al. (2018), we assumed for simplicity that the mantle is homogeneously mixed at all times, and that its hydrogen and carbon are continuously depleted upon melting. However, in the present study, we *a posteriori* employ a redox-dependent partitioning of carbonates into the melt based on Grott et al. (2011), Holloway (1981), Holloway et al. (1992), and consider partitioning of water into the melt based on Katz et al. (2003). We apply a batch melting model, based on our assumption that the melt is in equilibrium with the source rock before it rises to the surface. The partitioning of volatiles from the rock to the melt depends on the mantle-averaged melt fraction F and partition coefficient $D_{\mathrm{H_2O}}$ via,

$$X^{\mathrm{melt}}_{\mathrm{H_2O}} = \frac{X^{\mathrm{rock}}_{\mathrm{H_2O}}}{D_{\mathrm{H_2O}} + F(1 - D_{\mathrm{H_2O}})}, \tag{197}$$

where we take $D_{\mathrm{H_2O}}$ to be constant and equal to 0.01 Michael (1995).

We assume that carbon is stored in the mantle in the form of graphite, and dissolves into the melt in the form of carbonate ions, $\mathrm{CO_3^{2-}}$. The amount of carbonate present is directly linked to the oxygen fugacity, $f_{\mathrm{O_2}}$ (Grott et al., 2011; Holloway, 1998). The $\mathrm{CO_2}$ abundance in the melt used for the gas speciation model can then be calculated as follows:

$$X^{\mathrm{melt}}_{\mathrm{CO_2}} = \left[\frac{M_{\mathrm{CO_2}}}{\mathrm{fwm}} X^{\mathrm{melt}}_{\mathrm{CO_3^{2-}}}\right] \Big/ \left[1 - \left(1 - \frac{M_{\mathrm{CO_2}}}{\mathrm{fwm}}\right) X^{\mathrm{melt}}_{\mathrm{CO_3^{2-}}}\right], \tag{198}$$

where $M_{\mathrm{CO_2}}$ is the molar mass of carbon dioxide and fwm is the formula weight of the melt where the number of atoms considered in the lattice unit are expressed per oxygen atom. In this way we assume fwm=36.594 based on the 1921 Kilauea tholeiitic basalt following the approach of Holloway et al. (1992).

The amount of carbonates dissolved in the melt can be calculated from equilibrium constants K_1 and K_2:

$$
\begin{aligned}
X^{\text{melt}}_{\text{CO}_3^{2-}} &= \frac{K_1\, K_2\, f_{\text{O}_2}}{1 + K_1\, K_2\, f_{\text{O}_2}} \\
\log_{10} K_1 &= 40.07639 - 2.53932 \times 10^{-2}\, T \\
&\quad +5.27096 \times 10^{-6}\, T^2 + 0.0267\, \frac{p-1}{T} \\
\log_{10} K_2 &= -6.24763 - \frac{282.56}{T} - 0.119242\, \frac{p-1000}{T}
\end{aligned}
$$

for temperature, T, in K and pressure, p, in bar, and where f_{O_2} is calculated based on different assumed redox buffers as described in Section 3.1.5.

For a more realistic treatment of volatile depletion in the mantle upon melting, we divide the mantle into two different volatile reservoirs, namely the upper and lower mantle respectively. We assume here that the mineral phase transition for ringwoodite to perovskite which separates the mantle into these two reservoirs takes place at 23 GPa (hence not accounting for any thermal effects on the transition pressure). The mantle pressure profile is directly obtained from the interior structure model that also gives us depth-dependent profiles for material parameters such as density and thermal expansion coefficient depending on our input mantle composition. The assumed initial volatile content (see table 5) is homogeneously applied to the entire mantle. Melting depletes the upper mantle due to partitioning of volatiles into the melt (equations 197 and 198).

Mixing between upper and lower mantle depends on the convective velocity v of the mantle. While our convection simulation gives us information on the local convective strength, a global measure for the efficiency of mixing can be directly obtained from a common scaling law (Grott et al., 2011) linking the average mantle convective velocity with the composition-dependent Rayleigh number Ra, which is a non-dimensional indicator of the convection efficiency:

$$
v = 2 \cdot 10^{-12} \left(\frac{Ra}{450}\right)^{(1/3)} \text{(m/s)}, \tag{199}
$$

$$
Ra = \frac{\rho g \alpha \Delta T D^3}{\kappa \eta} \tag{200}
$$

The Rayleigh number Ra depends on the density ρ, gravitational acceleration g, thermal expansion coefficient α, mantle thickness D, thermal diffusivity κ and mantle viscosity η. ΔT is the temperature contrast across the mantle. Following common mantle convection parameterizations (which in our study are based on Grott et al. (2011)). The volume of mantle material transported from the lower into the upper mantle can then be estimated via:

$$V_{\text{exch}} = 0.5v\ dt\ A_{tr}, \tag{201}$$

where dt is the time step in seconds and A_{tr} is the surface area of the boundary between upper and lower mantle. Note we do not take into account that the phase transition from upper to lower mantle can reduce convective material exchange; we therefore overestimate volatile outgassing during the earlier stages of planetary evolution.

The average volatile content of the upper mantle ('um') and lower mantle ('lm') is then calculated in each time step as follows:

$$X_{\text{H}_2\text{O,new}}^{\text{rock,um}} = X_{\text{H}_2\text{O}}^{\text{rock,um}} \frac{V_{\text{um}} - V_{\text{exch}}}{V_{\text{um}}} + X_{\text{H}_2\text{O}}^{\text{rock,lm}} \frac{V_{\text{exch}}}{V_{\text{um}}} \tag{202}$$

$$X_{\text{H}_2\text{O,new}}^{\text{rock,lm}} = X_{\text{H}_2\text{O}}^{\text{rock,lm}} \frac{V_{\text{lm}} - V_{\text{exch}}}{V_{\text{lm}}} + X_{\text{H}_2\text{O}}^{\text{rock,um}} \frac{V_{\text{exch}}}{V_{\text{lm}}} \tag{203}$$

When melting occurs in the upper mantle, and if the melt is buoyant (Ohtani et al., 1995; Jing and Karato, 2009), we assume that it is transported instantaneously upwards to the surface. Based on modern Earth average values for continental crust (Crisp, 1984), we expect that about $X_{\text{extr}} = 10\%$ of the melt reaches the planet surface as extrusive melt and contributes to degassing into the atmosphere and we set this value as input in our model. In the discussion section, we further discuss possible contributions from intrusive melt pockets in the crust.

Gas speciation model To simulate the gas chemical speciation at different redox states we consider the Iron-Wustite (IW) and the Quartz-Fayalite-Magnetite (QFM) petrological mineral buffers. A mineral buffer is commonly employed in experimental petrology to keep constant the oxygen fugacity level in a reaction and to reproduce an oxidised or reduced state. By simulating the behaviour of mineral buffers, we calculate the oxygen fugacity of the system at different pressures and temperatures. For simulating a reducing case we simulate the QFM buffer while for the oxidising scenario we reproduce a redox state associated to the IW buffer. Normally, one would expect the oxidation state to change depending on the mantle composition, the proportion of FeO to Fe_3O_4, and the degassing of reduced species (Kasting et al., 1993; Frost and McCammon, 2008; Sharp, 2017). For simplicity, we hold oxidation states to constant values corresponding to IW and QFM mineralogical buffers.

Volatile chemical speciation in the C-O-H system is calculated via the "Equilibrium and mass balance method" (French, 1966; Holloway, 1981; Fegley, 2013; Gaillard and Scaillet, 2014; Schaefer and Fegley, 2017) for a wide range of pressures, temperatures and oxygen fugacities. Since the oxidation state of the melt strongly affects the chemical speciation of the volatiles therein, a speciation model has to calculate the oxygen fugacity, f_{O_2}, at a given temperature and pressure.

We assume the following common petrological mineral buffers:

$$2\,\mathrm{Fe} + \mathrm{O_2} \rightleftharpoons 2\,\mathrm{FeO}, (\mathrm{IW}) \tag{204}$$

$$3\,\mathrm{Fe_2SiO_4} + \mathrm{O_2} \rightleftharpoons 2\,\mathrm{Fe_3O_4} + 3\,\mathrm{SiO_2}, (\mathrm{QFM}) \tag{205}$$

Each mineral buffer has a characteristic temperature-dependent f_{O_2} curve (Holloway et al., 1992). Considering that the outgassing is simulated at the surface the pressure has only a negligible effect, as shown in figure 22. The calculated redox states are then used to estimate the partial pressures of each volatile (H_2, H_2O, CO and CO_2) as a function of oxygen fugacity (f_{O_2}) following (Holland, 1984). According to the approach of (Gaillard and Scaillet, 2014), to estimate the volume of volatiles that remain in solution in the melt and the outgassed species we combine the gas-melt (solubility) with the gas-gas equilibria (degassing).

The gas-melt equilibria involved are:

$$\mathrm{H_2O^{(fluid)}} + \mathrm{O^{2-(melt)}} \rightleftharpoons 2\,\mathrm{OH^{-(melt)}} \tag{206}$$

$$\mathrm{CO_2^{(fluid)}} + \mathrm{O^{2-(melt)}} \rightleftharpoons \mathrm{CO_3^{2-(melt)}} \tag{207}$$

$$\mathrm{H_2^{(fluid)}} \rightleftharpoons \mathrm{H_2^{(melt)}} \tag{208}$$

Considering the atmospheric pressure at the surface as degassing pressure, equilibria 206 and 207 are simulated according to (Iacono-Marziano et al., 2012) while we assume that all the H_2 and the CO are outgassed because of their low solubilities in silicate melts (Gaillard et al., 2003; Morizet et al., 2010; Pawley et al., 1992).

Hydrogen is distributed between H_2 and H_2O via the following gas-gas equilibrium:

$$2\,\mathrm{H_2^{(fluid)}} + \mathrm{O_2} \rightleftharpoons 2\,\mathrm{H_2O^{(fluid)}}. \tag{209}$$

The equilibrium constant (K_3) for this reaction can be expressed:

$$K_3 = \exp\left(\frac{-\Delta_r G_3^0}{R \cdot T}\right), \tag{210}$$

where R is the universal gas constant (8.314 J K^{-1} mol^{-1}), T denotes the temperature of the degassed

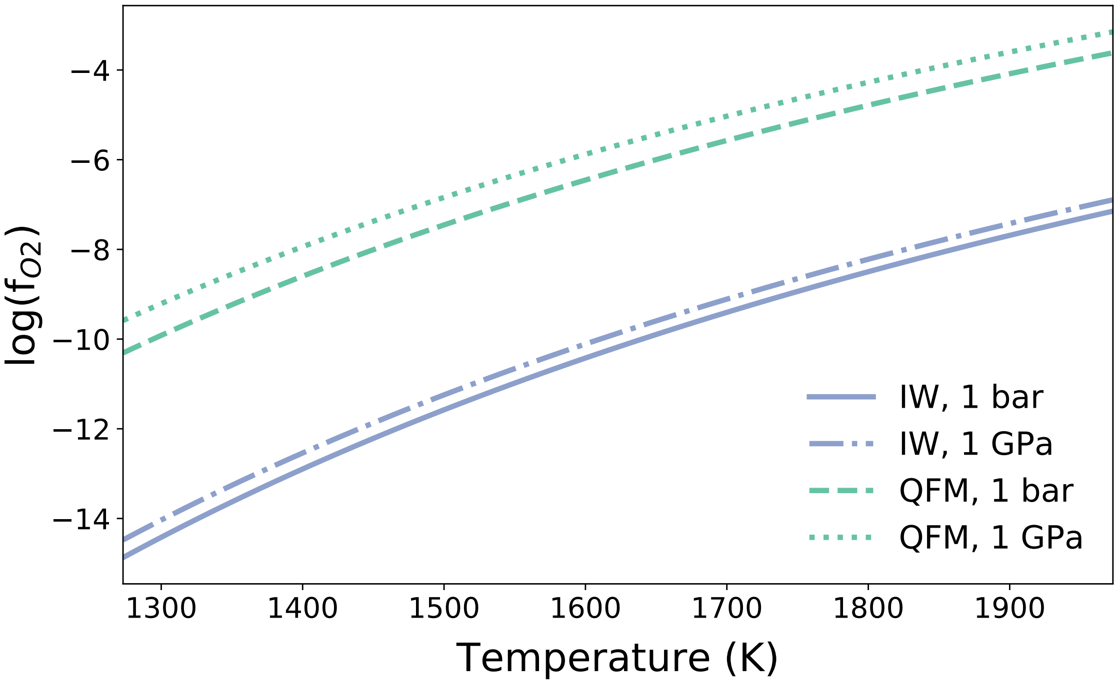

Figure 22: The variation of oxygen fugacity with melt temperature at different pressures for the IW and QFM redox buffers.

material in Kelvin, and $\Delta_r G_3^0$ denotes the Gibbs free energy of the reaction in equation (209). The latter depends only on the Gibbs free energy of formation of water, $\Delta_f G^0_{H_2O}$, via

$$\Delta_r G_3^0 = 2\Delta_f G^0_{H_2O}. \tag{211}$$

Knowing K_3 one can calculate the ratio of H_2O to H_2 at equilibrium. This has a direct dependence on f_{O_2}:

$$\left(\frac{X_{H_2O}}{X_{H_2}}\right)^2 = K_3 f_{O_2}, \tag{212}$$

Carbon is distributed with the gas-gas equilibrium between CO and CO_2 via:

$$CO^{(fluid)} + \frac{1}{2}O_2 \rightleftharpoons CO_2^{(fluid)}, \tag{213}$$

whose relative pressures are similarly set by the corresponding equilibrium constant,

$$K_4 = \exp\left(\frac{-\Delta_r G_4^0}{RT}\right) = \frac{X_{CO_2}}{X_{CO}}\frac{1}{f_{O_2}^{1/2}}, \tag{214}$$

where

$$\Delta_r G_4^0 = \Delta_f G^0_{CO_2} - \Delta_f G^0_{CO}. \tag{215}$$

Table 6: Standard Gibbs free energies of formation used in this work are calculated via the gas reactions from Fegley (2013), valid for 1 bar pressure and the temperature (T) range 298–2500 K. Carbon is considered to exist in the form of graphite in our analysis.

$\Delta_f G^0 = a + bT \log T + cT$	a	b	c
$2\,C + O_2 = 2\,CO$	-214104.0	25.2183	-262.1545
$C + O_2 = CO_2$	-392647.0	4.5855	-16.9762
$2\,H_2 + O_2 = 2\,H_2O$	-483095.0	25.3687	21.9563

The values of $\Delta_f G^0$ for each species have been determined empirically and can be found in standard thermodynamic tables from the literature (Chase, 1999) (table 6). This enables the calculation of volatile chemical speciation at equilibrium from the temperature, pressure and oxidation state of the system.

We do not consider atmospheric climate, photochemistry or convection. Processes such as the hydrological cycle, surface-atmosphere exchange and atmospheric escape are the subject of future work. We set the degassing temperature to the liquidus melting temperature, which is about 2000 K (e.g., Katz et al., 2003) and the surface pressure as outgassing pressure. Furthermore, we do not include O_2 since the O_2 partial pressure in the mantle is at least five orders of magnitude lower (10^{-5} bar) compared to other volatile species (French, 1966; Holloway, 1981). Similarly, CH_4 concentrations in a high-temperature and low pressure magmatic context are insignificant, if present at all (Chiodini, 2009; Oppenheimer et al., 2014). As reported by (Wetzel et al., 2013; Ramirez et al., 2007; Zhang and Duan, 2009), methane starts to be present at redox conditions below the IW buffer and at very high pressure at depth within the lithosphere. Therefore, in our simulations we exclude the methane because we do not reproduce reducing states below the IW buffer and we simulate the degassing at the surface, where the atmospheric pressure never reaches values comparable to the lithostatic pressures.

Volatile outgassing and atmospheric height. We obtain melt fluxes over time from our mantle convection code, together with the gas fractions of the species CO, CO_2, H_2, and H_2O depending on volatile content, temperature, and redox state of the melt.

The masses of the various atmospheric species which accumulate over time k are calculated via:

$$\begin{aligned}
M_{\mathrm{atm}}^{\mathrm{H_2O}} &= X_{\mathrm{extr}} \sum_{k=2}^{n} X_{\mathrm{H_2O}}^{\mathrm{melt}}(t_k) F_k V_{\mathrm{mantle}} \rho_{\mathrm{mantle}} \frac{X_{\mathrm{H_2O}}}{X_{\mathrm{H_2}} + X_{\mathrm{H_2O}}} \\
M_{\mathrm{atm}}^{\mathrm{H_2}} &= X_{\mathrm{extr}} \sum_{k=2}^{n} X_{\mathrm{H_2O}}^{\mathrm{melt}}(t_k) F_k V_{\mathrm{mantle}} \rho_{\mathrm{mantle}} \frac{X_{\mathrm{H_2}}}{X_{\mathrm{H_2}} + X_{\mathrm{H_2O}}} \frac{M_{\mathrm{H_2}}}{M_{\mathrm{H_2O}}} \\
M_{\mathrm{atm}}^{\mathrm{CO_2}} &= X_{\mathrm{extr}} \sum_{k=2}^{n} X_{\mathrm{CO_2}}^{\mathrm{melt}}(t_k) F_k V_{\mathrm{mantle}} \rho_{\mathrm{mantle}} \frac{X_{\mathrm{CO_2}}}{X_{\mathrm{CO}} + X_{\mathrm{CO_2}}} \\
M_{\mathrm{atm}}^{\mathrm{CO}} &= X_{\mathrm{extr}} \sum_{k=2}^{n} X_{\mathrm{CO_2}}^{\mathrm{melt}}(t_k) F_k V_{\mathrm{mantle}} \rho_{\mathrm{mantle}} \frac{X_{\mathrm{CO}}}{X_{\mathrm{CO}} + X_{\mathrm{CO_2}}} \frac{M_{\mathrm{CO}}}{M_{\mathrm{CO_2}}},
\end{aligned}$$

where F_k is the average melt fraction at time t_k. X_{H_2}, X_{H_2O}, X_{CO} and X_{CO_2} are mole fractions determined as described in Section 3.1.5. V_{mantle} is the volume of the mantle and ρ_{mantle} is the average mantle density. X_{extr} denotes the fraction of melt that we assume to reach the surface via extrusive volcanism, which we set here to 10%, which is in the range of observed values for Earth's continental crust (Crisp, 1984).

To estimate atmospheric extent one has to relate the molecular weight of outgassed species M^i_{atm} to their partial pressures p^i_{s}. The *total* pressure p_{s} at a given point in the atmosphere is proportional to the *total* overhead weight of the atmospheric column which can be estimated via the hydrostatic relation assuming vertical motions are negligible via:

$$p_{\mathrm{s}} = \frac{g}{A} M_{\mathrm{atm}} \, , \tag{216}$$

where g is the surface gravity and A the total surface area of the planet. The total pressure and mass are given given by:

$$p_{\mathrm{s}} = \sum_i p^i_{\mathrm{s}} \quad \text{and} \quad M_{\mathrm{atm}} = \sum_i M^i_{\mathrm{atm}} \, . \tag{217}$$

Using the volume mixing ratio x_i, the partial pressure of a species i is determined by $p^i_{\mathrm{s}} = x_i p_{\mathrm{s}}$, while the corresponding atmospheric mass is determined via the mass mixing ratio w_i according to: $M^i_{\mathrm{atm}} = w_i M_{\mathrm{atm}}$.

The relationship between these two mixing ratios - assuming an ideal gas - is given by:

$$w_i = \frac{\rho_i}{\rho} = \frac{m_i}{\bar{m}} \frac{n_i}{n} = \frac{m_i}{\bar{m}} \frac{p^i_{\mathrm{s}}}{p_{\mathrm{s}}} = \frac{m_i}{\bar{m}} x_i \, , \tag{218}$$

where ρ is the mass density, n the number density, m_i the molecular weight of species i, and $\bar{m}$ the mean molecular weight, given by:

$$\bar{m} = \sum_i x_i m_i \, . \tag{219}$$

Using this relation, equation (216) for a single species i, that is well-mixed throughout the atmosphere, is given by:

$$p^i_{\mathrm{s}} = \frac{g}{A} \frac{\bar{m}}{m_i} M^i_{\mathrm{atm}} \, . \tag{220}$$

Consequently, the partial pressure of a given atmospheric species depends on both the number densities as well as the molecular masses of all species present. For a given column mass density, going from a composition of rather heavy molecules (e.g. CO_2 or H_2O) to lighter species (e.g. H_2) will reduce the total surface pressure and, hence, could strongly impact habitability. The effect is even stronger at larger surface gravities.

In our work, the atmospheric thickness (ΔR_p) is defined from the planetary surface to the pressure p_{min}. To calculate the atmospheric thickness, given the accumulated amounts of outgassed species (e.g. H_2O,

CO_2, H_2), we use a simple scale height model following Dorn and Heng (2018):

$$\Delta R_p = H \ln \left(\frac{p_{\text{tot}}}{p_{\text{min}}} \right), \tag{221}$$

where p_{tot} is the total gas pressure. p_{min} is the pressure at which the atmosphere becomes opaque that is where the chord optical depth becomes 0.6. p_{min} is defined as:

$$p_{\text{min}} \approx \frac{g}{\kappa} \sqrt{\frac{H}{2\pi R_p}}. \tag{222}$$

If we assume a mean opacity of $\kappa = 0.1$ cm^2 g^{-1} (Freedman et al., 2014) , then we obtain $p_{\text{min}} \approx 1$ mbar. Our main focus is the relevance for habitable planets. To this end, the pressure scale height H is calculated assuming a mean atmospheric temperature T_{atm} of 288 K, which is the Earth´s average surface temperature:

$$H = \frac{R \cdot T_{\text{atm}}}{\bar{m} \cdot g} \tag{223}$$

where g is surface gravity, R is the universal gas constant (8.3144598 J mol^{-1} K^{-1}), and $\bar{m}$ is again the mean molecular weight of the gas mixture.

Acknowledgement. We thank Sebastian Tappe for the editorial handling. We acknowledge James Kasting, Fabrice Gaillard and three anonymous reviewers for constructive comments and Harry Becker, Timm John and Stephan Klemme for helpful discussions during the preparation of the manuscript. H.R., J.L.G. and L.N. acknowledge the DFG priority program SPP 1992 "Exploring the Diversity of Extrasolar Planets" and participation in ISSI teams 370 and 464 as well as several ISSI workshops with useful discussions. L.N. and S.V. acknowledge the support from DFG project NO 1324/2-1. C.D. acknowledges the support of the Swiss National Foundation under grant PZ00P2_174028, and that this work was in part carried out within the frame of the National Center for Competence in Research *PlanetS*. D.K. acknowledges the financial support from the Center for Space and Habitability (CSH) of the University of Bern. This work was supported by the Deutsche Forschungsgemeinschaft (DFG, German Research Foundation) – Project-ID 263649064 – TRR 170. This is TRR 170 Publication No 103.

Author contributions. All authors contributed to the preparation of the manuscript. Specifically, G.O., L.N. and F.S. were responsible for the numerical simulations to obtain redox-dependent outgassing data. D.K. and C.D. provided the partial pressure and atmosphere thickness calculations. J.L.G., N.K. and H.R. contributed to the work on atmosphere erosion and possible future observations. C.G., J.S. and L.N. created the graphical visualizations. J.S., S.V., G.O. and L.N. worked on the solubility of volatiles in intrusive and

extrusive magma.

3.1.6 Supplementary materials

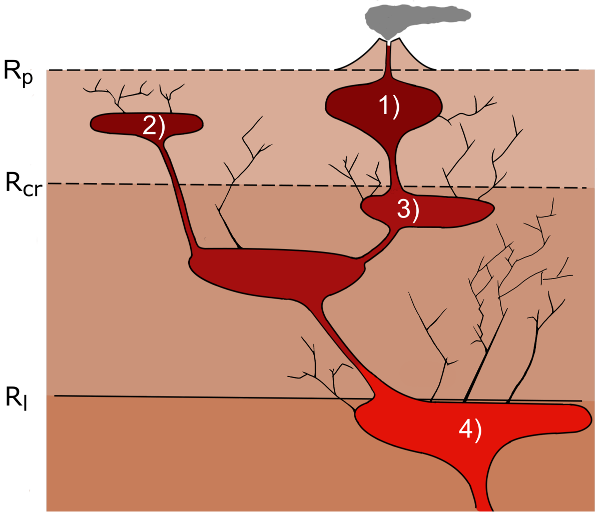

Figure 23: Magma chamber depth zones. 1) extrusive shallow volcanism, 2) intrusive crustal magmatism, 3) magmatic underplating, 4) chambers below the lithosphere. Rp: Planet radius, Rcr: Crust radius and Rl: Lithosphere radius. Through the illustrated cracks (black), outgassing from lower magma levels is becoming possible. In the analysed cases, we consider the outgassing contribution from the magma at the surface.

Passive outgassing and solubility effect. Depending upon the depth (hence pressure) at which the melt is produced, degassing could begin soon after magma formation. The total amount of outgassing is the combination of gases released both from deep magmatic emplacements (passive degassing) and from the melt extruded to the surface. Figure 23 shows magma chambers at different depths within or directly below the lithosphere and cracks and fissures where the gas ascends to the surface. The lithostatic pressure and the mantle redox state affect the volatile content in the melt and the final outgassing. Figure 24 illustrates how pressure influences gas species' amounts; the effect is stronger under reducing conditions (QIF and IW mineral buffers). On increasing the pressure, the H_2O and CO_2 content increase with similar trends while the volume of CO and H_2 decrease. For oxidising states (NiNiO and QFM mineral buffers) the pressure effect on the speciation is negligible. In our example we assume as initial volatile content in the melt 50 mol % of both H_2O and CO_2. Global mean values based on modern Earth (Crisp, 1984) suggest that 10% of the generated melt reaches the surface and directly contributes to the outgassing. Passive degassing on the Earth is larger than the extrusive component (Crisp, 1984; Shinohara, 2008). Intrusive magma bodies emplaced at the bottom or within the lithosphere, continuously crystallise due to cooling. Since volatiles such as H_2O or CO_2 are incompatible in the crystal lattice of mafic minerals, they tend to concentrate in the melt. At a certain point, the concentration exceeds the solubility and a gas-phase forms (Burnham, 1967; Holloway

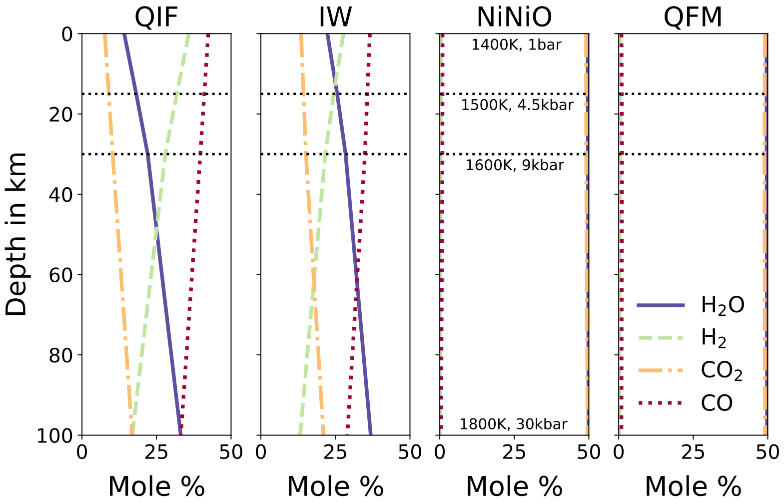

Figure 24: Depth profiles of the gas speciation variation depending on redox state, pressure and temperature for intrusive melt. We assume here a fixed volatile ratio of 50 mol% H_2O and 50 mol% CO_2 in the melt. Temperature and pressure values for cases 1) to 4) in Fig. 23 are shown in the NiNiO panel.

and Blank, 1994; Wallace et al., 1995; Zhang et al., 2007; Parfitt and Wilson, 2008; Shinohara, 2008). The gas is buoyant and ascends either through already-existing cracks and fissures or leads to overpressure which may itself result in cracks. Such intrusive degassing should strongly influence the amount as well as the composition of the outgassed volatiles, especially since the solubility of CO_2 is much lower compared to H_2O (e.g., Holloway, 1976; Holloway and Blank, 1994; Parfitt and Wilson, 2008; Shinohara, 2008; Petrelli et al., 2018), see figure 25.

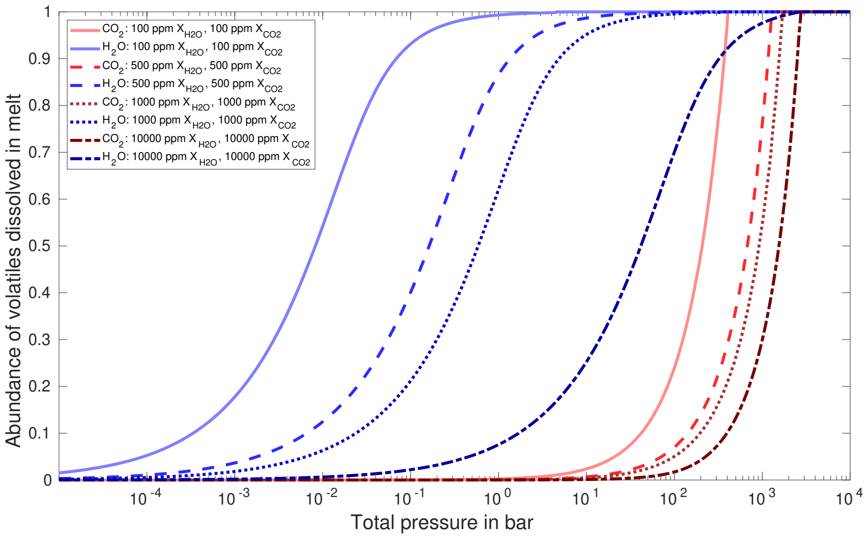

Figure 25: Solubility profiles for H_2O and CO_2 degassing depending on pressure for different volatile contents in the melt calculated after Iacono-Marziano et al. (2012).

Therefore, CO_2 degasses rather quickly, especially at low pressures, while H_2O is assumed to remain in the melt. Only at the very end of the crystallisation sequence, H_2O can be degassed at these low pressures, if the saturation limit is exceeded (Bower et al., 2019). This tendency toward earlier CO_2 degassing should strongly affect both the amount as well as the composition of the outgassed volatiles. Since we performed the outgassing simulations at surface pressure, the contribution of passive degassing was negligible as the effect of crystallisation and the related oversaturation of the melt is not considered in our work. Even though, at higher pressures there should be a strong influence of passive degassing, especially since the pressure has a direct influence on degassed volatile species under reducing conditions (considered for early Earth), which is shown in figure 24. Depending on the redox buffer (QIF or IW), at very low pressures mainly CO and H_2 are degassed, while at higher pressures CO and H_2O degassing dominates. For oxidised conditions, the effect of pressure is negligible and for both buffers (NiNiO and QFM) only H_2O and CO are degassed. However, the effect of crystallization in magmatic intrusions is not considered here and should be a point for future studies.

Volatile chemical speciation. In figures 26 and 27 we show how the melt oxidation state plays a crucial role for the gas chemical speciation and therefore for atmospheric evolution.

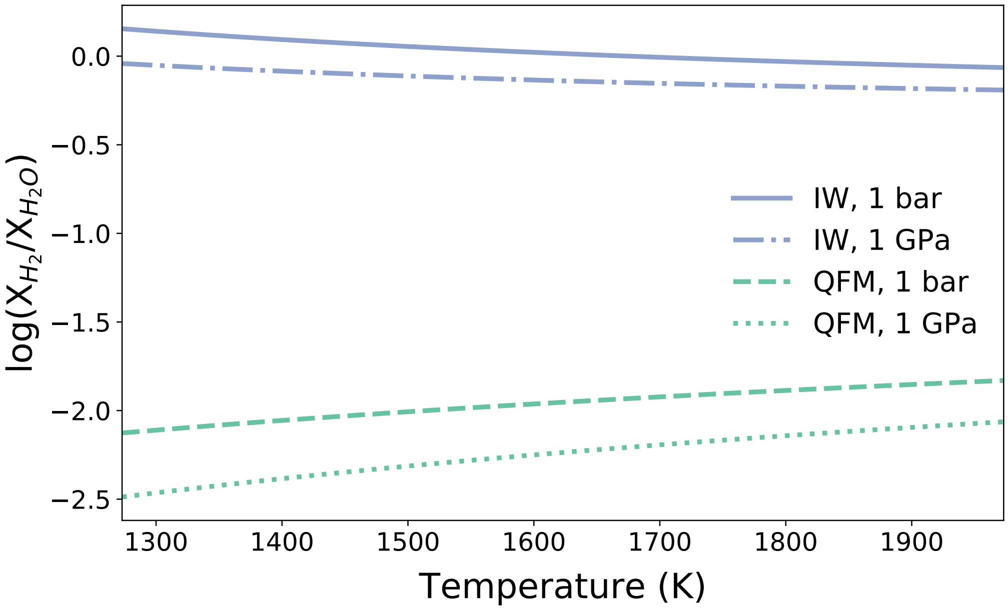

Figure 26: H_2-to-H_2O mole ratio for different temperatures and mineral redox buffers where QFM is the oxidising case and IW the reducing scenario. H_2-to-H_2O mole ratio for the IW buffer is described at 1 bar with the solid line and at 1 GPa (1 Gpa = 10000 bar) by the dashed and dotted line. H_2-to-H_2O mole ratio for the QFM buffer is represented at 1 bar with the dashed line and at 1 GPa by the dotted line.

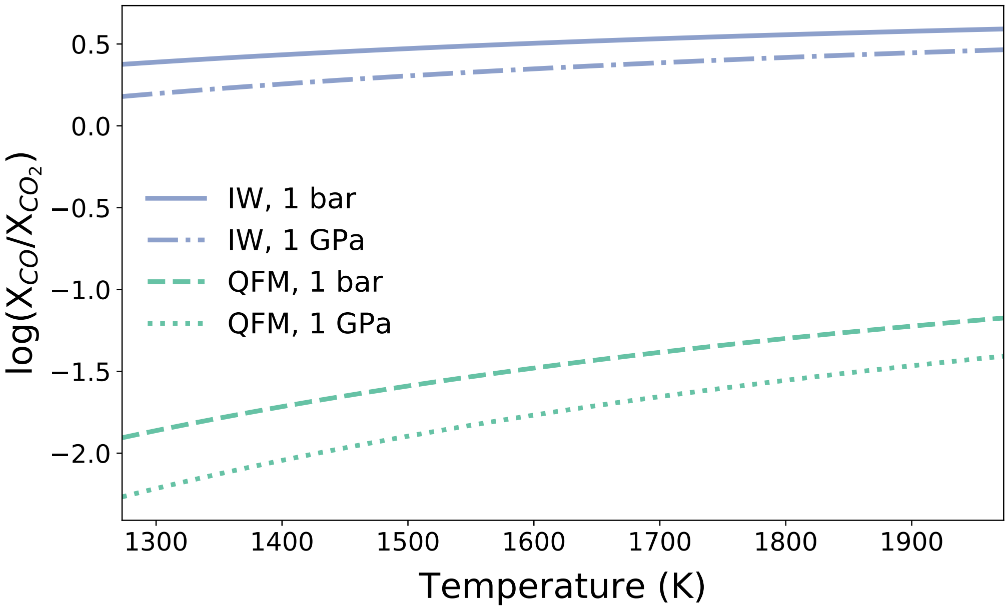

Figure 27: CO-to-CO_2 mole ratio for different temperatures and mineral redox buffers where QFM is the oxidising case and IW the reducing scenario. CO-to-CO_2 mole ratio for the IW buffer is described at 1 bar with the solid line and at 1 GPa (1 Gpa = 10000 bar) with the dashed and dotted line. CO-to-CO_2 mole ratio for the QFM buffer is represented at 1 bar by the dashed line and at 1 GPa by the dotted line.

3.2 The early Earth's volcanic outgassing rates from mantle convection, melting, and volatile speciation

Guimond C.M., Noack L., Ortenzi G. and Sohl F. *The early Earth's volcanic outgassing rates from mantle convection, melting, and volatile speciation*. Submitted to: ”Physics of the Earth and Planetary Interiors” (in revision).

3.2.1 Abstract

Before the origin of life, Earth's atmosphere was built up by outgassing of the mantle. Here we model how C-O-H outgassing evolved through the late Hadean and early Archean, if global plate tectonics had not yet initiated and all outgassing were subaerial. The model couples numerical mantle convection, partitioning in the melt, and volatile chemical speciation. The mantle oxidation state controls both the volatile speciation and the carbon partitioning in the melt. Below the iron-wüstite mineral redox buffer, virtually no CO_2 would be outgassed: in such reducing conditions, (i) carbonate can only partition into the melt in very limited amounts, and (ii) almost all carbon takes the form of CO instead of CO_2. We report outgassing fluxes of CO_2, CO, H_2O, and H_2, as a function of mantle oxygen fugacity, for a wide range of initial conditions. Even for oxidized scenarios near the quartz-fayalite-magnetite buffer, we find CO_2 outgassing rates about an order of magnitude lower than the present-day value—contrasting with common assumptions in Archean climate studies. This result is in part due to the strong dependence of CO_2 outgassing on the mantle oxidation state (which may not have reached late Archean values in the Hadean). Lower outgassing is also related to a stagnant lid, illustrating the importance of the presumed tectonic mode on volcanic outgassing rates, especially if outgassing must supply greenhouse gases to warm early Earth under the Faint Young Sun.

3.2.2 Introduction

Somewhere in the early Archean existed the most likely life-spawning environment in the universe. Whilst leaving hardly any observable record, the young atmosphere of the time was fed by volatiles from the deep interior (Holland, 1984; Kasting et al., 1993; Gaillard and Scaillet, 2014)—with possible contributions from both extraterrestrial impacts (Zahnle et al., 2020) and a lingering, degassed magma ocean atmosphere (Katyal et al., 2020). This work focuses on the volcanic outgassing flux of volatiles. Using a coupled 2D numerical model, we investigate the possible mass range of CO_2, CO, H_2O, and H_2 outgassed during the first 700 Myr of solid-state convection, corresponding to approximately 4.5–3.8 Ga. These mass fluxes would be inputs to the processes governing the contemporaneous atmosphere's consummate composition.

The chemical speciation of volcanic gas is controlled by the oxidation state of the upper mantle. Increasing the mantle's oxygen fugacity, f_{O_2}, raises the ratio of oxidized to reduced volatile species in the melt phase. This refers to CO_2/CO and H_2O/H_2 in the C-O-H system (Holland, 1984). As the melt rises adiabatically through conduits, its f_{O_2} re-equilibriates with the decreasing pressure; thus gas abundances at the surface are also linked to the mantle source (Kasting et al., 1993). On modern Earth, for example, the dominant species in volcanic gas are H_2O and CO_2, in line with a mantle f_{O_2} in equilibrium with the quartz-fayalite-magnetite (QFM) mineral buffer (Holland, 1984).

In addition to the effect of f_{O_2} on volatile speciation, the outgassed carbon flux to the atmosphere also depends on how much mantle carbon (as CO_3^{2-}) enters the melt phase, which is likewise controlled by f_{O_2}. In sufficiently reduced conditions where graphite is the stable carbon phase, this graphite reacts with molecular oxygen to produce CO_2 vapour, which again reacts with oxygen to produce CO_3^{2-} (Holloway et al., 1992). Hence a more-rigorous forward model of planetary-scale volcanic outgassing would numerically couple melt partitioning with volatile speciation. To our knowledge, such a model has not yet been presented.

Whilst these two redox controls are well-known, the value of the Archean mantle f_{O_2} itself remains poorly constrained. Immediately after core formation, the magma ocean must have been reduced (Wood et al., 2006); meanwhile, scant geological evidence suggests that by $\sim$3.8 Ga before present at the latest, the uppermost mantle was already about as oxidized as today (Canil, 1997; Delano, 2001; Trail et al., 2011; Nicklas et al., 2019; Armstrong et al., 2019). A lack of certainty persists on the timing of this oxidation (see section 3.2.3). Therefore, to cover the possible spread of redox states, we investigate outgassing fluxes under a wide range of mantle f_{O_2}, especially in proportion to other unknown parameters such as the mantle volatile content and thermal state.

By numerically coupling redox-dependent melt partitioning with speciation, and by investigating a broader range of mantle oxidation states, we can advance the current literature dedicated to C-O-H outgassing from solid-state mantles of rocky planets in the solar system and elsewhere (O'Neill et al., 2007; Grott et al., 2011; Noack et al., 2014, 2017; Tosi et al., 2017; Dorn et al., 2018; Ortenzi et al., 2020). Previous models have tended to assume an oxidizing mantle, akin to that of present-day Earth—with the exceptions of Grott et al. (2011) on early Mars, Tosi et al. (2017) on Earth-size exoplanets, and more recently Ortenzi et al. (2020) on exoplanets of various size. We apply our coupled model to Archean Earth, a case which has not yet been the dedicated subject of a numerical outgassing study.

A parallel approach used to estimate planetary outgassing fluxes is to parameterize them in terms of melt production (or seafloor spreading at ridges) (e.g., Sleep and Zahnle, 2001; Papuc and Davies, 2008; Kite et al., 2009; Kadoya and Tajika, 2015; Foley and Driscoll, 2016; Charnay et al., 2017; Krissansen-Totton et al., 2018; Foley and Smye, 2018; Krissansen-Totton and Catling, 2020). In this approach, either melt production rates are estimated from parameterized 1D convection models, or a value for the heat flow is assumed, which is used to scale melting. Outgassing may then be calibrated to present-day estimates. Because parameterized convection models produce high heat flow early in a planet's evolution (e.g., Turcotte, 1980), the approach outlined here correspondingly begets high outgassing rates. This can be misleading for two reasons. First, parameterized models tend to overestimate melt fractions early on: they do not spatially resolve depletion upon melting, which should inhibit further melting locally with the same mantle temperatures. Secondly, heat flow considerations alone may underestimate the importance of other factors which control the melt concentrations and speciation of volatiles. Thirdly, possible transitions between tectonic regimes would alter the relationship between temperatures, heat flow, and melting.

We assume a stagnant lid tectonic mode as an end-member scenario (Debaille et al., 2013), which might be complemented by other studies of mobile lids. There is no consensus on whether plate tectonics operated globally on Earth during the Hadean and Eoarchean, the nominal subject of our investigation (see discussion in Korenaga, 2006). The decision to only consider a stagnant lid mode is an important caveat because, as it appears, mobile lids can generate much higher outgassing rates than stagnant lids (Noack et al., 2014, 2017). As we will discuss in section 3.2.5, the reasons why are not straightforward—being a combination of competing effects—and would benefit from dedicated work in the future.

Mantle outgassing represents a missing piece of the Archean atmosphere puzzle. Firstly, reduced gases such as H_2 and CO seem necessary for prebiotic chemistry; the production of HCN requires a reducing atmosphere with $C/O \geqslant 1$, for example (Rimmer and Rugheimer, 2019). However, whether or not H_2 and CO comprised a significant part of volcanic gas at the time remains debated (e.g., Zahnle et al., 2020). Secondly, sufficiently large partial pressures of greenhouse gases—such as oxidized species H_2O and CO_2—are proposed to have kept the incubating planet from freezing under lower solar luminosity (Charnay et al., 2020), in order to make sense of liquid surface water (Sagan and Mullen, 1972). Investigations into this paradox tend to assume that Archean CO_2 outgassing fluxes were the same as or greater than the present day flux given plate tectonics (e.g., Sleep and Zahnle, 2001; Wordsworth and Pierrehumbert, 2013; Kanzaki and Murakami, 2018). These two questions may never be fully resolved without definite knowledge of the mantle oxidation state (or the tectonic mode). Nevertheless, this study, by more rigorously linking stagnant lid outgassing fluxes to the unknown oxidation state, might help contextualize these problems within Earth system evolution.

3.2.3 Methods

We trace the movement of volatiles through the mantle to the atmosphere for a stagnant-lid Earth, from just after the moon-forming impact to around the first rock record. Our model is similar to the one described in Ortenzi et al. (2020); they additionally calculated gas solubility in the melt (relevant for the higher outgassing pressures expected on exoplanets greater than an Earth mass), but did not couple partitioning and volatile speciation within the convection simulations.

To simulate mantle dynamics, we use a 2D convection model, which is detailed in Noack et al. (2016). The heavily-benchmarked model couples solid-state convection in the mantle with petrological melt production and volatile partitioning (Holloway et al., 1992; Katz et al., 2003; Grott et al., 2011). This is further coupled with a chemical speciation model (French, 1966; Holloway, 1981; Fegley, 2013; Gaillard and Scaillet, 2014; Schaefer and Fegley, 2017). At each time step we estimate the outgassed flux of H_2O, H_2, CO_2, and CO. We simulate 700 Myr of convection, taking the model start time to correspond to 4.5 Ga before present—around the time when the magma ocean might have started crystallizing.

Numerical convection model. The convection code solves the conservation equations of mass, momentum and energy in the rocky mantle by using a particle-in-cell method. We use the 2D spherical annulus method in Hernlund and Tackley (2008) to divide the mantle into a grid of cells with uniform height of 25 km. To reduce computational costs, we only model one quarter of the 2D annulus, leading to 307 by 111 cells in the lateral and radial directions. We model compressible convection based on the truncated anelastic liquid approximation (TALA), using pre-calculated depth-dependent profiles for thermodynamic parameters such as the mineral-dependent density, the thermal expansion coefficient and the heat capacity for an adiabatic temperature profile. We neglect any possible initiation of plate tectonics or other surface recycling mechanisms and instead allow for a stagnant lid to form. We take into account time-dependent radiogenic heating and heat loss from the core.

We assume a hydrated pyrolitic mantle with an Arrhenius viscosity, η, that depends on temperature T and pressure p, following Karato and Wu (1993):

$$\eta(T,p) = \frac{1}{2A} h^m \exp\left(\frac{E + pV}{RT}\right), \tag{224}$$

with prefactor $A = 3.7 \times 10^{-19}$ Pa s^{-1}, grain size $h = 1$ mm, grain size exponent $m = 2.5$, activation energy $E = 240$ kJ mol^{-1}, activation volume $V = 5.0$ cm^3 mol^{-1} for the upper mantle. In the lower mantle, the rheological parameters are as listed in Noack et al. (2017), with a pressure-dependent activation enthalpy as derived in Tackley et al. (2013). In the Tackley et al. study, however, the viscosity was shifted by a factor of 100 to allow for numerically-feasible simulations of rocky planets larger than Earth. Here, we do not artificially scale η, but instead limit it to a minimum of 10^{21} Pa s to allow for numerical stability in the mantle for all investigated parameter combinations. That is, we do not implement an aesthenosphere, and may underestimate the convective strength locally in the upper mantle. Our initial Rayleigh number is therefore around $\sim 5 \times 10^7$, depending on the initial temperature profile.

The radiogenic heat sources decline over time and would reach present-day Earth values of 79.5 ppb Th, 240 ppm K and 20.3 ppb U after 4.5 Gyr of thermal evolution, following Breuer (2009). We did not include the partitioning of heat sources in the crust, and instead applied homogeneous radiogenic heat sources over the entire domain.

Melting model. The petrology model simulates partial melting of the silicate mantle. Melt forms if the local temperature is greater than the mantle solidus temperature, T_{solidus}, at that temperature and pressure. The local melt fraction, F, is

$$F = \frac{T - T_{\mathrm{solidus}}}{T_{\mathrm{liquidus}} - T_{\mathrm{solidus}}}. \tag{225}$$

We apply the melting temperatures of peridotite (Hirschmann, 2000; Noack et al., 2017). The liquidus temperature, T_{liquidus}, is constant for a given pressure. The solidus temperature varies with time; it increases with depletion due to previous melting (Hirschmann, 2000; Noack et al., 2017). We take into account the depression of the solidus due to H_2O in the melt (Katz et al., 2003).

The local melt fractions add up to give the total depletion of the mantle. Here, depletion is adapted to the fact that the solidus temperature increases upon dehydration. Depletion is recalculated at each time step depending on the updated solidus temperature. Upon 30% depletion of the primordial peridotite mantle, the residual mantle therefore always resembles the harzburgite composition, independently of if it having initially started wet or dry. We limit the maximum allowed depletion to 30%.

Compositional buoyancy occurs after the melt forms and is enriched in volatiles, which subsequently decreases the local density. This causes melt to rise to the surface. The upper mantle melt is buoyant only at mantle pressures of less than 12 GPa, hence we neglect any possible outgassing contribution from melt at greater depths. The melting temperature that we use is valid for this pressure range.

Volatile partitioning model. Knowing the local melt fractions, next we are interested in the concentrations of CO_2 and H_2O in the melt. Carbon partitions into the melt as CO_3^{2-}; its mole fraction, $X^{\mathrm{melt}}_{CO_3^{2-}}$, depends strongly on f_{O_2}:

$$X^{\mathrm{melt}}_{CO_3^{2-}} = \frac{K_{\mathrm{I}}\, K_{\mathrm{II}}\, f_{O_2}}{1 + K_{\mathrm{I}}\, K_{\mathrm{II}}\, f_{O_2}}, \tag{226}$$

where K_{I} and K_{II} are the equilibrium constants governing, respectively, the formation of CO_2 from graphite and CO_3^{2-} from CO_2,

$$\log_{10} K_{\mathrm{I}} = a - b\,T + c\,T^2 + d\,\frac{p-1}{T} \tag{227}$$

$$\log_{10} K_{\mathrm{II}} = e - \frac{f}{T} - g\frac{p - 1000}{T}, \tag{228}$$

where $a = 40.07639$, $b = 2.53932 \times 10^{-2}$, $c = 5.27096 \times 10^{-6}$, $d = 0.0267$, $e = -6.24763$, $f = 282.56$, $g = 0.119242$, T is in Kelvin, p is in bar, and f_{O_2} is the oxygen fugacity (Holloway et al., 1992; Grott et al., 2011). At each time step, if the local melt fraction is greater than zero, we subtract the amount of carbon that enters the melt from the local mantle carbon inventory. Carbon stops partitioning into the local melt once its mantle source inventory is emptied. The local amount of carbon (as well as other local information such the depletion) is traced via mass-independent particles that flow along convective stream lines, where we ensure that we always have between 3 and 8 particles in each cell.

The amount of CO_2 in weight percent, here denoted χ to distinguish from mole percent, is calculated from $X^{\text{melt}}_{\text{CO}_3^{2-}}$, assuming thermodynamic equilibrium:

$$\chi^{\text{melt}}_{\text{CO}_2} = \left[\frac{M_{\text{CO}_2}}{\text{FWM}} X^{\text{melt}}_{\text{CO}_3^{2-}}\right] \Big/ \left[1 - \left(1 - \frac{M_{\text{CO}_2}}{\text{FWM}}\right) \chi^{\text{melt}}_{\text{CO}_3^{2-}}\right], \tag{229}$$

where $\chi^{\text{melt}}_{\text{CO}_3^{2-}}$ is the weight percent of carbonate in the melt, M_{CO_2} is the molar mass of carbon dioxide, and FWM is the formula weight of the melt normalized to one oxygen, taken to be 36.594 for one example tholeiitic basaltic (Holloway et al., 1992; Grott et al., 2011). The formula weight typically varies only by few percent for different basalt compositions.

We assume that all solid carbon exists as graphite, since we only consider shallow melting below 12 GPa. This assumption may not be valid for the most oxidized cases (IW+4), as carbonate may become the stable carbon species for these pressures and f_{O_2} (Stagno, 2019). However, in such oxidized conditions we already know that CO_2 is outgassed, and thus neglect the influence of carbonate.

Meanwhile, we use the batch melting formula to calculate water partitioning into the melt:

$$\chi^{\text{melt}}_{\text{H}_2\text{O}} = \frac{\chi^{\text{rock}}_{\text{H}_2\text{O}}}{D_{\text{H}_2\text{O}} + F(1 - D_{\text{H}_2\text{O}})}, \tag{230}$$

where $\chi^{\text{rock}}_{\text{H}_2\text{O}}$ is the local weight fraction of water in the solid mantle, F is the local average melt fraction, and $D_{\text{H}_2\text{O}}$ is a partition coefficient, which we set at 0.01 based on the Ce partitioning coefficient (Michael, 1995; Katz et al., 2003).

We assume that the melt rises adiabatically towards the surface, but only allow a fraction of the melt, f_{extr}, to reach the surface as extrusive volcanism. Only extrusive melt contributes to outgassing into the atmosphere. The mantle volatile concentrations are rather small and below the saturation point (Katz et al., 2003). Once the melt has reached the surface, we only consider subaerial degassing, and not submarine; virtually all gases enter the atmosphere at these relatively lower pressures. For simplicity, our model assumes complete outgassing of the melt that reaches the surface, with no residual volatiles remaining in the melt. Further, we do not consider any possible re-equilibration or contamination as material rises through the lithosphere. Once melting occurs, it is extruded directly at the surface, neglecting interactions with the surrounding rock or with fluids at higher pressures.

Table 7: Thermodynamic parameters for basaltic melt.

Symbol	Description	Value	Units	Reference
α_{melt}	Thermal expansion coefficient	3×10^{-5}	K^{-1}	Afonso et al. (2005)
ρ_{melt}	Density	3000	kg m^{-3}	Lesher and Spera (2015)
$C_{p,\text{melt}}$	Heat capacity	1793	$\text{J kg}^{-1}\ \text{K}^{-1}$	Lesher and Spera (2015)

Volatile speciation model. We retrieve the masses of outgassed volatiles using the "Equilibrium constants and mass balance method" first appearing in French (1966), and used widely in other studies (Holland, 1984; Gaillard and Scaillet, 2014; Fegley, 2013; Schaefer and Fegley, 2017; Ortenzi et al., 2020). The H_2/H_2O and CO/CO_2 volatile molar ratios are governed by the chemical equilibria,

$$2\,\text{H}_2 + \text{O}_2 \rightleftharpoons 2\,\text{H}_2\text{O}, \tag{231}$$

$$\text{CO} + (1/2)\,\text{O}_2 \rightleftharpoons \text{CO}_2, \tag{232}$$

assuming that the volcanic gases are in equilibrium with their magmas. This is the second f_{O_2}-dependence in the model. These chemical reactions have respective equilibrium constants K_{III} and K_{IV}, which are calculated as follows:

$$K_{\text{III}} = \exp\left(\frac{-\Delta_r G^0_{(231)}}{RT}\right) = \frac{X^2_{\text{H}_2\text{O}}}{X^2_{\text{H}_2} f_{\text{O}_2}}, \tag{233}$$

$$K_{\text{IV}} = \exp\left(\frac{-\Delta_r G^0_{(232)}}{RT}\right) = \frac{X_{\text{CO}_2}}{X_{\text{CO}}}\frac{1}{f^{1/2}_{\text{O}_2}}, \tag{234}$$

where R is the universal gas constant (8.314 J K^{-1} mol^{-1}), and X_i is the mole fraction of species i. $\Delta_r G^0_{(231)}$ and $\Delta_r G^0_{(232)}$ are the Gibbs free energies of reaction in J mol^{-1} for (231) and (232) respectively; we calculate these energies as a function of temperature using the method outlined in Ortenzi et al. (2020), based on Fegley (2013). Equations (233) and (234) assume 1 bar pressure (equal to P_{surf}), whilst T is taken to be the temperature the melt would have once it has risen adiabatically to the surface:

$$T(p = p_{\text{surf}}) = T_{\text{melt}}(p_{\text{melt}}) \cdot \exp\left[-\frac{\alpha_{\text{melt}}}{\rho_{\text{melt}}\, C_{p,\text{melt}}}(p_{\text{melt}} - p)\right], \tag{235}$$

where $C_{p,\text{melt}}$ is the heat capacity of the melt, α_{melt} is the thermal expansion coefficient, ρ_{melt} is the density, and T_{melt} and p_{melt} are the local temperature (in Kelvin) and pressure (in bar) of the melt source. Values for the thermodynamic parameters are listed in Table 7.

From the model outlined above, we can calculate the outgassed masses M_i of each volatile species i at

Table 8: Free input parameters tested in this model. Values are drawn randomly from a uniform distribution given by the minimum and maximum values in the "Range" column.

Symbol	Description	Range	Units
$\log f_{O_2} - \mathrm{IW}$	Mantle redox shift from IW	-3, 4	-
$\chi_{\mathrm{H_2O,ini}}$	Initial mantle H_2O content	50, 450	wt. ppm
$\chi_{\mathrm{CO_2,ini}}$	Initial mantle CO_2 content	22, 180	wt. ppm
T_{surf}	Temperature at surface	273, 333	K
T_{ini}	Initial temperature at top of convecting layer	1750, 2100	K
D_{lid}	Initial lid thickness	10, 43	km
ΔT_c	Initial core temperature jump	0, 1750	K
f_{extr}	Extrusive volcanism percentage	10, 40	%

a specific time, accumulated over all previous time steps and over all cells in the mantle:

$$\begin{aligned}
M^{\mathrm{atm}}_{\mathrm{H_2O}} &= f_{\mathrm{extr}} \sum_{j=2}^{\mathrm{times}} \sum_{k=1}^{\mathrm{cells}} \chi^{\mathrm{melt}}_{\mathrm{H_2O}} F_{j,k} V_k \frac{X_{\mathrm{H_2O}}}{X_{\mathrm{H_2}} + X_{\mathrm{H_2O}}} \rho_{\mathrm{mtl}} \\
M^{\mathrm{atm}}_{\mathrm{H_2}} &= f_{\mathrm{extr}} \sum_{j=2}^{\mathrm{times}} \sum_{k=1}^{\mathrm{cells}} \chi^{\mathrm{melt}}_{\mathrm{H_2O}} F_{j,k} V_k \frac{X_{\mathrm{H_2}}}{X_{\mathrm{H_2}} + X_{\mathrm{H_2O}}} \frac{m_{\mathrm{H_2}}}{m_{\mathrm{H_2O}}} \rho_{\mathrm{mtl}} \\
M^{\mathrm{atm}}_{\mathrm{CO_2}} &= f_{\mathrm{extr}} \sum_{j=2}^{\mathrm{times}} \sum_{k=1}^{\mathrm{cells}} \chi^{\mathrm{melt}}_{\mathrm{CO_2}} F_{j,k} V_k \frac{X_{\mathrm{CO_2}}}{X_{\mathrm{CO}} + X_{\mathrm{CO_2}}} \rho_{\mathrm{mtl}} \\
M^{\mathrm{atm}}_{\mathrm{CO}} &= f_{\mathrm{extr}} \sum_{j=2}^{\mathrm{times}} \sum_{k=1}^{\mathrm{cells}} \chi^{\mathrm{melt}}_{\mathrm{CO_2}} F_{j,k} V_k \frac{X_{\mathrm{CO}}}{X_{\mathrm{CO}} + X_{\mathrm{CO_2}}} \frac{m_{\mathrm{CO}}}{m_{\mathrm{CO_2}}} \rho_{\mathrm{mtl}},
\end{aligned} \tag{236}$$

where f_{extr} is the percentage of volcanism that is extrusive, $F_{j,k,}$ is the local melt fraction in a cell, V_k is the volume of that cell, m_i is molar mass of species i in kg mol^{-1}, and ρ_{mtl} is the local density of the solid mantle. Note f_{extr} has units of weight fraction and X has units of mole fraction. These calculations and the associated volumes correspond to a 2D sphere, later scaled up to 3D by a dimensionalization factor.

The ultimate partial pressure outgassed to the atmosphere, for each species i, is given by

$$p_i = \frac{M_{\mathrm{tot}} X_{i,\mathrm{tot}} g}{4\pi R_E^2}, \tag{237}$$

where M_{tot} is the sum of the outgassed masses from equation (236), X_{tot} is the species' mole fraction with respect to M_{tot}, g is the acceleration due to gravity at the surface (9.8 ms^{-2}), and R_E is the radius of Earth (6371 km). We assume that the gas reaches the surface instantaneously.

Initial conditions and free parameters. The main study consists of 500 cases with randomly selected values for eight free input parameters (Table 8). These eight parameters were identified based on their expected effects on the thermal and chemical evolution of the mantle, and to avoid redundancy between effects given the computational demand. Input values for each case are drawn from uniform distributions, with this section outlining the choice of bounds.

Choice of initial temperatures. The initial mantle temperature profile is set by four unknown parameters: planet surface temperature, T_{surf}, initial stagnant lid thickness, D_{lid}, initial temperature at the base of the lithosphere, T_{ini}, and core temperature jump, ΔT_c. Temperatures increase linearly from T_{surf} to T_{ini}, and then follow an initially adiabatic profile from below the upper thermal boundary layer to the core-mantle boundary. The temperature contrast between the base of the mantle and the core is fixed at ΔT_c, which varies across runs. We enforce an initial temperature cut-off at the solidus.

Although evidence of surface temperatures covering our age of interest is scant, oxygen isotope ratios from the 4.4 Ga Jack Hills zircons imply a temperate surface which could host liquid oceans (Valley et al., 2002). Thus we allow T_{surf} to vary from 0 to 60°C, but note that oceans could be stable even with much higher surface temperatures (Kasting, 1988). Our constant T_{surf} is an approximation; in reality this value varies spatially and is linked to outgassing via greenhouse warming.

The temperatures in Earth's mantle after the last magma ocean stage are unknown; we adopt a range of 1750–2100 K in T_{ini}. Archean komatiite records suggest an upper mantle potential temperature of at most $\sim$1970 K (Herzberg et al., 2010), corresponding to upper mantle temperatures comparable with those investigated here (our T_{ini} values refer to the actual temperatures below an initial upper thermal boundary layer, hence the potential temperatures would be slightly smaller).

The initial adiabatic profile implies an already-convecting mantle. However, in our 2D mantle convection simulations, the mantle is initially gravitationally stable. We slightly perturb the temperature field to trigger the initiation of convection. In reality, it is not unlikely that part of the solid mantle was already convecting when the magma ocean was still cooling (Maurice et al., 2017), which would lead to a slightly earlier initiation of volcanic outgassing than predicted here. Conversely, a mantle overturn may have occurred within Earth's interior, after the solidification of the final, iron-enriched magma ocean close to the surface, which would bring colder material to the lower mantle (Brown et al., 2014). Our initial temperature profile is in between these two end-member scenarios. Regardless, this profile quickly starts evolving over time, and its initial shape is not significant to the results. The stagnant lid thickness also adjusts according to the temperature profile, yet very thick lithospheres ($\sim$100 km) would inhibit melt production to the extent that no outgassing would occur within 700 Myr.

Choice of initial volatile contents. Most of the solid Earth's accreted volatile content was lost to magma ocean degassing. For the initial H_2O and CO_2 contents in the crystallized mantle, $\chi_{\text{H}_2\text{O,ini}}$ and $\chi_{\text{CO}_2\text{,ini}}$ in weight percent, we adopt the amounts of volatiles remaining after degassing from Elkins-Tanton (2008). The most water-rich scenario corresponds to just below 1 Earth ocean mass. These estimates are consistent with more recent modelling work by Barth et al. (2020). Hier-Majumder and Hirschmann (2017) found comparable but slightly elevated values considering faster freezing of the magma ocean. Elkins-

Tanton (2008) considers primordially-accreted volatile contents of 0.05–0.5 weight percent H_2O and 0.01–0.1 weight percent CO_2, although the true values are poorly constrained.

Choice of mantle oxidation states. Geochemical clues mostly agree that since around 3.8 Ga or earlier, the Archean upper mantle was about as oxidized as present (Canil, 1997; Delano, 2001; Trail et al., 2011; Nicklas et al., 2018; Armstrong et al., 2019), although other analyses suggest a more gradual oxidation up to the quartz-fayalite-magnetite buffer (QFM) (Aulbach and Stagno, 2016; Nicklas et al., 2019). Trail et al. (2011) investigated Hadean zircons with ages between 4.0 and 4.36 Ga and derived an oxidation state around QFM. If these zircons did indeed come from primitive mantle melts as suggested by Trail et al. (2011), this would suggest an oxidized mantle almost directly after the Moon-forming impact.

We allow mantle f_{O_2} to vary between the minimum Hadean value of three log-units below the equilibrium with the IW buffer (Wood et al., 2006), and a typical modern value of four log-units above the equilibrium. Because we are agnostic to mantle oxidation's specific timing, we test these endpoint values assuming a constant oxidation state. Later we test the effect of forcing $\log(f_{O_2})$ to increase linearly.

Choice of extrusive volcanism percentages. Only a fraction of magma will rise high enough to extrude and outgas at the surface. The remaining melt in the intrusive component will eventually replenish the mantle. Crisp (1984) estimate an extrusive volcanism percentage of 10% in the modern day. Because this value is unknown for early Earth, we allow it to vary between 10% and 40% (Grott et al., 2011). We do not consider any diffuse degassing from intrusive volcanism, although fluid pressure would indeed bring some intrusive magmatic gas to the surface via rock fissures.

3.2.4 Results

Thermal history and melt production. The thermal histories underlying the outgassing model are firstly presented in figure 28. Mean mantle temperatures gradually increase due to powerful primordial radiogenic heating and relatively sluggish stagnant lid convection. Melting increases with hotter initial temperatures, but shows higher scatter due to the influence of dehydration on the solidus temperatures.

Hot scenarios show initial spikes in melting, of magnitude depending on T_{ini}, followed by a decrease and subsequent settling to a steady value. Directly after magma ocean solidification, the mantle temperature is still very close to the solidus. Small mass movement by convection can lead to immediate re-melting. It then becomes more difficult for the depleted mantle to melt further. Melting increases again once either radiogenic heating warms the upper mantle, or undepleted material from the lower mantle is brought up to shallower depths. The assumption of the initial thermal state thus affects the early melt production, but becomes less important later.

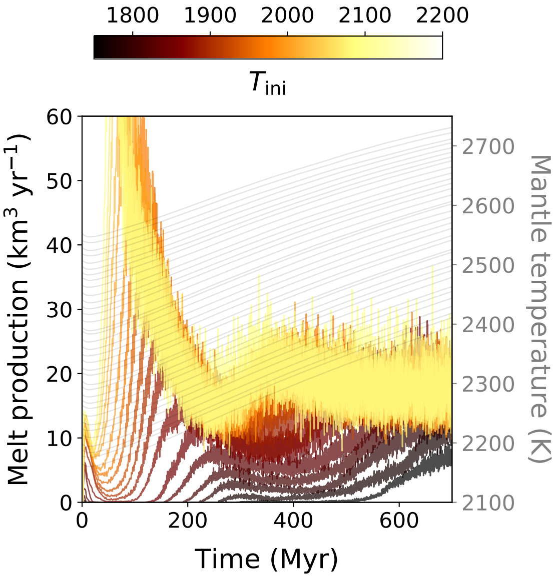

Figure 28: The evolution of the extrusive volumetric melt production rate with density $\rho = 3000$ kg m^{-3}. Cases are binned to 10-K increments in initial temperature at the base of the stagnant lid, and averaged over other the input parameters (table 8). Lighter colours indicate hotter initial conditions; darker colours indicate cooler initial conditions. Overlain in solid grey lines and corresponding to the secondary y-axis is the evolution of the mean temperature over the whole mantle, for the same bins.

Near steady state, all melting is capped below $\sim$35 km^3 yr^{-1}. This value is not much higher than the Earth's total magma supply rate at present (20–25 km^3 yr^{-1}; Janle et al., 1992), despite the cooler modern mantle. Higher initial temperatures would lead to unphysical conditions with most of the mantle above the solidus temperature. A much wetter mantle might aid melting somewhat, although our model does not show a strong effect of $\chi_{\mathrm{H_2O,ini}}$ on the overall melt production.

Melt H_2O and CO_2 contents. Due to the different chemistry controlling partitioning for C and H_2O (section 3.2.3), $\chi^{\mathrm{melt}}_{\mathrm{H_2O}}$ and $\chi^{\mathrm{melt}}_{\mathrm{CO_2}}$ respond separately to model parameters. These behaviours are reflected in figure 29.

H_2O partitioning into the melt depends directly on the local mantle H_2O abundance, the maximum of which is set by $\chi_{\mathrm{H_2O,ini}}$. The effect of mantle content on melt content is non-linear: in equation (230), $\chi^{\mathrm{melt}}_{\mathrm{H_2O}}$ depends on the local melt fraction, whilst the presence of water facilitates melting by suppressing the solidus.

C partitioning does not depend directly on the local mantle abundance, but is strongly redox-dependent. This is true for the regime we model, where graphite is the stable phase, but would not apply to more oxidizing conditions (Stagno, 2019). The local mantle C only affects the melt concentration at very low values of $\chi_{\mathrm{CO_2,ini}}$ below 50 ppm, or for cases approaching maximum outgassing. Further, the effect of $f_{\mathrm{O_2}}$ on $\chi^{\mathrm{melt}}_{\mathrm{CO_2}}$ is severe. With every step of one log-unit below the IW buffer, we see $\chi^{\mathrm{melt}}_{\mathrm{CO_2}}$ quickly drop by an order

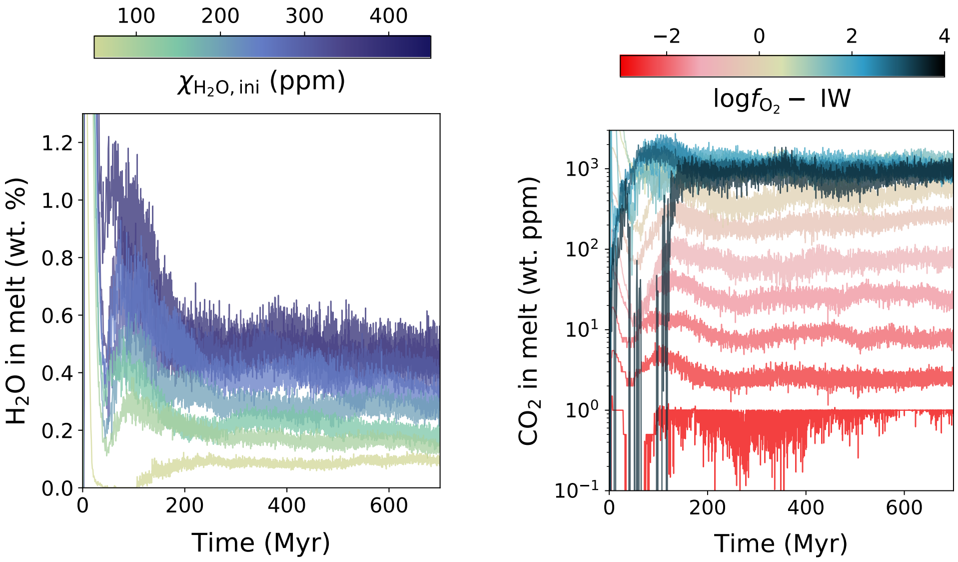

Figure 29: The evolution of melt volatile contents for H_2O (left; in weight percent) and CO_2 (right; in weight ppm). Cases are binned according to their values of the main input parameter controlling melt partitioning: for H_2O this is the initial mantle H_2O content (equation (230)), and for CO_2 this is the mantle f_{O_2} (equation 226)). Lines are coloured by bin and show the median melt concentration per time step, given random values for the other input parameters.

of magnitude.

For both CO_2 and H_2O, we see an early transient stage where the melt abundance drops steeply. This is associated with the early pulse of melting and hence depletion (figure 28). Notably, the sudden decline in $\chi^{\rm melt}_{CO_2}$ is very pronounced in the most oxidized cases: the highest amount of carbonate can enter the melt phase and temporarily empties local reservoirs in the upper mantle, illustrating a situation where the mantle inventory affects $\chi^{\rm melt}_{CO_2}$.

Exploration of outgassing scenarios. We confirm a heavy dependence of the outgassing rate on f_{O_2}. Figure 30 plots the evolution of each species' mean outgassing flux in mol yr^{-1}, where cases are binned by f_{O_2} and all other input parameters vary according to a random uniform distribution (Table 8). As expected (Holland, 1984; Kasting et al., 1993), a more oxidized mantle is associated with more CO_2 and H_2O outgassing, and a more reduced mantle is associated with more H_2 outgassing. The story for CO is more complicated, showing a maximum around IW: low f_{O_2} limits the amount of total carbonate that can dissolve into the melt, despite the gas-phase equilibrium favouring CO over CO_2. For all cases, the outgassing rate is fairly constant with time during the 700 Myr modelled.

The early pulse of outgassing is associated with the early pulse of melting (figure 28). This behaviour may be less pronounced if the mantle were already convecting during magma ocean crystallization (Maurice et al., 2017). However, the initial temperature profile has no effect on the longer-term outgassing fluxes.

Although figure 30 might seem to suggest that CO_2 outgassing never surpasses 1 Tmol yr^{-1} in our

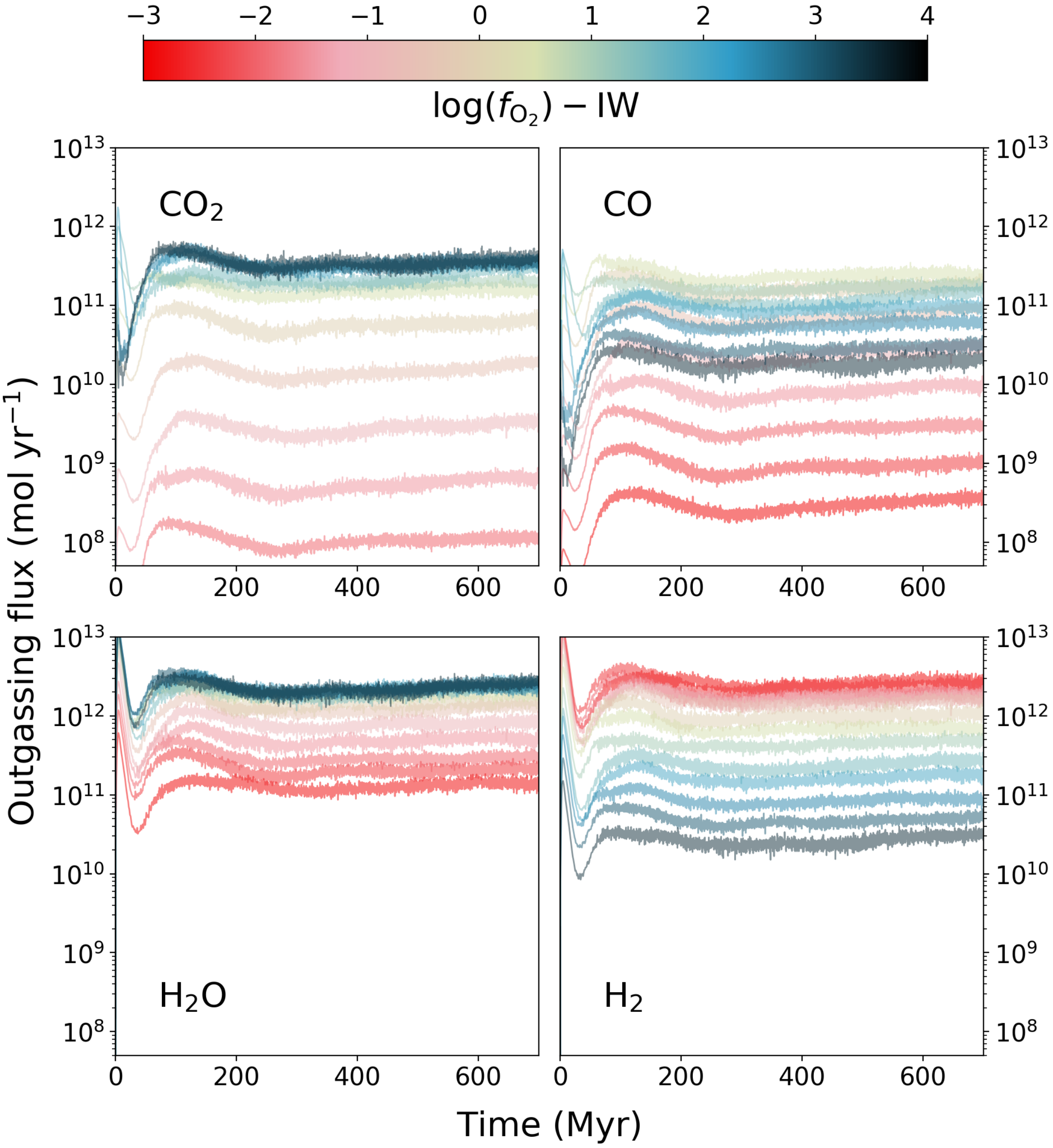

Figure 30: The evolution of outgassing fluxes for CO_2 (top left), CO (top right), H_2O (bottom left), and H_2 (bottom right), binned to 0.5-logf_{O_2} increments and averaged over the other input parameters. Each logf_{O_2} bin is coloured from red (reduced) to dark blue (oxidized).

Table 9: Outgassed partial pressures in bar, masses in kg, and mean mole fluxes in mol yr^{-1}, split over mantle redox and initial mantle thermal state (cool: 1750–1925 K; warm: 1925–2100 K). Results are shown as the medians, with 1-σ deviations super- and subscripted. The first 100 Myr of outgassing is not included in the mean flux due to the initial transience explained in the text.

	Redox shift from IW	Initial mantle thermal state								
		cool			warm			**all**		
		pressure	mass ($\times 10^{17}$)	flux ($\times 10^{11}$)	pressure	mass ($\times 10^{17}$)	flux ($\times 10^{11}$)	**pressure**	**mass** ($\times 10^{17}$)	**flux** ($\times 10^{11}$)
CO_2	[-3,-1)	$0.0^{+0.0}_{-0.0}$	$0.0^{+0.1}_{-0.0}$	$0.0^{+0.0}_{-0.0}$	$0.0^{+0.0}_{-0.0}$	$0.0^{+0.1}_{-0.0}$	$0.0^{+0.0}_{-0.0}$	$0.0^{+0.0}_{-0.0}$	$0.0^{+0.1}_{-0.0}$	$0.0^{+0.0}_{-0.0}$
CO		$0.0^{+0.0}_{-0.0}$	$0.1^{+1.1}_{-0.1}$	$0.0^{+0.1}_{-0.0}$	$0.0^{+0.0}_{-0.0}$	$0.3^{+0.7}_{-0.3}$	$0.0^{+0.0}_{-0.0}$	$0.0^{+0.0}_{-0.0}$	$0.2^{+1.0}_{-0.2}$	$0.0^{+0.1}_{-0.0}$
H_2O		$0.1^{+0.3}_{-0.1}$	$24.9^{+50.0}_{-14.9}$	$2.1^{+2.9}_{-1.3}$	$0.1^{+0.2}_{-0.1}$	$37.9^{+39.9}_{-26.3}$	$2.6^{+2.6}_{-1.6}$	$0.1^{+0.3}_{-0.1}$	$33.2^{+43.5}_{-22.6}$	$2.2^{+2.9}_{-1.4}$
H_2		$1.1^{+0.8}_{-0.7}$	$29.8^{+20.8}_{-17.4}$	$18.1^{+11.5}_{-8.9}$	$1.3^{+1.4}_{-0.8}$	$31.8^{+42.6}_{-19.7}$	$19.5^{+20.2}_{-11.1}$	$1.2^{+1.3}_{-0.7}$	$30.1^{+35.1}_{-18.1}$	$19.2^{+17.7}_{-10.6}$
CO_2	[-1,0)	$0.0^{+0.0}_{-0.0}$	$1.3^{+3.2}_{-1.0}$	$0.1^{+0.1}_{-0.0}$	$0.0^{+0.0}_{-0.0}$	$2.0^{+4.2}_{-1.6}$	$0.1^{+0.1}_{-0.1}$	$0.0^{+0.0}_{-0.0}$	$1.6^{+3.6}_{-1.3}$	$0.1^{+0.1}_{-0.1}$
CO		$0.0^{+0.1}_{-0.0}$	$5.2^{+9.8}_{-3.1}$	$0.3^{+0.5}_{-0.2}$	$0.1^{+0.1}_{-0.0}$	$8.8^{+11.0}_{-6.6}$	$0.5^{+0.6}_{-0.3}$	$0.0^{+0.1}_{-0.0}$	$6.9^{+12.0}_{-4.7}$	$0.4^{+0.6}_{-0.3}$
H_2O		$1.1^{+1.3}_{-0.6}$	$134.2^{+115.9}_{-75.6}$	$9.3^{+8.0}_{-4.9}$	$1.4^{+1.5}_{-0.8}$	$144.3^{+150.5}_{-80.7}$	$9.7^{+9.4}_{-4.9}$	$1.3^{+1.3}_{-0.8}$	$135.5^{+139.0}_{-76.5}$	$9.3^{+9.2}_{-4.7}$
H_2		$2.0^{+1.7}_{-1.1}$	$22.4^{+18.4}_{-13.8}$	$14.7^{+10.8}_{-7.9}$	$2.0^{+1.9}_{-1.1}$	$22.2^{+26.7}_{-13.4}$	$13.6^{+12.2}_{-7.4}$	$2.0^{+1.8}_{-1.1}$	$22.4^{+23.9}_{-13.7}$	$14.3^{+11.6}_{-7.7}$
CO_2	[0,1)	$0.1^{+0.2}_{-0.1}$	$20.5^{+31.8}_{-13.9}$	$0.8^{+0.8}_{-0.5}$	$0.2^{+0.4}_{-0.1}$	$21.1^{+53.5}_{-14.1}$	$0.8^{+1.5}_{-0.5}$	$0.2^{+0.3}_{-0.1}$	$21.1^{+35.9}_{-14.3}$	$0.8^{+1.2}_{-0.5}$
CO		$0.3^{+0.4}_{-0.2}$	$27.1^{+34.3}_{-20.0}$	$1.5^{+1.7}_{-1.0}$	$0.4^{+0.4}_{-0.3}$	$37.6^{+43.3}_{-27.5}$	$2.2^{+1.6}_{-1.6}$	$0.4^{+0.4}_{-0.3}$	$36.5^{+34.9}_{-29.1}$	$1.7^{+1.9}_{-1.2}$
H_2O		$3.3^{+3.4}_{-2.1}$	$189.0^{+281.3}_{-123.0}$	$12.6^{+16.1}_{-6.4}$	$3.7^{+5.4}_{-2.1}$	$254.3^{+306.5}_{-170.6}$	$15.6^{+19.1}_{-10.5}$	$3.6^{+4.1}_{-2.4}$	$220.2^{+258.3}_{-150.6}$	$14.5^{+15.1}_{-9.0}$
H_2		$1.8^{+2.4}_{-1.3}$	$11.2^{+18.6}_{-7.3}$	$6.3^{+10.2}_{-3.3}$	$1.8^{+2.0}_{-1.1}$	$11.6^{+12.3}_{-7.9}$	$7.2^{+9.1}_{-4.7}$	$1.8^{+2.2}_{-1.3}$	$11.6^{+17.2}_{-7.8}$	$6.7^{+10.0}_{-4.0}$
CO_2	[1,2)	$0.5^{+0.5}_{-0.3}$	$58.5^{+47.5}_{-35.0}$	$1.7^{+1.4}_{-1.0}$	$0.5^{+0.8}_{-0.3}$	$64.0^{+77.1}_{-34.3}$	$2.1^{+1.7}_{-1.0}$	$0.5^{+0.6}_{-0.3}$	$58.8^{+63.3}_{-30.5}$	$2.0^{+1.5}_{-1.1}$
CO		$0.3^{+0.4}_{-0.2}$	$24.6^{+20.9}_{-14.0}$	$1.2^{+1.1}_{-0.7}$	$0.4^{+0.4}_{-0.2}$	$24.9^{+28.5}_{-9.8}$	$1.3^{+1.0}_{-0.8}$	$0.3^{+0.4}_{-0.2}$	$24.9^{+28.3}_{-12.7}$	$1.3^{+1.0}_{-0.8}$
H_2O		$4.4^{+3.7}_{-2.6}$	$192.3^{+198.4}_{-111.2}$	$13.6^{+14.2}_{-6.3}$	$6.5^{+8.2}_{-4.3}$	$328.8^{+417.5}_{-231.5}$	$24.8^{+25.0}_{-16.5}$	$5.4^{+5.6}_{-3.3}$	$252.8^{+250.3}_{-155.9}$	$16.7^{+21.3}_{-9.4}$
H_2		$0.7^{+0.8}_{-0.4}$	$3.7^{+4.0}_{-2.2}$	$2.1^{+1.9}_{-1.0}$	$1.0^{+1.4}_{-0.6}$	$5.4^{+8.1}_{-3.7}$	$3.8^{+5.0}_{-2.7}$	$0.7^{+1.1}_{-0.4}$	$3.8^{+6.9}_{-2.4}$	$2.6^{+4.2}_{-1.6}$
CO_2	[2,3)	$1.2^{+0.9}_{-0.7}$	$123.8^{+74.0}_{-70.9}$	$3.2^{+1.5}_{-1.7}$	$1.1^{+1.7}_{-0.5}$	$118.1^{+152.4}_{-54.8}$	$2.9^{+3.2}_{-1.1}$	$1.1^{+1.3}_{-0.6}$	$118.9^{+105.7}_{-58.2}$	$3.1^{+2.1}_{-1.4}$
CO		$0.3^{+0.2}_{-0.2}$	$18.2^{+10.5}_{-11.1}$	$0.7^{+0.4}_{-0.4}$	$0.2^{+0.3}_{-0.1}$	$14.6^{+20.1}_{-6.3}$	$0.6^{+0.7}_{-0.3}$	$0.2^{+0.2}_{-0.1}$	$15.5^{+15.4}_{-8.2}$	$0.7^{+0.5}_{-0.4}$
H_2O		$7.9^{+3.5}_{-5.1}$	$334.8^{+203.2}_{-219.5}$	$20.7^{+13.3}_{-10.7}$	$7.7^{+6.4}_{-4.7}$	$314.4^{+315.9}_{-208.6}$	$19.9^{+19.0}_{-12.5}$	$7.7^{+5.3}_{-4.8}$	$318.9^{+242.9}_{-211.0}$	$20.6^{+15.6}_{-11.6}$
H_2		$0.5^{+0.3}_{-0.3}$	$2.1^{+1.7}_{-1.5}$	$1.2^{+1.1}_{-0.8}$	$0.4^{+0.4}_{-0.2}$	$1.5^{+2.4}_{-0.9}$	$1.0^{+1.1}_{-0.6}$	$0.4^{+0.4}_{-0.2}$	$1.7^{+2.2}_{-1.1}$	$1.0^{+1.1}_{-0.7}$
CO_2	[3,4)	$1.4^{+1.6}_{-0.9}$	$143.2^{+154.0}_{-94.9}$	$3.5^{+3.2}_{-2.1}$	$1.1^{+2.3}_{-0.7}$	$109.6^{+169.5}_{-67.0}$	$2.6^{+3.5}_{-1.6}$	$1.3^{+1.8}_{-0.9}$	$123.0^{+169.7}_{-79.9}$	$3.1^{+3.6}_{-2.0}$
CO		$0.1^{+0.1}_{-0.1}$	$5.4^{+7.1}_{-3.5}$	$0.2^{+0.3}_{-0.1}$	$0.1^{+0.1}_{-0.1}$	$5.8^{+5.4}_{-4.1}$	$0.2^{+0.2}_{-0.2}$	$0.1^{+0.1}_{-0.1}$	$5.5^{+6.2}_{-3.6}$	$0.2^{+0.2}_{-0.1}$
H_2O		$7.5^{+8.4}_{-4.6}$	$294.8^{+377.5}_{-183.1}$	$22.0^{+21.8}_{-12.3}$	$6.8^{+6.7}_{-3.9}$	$258.0^{+293.6}_{-150.5}$	$19.1^{+14.5}_{-10.3}$	$7.0^{+8.2}_{-4.1}$	$285.1^{+322.5}_{-177.3}$	$20.9^{+17.0}_{-12.0}$
H_2		$0.1^{+0.2}_{-0.1}$	$0.5^{+0.9}_{-0.4}$	$0.3^{+0.5}_{-0.2}$	$0.1^{+0.1}_{-0.1}$	$0.5^{+0.5}_{-0.3}$	$0.3^{+0.2}_{-0.2}$	$0.1^{+0.2}_{-0.1}$	$0.5^{+0.8}_{-0.3}$	$0.3^{+0.4}_{-0.2}$

model, we should emphasize that this figure shows only the mean of each f_{O_2} bin for clarity. The standard deviations are quite large (see statistics in Table 9). Indeed, $\geqslant$1 Tmol yr^{-1} of CO_2 outgassing is more common for T_{ini} greater than $\sim$2000 K and $\chi_{CO_2,\mathrm{ini}}$ greater than $\sim$80 ppm, although an increase in f_{O_2} is the easiest way to guarantee higher outgassing.[1] Equally, some parameter combinations also produce substantially lower outgassing rates.

To illustrate the spread across all model runs, figure 31 shows every result for the cumulative outgassed mass per species, as a function f_{O_2}. C and H species are well-separated by mass, except for cases close to the IW buffer. Going from IW$-$2 to IW+4, the mass of H_2O increases by over an order of magnitude, and for CO and CO_2, at least four orders of magnitude, whilst the mass of H_2 decreases. The hydrogen speciation shows a gradient in redox. The carbon speciation also shows a gradient in redox, whilst the total amount of carbon depends on partitioning (itself a function of redox).

It is worth emphasizing that figure 31 does not show the actual gas masses residing in the atmosphere. For instance, the atmospheric partial pressure of H_2O is limited to the saturation vapour pressure of liquid

---

[1] These cutoff values should not be taken as rules of thumb, however.

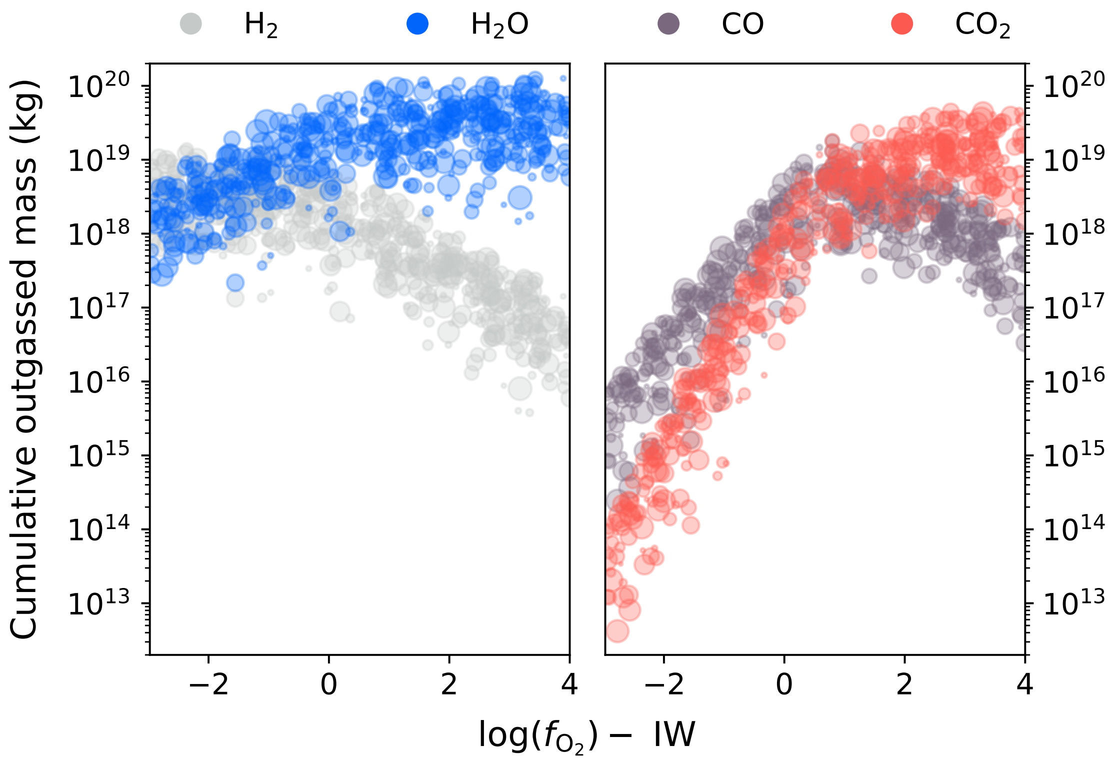

Figure 31: Each simulation's final cumulative outgassed masses of H_2 (grey dots), H_2O (blue dots), CO (aubergine dots), and CO_2 (coral dots), plotted as a function of mantle redox. Marker size increases with higher cumulative melt volume. All 500 parameter combinations are shown.

water; the cooling timescale of the outgassed plume to ambient temperatures is irrelevant on the Myr-timescales of this model. At $T_{\mathrm{surf}} = 333$ K, the saturation vapour pressure is 0.2 bar. Section 3.2.5 qualitatively discusses the main controls on atmospheric sinks. The cumulative masses also record the early pulse of outgassing, especially for H species.

The primary influence of f_{O_2} on the mass of outgassed volatiles is built into the model. Intrinsically, there are three reasons for the mass dependence in figure 31. The first two reasons comprise the redox-dependent speciation (setting total carbon) and volatile speciation (setting H_2O/H_2 and CO_2/CO) already described. The third reason is that the reduced gases investigated here (H_2 and CO) have a lower molecular mass than their oxidized counterparts (H_2O and CO_2). Thus, for equal moles outgassed, reduced atmospheres are necessarily less massive than oxidized atmospheres.

Correlation of outgassing with model parameters. Figure 32 summarizes the (nonlinear) Spearman's rank correlation coefficients between outgassing fluxes averaged over the final 10 Myr and the eight input parameters tested (Table 8). Beyond the mantle oxidation state, we find relatively moderate correlation with $\chi_{\mathrm{H_2O,ini}}$ and f_{extr}, weak correlation with $\chi_{\mathrm{CO_2,ini}}$, and no correlation with the initial thermal state.

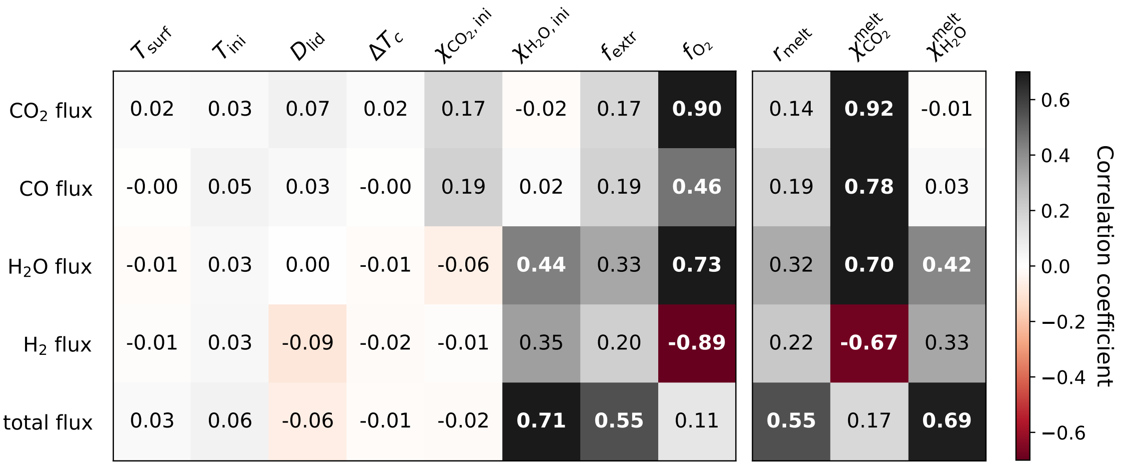

	T_{surf}	T_{ini}	D_{lid}	ΔT_c	$\chi_{CO_2,ini}$	$\chi_{H_2O,ini}$	f_{extr}	f_{O_2}	r_{melt}	$\chi^{melt}_{CO_2}$	$\chi^{melt}_{H_2O}$
CO_2 flux	0.02	0.03	0.07	0.02	0.17	-0.02	0.17	**0.90**	0.14	**0.92**	-0.01
CO flux	-0.00	0.05	0.03	-0.00	0.19	0.02	0.19	**0.46**	0.19	**0.78**	0.03
H_2O flux	-0.01	0.03	0.00	-0.01	-0.06	**0.44**	0.33	**0.73**	0.32	**0.70**	**0.42**
H_2 flux	-0.01	0.03	-0.09	-0.02	-0.01	0.35	0.20	**-0.89**	0.22	**-0.67**	0.33
total flux	0.03	0.06	-0.06	-0.01	-0.02	**0.71**	**0.55**	0.11	**0.55**	0.17	**0.69**

Figure 32: *(Left):* The matrix of Spearman's rank correlation coefficients between input parameters and outgassing fluxes averaged over the final 10 Myr, plus the summed flux of all outgassed molecules for the same time frame. Symbols are defined in Table 8. *(Right):* The same, but for key intermediate output variables—the volumetric melt production rate, r_{melt}, and the melt concentrations of CO_2 and H_2O, $\chi^{\mathrm{melt}}_{\mathrm{CO_2}}$ and $\chi^{\mathrm{melt}}_{\mathrm{H_2O}}$. Note that the moderate correlation between $\chi^{\mathrm{melt}}_{\mathrm{CO_2}}$ and H-species outgassing is due to the mutual effect of $f_{\mathrm{O_2}}$ on both quantities, while the correlation of $f_{\mathrm{O_2}}$ with the total flux appears low because it does not affect the sum of H_2 and H_2O.

Influence of initial temperatures. We find virtually no correlation between initial temperature conditions and outgassing fluxes after 700 Myr of convection. However, an initially hotter mantle closer to the solidus temperature forces a sharp pulse of melting in the first 100 Myr, expelling massive amounts of water and indeed raising the total moles of water outgassed. This is also not to say that instantaneous local temperatures are unimportant, as they affect the melt fraction as well as the equilibrium constants in equations (226), (233), and (234).

Influence of initial volatile budgets. The importance of the initial volatile budget varies between H and C species. For H_2O, initial mantle concentrations and instantaneous melt concentrations show a nearly identical correlation with outgassing flux, which illustrates how the mantle budget affects outgassing via melt partitioning. In contrast, $\chi_{\mathrm{CO_2,ini}}$ barely affects instantaneous melt concentrations, so it barely affects outgassing.

Influence of extrusive volcanism percentage. We expect an approximately linear relationship between the maximum outgassing flux and the fraction of melt allowed to contribute to outgassing. Although the correlation between this fraction and the computed outgassing fluxes is relatively moderate compared to certain other parameters (figure 32), note that accounting for extrusive volcanism in this model automatically downscales outgassing. For example, all else being equal, the difference in the outgassing flux between $f_{\rm extr} = 0.1$ and $f_{\rm extr} = 1$ is an order of magnitude.

Trade-offs between melt production and volatile concentration. In principle, the total C (or H) outgassing flux is proportional to the product of the C (or H) melt concentration times the volumetric melt production (but melt fractions are not independent of H_2O mantle concentrations). To see how much this trade-off matters, figure 32 also compares the correlation of outgassing flux with the instantaneous volatile melt concentrations and melt production rates. CO_2 and H_2O outgassing fluxes both correlate more strongly with their respective melt concentrations than with melt production rates.

Therefore, simply scaling outgassing with melting may neglect the high variability of volatile content in melts and could misrepresent fluxes in a stagnant lid regime. Whilst this is especially true for carbon species, where melt content overwhelmingly depends on f_{O_2}, it also holds for H_2O and H_2, and so is not restricted to redox-dependent partitioning.

Composition, flux, and total mass of early Archean outgassing. Following the parameter study from the previous section, figure 33 shows the posterior probability distributions of cumulative outgassed masses for different redox scenarios. Confidence intervals for masses, pressures, and fluxes are listed in Table 9. For a constant mantle oxidation state between 3 and 4 log-units above the IW buffer, for example, our median and 68% confidence intervals for the mean volcanic outgassing fluxes are $0.31^{+0.36}_{-0.20}$ Tmol yr^{-1} CO_2, $0.02^{+0.02}_{-0.01}$ Tmol yr^{-1} CO, $2.09^{+1.70}_{-1.20}$ Tmol yr^{-1} H_2O, and $0.03^{+0.04}_{-0.02}$ Tmol yr^{-1} H_2. The corresponding cumulative masses of H_2O are about 2% of an Earth ocean, verifying that earlier magma ocean degassing supplied most of the original ocean mass (Pahlevan et al., 2019).

Sensitivity to gradual mantle oxidation scenarios. Several mechanisms for mantle oxidation have been proposed (e.g., Wood et al., 2006; Sharp et al., 2013; Gaillard and Scaillet, 2014; Wordsworth et al., 2018; Schaefer and Elkins-Tanton, 2018; Nicklas et al., 2019), including degassing itself (Kasting et al., 1993). By tracking the concentration of abundant multivalent cations, one could self-consistently evolve the mantle redox state within our outgassing scenarios.

We leave this to future work, and as a first step, simply consider a linear increase of $\log f_{O_2}$ from IW-2 to IW$+2$, for a new set of 50 runs with otherwise random parameters.

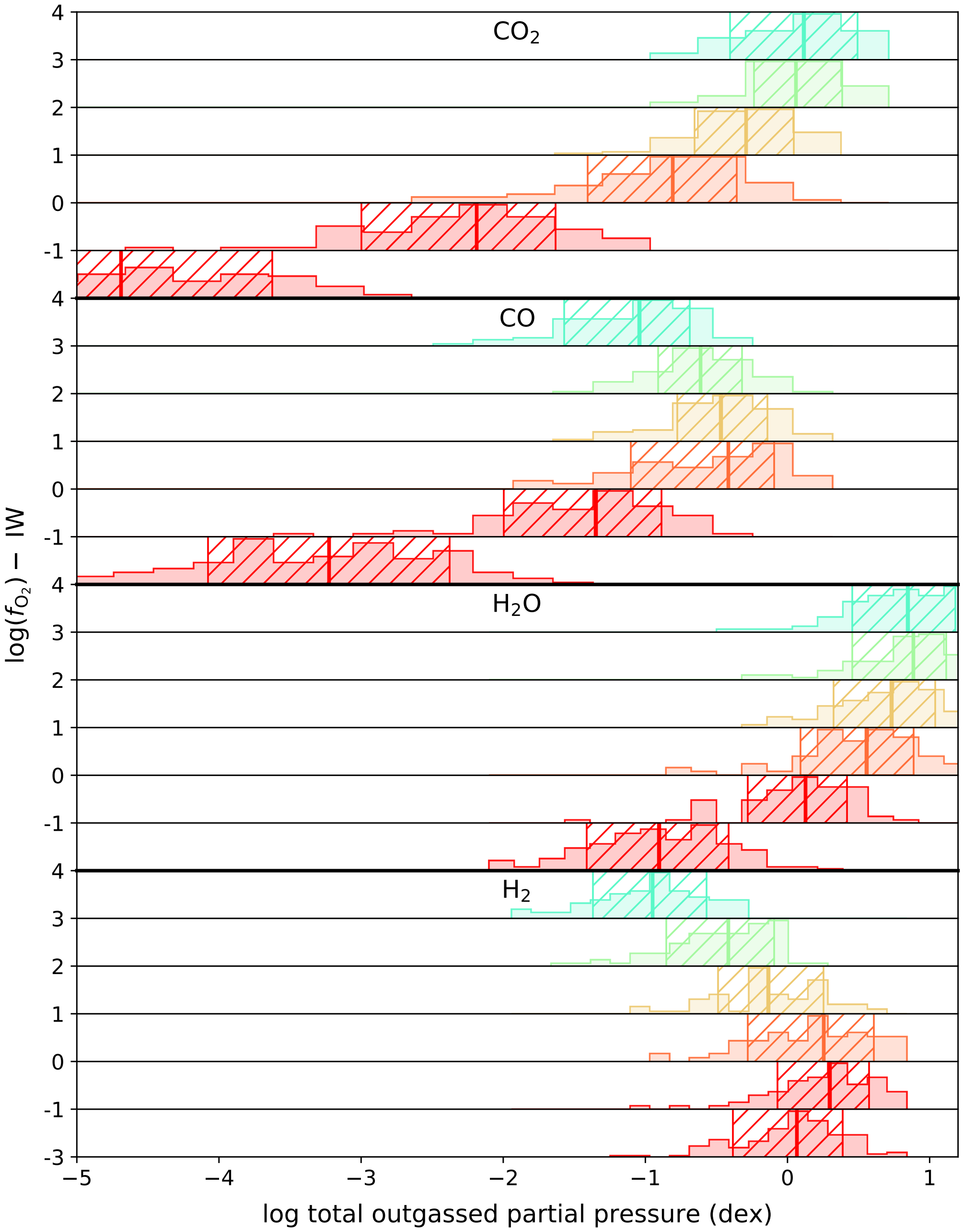

Figure 33: Histograms showing the empirical distribution of 700-Myr-cumulative outgassed masses for CO_2 (top), CO, H_2O, and H_2 (bottom). Distributions are “marginalized” across mantle redox states, where each colour shows one of five f_{O_2} ranges, as indicated by the y-axis labels. Bold vertical lines indicate the medians; hatched regions mark the 68% confidence interval.

Figure 34 demonstrates that secularly increasing $\log f_{O_2}$ results in H_2O and H_2 outgassing which is not very distinguishable from a constant $\log f_{O_2} - \mathrm{IW} \in [0, 2]$. Low f_{O_2} does not affect melt concentrations, so the same total amount of H_2O plus H_2 can be outgassed. Meanwhile, carbon is drastically limited in melts during the early reduced stage, permitting lower total outgassing. Small differences in cumulative outgassing could represent dramatic differences in the ultimate atmospheric composition.

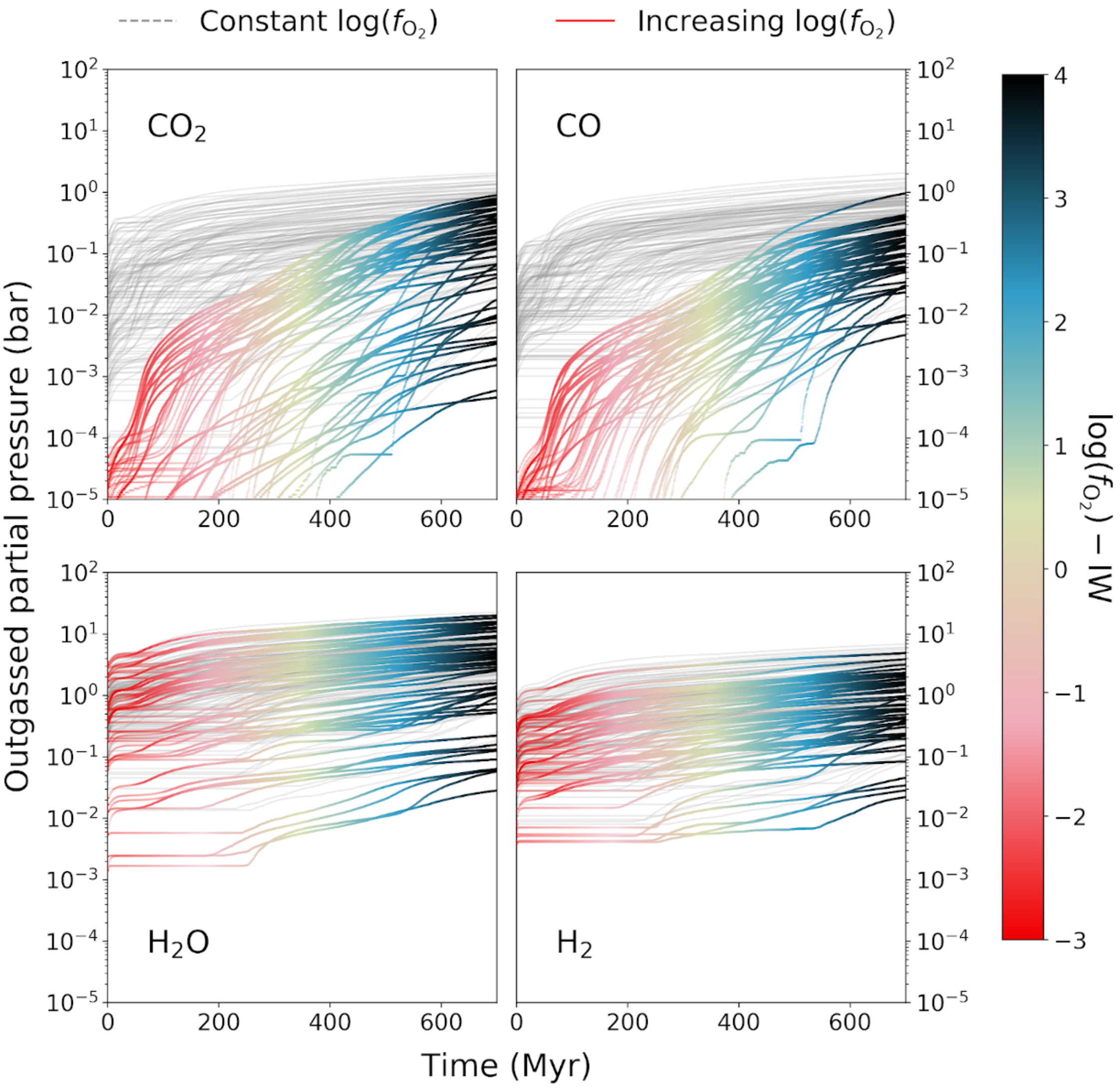

Figure 34: The modelled evolution of total outgassed pressure, compared between scenarios where $\log(f_{O_2})$ is fixed randomly between IW+0 and IW+2 (dashed grey lines; $N = 118$), and scenarios where f_{O_2} linearly increases from IW−2 to IW+2 over 700 Myr (solid gradient lines; $N = 50$). The colour gradient indicates the instantaneous mantle redox.

3.2.5 Discussion

Novelties introduced with this model. Earlier theoretical works on redox-dependent gas speciation predicted that both H_2 and CO would dominate the outgassing of a reduced early mantle (e.g., Kasting et al., 1993). This work suggests that CO_2 outgassing is lower than what one would expect from speciation alone, since its concentration is also limited in reduced melts. Direct comparisons of our results with previous model predictions of planetary outgassing are encumbered, however, by different model assumptions and choices of what physics to include. For example, in their outgassing model of an Earth-mass stagnant-lid planet, Tosi et al. (2017) did not calculate speciation. Still, their 700-Myr-cumulative partial pressures for H_2O ($\sim$5.1 bar) and CO_2 ($\sim$0.25 bar) are within the range of our corresponding results for H_2O + H_2 and for CO_2 + CO (IW; $\chi_{\mathrm{H_2O,ini}} = 500$ ppm).

Submarine versus subaerial outgassing. We have assumed that all outgassing is subaerial. Because crust is not subducted, volcanic eruptions might build up land above sea level relatively quickly, and volatiles would degas freely from surface lavas.

At surface pressures near 1 bar there is almost no effect on solubility or f_{O_2} in our chosen parameterizations. Several independent constraints place an upper limit on either the surface barometric pressure or pN_2 at 1.1 bar for the 3.5–2.7 Ga period (Marty et al., 2013; Catling and Zahnle, 2020). As such, we do not include any pressure-dependence of gas solubility in the melt, or of the redox change during degassing.

If most outgassing were submarine instead of subaerial, then the higher degassing pressures would cause melts to retain more volatiles, and global outgassing rates would be even lower than predicted here.

The effects of a stagnant lid on outgassing rates. In theory, some net effects of imposing a stagnant lid on outgassing are:

(i) The magmas generated under a stagnant lid dissolve less CO_2 and H_2O than those supplying arc volcanism, which samples recycled crustal material heavy in carbonates, organic carbon, and water (Wallace, 2005). Hotspot plumes also show evidence of crustal recycling (e.g., Shorttle et al., 2015; Tucker et al., 2019) and are associated with volatile-rich magmas. In any case, the modern mantle source is likely highly processed.

(ii) Less continuous melting may occur under a stagnant lid *despite higher interior temperatures* because, three-fold, mantle convection is less vigorous due to its lower temperature contrast, the melt zone is separated from the surface by a thick lithosphere unlike arc or ridge volcanism, and the depleted mantle is not refertilized by subducting plates.

(iii) The presence of water in recycled near-surface rock under plate tectonics would also lower the solidus, facilitating even greater melting near subduction zones (Katz et al., 2003). These arguments are tentatively supported by the observation that Venus appears to be less volcanically active than Earth (Smrekar et al., 2010).

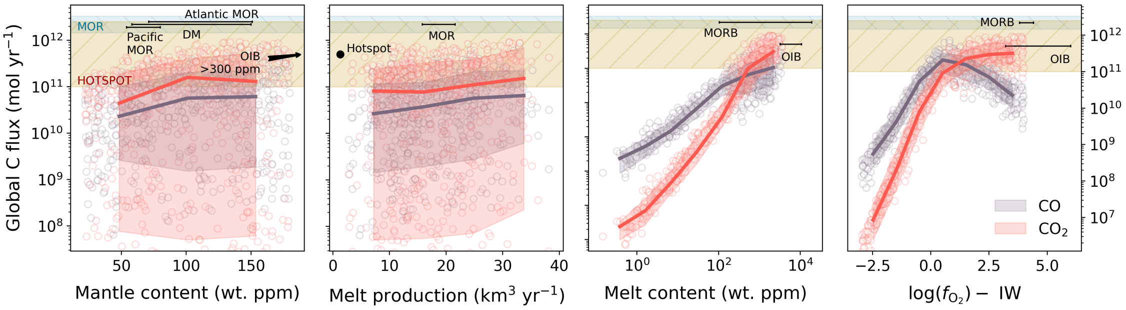

Figure 35: Summary of C outgassing fluxes with respect to (from left to right) mantle source CO_2 content, melt production rate, melt CO_2 content, and mantle oxidation state; note the log scale in melt content. Time-dependent variables represent the mean of the final 10 Myr. Each circle denotes an individual model run. Solid lines show the median of all runs. Solid swaths show the 68% confidence interval, with CO flux in blue and CO_2 flux in red. For context, modern Earth estimates are also shown for CO_2. The light blue rectangle spans the estimate from Hauri et al. (2017) of total CO_2 outgassing flux from the mid-ocean ridge (MOR) system. The beige rectangle spans the same estimate from Dasgupta and Hirschmann (2010) for hotspot volcanism. MOR mantle source concentrations are from Hauri et al. (2017); depleted mantle (DM) concentrations are from Marty (2012); ocean island basalt (OIB) mantle source concentrations are from Hauri et al. (2019); hotspot melt production is from Mjelde et al. (2010); MOR melt production is from Cogné and Humler (2006); mid-ocean ridge basalt (MORB) and OIB melt concentrations of CO_2 are from Hauri et al. (2019); MORB f_{O_2} is from O'Neill et al. (2018), and OIB f_{O_2} is from Amundsen and Neumann (1992). f_{O_2} relative to IW was converted from QFM roughly assuming 1 bar and 1000 K.

Further discussion of the effect of tectonic mode on mantle outgassing can be found in Tosi et al. (2017) and Foley and Smye (2018).

Observational context. Few proxy constraints exist on Archean outgassing rates. Avice et al. (2017) use a Xe isotope anomaly in Archean quartz to suggest mantle degassing was about tenfold greater at 3.3 Ga than at present. This proxy would apply to C-O-H outgassing rates at 3.3 Ga if they were derived directly from magma production rates. In our model, though, the volatile content of the melt is at least as important as the volume of the melt in determining C-O-H outgassing rates. Still, these high melting rates suggested by Xe isotopes are not matched by our stagnant lid model, despite testing realistic prior ranges of different input parameters. Speculatively, this could indicate that plate tectonics was already active by 3.3 Ga, which would lead immediately to orders of magnitude-higher melting rates (Noack et al., 2014).

It might help bring context to the results here if we imagine how they collate with modern volcanic outgassing. This would require comparing the same ends across different means, however; modern outgassing is almost entirely inseparable from plate tectonics (see section 3.2.5 above). Hence, a comparison would mostly provide a platform to understand the trade-offs between different components of the outgassing flux. Figures 35 and 36 summarize our modelled outgassing fluxes as a function of their components (melt production, mantle f_{O_2}, and source and melt volatile concentrations), with present-day estimates overplotted for hotspot and ridge volcanism. Arc volcanism is omitted because it tends to fall beyond these axis limits—arc magmas can typically have a few weight percent H_2O and CO_2 (Blundy et al., 2010; Plank et al., 2013).

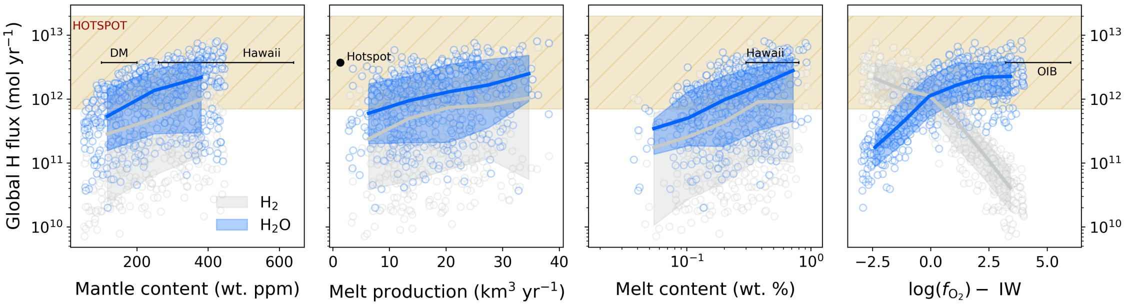

Figure 36: Analogous to Figure 35, but for H species. Subplots show outgassing fluxes with respect to (from left to right) mantle source H_2O content, melt production rate, melt H_2O content, and mantle oxidation state; note the log scale in melt content. Time-dependent variables represent the mean of the final 10 Myr. Each circle denotes an individual model run. Solid lines show the median of all runs. Solid swaths show the 68% confidence interval, with H_2 flux in grey and H_2O flux in blue. For context, modern Earth estimates are also shown for H_2O. The beige rectangle spans the estimate from Dasgupta and Hirschmann (2010) for CO_2 hotspot volcanism, multiplied by 7–8, the typical ratio of H_2O to CO_2 in volcanic gas from Holland (1984). Depleted mantle (DM) concentrations are from (Marty, 2012); Hawaii mantle source concentrations are from Wallace (1998); hotspot melt production is from Mjelde et al. (2010); Hawaii melt concentrations are from Wallace and Anderson (1998), and OIB f_{O_2} is from Amundsen and Neumann (1992). f_{O_2} relative to IW was converted from QFM roughly assuming 1 bar and 1000 K.

These figures demonstrate, for instance, how our model tends to produce carbon-poor melts compared to modern magmas (Hauri et al., 2019). Hotspot volcanism in particular has been associated with mantle sources even higher in f_{O_2}, up to the nickle-nickle oxide buffer (e.g., Amundsen and Neumann, 1992; Moussallam et al., 2016), which is outside the range of graphite stability—making the redox-dependent carbon partitioning model we use here inapplicable. The somewhat-higher integrated melt production compared to hotspots (Mjelde et al., 2010) barely compensates for the low CO_2 content, and we ultimately find CO_2 fluxes approaching the lowest estimates of the hotspot outgassing flux (Dasgupta and Hirschmann, 2010; Hauri et al., 2019). Overall, even for the most fortuitous parameter combinations, outgassing fluxes predicted in this model are at most still several times lower than the modern sum of hotspot, ridge, and plume outgassing (3–10 Tmol yr^{-1} CO_2; Gerlach, 2011).

From outgassing to atmospheric composition. Even before biological influence, many complex atmospheric processes ensure that the steady-state atmospheric composition does not mimic the volcanic gas composition. Neither does the oxidation state of atmosphere mimic the oxidation state of mantle: photochemical reactions and H escape can oxidize reduced gases, and extraterrestrial impactors could provide significant reducing power (Zahnle et al., 2020). Further, it is entirely possible that an earlier atmosphere degassed from the magma ocean was in some part still present at the end of the Hadean (Elkins-Tanton, 2012). Even the solar nebula cannot be discounted as an additional component of the atmospheric composition on top of outgassing, since there is no strong evidence that the primary atmosphere was lost completely by 4.5 Ga (although such a hypothesis is not favoured by studies cited throughout this section). We do not model the atmospheric composition here because the complexities described above deserve more astute attention. For completeness, though, this section discusses several key processes that modulate atmospheric partial pressures post-outgassing.

Weathering. The equilibrium between outgassing sources and silicate weathering sinks generally balances atmospheric CO_2, with seafloor weathering as a potential additional sink (Charnay et al., 2017; Krissansen-Totton and Catling, 2017). Weathering is thought to regulate the surface temperature via a negative feedback (Walker et al., 1981). Once the carbon cycle reaches steady state, the partial pressure of CO_2 becomes largely independent of initial conditions, assuming a single equilibrium combination of pCO_2 and surface temperature for a given outgassing flux. With an equilibrium time scale for atmospheric CO_2 of $\sim$1 Gyr (Kanzaki and Murakami, 2018), however, the early Archean carbon cycle could have still be adjusting to any historical magma ocean degassing.

All else being equal, lower outgassing means a cooler climate, a weaker need to weather, and a lower weathering flux. Krissansen-Totton et al. (2018) provide a rare example of a carbon cycle model tested with sub-modern total CO_2 outgassing rates; possible, they acknowledge, with a less-active lid or a low-f_{O_2} mantle. They find pCO_2 as low as $\sim 10^{-3}$ bar using a minimum outgassing of 1.4 Tmol yr^{-1} (Tosi et al., 2017), a flux which is higher than the maximum calculated in this study. The Krissansen-Totton et al. (2018) model would suggest that pCO_2 was probably not higher than 10^{-3} bar if the total outgassed input were less than 1.4 Tmol yr^{-1}. This model assumes weathering is not limited by mineral supply; following Foley and Smye (2018), the supply limit to silicate weathering would only be reached at CO_2 fluxes of over 100–1000 Tmol yr^{-1} for our stagnant lid scenarios (i.e., it is not reached). For comparison, the earliest likely proxy measurement (3.2 Ga) gives a lower limit of 2.5×10^{-3} bar, based on weathering rind analyses (Hessler et al., 2004).

Hydrogen escape. In the Archean, the atmospheric mixing ratio of hydrogen would have been determined by the balance between H_2 outgassing plus impact degassing on one hand, and atmospheric escape on the other hand. In an anoxic atmosphere, the reduction of oxidized volatiles would have been negligible. Because the H_2 mixing ratio depends on more than just the H_2 outgassing flux—for example, the partial pressure of H_2O at the tropopause cold trap, which is also a source of escaping hydrogen—we do not attempt to constrain the mixing ratio in this work. However, we can put our results in context.

Kuramoto et al. (2013) modelled Archean H_2 escape rates and suggest H_2 mixing ratios below 1% by volume at the homopause—this is employing a higher-than-modern outgassing flux, 2.4×10^{13} mol yr^{-1}, although the Kuramoto et al. (2013) model depends more on solar EUV flux than on outgassing because of escape rates below the diffusion limit. Meanwhile, Zahnle et al. (2019) invoked Xe fractionation to suggest that hydrodynamic escape could have taken place over a lengthy 1–2 Gyr, with a minimum H_2 mixing ratio of 1% (or equivalent CH_4) at times during the Archean, but not necessarily throughout. At face value, then, our results taken with the <1% H_2 mixing ratios (based on higher outgassing rates) from Kuramoto et al. (2013) imply that additional sources of hydrogen (i.e., impactors) are required to replenish escaping H_2 and meet Xe constraints.

Condensation of oceans. Unlike carbon dioxide and hydrogen, the portion of outgassed water remaining in the atmosphere is small because the condensation timescale is short. We can assume that outgassed H_2O condensed up to the vapour pressure of liquid water (0.2 bar at 333 K), which sets a maximum tropospheric partial pressure. If all outgassed water condenses, then our results imply an equivalent global layer on the order of 1 m (most reduced cases) to 100 m (most oxidized cases). This suggests that the collapse of an earlier steam atmosphere was likely to have produced the majority of the volume of Earth's first ocean.

Other carbon species. CO molecules carried to the atmosphere by both outgassing and impacts would be oxidized to CO_2 by the products of H_2O photodissociation, H and OH, followed by OH dissociation into O^- and H^+. The H^+ ions are driven away by solar wind, and the O^- reacts with CO to form CO_2. Hence estimates of pCO also require a more detailed atmospheric chemistry model (e.g., Kasting, 1990).

This work has ignored CH_4 outgassing entirely because CH_4 is not stable at the pressure, temperature, and redox ranges we consider (Zhang and Duan, 2009; Wetzel et al., 2013; Ramirez et al., 2014). At high pressures deep in the lithosphere, some CH_4 would be produced from a reduced source, but we only consider outgassing at the surface. Although CH_4 can be stable at surface pressures, it is not directly outgassed from the magma due to the high temperatures.

Implications of low Archean outgassing rates for greenhouse warming under the Faint Young Sun. Despite the fainter luminosity of the young sun, there is geochemical evidence for a temperate climate and stable oceans on Earth as early as 4.4 Ga (e.g., Wilde et al., 2001; Valley et al., 2002, 2014). Popular attempts to resolve this paradox invoke a stronger-than-modern greenhouse of CO_2 or CH_4 (see review in Charnay et al., 2020). Volcanic outgassing would have been the main source of these greenhouse gases; we expect outgassing to have order-of-magnitude effects on steady-state pCO_2 and surface temperature (Walker et al., 1981; Sleep and Zahnle, 2001; Kadoya and Tajika, 2014; Höning et al., 2019). In the classic Walker et al. (1981) framework, one would generally expect a lower CO_2 outgassing rate to always produce both a cooler climate and correspondingly lower weathering rates, with a lower pCO_2 at steady state. Here we are discounting the additional source of carbonate metamorphism, assuming that this process primarily occurs in tectonic settings.

Indeed, the CO_2 outgassing rates predicted here are at best almost an order of magnitude lower than the values tending to be presumed in Archean Earth climate models, including those investigating solutions to the Faint Young Sun paradox (e.g. Sleep and Zahnle, 2001; Wordsworth and Pierrehumbert, 2013; Charnay et al., 2017; Kanzaki and Murakami, 2018; Krissansen-Totton et al., 2018). The elevated outgassing rates used in many of these models might relate to a plate tectonics setting at the time, or a higher ratio of extrusive to intrusive melt than modelled here. Fundamentally, the notion of higher outgassing in the past seems to be based on the notion of higher mantle heat flow in the past (e.g., Turcotte, 1980). As we have argued throughout this study, such a calibration assumes that variations in outgassing are mostly explained by variations in melt production, and that the Archean melt production was necessarily higher. Our results would refute both these assumptions under a stagnant lid scenario. Firstly, CO_2 magma concentrations show a stronger correlation with CO_2 outgassing than do melt production rates. Secondly, we nevertheless fail to produce high global melt production rates.

We cannot quantify the likelihood of a temperate 15°C Archean without climate models—however, a planet warmed purely by CO_2 does seem more difficult to justify given our results. For example, Wolf and Toon (2014) use a 3D general circulation model to show that maintaining 15°C requires 200 mbar of pure CO_2 at 3.8 Ga, if other climate parameters (e.g., day length) are not optimal, and tens of mbar if they are. This partial pressure lower limit surpasses the tentative $\sim$1 mbar pCO_2 result given $\geqslant$ 1.4 Tmol yr^{-1} outgassing from Krissansen-Totton et al. (2018). Given the amount of uncertainty, this order-of-magnitude discrepancy does not cancel prevailing possibilities. Dedicated atmospheric modelling should estimate the feasibility of greenhouse warming fed by weaker outgassing under various unconstrained climate parameters.

If anything, our results suggest that if early Archean outgassing could be described by a stagnant lid model and if mantle f_{O_2} were below the IW buffer, then virtually no CO_2 would be outgassed. For CO_2 melt concentrations of 600 ppm (figure 29), outgassing 6 Tmol yr^{-1} (the low end of the present-day estimate) with 40% extrusive melt would require a magma supply of 370 km^3 yr^{-1}, equivalent to producing the Deccan Traps in 3000 years. Any reliance on a CO_2 greenhouse to address the Faint Young Sun problem for Earth might then seem to put implicit constraints on the contemporaneous mantle oxidation state, or else require obscene volcanism.

3.2.6 Conclusions

This work has coupled a 2D numerical convection model with melting, partitioning, and volatile speciation models to calculate the redox-dependent volcanic outgassing fluxes of C-O-H species for a stagnant lid planet. We have applied this model to Earth in the Hadean and early Archean, finding typical global CO_2 and H_2O outgassing fluxes of less than 1 Tmol yr^{-1} and 10 Tmol yr^{-1} respectively, depending on the mantle oxidation state. For an oxidation state at least two log-units above the IW buffer, we predict outgassing fluxes as low as a few percent of the modern day value. For all species considered, outgassing is predominantly controlled by mantle f_{O_2}, whilst the assumption of a stagnant lid in our model explains the low outgassing rate compared to modern Earth.

These flux calculations could be used to constrain the early Earth's atmospheric evolution. An estimate of H_2O, CO_2, H_2, and CO partial pressures would have to consider not only photochemistry, silicate weathering, and hydrogen escape, but also constraints on the atmosphere left over from accretion and magma ocean degassing, as well as extraterrestrial volatile delivery.

Atmospheric CO_2, in particular, represents a balance between outgassing and weathering. The evolution of CO_2 outgassing through the early Archean represents a large uncertainty on greenhouse gas-based solutions to the Faint Young Sun problem. Although many studies of the early Earth climate have focused on constraining weathering fluxes, outgassing fluxes—especially in a stagnant lid scenario—have gone underexplored. It is perhaps not wholly appreciated that the CO_2 outgassing flux could be over an order of magnitude lower in the absence of plate tectonics. Considering the fairly high CO_2 partial pressures needed to produce clement conditions (Charnay et al., 2020), these results could be used to test whether an early initiation of plate tectonics—combined with an early date of mantle oxidation—may be relevant for a temperate young planet.

We acknowledge the two anonymous reviewers whose feedback has critically improved the manuscript. CMG also wishes to thank R. J. Graham and J. Krissansen-Totton for sharing their expertise. This work was funded by the Deutsche Forschungsgemeinschaft (DFG, German Research Foundation) – Project-ID 263649064 – TRR 170. This is TRR 170 Publication No. XX.

3.3 Effect of mantle oxidation state and escape upon the evolution of Earth's magma ocean atmosphere

Katyal N., Ortenzi G., Grenfell J.L., Noack L., Sohl F., Godolt M., Muñoz A.G., Schreier F., Wunderlich F. and Rauer H. *Effect of mantle oxidation state and escape upon the evolution of Earth's magma ocean atmosphere*. A&A 643, A81 (2020) https://doi.org/10.1051/0004-6361/202038779

3.3.1 Abstract

Context. The magma ocean period was a critical phase determining how Earth's atmosphere developed into habitability. However, there are major uncertainties in the role of key processes such as outgassing from the planetary interior and escape of species to space that play a major role in determining the atmosphere of early Earth.

Aims. We investigate the effect of outgassing of various species and escape of H_2 for different mantle redox states upon the composition and evolution of the atmosphere for the magma ocean period.

Methods. We included an important new atmosphere-interior coupling mechanism: the redox evolution of the mantle, which strongly affects the outgassing of species. We simulated the volatile outgassing and chemical speciation at the surface for various redox states of the mantle by employing a C-H-O based chemical speciation model combined with an interior outgassing model. We then applied a line-by-line radiative transfer model to study the remote appearance of the planet in terms of the infrared emission and transmission. Finally, we used a parameterized diffusion-limited and XUV energy-driven atmospheric escape model to calculate the loss of H_2 to space.

Results. We have simulated the thermal emission and transmission spectra for reduced and oxidized atmospheres present during the magma ocean period of Earth. Reduced/thin atmospheres consisting of H_2 in abundance emit more radiation to space and have a larger effective height than oxidized/thick atmospheres, which are abundant in H_2O and CO_2. We obtain that the outgassing rates of H_2 from the mantle into the atmosphere are a factor of ten times higher than the rates of diffusion-limited escape to space. We estimate the timescale of total mass loss of outgassed H_2 via escape to be few tens of million years, which is comparable to other studies.

Conclusions. Our work presents useful insight into the development of the terrestrial atmosphere during the magma ocean period and provides input to guide future studies that discuss exoplanetary interior compositions and their possible links with atmospheric compositions that might be estimated from observed infrared spectra by future missions.

3.3.2 Introduction

Understanding how the early atmosphere of Earth emerged into habitable conditions is a central question not only for addressing our own origins, but also for interpreting the fascinating new data in exoplanetary science (for recent reviews, see, e.g., Jontof-Hutter, 2019; Madhusudhan, 2019). Magma oceans (MOs) consisting of hot and molten silicates in the mantle exist during the planetary accretion phase (Elkins-Tanton, 2012) and facilitate the formation of an atmosphere by outgassing of volatile species such as H_2O, CO_2, H_2, CH_4 , and CO . Thus, the MO period likely represents a key juncture on the pathway to habitability because atmosphere-interior couplings (e.g., Elkins-Tanton, 2012; Lebrun et al., 2013; Hamano et al., 2013; Schaefer et al., 2016) established during this phase could have set the stage for subsequent atmospheric evolution. The duration of the magma ocean phase is potentially affected by the absence or presence of an atmosphere and the interior dynamics of the mantle (e.g., Lebrun et al., 2013; Nikolaou et al., 2019) that affect the thermal spectral evolution of the planet (e.g., Hamano et al., 2015; Katyal et al., 2019). Other uncertainties such as the initial volatile inventory of the mantle, for example, the amount of H_2O stored in the mantle (Genda et al., 2017; Meech and Raymond, 2019), and compositional constraints such as the mantle oxygen fugacity (Hirschmann, 2012; Schaefer and Fegley, 2017) are also important quantities that might critically affect the oxidation state of outgassed volatiles and hence the subsequent climate and compositional evolution of the atmosphere.

The budget and origin of volatiles in the mantle of Earth is one of the main questions in geo-science (see, e.g., Meech and Raymond, 2019). Recent studies suggest quite diverse scenarios that range from a wet, late accretion to a dry accretion to which water was added mostly during the "late veneer", which is proposed to have occurred roughly around 80-130 Myr after the isolation of protoplanetary nebula at around 4.5 Gyr before present (Albarede et al., 2013). Abundances of highly siderophile elements (HSE) and other volatile species such as H_2O suggest that volatile-rich material was added to Earth after its core formed (Albarède, 2009). Measurements of the abundances of water and carbon in the bulk silicate Earth (BSE) show that the late veneer might indeed have supplied 20% - 100% of the budget of the total hydrogen (H) and carbon (C) in the BSE (Wang and Becker, 2013). Some recent studies do not support the late veneer as the main source of water on Earth (Dauphas, 2017; Fischer-Gödde and Kleine, 2017; Hopp and Kleine, 2018) and argue that water was likely added to Earth already during the waning stages of accretion and thus was already present during the late veneer. Interestingly, the reaction of terrestrial water and Fe from the late veneer produced much hydrogen as a byproduct (Zahnle et al., 2020). There is increasing isotopic evidence indicating that the late veneer might also have supplied a significant amount of reducing material onto the surface of Earth and into the atmosphere (Genda et al., 2017; Greenwood et al., 2018; Zahnle et al., 2020).

The impact-degassing studies by Schaefer and Fegley (2007); Hashimoto et al. (2007); Schaefer and

Fegley (2010) and Fegley and Schaefer (2014) also in general favored the outgassing of reduced gases upon impacts by certain types of reduced meteoritic materials such as ordinary and enstatite chondrites. Furthermore, changes in chondrites delivery rate are likely to affect the redox state of the mantle and hence the atmospheric composition and amount, as suggested recently by Schaefer and Fegley (2017). Their work also showed that the variation in oxygen fugacities for mixtures of primitive meteoritic material could lead to atmospheres ranging from highly oxidizing to highly reducing ones (also see Hirschmann, 2012).

The redox state of the minerals and melts is related to the oxygen fugacity fO_2 of the system that is equivalent to the partial pressure of the gas or the availability of oxygen (Gaillard et al., 2015). This quantity is poorly constrained for the early Earth (Frost and McCammon, 2008). The current understanding is that before the formation of the Earth core ∼4.56 Gyr before present (Stevenson, 1983), the lower fO_2 of the upper mantle was approximately three log units below the reducing iron-wüstite (IW) buffer, that is, IW-3 and it evolved to a higher fugacity value that was approximately equivalent to the current mantle of Earth, which resembles the quartz-fayalite-magnetite (QFM) buffer, that is, IW+3.5 (Wood et al., 1990; O'Neill, 1991). Direct geological evidence regarding the redox state of the mantle is sparse, and it is not clear when the Earth may have been oxidized during the Hadean (Trail et al., 2011). However, the geological record mainly suggests that the upper mantle was initially reduced and became progressively oxidized between 4.6 and 3.9 Gyr before present (Kasting et al., 1993; Delano, 2001; Schaefer and Fegley, 2017), with a possible later further increase in redox state by ≈ 1.3 at the end of the Archean (Aulbach and Stagno, 2016).

Previous interior modeling studies investigating atmospheres at and around the time of the magma ocean (e.g., Lebrun et al., 2013; Hier-Majumder and Hirschmann, 2017; Nikolaou et al., 2019) have considered outgassing of volatiles such as H_2O and CO_2, which means that they considered the mantle to be constantly oxidized. These studies suggested outgassed pressures of H_2O and CO_2 ranging from a few tens to hundreds of bar depending upon uncertainties, for instance, in the initial volatile content, the timing of the MO, and internal properties of the mantle. Recent modeling studies have now started to investigate the effect of the redox state on the outgassing. Pahlevan et al. (2019) investigated the effect of fO_2 on the outgassing and atmosphere losses and provided evidence for an early oxidation of silicate Earth using the D/H of the oceans. Most recently, Ortenzi et al. (2020) calculated the expected outgassing rates for the reduced and oxidized rocky planets and focused on exploring the observational constraints for the atmospheric (and interior) redox state of exoplanets.

Hydrodynamic escape of H_2 during this time (∼4.5 Gyr before present) was likely not sufficient to desiccate the planet (Kasting et al., 1993), so that conditions remained wet after the Moon-forming impact and crystallization of the final MO (Lammer et al., 2018). Hydrogen would therefore have been a sufficiently major component of an accretionary steam-based atmosphere during the MO phase. However, hydrogen evolution around the time of the MO is poorly understood because of the uncertainties in accretion, outgassing, ingassing, and escape (see, e.g., Tian, 2015). Several studies have considered the energy-limited hydrodynamic escape of hydrogen from the early atmosphere (Archean) of Earth (Tian et al., 2005; Kuramoto et al., 2013; Zahnle et al., 2019) and calculated somewhat differing results based on including or excluding the effect of H_2 diffusive flux on the gas-density profile and processes such as radiative cooling and thermal conduction that these escape models treat, for example. Johnstone et al. (2019) have also discussed uncertainties in the energy-limited mass-loss formula when applied to the early atmospheres. For rocky planets around M dwarfs, large amounts of water could be lost depending on the uncertainties in the stellar luminosity, for instance (e.g., Tian and Ida, 2015; Schaefer et al., 2016).

We apply a coupled suite of interior and atmospheric models to investigate outgassing and escape during the MO period and study the effect of varying the mantle fugacity on the atmospheric evolution. We also calculate theoretical atmospheric spectra that serve as a link for observations with early Earth-sized planets. In Section 3.3.3 we present the volatile speciation model and the atmospheric model. Section 3.3.4 presents the scenarios we adopted. Section 3.3.5 provides results of the effect of the redox state of the mantle on the infrared emission and transmission spectra. The interplay between outgassing and atmospheric loss of H_2 is also presented in this section. In Section 3.3.6 we discuss our findings. Finally, we provide a conclusion of our work in Section 3.3.7.

3.3.3 Methods and models

C-H-O based volatile speciation model. The outgassing and volatile chemical speciation were simulated following the equilibrium and mass balance method (French, 1966; Holloway, 1981; Fegley, 2013; Gaillard and Scaillet, 2014; Schaefer and Fegley, 2017) that has recently been presented in detail by Ortenzi et al. (2020). We calculated the outgassed composition of the volatiles considering a broad range of temperatures, pressures, and redox states. The four common petrological buffers used in the literature and their mantle oxidation states are

$$2\,\mathrm{Fe} + \mathrm{SiO_2} + \mathrm{O_2} \rightleftharpoons \mathrm{Fe_2SiO_4}, \mathrm{QIF} \tag{238}$$

$$2\,\mathrm{Fe} + \mathrm{O_2} \rightleftharpoons 2\,\mathrm{FeO}, \mathrm{IW} \tag{239}$$

$$3\,\mathrm{Fe_2SiO_4} + \mathrm{O_2} \rightleftharpoons 2\,\mathrm{Fe_3O_4} + 3\,\mathrm{SiO_2}, \mathrm{QFM} \tag{240}$$

$$\mathrm{Ni} + \frac{1}{2}\mathrm{O_2} \rightleftharpoons \mathrm{NiO.NiNiO} \tag{241}$$

Quartz-iron-fayalite (QIF) and IW buffers represent reduced conditions, and quartz-fayalite-magnetite

(QFM) and nickel-nickel-oxide (NiNiO) describe the oxidizing redox states. The oxidation state (oxygen fugacity) for these buffers was calculated following the parameterization from Holloway et al. (1992),

$$\log_{10} \mathrm{fO_2} = \mathrm{A} - \mathrm{B/T} + \mathrm{C(P-1)/T} \ + \mathrm{Z}, \tag{242}$$

where the pressure (P) is in bars, the temperature (T) in is Kelvin, and the parameters A, B and C are defined in Table 10. Z is a positive or negative number denoting the deviation from the fugacity values with respect to the buffers, as stated in the table. We mainly used the IW buffer and chose Z to be -4 (highly reducing), 0 (reducing), and 4 (oxidizing) in order to investigate the effect of a range of redox mantle states on outgassing.

Buffer	A	B	C
QIF	7.679	29673	0.05
IW	6.899	27714	0.05
QFM	8.555	24014	0.092
NiNiO	8.951	24556	0.046

Table 10: Data collected from Holloway et al. (1992) to obtain the oxygen fugacity of the mantle buffers as listed.

By simulating the oxidation state, that is, the oxygen fugacity $\mathrm{fO_2}$ of the system, we are able to simulate the gas chemical speciation via the following equilibria:

$$\mathrm{CO} + \frac{1}{2}\,\mathrm{O_2} \rightleftharpoons \mathrm{CO_2}, \text{ and} \tag{243}$$

$$2\,\mathrm{H_2} + \mathrm{O_2} \rightleftharpoons 2\,\mathrm{H_2O}. \tag{244}$$

To calculate the ratio between the carbon species (Eq. 243), we considered the equilibrium constant K_1 for the equilibrium as

$$K_1 = \exp\left(\frac{-\Delta_r G_1^0}{RT}\right) = \frac{X_{\mathrm{CO_2}}}{X_{\mathrm{CO}}} \frac{1}{\mathrm{fO_2}^{1/2}}, \tag{245}$$

where R is the universal gas constant (8.314 J K^{-1} mol^{-1}), T is the temperature of the outgassed material in Kelvin, and $\Delta_r G_1^0$ is the Gibbs free energy of the reaction in Eq. (243), where

$$\Delta_r G_1^0 = \Delta_f G_{\mathrm{CO_2}}^0 - \Delta_f G_{\mathrm{CO}}^0. \tag{246}$$

Substituting $\Delta_r G_1^0$ and the calculated $\mathrm{fO_2}$ in Eq. (243) gives us all the necessary parameters needed to calculate the carbon species. For Eq. (244), the Gibbs free energy of reaction $\Delta_r G_2^0$ is related only to the

Gibbs free energy of formation of water ($\Delta_f G^0_{H_2O}$),

$$\Delta_r G^0_2 = 2\Delta_f G^0_{H_2O}. \tag{247}$$

The values of $\Delta_f G^0$ for the different species were calculated following the example of Fegley (2013) and compared to the literature (Chase, 1999).

Similarly, the abundances of H_2 and H_2O Eq. (244) are related to the equilibrium constant K_2 and the fugacity fO_2 via

$$\left(\frac{X_{H_2O}}{X_{H_2}}\right)^2 = K_2 \ fO_2, \tag{248}$$

where X_{H_2O} and X_{H_2} are the mole fractions of H_2O and H_2 and are related to the partial pressure of each of the species. The rate of outgassing of H_2O can therefore be related to the rate of outgassing of H_2 as

$$r_{H_2O} = R_1 \ r_{H_2}, \tag{249}$$

where $R_1 = (K_2 \ fO_2)^{0.5}$, r_{H_2} , and r_{H_2O} are the outgassing rates of H_2 and H_2O in units of m^{-2} s^{-1}, respectively.

Coupled interior-atmospheric evolution. A schematic for interior-atmosphere coupling is presented in Figure 37. We started by taking the variation in surface pressure p_s, surface temperature T_s , and volatile abundances $f^{init}_{H_2O}$ and $f^{init}_{CO_2}$ from the interior model output of Nikolaou et al. (2019), that is, a mantle temperature of 4000 K and an initial mantle composition of $X_{H_2O} = 0.05$ weight percent (wt%) (550 ppm) and $X_{CO_2} = 0.01$ wt% (130 ppm) as the input. We then applied the volatile speciation model from Ortenzi et al. (2020) as described in Sect. 3.3.3 to obtain the final outgassed molar abundance of the species as a function of oxygen fugacity fO_2 relative to the given mineral buffer (IW), as shown in Figure 38. This figure shows that for a reduced mantle (between IW and IW-4) and increasing input H/C from top to bottom, we obtain atmospheres that are rich in CO, CO+H_2 mixtures, and H_2. On the other hand, for a more oxidized mantle with typically higher fugacity values (between IW and IW+4) and increasing input H/C from top to bottom (Fig. 38), we obtain an atmosphere that is rich in CO_2, H_2O+CO_2 , and H_2O. The bottom panel of Fig. 38 corresponds to an initially assumed 100% H_2O which results in a almost pure H_2 atmosphere for a reduced mantle and a pure H_2O atmosphere for an oxidized mantle.

The initial outgassed volatiles H_2O and CO_2 taken from Bower et al. (2019) with a mean molar mass μ_v react with the melt and result in a different composition of the species outgassed to the atmosphere as calculated from the speciation model (Section 3.3.3). When the number of moles of the species C-H-O

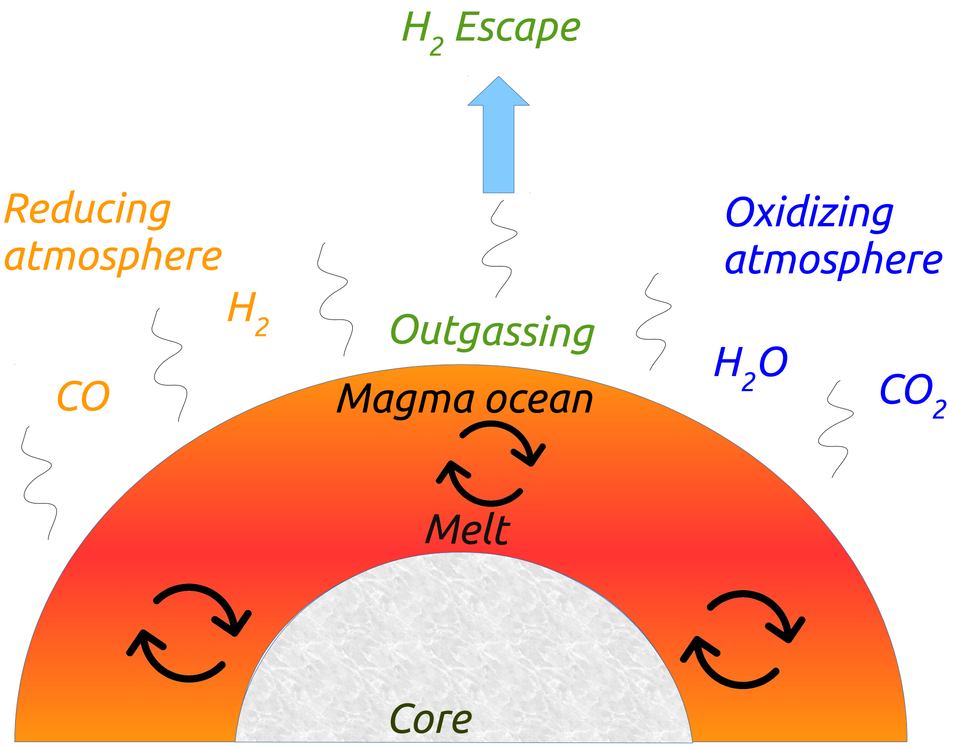

Figure 37: Schematic showing coupled interior-atmosphere exchange via outgassing of reduced species such as H_2 and CO (orange) for a reduced mantle (e.g., IW buffer) and oxidized species such as H_2O and CO_2 (blue) for an oxidized mantle (e.g., QFM buffer) as the magma ocean solidifies. The H_2 in the atmosphere is lost to space via escape.

is kept constant in the speciation model, a different atmosphere with a new mean molar mass μ_{atm} results, which has a different pressure at the bottom (surface) of the atmosphere, which we now call p_{boA}. This pressure is calculated based on the volatile mass balance (Bower et al., 2019),

$$p_{\text{boA}} = p_s \left(\frac{\mu_{\text{atm}}}{\mu_v} \right), \tag{250}$$

where p_s is the initial (surface) pressure of the volatiles calculated as a mono-gas atmosphere.

Starting from the mass of the outgassed species H_2O given by $M = P{*}A/g$, we obtained the following equation for the initial H_2O outgassing rate from the interior.

$$R^{\text{init}}_{H_2O} = \frac{1}{A}\frac{dN}{dt} = \frac{N_A\ 1000}{g\ m_{H_2O}} \left(\frac{dP}{dt} \right) \text{ molecules m}^{-2}\text{s}^{-1}, \tag{251}$$

where dN is the number of H_2O molecules outgassed in a time interval dt, N_A is Avogadro's number (6.022 $\times 10^{23}$), A is the area of the Earth surface (5.1×10^{14} m^2), m_{H_2O} is the molecular weight (18 g/mol), $g = 9.81$ m/s^2 is the surface gravity, and dp is the difference in outgassed pressure at a time interval dt taken from coupled model result of Katyal et al. (2019) and Bower et al. (2019).

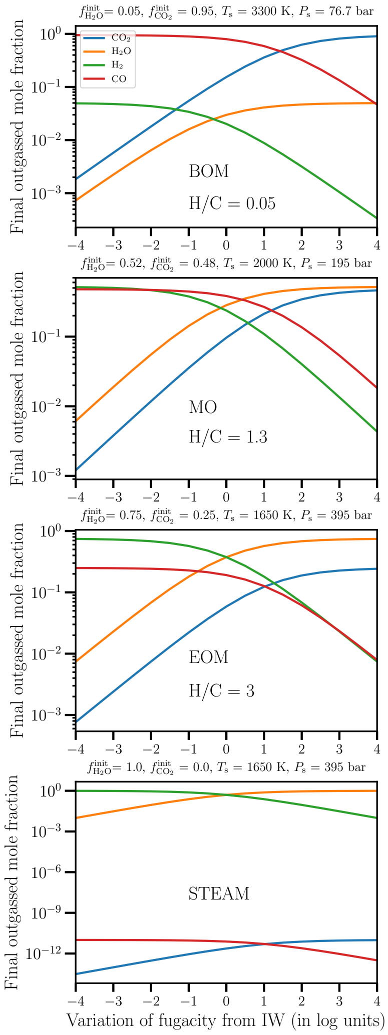

Figure 38: Volatile chemical speciation in terms of outgassed mole fraction vs. oxygen fugacity of the mantle. The x-axis indicates the oxygen fugacity range in logarithmic units relative to the IW buffer. For reference (in log units), buffers QIF = IW-1, QFM = IW+3.8, and NiNiO = IW+4.2 approximately (Wood et al., 1990). From top to bottom, we show the BOM, active MO phase, EOM and a steam-atmosphere phase that are characterized by different initial H/C between hydrogen and carbon. The corresponding input values of the initial volume mixing ratio of volatiles, surface pressures P_s , and temperatures T_s (Nikolaou et al., 2019) for the speciation model are indicated at the top of each panel.

To obtain the outgassing rate of H_2, we used Eq. (249) and Eq. (251). To account for the redox variation of the mantle and the volatile mass balance, we assumed that the initial rate of H_2O outgassing $R^{init}_{H_2O}$ in Eq. (251) is the total outgassing rate of combined (H_2+H_2O). Therefore, $R^{init}_{H_2O} = r_{H_2} + r_{H_2O}$. Inserting Eq. (249) here, we obtain the rate of H_2 outgassing as

$$r_{H_2} = \frac{R^{init}_{H_2O}}{1 + R_1} \text{ molecules m}^{-2}\text{s}^{-1}. \tag{252}$$

Convective lapse rate. The convection takes into account the heat transport by adiabatic expansion of a mixture of a nonideal condensable gas H_2O (because the critical point of water at $T_c = 647$ K and $p_c = 220$

bar is close to the T-p range considered in this study), denoted with subscript c, and ideal, noncondensable gases (mixture of CO_2, CO, and H_2) denoted with the subscript d.

For a saturated water vapor atmosphere, the pressure exerted by the condensable is given by the Clausius-Clapeyron equation,

$$\frac{dp_s}{dT} = \frac{L_c(T)}{RT^2} p_s, \tag{253}$$

where p_s is the saturation vapor pressure and $L_c(T)$ is the latent heat of vaporization of the condensable, that is, H_2O in this case. Inserting this expression for $d\ln p_c/d\ln T$ into the formula given in Pierrehumbert (2010) leads to the pseudoadiabatic slope as used in this study, which is given by (see also Ding and Pierrehumbert, 2016)

$$\frac{d\ln P}{d\ln T} = \frac{p_s}{P}\frac{L_c(T)}{R_c T} + \frac{p_d}{P}\frac{c_{pd}}{R_d}\frac{1 + \left(\frac{c_{pc}}{c_{pd}} + \left(\frac{L}{R_c T} - 1\right)\frac{L}{c_{pd}T}\right) r_{\text{sat}}}{1 + \frac{L}{R_d T} r_{\text{sat}}}, \tag{254}$$

where c_{pd} and c_{pc} are the specific heat capacities of the noncondensable and condensable species, respectively. r_{sat} is the saturation mass mixing ratio, given as (Catling and Kasting, 2017)

$$r_{\text{sat}} = \epsilon f_{\text{sat}}(H_2O) = \epsilon \frac{p_{sat}}{P}. \tag{255}$$

Here, ϵ is the ratio of mass of condensable and noncondensable species, P is the total pressure, and f_{sat} is the volume mixing ratio of condensable at saturation. Eq. (254) reduces to Eq. (A13) of Kasting (1988) at $r_{\text{sat}} \rightarrow 0$. In this case, the atmosphere is dry and the temperature profile is obtained by the dry adiabatic lapse rate given by (from Eq. 254)

$$\frac{d\ln p_d}{d\ln T} = \frac{c_{pd}(T)}{R_d}, \tag{256}$$

where R_d is the gas constant for the noncondensable or the dry component of the mixture and is obtained by Eq. (277) of Appendix 3.3.8. When more than one noncondensable species is present, the mean molecular weight of the mixture of noncondensable is accounted for.

At temperatures that are high enough and for a condensable species reservoir much larger than the atmospheric pressure exerted by the dry gases such that $r_{\text{sat}} \gg 1$, $P \rightarrow p_{\text{sat}}$ and $p_d/P \rightarrow 0$, Eq. (254) reduces to the Clausius-Clapeyron relation (Pierrehumbert, 2010), which is valid for an ideal gas equation. The temperature dependence of the latent heat of vaporization $L_c(T)$ and saturation vapor pressure p_s of water cannot be neglected. For this, we used one of the most accurate formulations for calculating the saturation vapor pressure of water known as the Tetens formula (Tetens, 1930). This formula provides a very good approximation for the saturation vapor pressure of water with an error lower than $\sim 1\%$ (Huang, 2018) in the temperature range 0-100 °C and is given as follows:

$$p_s(T) = \begin{cases} p_s^{\mathrm{ref}} \exp\left(\frac{17.625T}{T+238.3}\right), & \text{if } T \geqslant 0 \\ p_s^{\mathrm{ref}} \exp\left(\frac{21.875T}{T+265.5}\right), & \text{otherwise.} \end{cases} \tag{257}$$

Here $p_s^{ref} = 610.78\,\mathrm{Pa}$ is the reference water vapor pressure at the triple point, and T is given in °C and equal to T- 273 for T in units of Kelvin.

Next the term c_{pc} in Eq. (254) is the temperature-dependent specific heat capacity of water adapted from Wagner and Pruß (2002) and applicable to high-temperatures conditions given by (also see Katyal et al., 2019)

$$\frac{c_{pc}(T)}{R_c} = 1 + n_3 + \sum_{i=4}^{8} n_i \frac{(\gamma_i \tau)^2 \exp(-\gamma_i \tau)}{[1 - \exp(-\gamma_i \tau)]^2}, \tag{258}$$

where $\tau = T_{\mathrm{c}}/T$ and T_{c} is the critical temperature (647 K). The values of the coefficients n_i and γ_i are taken from Table 6.1 of Wagner and Pruß (2002). The total heat capacity of the dry mixture c_{pd} is calculated as a linear combination of individual heat capacities of the noncondensable species weighted by their volume mixing ratios. The total c_p is thus the sum of specific heat capacity of moist and dry component, weighted by the respective volume mixing ratios, and is given by

$$c_p(T) = \frac{\sum_i x_{di} c_{pdi}(T) + \sum_i x_{vi} c_{pci}(T)}{\sum_i x_{di} + \sum_i x_{ci}}, \tag{259}$$

which is valid for temperatures in the range 200-2000 K. The denominator in this equation is equal to 1 for our case. The specific heat capacity of dry gases such as CO_2, CO, and H_2 is derived from the Shomate equation (Parks and Shomate, 1940) in units of kJ/kg K,

$$c_p = A + BT + CT^2 + DT^3 + E/T^2, \tag{260}$$

where the coefficients $A, B, C, D,$ and E are taken from Chase (1999) and T = Temperature/1000 K for the temperature range valid between 298-6000 K. For temperatures below 298 K, the specific heat capacities of CO, CO_2 , and H_2 are taken from analytical expressions based on a least-squares fit of data from Lide (2000). The specific heat capacity as a function of temperature in the range 200-3000 K for the four gases we considered is shown in Fig. 39.

In order to obtain the temperature profiles, we followed the same procedure as in Katyal et al. (2019) , that is, for surface temperatures $T_s > 647$ K, we used the dry adiabatic lapse rate (Eq. 256) by assuming a fixed surface temperature and pressure at the bottom of the atmosphere (Eq. 250). The temperature profile follows the moist adiabatic lapse rate (second term in Eq. 254) when the dry adiabatic lapse rate intersects

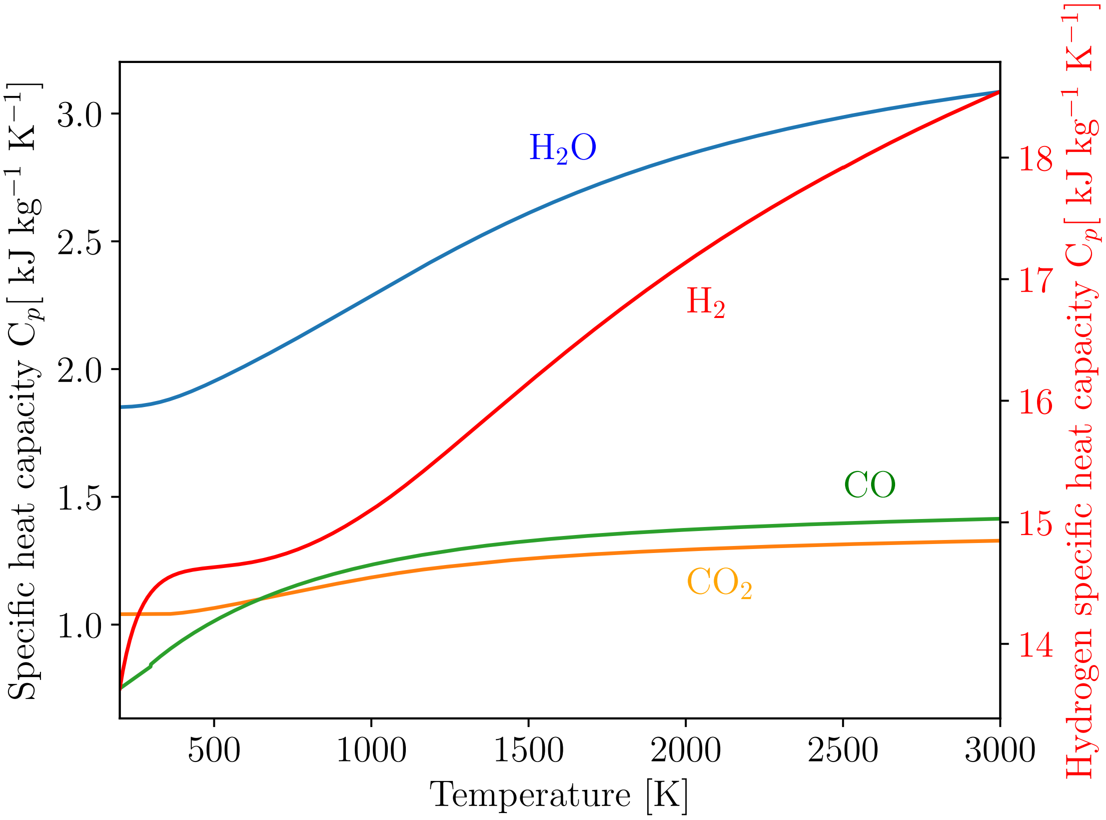

Figure 39: Specific heat capacities as a function of temperature for volatile species H_2O, CO, and CO_2 on the left x-axis and H_2 on the right x-axis as obtained from the Shomate equation described in the main text.

with the moist adiabatic lapse rate. The related work of Katyal et al. (2019) calculated temperature profiles with only one gas species, that is, H_2O, in the atmosphere. We have additionally included CO_2, CO, and H_2 calculated from the volatile speciation model described in Sect. 3.3.3. Our model accounts for the convective processes in the atmosphere up to an altitude corresponding to the top of the atmosphere pressure $p_{\mathrm{ToA}} = 0.1$ Pa (similar to Pluriel et al. (2019)). The atmospheric layers are vertically spaced in log pressure coordinates. When the temperatures in the dry/moist adiabat fall below 200 K, the temperature structure in our calculations follows an isothermal profile with a constant tropospheric temperature of 200 K.

Radiative transfer code. The generic atmospheric radiation line-by-line infrared code (GARLIC; Schreier et al. (2014)) was used to compute thermal emission and transmission spectra from 10 to 30,000 cm^{-1} with p,T and the composition of the atmosphere as the input. A detailed description of the radiative transfer code is also available in Katyal et al. (2019). For the verification and validation of GARLIC, see Schreier et al. (2018a,b). The absorption coefficients were calculated line-by-line (lbl) for H_2O, CO_2, H_2, and CO from the HITRAN2016 database (Gordon et al., 2017). Table 11 shows the list of various molecules and sources for the continuum available and relevant for this study.

Molecule	Continuum
$H_2 - H_2$	Abel et al. (2011)
$CO_2 - CO_2$	Baranov (2018)
H_2O_{self}	MT_CKD_2.5$^{(a)}$
H_2O_{foreign}	MT_CKD_2.5$^{(a)}$
$CO_{2\ \mathrm{foreign}}$	MT_CKD_2.5$^{(a)}$

Table 11: List of continua from the HITRAN CIA list $^{(a)}$; www.hitran.org/cia/ (Karman et al., 2019) and http://rtweb.aer.com/continuum_frame.html (Mlawer et al., 2012).

Table 12: List of measured reference Rayleigh cross sections $\sigma_{0,i}$ and central wavelengths $\lambda_{0,i}$ for the molecules.

Molecule	$\sigma_{0,i}$ [cm^2]	$\lambda_{0,i}$ [μm]	Reference
CO_2	$12.4 \cdot 10^{-27}$	0.53224	Sneep and Ubachs (2005)
CO	$6.19 \cdot 10^{-27}$	0.53224	Sneep and Ubachs (2005)
H_2	$1.17 \cdot 10^{-27}$	0.5145	Shardanand and Rao (1977)

Rayleigh scattering by molecule H_2O was obtained using the formalism described in Murphy (1977) (also see Scheucher et al., 2020). For other molecules such as CO_2, CO, and H_2, we have used the Rayleigh cross sections using the formalisms of Sneep and Ubachs (2005) and Shardanand and Rao (1977) across the whole spectrum in units of cm^2/molecules expressed as

$$\sigma_{\mathrm{Rayleigh,i}}(\lambda) = \sigma_{0,i} \left(\frac{\lambda_{0,i}}{\lambda}\right)^{\alpha}. \tag{261}$$

Here, $\alpha = 4$, $\sigma_{0,i}$ and $\lambda_{0,i}$ are the reference cross sections and wavelengths for the various molecules used in this study that are listed in Table 12.

To mimic optically thick clouds in our simulations (Section 3.3.6), we assumed clouds were present throughout the atmosphere (Kaltenegger and Traub, 2009) with the uppermost cloud deck coinciding with the lowermost $T = 200$ K altitude. The cloud-scattering cross section is expressed in a similar formalism as Eq.(261), but with $\alpha = 0$. This therefore acts as a scaling term with no wavelength dependence. For reference, the terrestrial aerosol-scattering cross section is about 10^{-27} cm^2 (Moran et al., 2018). That study (Moran et al., 2018) ruled out haze-scattering cross sections smaller than 9×10^{-25} cm^2 to 3σ and 3×10^{-23} cm^2 to 1σ. Therefore we assumed a cloud cross section $\sigma_{\mathrm{cloud}} \equiv \sigma_{0_i} = 6 \times 10^{-25}$ cm^2 , that is, 6×10^2 times larger than the Earth-scattering cross section in our simulations as presented in Section 3.3.6.

The aerosol optical depth integrated along the path is then given by

$$\tau_{\mathrm{aerosol}} = \sigma_{\mathrm{aerosol}} \cdot N_z, \tag{262}$$

where N_z is the column density of the molecular species in units of molecules cm^{-2} (see also Kaltenegger and Traub, 2009; Yan et al., 2015).

As a first step, we performed convective-radiative calculations without coupled chemistry similar to previous modeling studies of the magma ocean period. For future work, we plan to include the effect of chemical equilibrium in the lower atmospheric layers by applying the self-consistent convection-climate-photochemistry column model (Scheucher et al., 2020; Wunderlich et al., 2020) to the magma ocean period in order to study the effect upon transmission and thermal emission spectra and atmospheric escape, for example.

Transmission spectra. The volatile chemical speciation model along with the atmospheric model described in Sections 3.3.3-3.3.3 applicable to the early Earth magma ocean phase can be used to characterize exoplanets in the magma ocean phase (see Figure 12 of Nikolaou et al., 2019), for instance, to detect the spectral features and obtain the vertical extent of the atmosphere observationally. We used a well-established diagnostic tool, transmission spectroscopy, to probe the molecular composition of exoplanetary atmospheres. It provides the effective height of the atmosphere as a function of wavelength (see, e.g., Benneke and Seager, 2012).

In GARLIC, the theoretical transmission spectrum is expressed as the effective height of the atmosphere given as follows (Kaltenegger and Traub, 2009; Schreier et al., 2018b; Katyal et al., 2019):

$$h(\lambda) = \int_0^\infty A(z,\lambda)\ dz = \sum_i A_i(\lambda)\ \Delta h_i, \tag{263}$$

where $A_i = 1 - \mathcal{T}_i$ is the absorption along the ith incident ray with a transmission $\mathcal{T}_i$ that traverses through the (exo)planetary atmosphere tangentially at a height h_i and continues to travel to the observer at Earth.

The atmospheric transit depth, t_{atm} is given by (Wunderlich et al., 2020)

$$t_{\text{atm}}(\lambda) = \frac{(R_p + h(\lambda))^2}{R_s^2} - \frac{R_p^2}{R_s^2}, \tag{264}$$

where R_{p} is the planetary radius, and R_{s} is the stellar radius.

Atmospheric escape. For the atmospheric escape of H_2, we considered hydrodynamic fluxes of escaping H_2, possibly diffusion-limited at the homopause $\sim$ 100 km, in the presence of a static background atmosphere, similar to the approach of Kuramoto et al. (2013); Zahnle and Catling (2017) and Zahnle et al. (2019).

At higher levels above the homopause, where the escaping H_2 gas is accelerated as a result of the absorption of stellar high-energy photons, hydrogen exists mainly in atomic form.

For the quantitative implementation of the escape fluxes, we relied on Zahnle et al. (2019), who solved the hydrodynamic, possibly diffusion-limited, problem in the atmosphere. In particular, we used their Eq.

3, which parameterizes the transition from energy-limited escape to diffusion-limited escape. Diffusion-limited escape becomes effective when the atmosphere is more strongly irradiated and the escaping hydrogen cannot be replenished from below the homopause.

The diffusion-limited flux ϕ_{dl} generally provides an upper limit to the escape of lighter species such as hydrogen in a background heavier and stationary gas. The escape rate for H_2 can be written as (Hunten, 1973)

$$\phi_{dl} = b_{aj}\, f_{\mathrm{tot}}(\mathrm{H_2}) \left(\frac{1}{H_a} - \frac{1}{H_{\mathrm{H_2}}} \right), \tag{265}$$

where b_{aj} is the binary diffusion coefficient between the background heavier gas a such as CO_2, CO and H_2O and the escaping gas H_2. Here, $f_{\mathrm{tot}}(\mathrm{H_2})$ is the hydrogen volume mixing ratio (VMR) at the homopause. H_a and $H_{\mathrm{H_2}}$ represent the unperturbed scale heights ($= kT/mg$) of the heavier gas a and the escaping gas H_2 at the homopause, respectively. We consider H_2 as the dominant H-bearing species, that is, $f_{\mathrm{tot}} \equiv f(\mathrm{H_2})$. The binary diffusion coefficients b_{aj} for H_2 in CO and CO_2 are roughly similar and taken to be $3 \times 10^{21}\ \mathrm{m^{-2}\ s^{-1}}$ (Marrero and Mason, 1972). We validated the escape rate obtained for the current Earth using Eq. (265). The total hydrogen VMR was taken to be $f_{\mathrm{tot}}(\mathrm{H_2}) = 7.15$ ppm with the background-dominant gas as N_2. The diffusion coefficient between the H_2 and N_2, b_{aj} of $1.7 \times 10^{21}\ \mathrm{m^{-2}\ s^{-1}}$ was taken from Hunten (1973). We verified that the diffusion-limited escape of H_2 is $\sim 1.5 \times 10^{12}\ \mathrm{H_2\ molecules\ m^{-2}\ s^{-1}}$, as also reported by Hunten and Donahue (1976). In terms of the loss of H-atoms to space, this is equivalent to a mass-loss rate of ~3 kg/s.

The energy-limited flux was obtained as the ratio of stellar XUV energy incident upon the planet and the energy required to lift a given mass out of the Earth potential well and into the space. The mass-loss rate of hydrogen using the energy-limited formula (Watson et al., 1981) for hydrodynamic escape (also see Koskinen et al., 2014; Hamano et al., 2015) is given by

$$\dot{M}_{\mathrm{el}} = \frac{\pi \epsilon R_p R_{\mathrm{XUV}}^2 F_{\mathrm{XUV}}(t)}{G M_p}\ \mathrm{g\ s^{-1}}, \tag{266}$$

where R_{XUV} is the radial distance at which the XUV energy from the star is deposited, and satisfies $R_{\mathrm{XUV}} > R_p$, and ϵ is the heating efficiency < 1. Upon assuming $R_{\mathrm{XUV}} \equiv R_p$ (Zhang, 2020), this equation can be written as

$$\dot{M}_{\mathrm{el}} = \frac{\pi \epsilon R_p^3 F_{\mathrm{XUV}}(t)}{G M_p}\ \mathrm{g\ s^{-1}}. \tag{267}$$

Here, R_{p} is the Earth radius (6.4×10^8 cm), M is the mass of Earth (5.4×10^{27} gm), G is the gravitational constant ($6.67 \times 10^{-8}\ \mathrm{cm^3\ g^{-1} s^{-2}}$), $F_{\mathrm{XUV}}(t)$ is the time-evolving flux from the host star at XUV wavelengths at 1 AU obtained by the relation $F_{\mathrm{XUV}}(t) = 5(4.5/t)^{1.24}$ in units of $\mathrm{erg\ cm^{-2} s^{-1}}$, where t is the age of the Sun in billion years (Zahnle et al., 2019), and ϵ is taken to be 0.5 to be consistent with Zahnle et al. (2019). Owing to the fast temporal evolution in the XUV output of the young Sun (related to whether it was a fast, moderate, or slow rotator), the S value defined as $S(t) \equiv F_{\mathrm{XUV}}/F_{\mathrm{XUV}\odot}$ can range between 10 and 100 during the Hadean (Tu et al., 2015; Lammer et al., 2018). The lifetime of H_2 atmospheres on early Earth is calculated as the ratio of mass-loss rate (Eq. 267) to the total mass of H_2 in grams, m_{H_2} , in the atmosphere as

$$t \sim \left[\frac{G}{\epsilon\pi}\right]\left(\frac{M_p}{R_p^3}\right)\frac{m_{\mathrm{H}_2}}{F_{\mathrm{XUV}}}. \tag{268}$$

Zahnle et al. (2019) have shown that the diffusion-limited escape applies to conditions of higher levels of irradiation, whereas energy-limited escape may be a better approximation for lower levels of irradiation. Building upon their findings, we assumed that the flux is given by the expression

$$\phi_{\mathrm{H}_2} = \frac{1 \times 10^{12} f_{\mathrm{H}_2} S}{\sqrt{1 + 0.006S^2}} \text{ molecules cm}^{-2}\text{s}^{-1}, \tag{269}$$

which is a good fit to their figure 5 if the VMR of H_2 is lower than 0.2.

The hydrogen mass-loss dM (in grams) due to escape at a particular time step dt is approximated as follows:

$$dM = 4\pi R_p^2\, \phi_{\mathrm{H}_2} m_{\mathrm{H}_2}\, dt. \tag{270}$$

Here, m_{H_2} is the mass of H_2 in grams per molecule, and ϕ_{H_2} is the escaping flux from Eq. (265) or Eq. (269).

The actual radius contribution in Eq. (267) and Eq. (270) comes from the sum of the radius of the planet and height of the exobase, that is, $(R_p{+}H_e)$. The height of the exobase, H_e , is given by the altitude level where the Lyman-edge opacity of hydrogen becomes 1. For the scenario presented in Section 3.3.5, we obtain that $(R_p{+}H_e) \sim R_p$ (calculation not shown here).

3.3.4 Volatile outgassing scenarios

We used three main scenarios in this work. Scenario 1 is for a surface temperature of 3300K and surface pressure of 76.7 bar, that is, at the beginning of the magma ocean (BOM) period, as shown in Figure 38 (top) and Table 13. Scenario 2 is similar to scenario 1, but for a surface temperature of 1650 K and pressure of 395 bar, that is, at the end of the magma ocean (EOM) period, as shown in Figure 38 and Table 14. The conditions where the MO phase ends are $T_s = 1650$ K at a solidification timescale of ∼ 1 Myr according to the coupled interior-atmospheric model results of Katyal et al. (2019) and Nikolaou et al. (2019). Previously, a coupled atmospheric-interior model by Salvador et al. (2017), which was applied around the MO phase, delivered P-T conditions with a similar H_2O-CO_2 composition as this study.

Scenario 3 is for representative cases taken from the study of Pluriel et al. (2019), as shown in Table 15 referring to an H_2O dominated and a CO_2 dominated atmosphere. Scenarios 1 and 2 cover a representative range of P, T, and mantle oxidation state during the MO period. The buffers in the three scenarios were chosen to represent the mantle redox state, ranging from reducing to oxidizing.

Our choice of three scenarios (with varying initial volatile abundances of H_2O and CO_2) and varying mantle fugacity, hence leading to different atmospheric compositions, is motivated by previous works in the literature that also explored the effect of composition by varying key species such as H_2, CO, CO_2, H_2O for magma ocean studies (Katyal et al., 2019; Nikolaou et al., 2019; Bower et al., 2019), Venus-type planets with CO_2 dominated atmosphere (Hamano et al., 2013; Pluriel et al., 2019), pure steam-dominated atmosphere (Katyal et al., 2019; Schaefer et al., 2016; Hamano et al., 2015), and the effect of adding H_2 to the atmosphere of early Mars (Ramirez et al., 2014).

Table 13: Scenario 1 (BOM) for the three cases (1.1, 1.2, and 1.3). Columns 2 and 3 show the initial assumed mole fractions arising from H_2O and CO_2 outgassing, which is the input to the speciation model. The assumed buffer values for strongly reducing (IW-4), reducing (IW), and highly oxidizing (IW+4) have been used to study the effect of speciation under these conditions. The four columns on the right shows final outgassed species from the speciation model. For these scenarios, the surface p, T setting is fixed to be $T_s = 3300$ K and $P_s = 76.7$ bar. The p_{boA} calculated from the new molecular weight of the atmosphere is also shown. Scenario 1.1 with IW+4 case resembles the p,T during the BOM as obtained by Nikolaou et al. (2019). The most dominant species in the atmosphere are marked in bold for each of the cases.

Scenario	Initial outgassing		P_s (bar)	Buffer	p_{boA} (bar)	Final outgassing			
	$f^{init}_{H_2O}$	$f^{init}_{CO_2}$				f_{CO_2}	f_{H_2O}	f_{H_2}	f_{CO}
1.1	0.05	0.95	76.7	IW-4	48	0.0018	0.0007	0.049	**0.94**
				IW	53.2	0.15	0.029	0.02	**0.79**
				IW+4	75.3	**0.90**	0.049	0.000	0.046
1.2	0.75	0.25	76.7	IW-4	27.1	0.000	0.01	**0.74**	0.25
				IW	51	0.040	**0.44**	0.30	0.20
				IW+4	75.8	0.24	**0.74**	0.005	0.0122
1.3	1.0	0.00	76.7	IW-4	9.5	0.0	0.014	**0.98**	0.00
				IW	49.1	0.00	**0.60**	0.40	0.00
				IW+4	76.2	0.00	**0.99**	0.0069	0.00

Table 14: Same as Table 13, but for scenario 2 (EOM), investigating the effect of speciation under these conditions. The surface p,T setting is fixed at $T_s = 1650$ K and $P_s = 395$ bar. Scenario 2.2 with IW+4 resembles the p,T at the EOM, as obtained by Nikolaou et al. (2019).

Scenario	Initial outgassing		P_s (bar)	Buffer	p_{boA} (bar)	Final outgassing			
	$f^{init}_{H_2O}$	$f^{init}_{CO_2}$				f_{CO_2}	f_{H_2O}	f_{H_2}	f_{CO}
2.1	0.05	0.95	395	IW-4	247.5	0.003	0.0005	0.049	**0.94**
				IW	283.7	0.22	0.025	0.025	**0.72**
				IW+4	390.4	**0.92**	0.05	0.000	0.03
2.2	0.75	0.25	395	IW-4	139	0.0007	0.007	**0.74**	0.25
				IW	248	0.058	**0.37**	**0.37**	0.19
				IW+4	391	0.24	**0.74**	0.007	0.007
2.3	1.0	0.0	395	IW-4	47.3	0.00	0.009	**0.99**	0.00
				IW	219	0.00	**0.50**	**0.50**	0.00
				IW+4	391.5	0.00	**0.99**	0.0099	0.00

Table 15: Scenarios showing the output from the volatile speciation model applied to scenario 3.1, H_2O-dominated atmosphere and scenario 3.2, CO_2-dominated atmosphere at fixed $T_s = 1500$ K for two different surface pressures. The atmospheric pressure p_{boA} shown above is recalculated based on the new molecular weight of the outgassed species. The initial and final outgassed species are shown as mole fractions. The most dominant species in the atmosphere are marked in bold in each case.

Scenario	Initial outgassing		P_s (bar)	Buffer	p_{boA} (bar)	Final outgassing				Reference
	$f^{\mathrm{init}}_{\mathrm{H_2O}}$	$f^{\mathrm{init}}_{\mathrm{CO_2}}$				$f_{\mathrm{CO_2}}$	$f_{\mathrm{H_2O}}$	$f_{\mathrm{H_2}}$	f_{CO}	
3.1	0.66	0.33	300	None	300	0.33	0.66	-	-	Pluriel et al. (2019)
				IW	191.8	0.083	0.311	**0.35**	0.24	
				IW+4	297	0.32	**0.66**	0.006	0.007	
3.2	0.02	0.98	510	None	510	0.98	0.02	-	-	Pluriel et al. (2019)
				IW	371.2	0.25	0.009	0.01	**0.73**	
				IW+4	504.7	**0.95**	0.019	0.0	0.023	

3.3.5 Results

Temperature profiles. Figures 40 and 41 show the pressure-temperature (p-T) and altitude-temperature (z-T) profiles obtained using the convection lapse-rate formulation as described in Section 3.3.3 for scenarios 1 and 2 as shown in Tables 13 and 14, respectively. In Figure 40 scenario 1.1 (95% initial CO_2, 5% initial H_2O, top left panel, p-T), the results suggest a dry adiabat in the lower unsaturated troposphere that is related to the high surface temperature. The green curve (oxidized buffer case) adiabat is steeper in this region than the blue and orange curves because it is CO_2-dominated, leading to a low heat capacity (Figure 39) and accordingly to a steeper calculated lapse rate (equation 256). This steep slope results in the green curve that intersects the saturated vapor curve (dashed red line) at lower pressures than for the blue and orange curves, which have lower CO_2 but more CO and H_2O (Table 14) owing to higher heat capacities (Figure 39) and therefore shallower dry lapse rates (equation 256).

In Figure 40 for z-T (top right panel), the green curve features the lowest atmospheric height (geometric thickness) due to its larger atmospheric molecular weight and therefore smaller scale height than the other, lighter atmospheres shown by the orange and blue curves. Above the dry adiabat regime (e.g., above about 320 km for the orange line), the slope steepens corresponding to the wet adiabat as temperatures are low enough to allow for condensation. In the uppermost atmosphere, a fixed iso-profile temperature ($T = 200$ K) (e.g., occurring above about 380 km for the orange line) is imposed in our model for the radiative regime, thereby following other studies (Lupu et al., 2014; Pluriel et al., 2019; Katyal et al., 2019).

In the middle and lower panels of Figure 40, the initial H_2O (CO_2) amounts are increased (decreased) (see scenarios 1.2 and 1.3 in Table 13), which leads to light, hydrogen-dominated atmospheres for the reduced buffer cases. Because H_2 has a heat capacity between that of H_2O and CO_2 **or** CO (Figure 39), the green slope in the middle and lower left panels is now closer to the blue and orange slopes compared with the upper panel because the difference in heat capacities is now smaller.

In the middle and lower right panels, results suggest extended scale heights for highly reduced atmospheres with dominant H_2 (e.g., scenario 1.3, IW-4) because its molecular weight is lower than that of oxidized species such as H_2O or CO_2 in the atmospheres (e.g., scenario 1.1 and 1.2, IW+4) and subsequently the change in altitude range of the figure is notable.

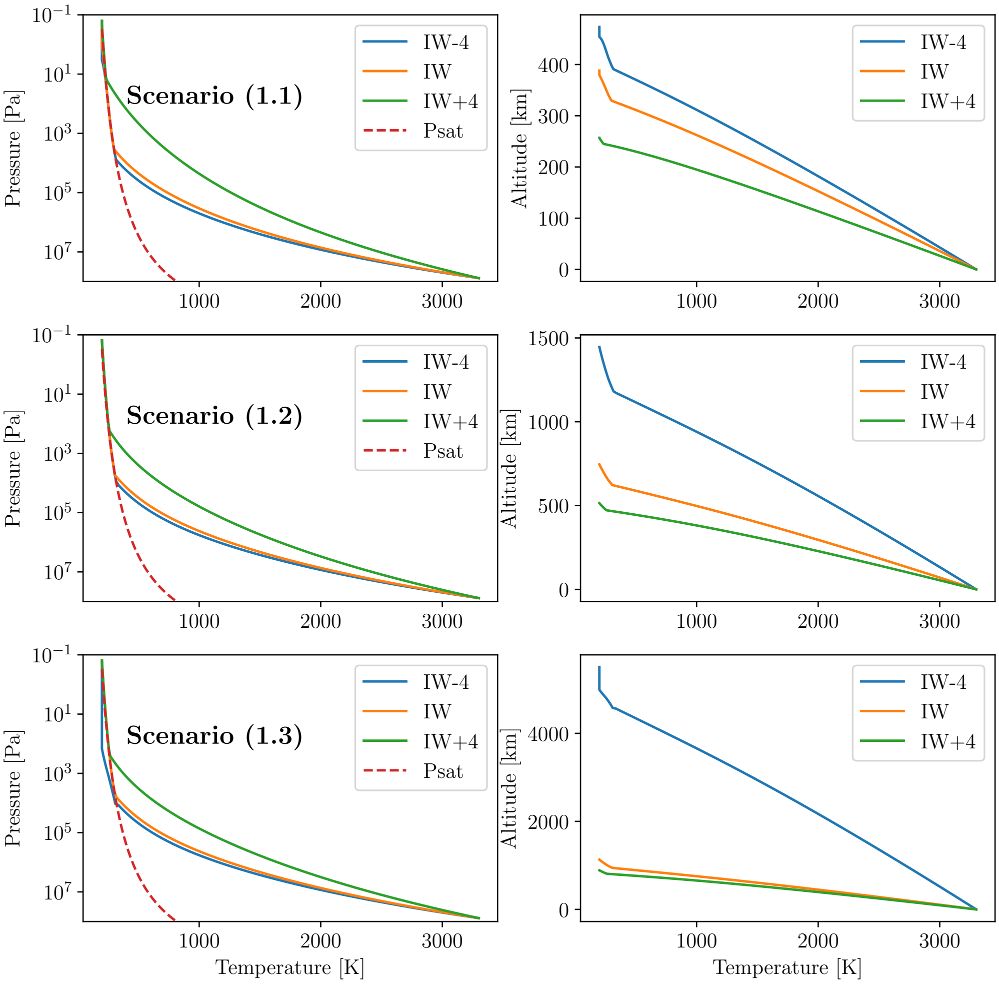

Figure 40: *Left:* Pressure-temperature profiles for the BOM scenarios 1.1 (upper), 1.2 (middle), and 1.3 (lower panel) for three different buffers IW-4, IW, and IW+4. The dashed red line represents the saturation water vapor curve. Pressures at the bottom of atmosphere values are taken from Table 13. *Right*: Altitude-temperature profiles for scenarios 1.1 (upper), 1.2 (middle), and 1.3 (lower panel). We note the different altitude ranges for the panels on the right.

Figure 41 illustrates the EOM scenarios (Table 14). Compared with the earlier BOM case (Figure 40) with a surface temperature of 3300 K, the surface temperature for the EOM scenario has cooled to 1650 K and the surface pressure has increased from 76.7 bar (BOM) to 395 bar (EOM). The cooler temperatures generally favor the formation of chemical species with weaker bond dissociation energies, that is, H_2 (4.52 eV) over H_2O (5.1 eV) and CO_2 (5.51 eV) over CO (11.1 eV) (where eV denotes electron Volt), which is consistent with the changes produced by the chemical speciation model (compare Table 14 with Table 13). Larger changes of up to a few dozen percent in the species mole fraction occur for scenario 2.2 compared with scenario 1.2, in which the relative amount of C-H-O (0.75:0.25 for H_2O:CO_2) is the most similar.

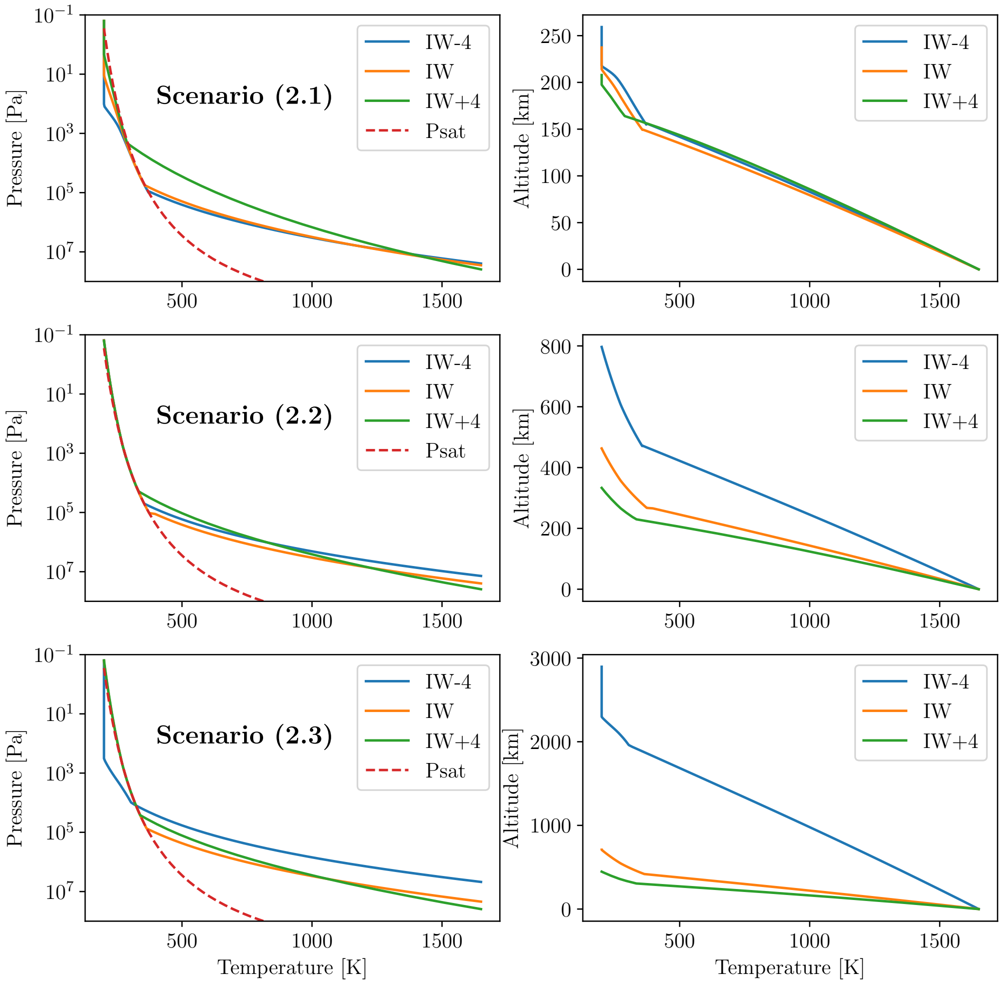

Figure 41: Same as Fig. 40, but for p, T conditions and scenarios as summarized in Table 14, representing the EOM.

Figure 41 (EOM) shows modest changes in comparison to Figure 40 (BOM), which are associated with the change in p,T and corresponding changes in speciation and heat capacity, hence in the slope of the adiabats. The altitude decrease is mainly associated with the decrease in temperature.

Figures 40 and 41 show that (1) the transition between dry and moist adiabat (slope change) always appears to be located on the saturation curve P_{sat} and it effectively occurs at lower temperature than the saturation temperature (for similar pressure); and (2) for $f_{H_2O} \geqslant 0.1$ in the atmosphere, the moist adiabat always coincides with the water vapor saturation curve P_{sat}.

Figure 42 shows the temperature-pressure profiles obtained for scenarios 3.1 (upper panel) and 3.2 (lower panel) with H_2O and CO_2 dominated atmospheres of Table 15, respectively. In the case of scenario 3.1 with its initially H_2O-dominated atmosphere (Fig. 42 upper panel), for the reducing buffer IW case, the gradient of the dry adiabatic lapse rate is slightly reduced (orange line) due to chemical speciation of H_2 and CO as compared to the ”no speciation” case (blue line). However, for an oxidizing buffer IW+4

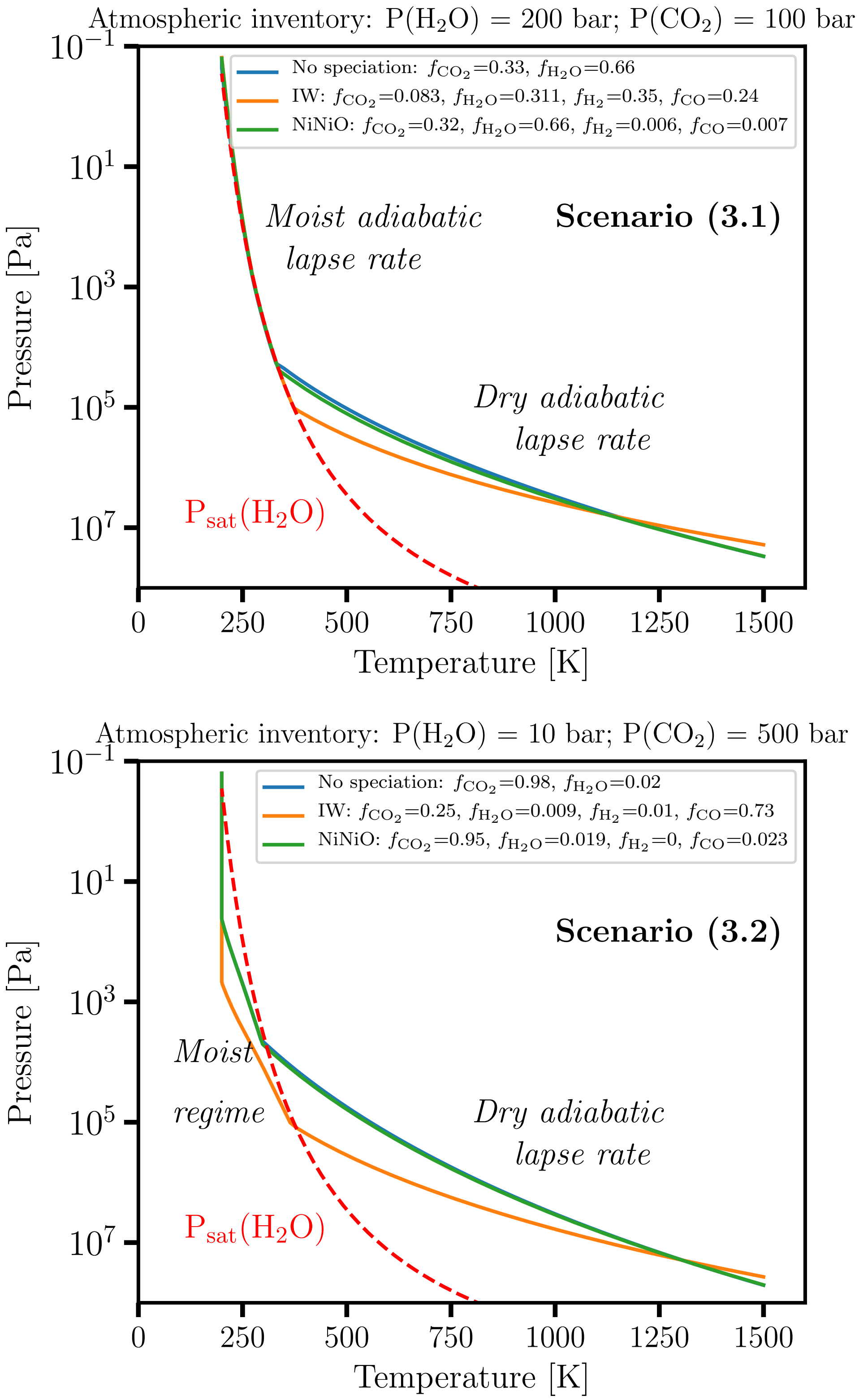

Figure 42: Temperature profiles p-T for scenario 3.1 (upper panel) with an initially H_2O-dominated atmosphere and scenario 3.2 (lower panel) with an initially CO_2-dominated atmosphere (Table 15). The molar fraction of each species is shown in the legend. "No speciation" indicates that the values were input directly by the user and were not calculated by the C-O-H speciation model.

(green line), the dry adiabatic lapse rate is similar to the case for "no speciation" because the volume mixing ratio of outgassed species is similar to the initial volatile outgassing. In Fig. 42, scenario 3.2 (lower panel), the chemical speciation of the initially assumed CO_2-dominated atmosphere (see Table 15), leads to a CO-rich (IW buffer) and CO_2-rich (IW+4 buffer) atmosphere. Thus, the moist adiabatic lapse rate changes as compared to the upper panel results and shows a deviation from pure water vapor saturation curve (dotted red line). This is because of a low water vapor volume mixing ratio $f_{H_2O} = 0.02$ and a higher CO_2 volume mixing ratio $f_{CO_2} = 0.98$, leading to an unsaturated troposphere. Moreover, the vertical range of the wet adiabat regime (scenario 3.2) is smaller than in scenario 3.1 (upper panel), and the radiative regime ($T = 200$ K isothermal profile) is evident at 40 Pa, for instance, for the green curve (lower panel) but occurs near the top of the atmosphere, that is, around 0.1 Pa, for scenario 3.1. The differing behavior in scenario 3.2 compared with scenario 3.1 arises mainly from the different chemical speciation (see panel legends), which affects the heat capacity and therefore the adiabatic gradients.

Thermal spectral emission. Using the temperature profiles as obtained in Fig. 40, Fig. 41 and composition of various species for various scenarios of Table 13 and Table 14 as input to the line-by-line (lbl) radiative transfer code GARLIC, we obtain the thermal spectral emission from the atmosphere, also known as the outgoing longwave radiation (OLR). Figure 43 shows the thermal emission spectra of scenario 1.1 (upper), 1.2 (middle), and 1.3 (lower) panel of Table 13 for the BOM. The spectral features that arise due to the presence of reduced species such as CO versus the oxidized species such as H_2O and CO_2 are easily distinguishable in the three panels. In the top panel of Fig. 43 (scenario 1.1), a prominent CO absorption feature is seen at 2.3 and 4.6 μm for the reduced buffer case IW-4 (blue curve), whereas distinct CO_2 features at 2.1, 4.3 and 15 μm are seen for the oxidized buffer case IW+4 (green curve). When the input H_2O outgassing value is increased (scenario 1.2), stronger H_2O features start to appear (orange and blue curves) along with the CO_2 absorption features for the oxidized buffer (green curve). Finally, when the input H_2O outgassing is increased to 100% (scenario 1.3), we obtain thermal spectra that are dominated by water vapor with distinct water features between 1 to 2.6 μm and at 6.2 μm for the oxidized case (green curve). The reduced atmosphere with IW-4 buffer produces an almost pure H_2 atmosphere with a similar spectrum as H_2O but with a higher emitted flux.

Figure 44 shows the thermal emission spectra of scenario 2.1 (upper), scenario 2.2 (middle), and scenario 2.3 (lower) of Table 14 for the EOM. One notable difference between Fig. 43 and Fig. 44 is a significant reduction in the emitted flux especially at the smaller wavelengths, which is mainly related to the lower surface temperature (i.e., 1650 K) for the latter. The effect of pressure at the bottom of the atmosphere on the thermal spectra is also seen and is discussed in detail in Section 3.3.5. The effect of the large H_2 continuum at 5-7 μm caused by self-collision of the H_2 molecules could reveal molecular H_2 as a main constituent of an atmosphere not known a priori.

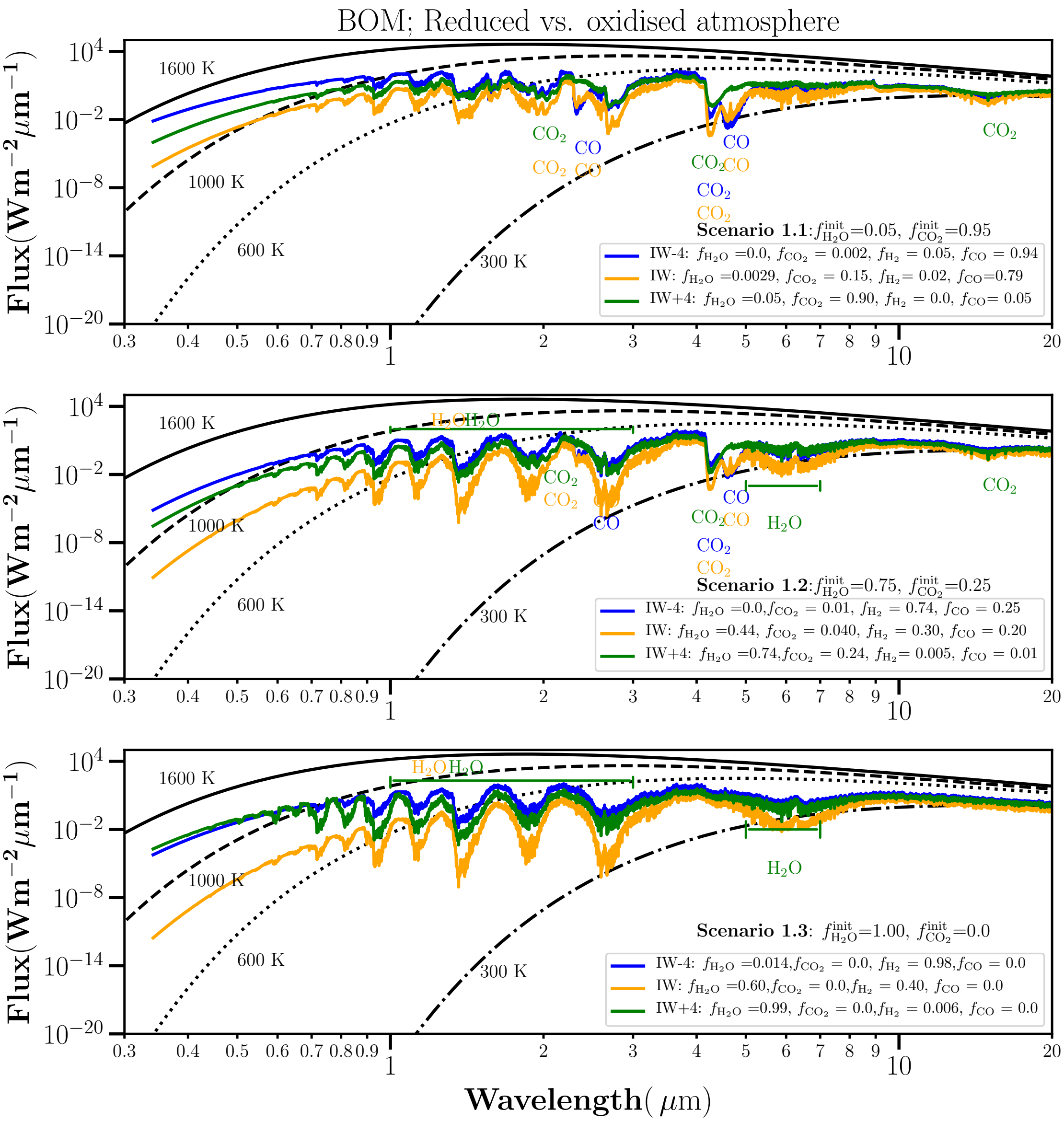

Figure 43: Comparison of thermal emission spectra for a reduced vs. an oxidized mantle during the BOM presented for scenario 1.1 (upper panel), 1.2 (middle panel), and 1.3 (lower panel) of Table 13. The output of the volatile speciation model is shown in the legend. Values written above the legend show the initial input values to the speciation model. Reference blackbody curves for four different temperatures are plotted. Absorption features of key chemical species are indicated. The spectra shown here have been binned to a resolution of $\lambda/\Delta\lambda = 1000$.

Figure 45 compares the thermal emission spectra for reduced atmospheres overlying a reducing buffer (IW-4) for the various scenarios 2.1, 2.2, and 2.3 of Table 14. In this figure, the prominent absorption features are seen for CO at 2.3 and 4.6 μm, while CO_2 stands out at 2.1, 4.3, and 15 μm. A small amount of CO_2 is always present even for this very reducing buffer calculated by the mass-equilibrium method (Sect. 3.3.3). However, the strength and width of CO_2 absorption features are seen to decrease as the

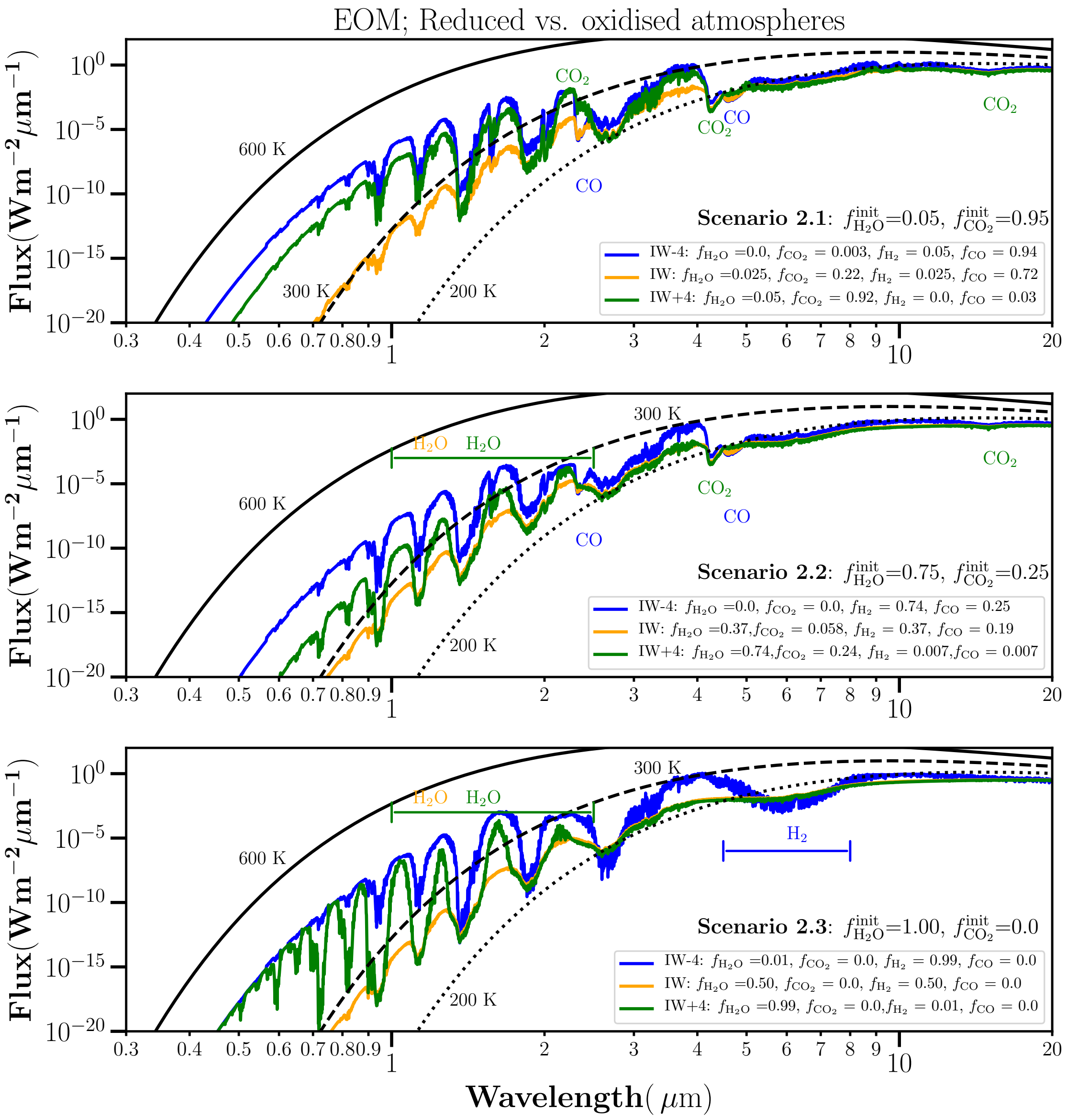

Figure 44: Same as Fig. 43, but for scenarios of Table 14. The blackbody curves for three different surface temperatures bracketing the emission spectra are plotted for reference.

volume fraction of initial CO_2 decreases from 0.95 to 0.0 (see the zoomed 15 μm feature in the right inset of Fig. 45). Another notable feature is visible in scenario 2.3 with pure H_2O (dissolved in the melt), which results in a H_2 -dominated atmosphere and displays a large continuum absorption in the 5-7 μm region caused by collision-induced absorption.

Figure 46 is same as Fig. 45, but now for the oxidizing atmosphere cases (IW+4) for scenarios 2.1, 2.2, and 2.3 of Table 14.

A reduction in the emitted flux is seen compared with the reduced atmosphere case (Fig. 45). This is because of enhanced absorption by higher concentrations of greenhouse gases such as CO_2 and H_2O that are present in the oxidized atmosphere. Thus, as the initial H_2O volume mixing ratio (VMR) increases (from scenario 2.1 through 2.3), a further reduction in the emitted flux is obtained. The most prominent absorption features are seen for CO_2 at 2.1, 4.3, and 15 μm and H_2O at 1.0, 1.2, 1.4, 1.9, and 2.6 μm, respectively.

As a result of the thick overlying steam atmosphere, the atmospheric window (8-10 μm) becomes optically thick and the 6.2 μm H_2O feature is not prominent (green curves in scenarios 2.2 and 2.3). The inset of this figure shows the zoomed-in 4.3 μm CO_2 feature. The CO feature at 4.6 μm is not seen here as compared to the reduced case in Fig. 45. The inset on the far right shows a zoomed-in view of the 15 μm CO_2 absorption band as a function of CO_2 VMR and indicates the change in band depths when the input CO_2 VMR is reduced from 0.95 to 0.25 (red to blue curve) and is then absent for the green curve with no CO_2. In summary, the main result is a diminishing of the CO band at 4.6 μm and the appearance of distinct H_2O bands from $\sim$ 1 - 2.6 μm. The H_2O feature at 6.2 μm is less prominent because of the thick steam atmosphere.

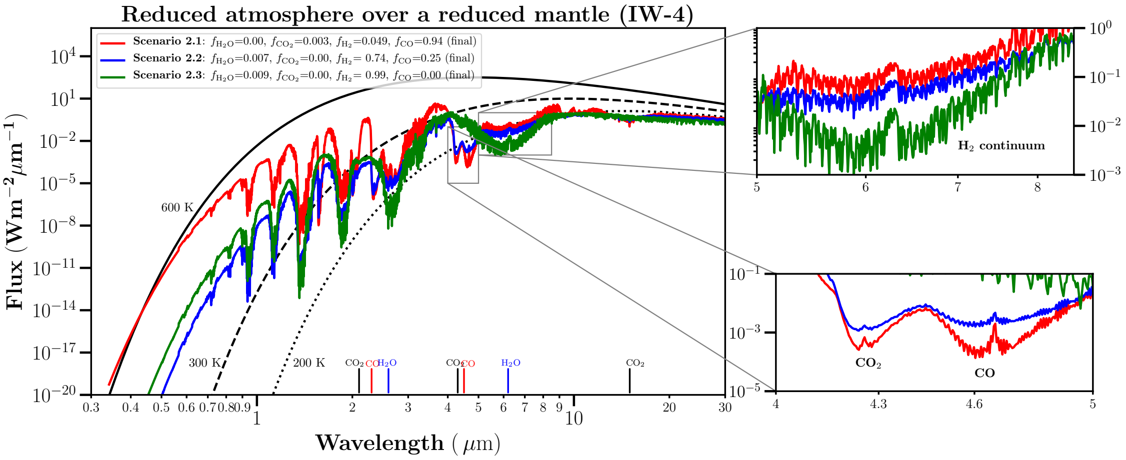

Figure 45: Thermal spectral emission for a reducing atmosphere overlying a reduced mantle (IW-4) for scenarios 2.1, 2.2, and 2.3 of Table 14. The legend shows the mole fraction of the outgassed species obtained from the speciation model. Prominent features of absorbing species are seen at wavelengths marked in the figure. Reference blackbody curves for three different surface temperatures are plotted. The insets show the zoomed-in thermal spectra with the most prominent absorption features of CO_2, CO and H_2. The spectra have been binned to a resolution of $\lambda/\Delta\lambda$ = 1000.

Dependence of OLR upon mantle fugacity. The thermal emission spectra were then averaged over the entire wavelength range to obtain the outgoing longwave radiation (OLR) as shown in Figure 47 (right panels). The variation in pressure at the bottom of atmosphere p_{boA} (using Eq. 250) for three different buffers is shown in Figure 47 (left panels). The details of the various cases for which we investigated the effect of speciation on the $p_{\rm boA}$ and subsequently on the OLR for the BOM and EOM are shown in Tables 17 and 18 of Appendix 3.3.8, respectively.

For the BOM (Fig. 47; top right panel) with T_s = 3300 K, the highest OLR is obtained for the most reduced atmosphere (blue curve; IW-4 buffer) because the absorption bands are weaker and the atmospheric

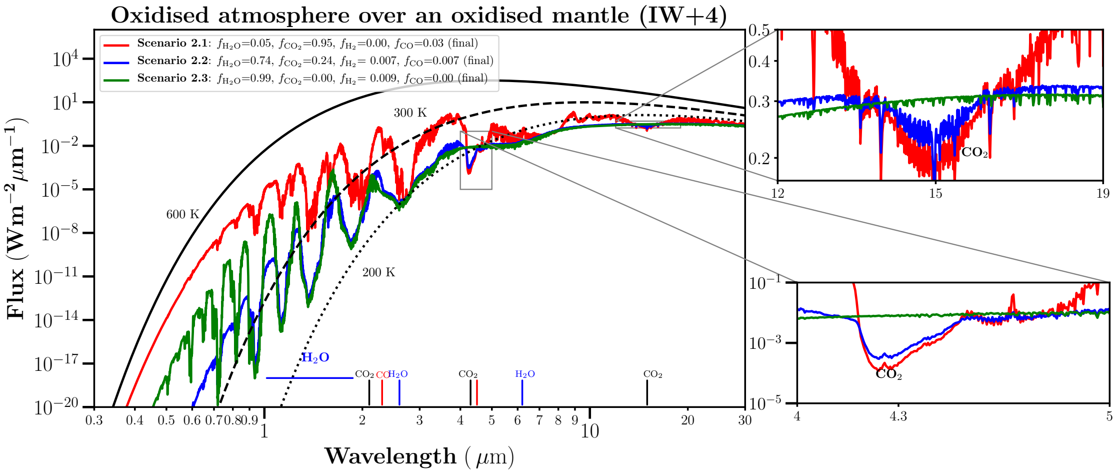

Figure 46: Same as for Fig. 45, but for an oxidizing atmosphere overlying an oxidized mantle (IW+4). Notable features are the emergence of prominent H_2O features between $1-2$ μm (scenario 2.3) and the disappearance of CO feature at 4.6 μm as compared to Fig. 45 (scenario 2.1 and 2.2).

pressures (top left panel) are lower than the IW buffer (orange curve), wherein a mix of reduced and oxidized species are present in the atmosphere (see Table 17) that contribute far more effectively to block radiation. It is interesting to note that even for the most oxidizing atmosphere (green curve; IW+4 buffer), less radiation is blocked by the atmosphere, which is mainly dominated by H_2O , than for the IW buffer.

At lower temperatures (Fig. 47; bottom right panel) with $T_s = 1650$ K (EOM), the emitted radiation is far lower than in the high temperature case ($T_s = 3300$ K) because for the latter, the radiation is emitted in the infrared and visible wavelengths, which leads to a stronger outgoing longwave radiation (OLR). Moreover, for the low temperature case ($T_s = 1650$ K), the OLR reaches a limit of $\sim$280 W/m^2 (Nakajima et al., 1992; Goldblatt et al., 2013; Marcq et al., 2017) for water-dominated atmospheres (green curve; IW+4 buffer) at $\sim$1800 K (also see Katyal et al., 2019). The calculated OLR does not drop below the OLR limit because of the impeding effect of absorption of radiation by H_2O even if present in moderate quantities. This is an important result that suggests that for a specific surface temperature, atmospheres with lower surface pressures ($\sim$4-200 bar) can lead to strong outgoing emission of radiation and therefore to a more effective cooling of the MO than for atmospheres with a high surface pressure (¿ 200 bar). Studying the effect of pressure on OLR in this manner is analogous to the effect of a threshold temperature as shown in Marcq et al. (2017). We also refer to Figure 10 of Nikolaou et al. (2019), where the OLR for pure steam atmospheres is plotted as a function of surface temperature and surface pressures. According to their Figure 10 and Katyal et al. (2019), higher OLR values are obtained for atmospheres with lower surface pressure (for a similar surface temperature). This means that the outgoing radiation for lower pressure cases may reach the OLR limit, but at temperatures lower than $\sim$ 1800 K as previously reported (Kopparapu et al., 2013; Katyal et al., 2019).

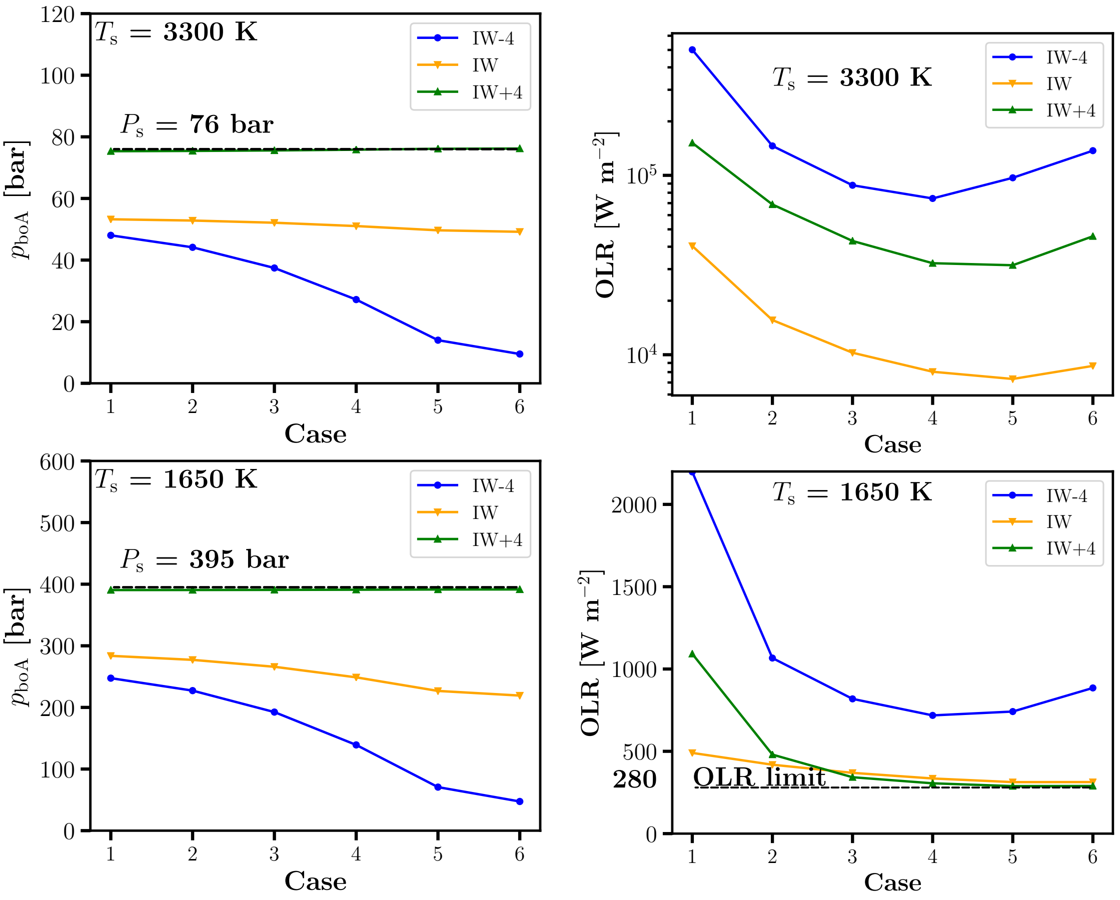

Figure 47: *Left*: Pressure at the bottom of the atmosphere p_{boA} for various cases referring to different initial volatile abundances and three different mantle buffers: reduced (IW-4), IW, and oxidized (IW+4). The details of speciation for various cases on the x-axis are shown in Table 17 (T_s = 3300 K) and Table 18 (T_s = 1650 K) in the Appendix 3.3.8. The horizontal dashed black line indicates the total surface pressure of the initial outgassed volatile for the various cases. *Right*: Outgoing longwave radiation (OLR) for various cases corresponding to the atmospheric surface pressure shown in the left panels and for three different buffers.

In Figure 47, cases 1 and 2 are mainly dominated by CO_2 and/or CO (see Tables 17 and 18), which show only few absorption bands and thus display the strongest OLR. Cases 3 and 4, which are composed of a mixture H_2O+CO_2+CO+H_2 (see Tables 17 and 18), result in a minimum OLR where the spectra shows absorption lines of almost all the species present. Cases 5 and 6 are dominated by absorption through H_2O and/or H_2, which leads to a stronger OLR than the mixed-species cases 3 and 4, where absorption of all species strongly reduces the OLR for the high-temperature cases. For the low-temperature cases (lower right panel), the effect of the absorption by H_2O dominates because the H_2O band and continuum absorption cover the entire infrared wavelength regime.

Early H_2 atmosphere scenario. While hydrogen is prone to escape to space via strong incoming extreme UV (EUV) during the Hadean (more details in Section 3.3.5), it is also an important gas in enhancing the greenhouse effect in the atmosphere. The efficiency of heating the atmosphere, however, depends upon the surface partial pressure of hydrogen.

We explored a case similar to scenario 2.3 of Table 13 and shown previously in Figure 45 with a pure H_2 atmosphere, but with a varying hydrogen surface pressure p_{H_2} and a fixed surface temperature $T_s = 2800$ K. We obtained the thermal emission of radiation by varying the surface pressure p_{H_2} in the range 0.6-185 bar, as shown in Figure 52 (upper panel) of Appendix 3.3.8. We observe a large number of undulations around 2 μm in the obtained thermal spectra, especially at higher surface pressures. These undulations are caused by the effects of collision-induced absorption (CIA) by H_2.

The lower panel of Fig. 52 shows a decrease in the OLR with the (surface) partial pressure of H_2 attributed to the higher absorption of radiation at higher pressures, as also shown in Fig. 47 (left panels). We therefore conclude that several bars of H_2 in the atmosphere could significantly affect the climate in the cases studied, leading to additional greenhouse warming (also see Ramirez et al., 2014). A similar trend in the OLR versus p_{H_2} as shown here was suggested by Pierrehumbert and Gaidos (2011).

Transmission spectra. We obtained the transmission spectra for the BOM and the EOM using the lbl radiative transfer code GARLIC and the temperature profiles (Sect. 3.3.5) and concentration as an input. The resultant spectra are shown as the wavelength-dependent effective height of the atmosphere (see Eq. 263 in Figure 48). The spectra were binned to a resolution of $R = \lambda/\Delta\lambda = 1000$ over the wavelength range shown.

As shown in Fig. 48, the effective height of the atmosphere increases to one order of magnitude for the reduced atmospheres (IW-4) from scenarios 1.1 to 1.3 (and 2.1 to 2.3) for both BOM (left panel) and EOM (right panel) scenarios. This is related to the increasing atmospheric scale height for the lighter H_2 -dominated atmospheres. Similarly, for the oxidized atmospheres (IW+4), the effective height increases from a dense and thick CO_2 -dominated atmosphere (scenarios 1.1 and 2.1) to lighter H_2O -dominated atmospheres (scenarios 1.2, 1.3, 2.2, and 2.3). In the visible-optical range, the slope of the so-called Rayleigh-scattering extinction feature is somewhat steeper for the reducing atmosphere (blue line) because of the different scale heights. For scenarios 1.3 and 2.3, H_2O absorption features are seen ubiquitously from roughly 0.9 to 2.6 μm. For a high CO_2 initial volatile outgassing (scenario 1.1 and 2.1), CO absorption features are seen at 2.3, 4.6 μm for IW-4 buffer, and CO_2 absorption features are seen as shown for 2.1, 4.3, and 15 μm for the IW+4 buffer. For the EOM scenarios (right panels), the cooler surface temperature (1650 K) leads to a decrease in scale height ($H = kT/mg$) compared with the BOM (left panels) scenarios with higher surface temperature (3300 K).

A decrease in the depth of the absorption bands for CO (IW-4) and CO_2 (IW+4) is seen at 4.3 and 15 μm, respectively, which is related to a decrease in the input CO_2 from scenarios 1.1 to 1.2 at $T_s = 1650$ K (right

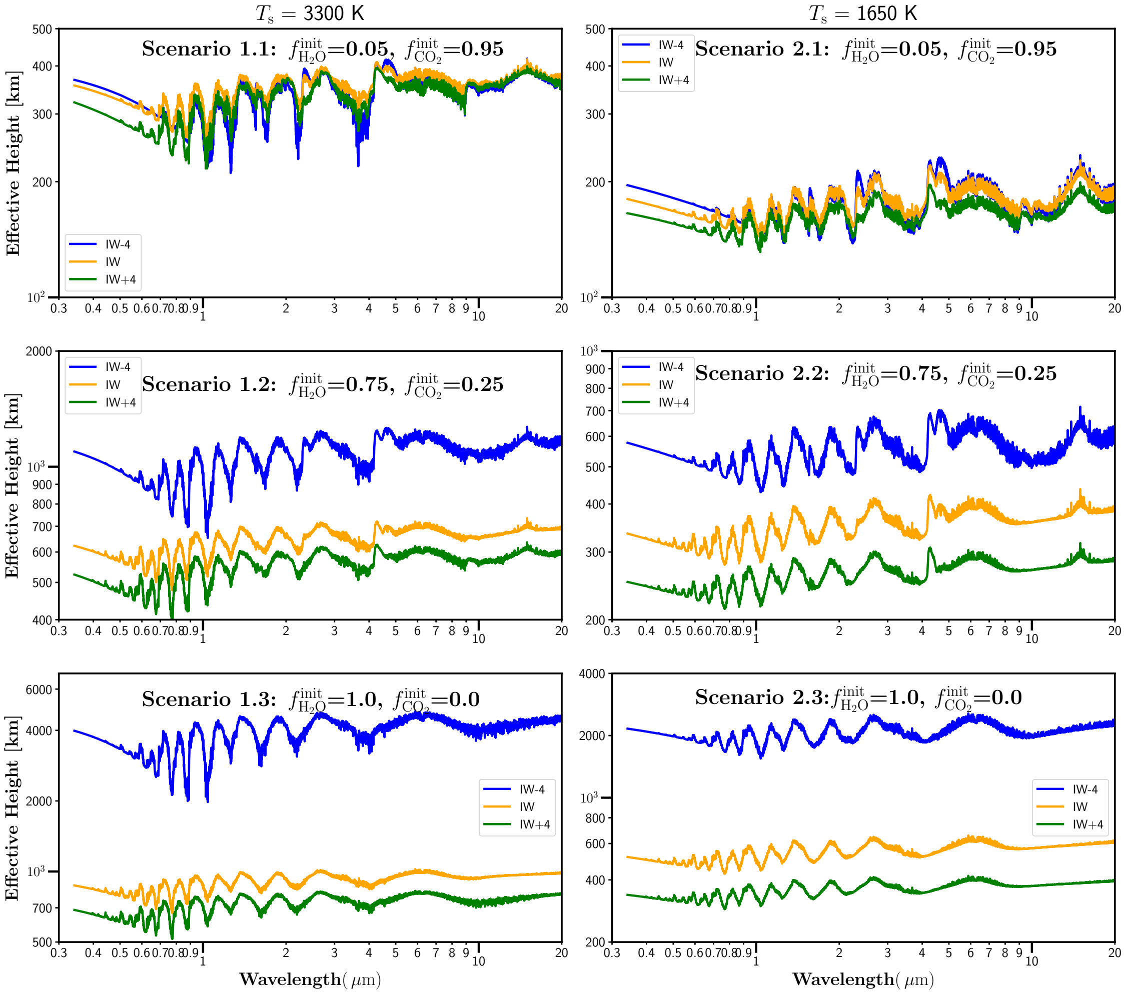

Figure 48: Transmission spectra calculated by GARLIC shown as atmospheric effective height vs. wavelength for the BOM scenarios (left panels) and EOM scenarios (right panels) for three different redox buffers IW-4, IW, and IW+4. The mole fraction of final outgassed species in the atmosphere for various scenarios is the same as provided in Tables 13 and 14. The effective height of a reduced atmosphere (with low molecular weight) for the case of reduced mantle IW-4 (blue curve; scenarios 1.2, 1.3, 2.2, and 2.3) is lower than an atmosphere with larger molecular weight (blue curve; scenarios 1.1 and 2.1) and oxidizing atmospheres (green curve; all scenarios). For more details, see the text. The spectra have been binned to a resolution of $\lambda/\Delta\lambda$ = 1000.

panel). A similar trend is seen for scenarios at $T_s = 1650$ K (right panel). For the oxidizing atmospheres (IW+4) in scenarios 1.3 and 2.3, the most prominent H_2O features between $1 - 2$ μm are seen, but the 6.2 μm H_2O feature is suppressed. This is likely related to the overlying optically thick atmosphere of H_2O (blanketing effect) with a very high surface pressure ($\sim$ 395bar), wherein the radiation will be dominated by the emission from the top of the atmosphere. This hinders chemical species in the lower atmosphere from being detected in the upper regions sampled by transmission spectroscopy. It is therefore difficult to probe dense atmospheres with high optical depths.

Atmospheric evolution and escape over the MO period. Table 16 shows the range of surface partial pressure of H_2 for a highly reduced (IW-4) and an oxidized mantle (IW+4) over a period of MO solidification $\sim$ 1 Myr. For the reducing-buffer case (IW-4), over the period of MO, the surface pressure of atmospheric hydrogen increases from 2.3 to 102 bar, while for the oxidized case, it increases from 0.02 to 2.7 bar. To investigate the evolution of H_2 along with other species in the atmosphere, we split the MO period into ten time steps where the change in species abundance from scenario 1.1 (BOM) to scenario 2.2 (EOM) in Table 16 is set to change with a linear time step of 0.1 Myr (only shown for H_2 in the table). The resulting changes in species abundances across the MO can be attributed to outgassing and chemical speciation. As a first step, the input data for the various scenarios were taken from Nikolaou et al. (2019); Katyal et al. (2019), but in a future study, we plan to perform time-dependent, coupled interior-atmosphere evolutionary scenarios over the magma ocean phase applying a newly developed climate-chemistry atmospheric model (Scheucher et al., 2020; Wunderlich et al., 2020).

Table 16: Hydrogen abundance in the atmosphere from the beginning (scenario 1.1) to the end (scenario 2.2) of the magma ocean for a reduced (IW-4) and oxidized (IW-4) mantle.

Buffer	t = 1 yr (scenario 1.1)			t = 1 Myr (scenario 2.2)		
	p_{boA}(bar)	p_{H_2} (bar)	f_{H_2}	p_{boA}(bar)	p_{H_2} (bar)	f_{H_2}
IW-4	48	2.3	0.05	139	102.8	0.74
IW+4	75.3	0.02	0.0003	391	2.7	0.007

We now consider the evolution of atmospheric species over the MO period. The mole fraction f of the resultant outgassed species i is translated into the mass fraction via $w_i = f_i \ M_i/\bar{M}$, where M_i is the molecular weight of the species i and $\bar{M}$ is the mean molar mass of the atmosphere. The atmospheric mass of the individual species is obtained by multiplying the calculated mass fraction w_i with the total mass of the atmosphere $M = P*A/g$.

Figure 49 shows the resulting atmospheric mass evolution of a reducing atmosphere lying above a reduced mantle, that is, IW-4 (upper panel) and an oxidizing atmosphere lying above an oxidized mantle, that is, IW+4 (lower panel) during the MO period. The circles show the mass of the H_2 escaping via diffusion-limited escape according to Eq. (270) as described in Section 3.3.3, where the color of the circles indicates the total mass-loss rate (g/s). The mass-loss rate obtained from energy-limited escape formalism as in Eq. (267) is obtained to be 5.2×10^7 g/s for $S = 10$ and 5.2×10^8 g/s for $S = 100$. As described in Sect. 3.3.3, $(R_p+H_e) \sim R_p$ for this scenario (see Table 16). The mass loss of H_2 (in grams) is then calculated and shown as the yellow shaded region within these S ranges in Fig. 49 (both upper and lower panels). In general, the atmospheric H_2 mass loss (in grams) is seen to increase for both the escape processes because the H_2 abundance increases throughout the MO evolution timescale. The residual H_2 in the atmosphere after accounting for escape is seen to overlie the total H_2 content of the atmosphere, implying that a significant amount of H_2 remains in the atmosphere. We also show a shaded region obtained from the parameterized Eq.(269) of Zahnle et al. (2019), where the lower and upper boundaries of the shaded region indicate $S = 10$ and $S = 100$, respectively, and f_{H_2} values are taken over the evolution timescale (see Table 16).

For the oxidized-mantle (IW+4) case (Fig. 49 lower panel), the H_2 abundance is very low (see Table 16), causing this to be the bottleneck for H_2 to diffuse through heavy CO_2 or H_2O up to the homopause. Moreover, the plentiful amount of XUV energy available here (with a high loss rate) can in fact lead to the complete removal of hydrogen. For the oxidizing atmosphere lying above an oxidized mantle, that is, IW+4, escape of H_2 is therefore not energy limited but diffusion limited. Finally, we conclude that for both the redox states of the mantle, the outgassing of H_2 into the atmosphere dominates the escape of H_2 (Kuramoto et al., 2013; Ramirez et al., 2014).

As an illustration, Figure 50 compares the escape rates for scenario 2.2 (EOM) calculated for H_2 with our estimated H_2 outgassing rate obtained using Equation (251) as described in Section 3.3.3.

The outgassing rates obtained by us during the magma ocean period in the Hadean (3.8-4.0 Gyr before present) for a variable redox state of the mantle are higher than in the Archean (2-4.0 Ga), that is, 9×10^{14} molecules $m^{-2}s^{-1}$ (Tian et al., 2005; Kuramoto et al., 2013). First, one of our central results is that outgassing (red solid line) proceeds faster than diffusion-limited escape (closed red circles) by a factor of x10 and energy-limited escape depending upon the uncertainty in the XUV radiation as evident from the S values displayed in the figure. Second, for an atmosphere with a high hydrogen abundance, that is, VMR(H_2) > 0.2 ($-4 < \mathrm{IW} \leqslant 0.5$), the energy-limited escape is more effective, whereas for an atmosphere with lower hydrogen abundances, that is, $\mathrm{VMR}(H_2) < 0.2$ $(0.5 < \mathrm{IW} < 4)$, the diffusion-limited escape is more effective, as shown in Fig. 50.

3.3.6 Discussion

We have studied the effect of the redox state of the mantle and volatile outgassing of major outgassed species H_2O and CO_2 from the interior and their interaction with the melt resulting in outgassing of newer species at the surface. The effect on the atmospheric profiles, thermal infrared emission, transmission, and

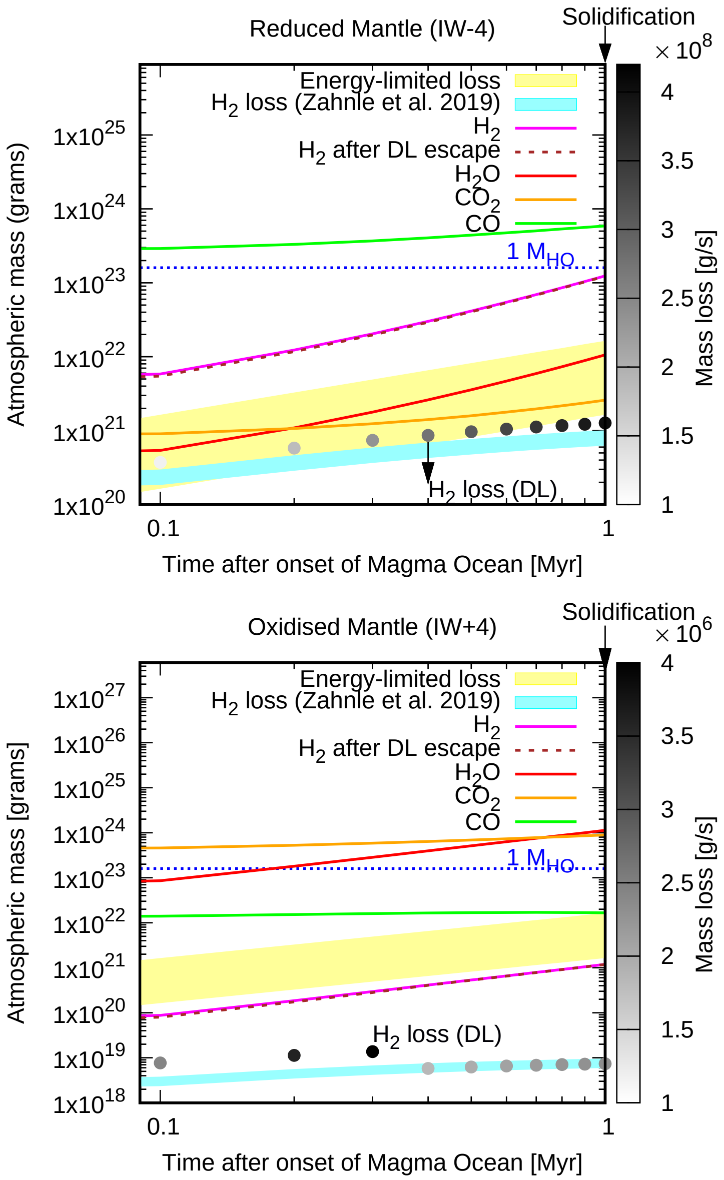

Figure 49: Evolution/escape of atmospheric species in terms of the atmospheric mass (left axis) for the duration of the magma ocean (x-axis) for a reduced mantle case (upper panel) and an oxidized mantle case (lower panel). The colored solid lines refer to atmospheric masses integrated over the whole planet that change due to outgassing and chemical speciation (see text). The dotted brown line shows the residual mass of H_2 in the atmosphere after accounting for outgassing and DL escape. The shaded region in cyan shows the mass loss of H_2 in the range for $S = 10$ to $S = 100$ (XUV relative to the modern value) using the Zahnle et al. (2019) best-fit formalism (see text). The shaded region in yellow shows the energy-limited loss of H_2 for the lower range $S = 10$ to upper range $S = 100$. The dotted blue horizontal line shows the hydrogen content of one (modern) Earth ocean ($M_{HO} = 1.6 \times 10^{23}$ g). The filled circles indicate the escaping mass of H_2 obtained using DL. The colors indicate the respective mass-loss rates (right axis).

escape of H_2 is discussed below.

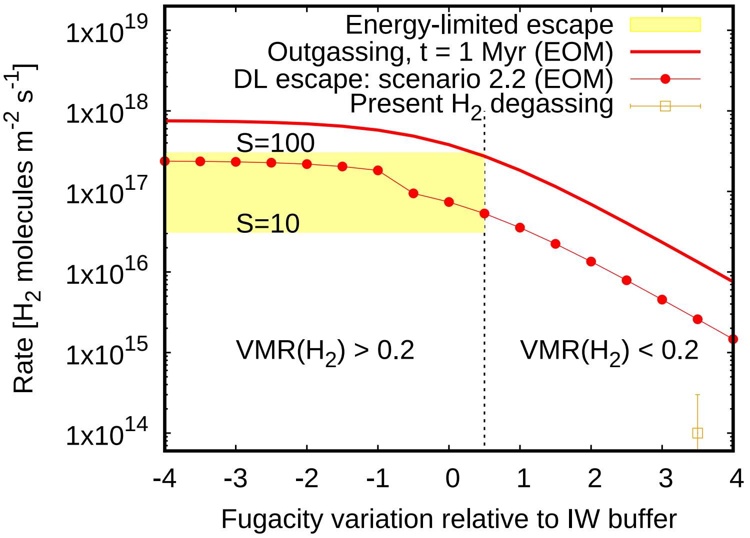

Figure 50: Hydrogen escape and outgassing rates as a function of redox state of the mantle for scenario 2.2 (EOM). The solid red line shows the H_2 outgassing rate at the end of magma ocean. The closed red circles show the diffusion-limited escape of H_2 for the EOM. The shaded region in yellow shows the loss rate due to energy-limited escape within the range S=10 (lower boundary) to S=100 (upper boundary) i.e. XUV relative to the modern value. The vertical dotted line marks the region separating a high H_2 VMR to low H_2 VMR and illustrates the most efficient escape process occurring. The present Earth H_2 degassing rate with an uncertainty range (Ramirez et al., 2014) is marked for reference.

Mantle redox and atmospheric temperature. Our study has suggested an interesting coupling between interior outgassing, volatile speciation due to the mantle redox state, atmospheric composition, and atmospheric temperature that affects atmospheric extent, mixing, and the location of the dry and moist adiabat. During the BOM, more oxidized atmospheres switch from dry to wet adiabat at lower pressures (Fig. 40, green lines) than reduced atmospheres due to differences in their mean molecular weight and heat capacities, which leads to a lower scale height. The pressure at which the moist adiabat is reached affects the onset of saturation, thereby affecting the microphysical processes such as condensation and ultimately ocean formation. Detailed microphysical processes are not included in our study and need further investigation with more detailed models. On the other hand, the more reduced atmospheres have larger scale heights, and the switch to the moist adiabat lies at higher altitudes (Fig. 40, blue curve). Precipitation initiated at high altitudes has to sediment over a greater distance to rain out, which could favor evaporation in the lower, warmer atmospheric layers, and which might therefore be less efficient at condensing to form the oceans. For the EOM case (Figure 41), although the atmosphere cools (from 3300K to 1650K at the surface) and the surface pressure increases by a factor of 5, the temperature structures for the EOM are similar to those for the BOM (Figure 40). This is because the pressure increase (which increases atmospheric thickness) is offset by the cooling effect (which decreases atmospheric thickness). In summary, the above processes likely affected the evolution of climate on the early Earth by affecting key processes such as cooling to space and greenhouse heating, but also the onset of condensation and accordingly, the formation of terrestrial ocean.

Thermal emission and transmission spectra. Our results suggest that the thermal emission of radiation is affected by key parameters such as surface temperature, surface pressure, mantle redox state, and initial volatile content of the two main species H_2O and CO_2 that are outgassed during the magma ocean phase. The most prominent absorption features of oxidized versus reduced species in the atmosphere for the three different mantle oxidation states IW-4, IW, and IW+4 are shown in Figs. 43 and 44. For the reducing mantle cases, the volatile speciation model would result in a mixture of both oxidized and reduced species in the atmosphere depending upon the initial volatile contents $f_{H_2O}^{\mathrm{init}}$ and $f_{CO_2}^{\mathrm{init}}$ (see Tables 13, 14, 17, and 18). As shown in Fig. 47 (right panels), the OLR for the most reduced atmosphere case overlying a reduced mantle (IW-4) consists of H_2, CO or CO+H_2 (depending upon the case) and results in the highest OLR because these molecules have only a few absorption bands. On the other hand, we obtain lower OLR for other moderately reduced buffer, that is, IW, resulting in a mixed atmosphere of CO_2+CO+H_2+H_2O with the largest number of absorption bands covering the entire spectral range. Finally, the lowest OLR is obtained for an oxidizing atmosphere overlying an oxidizing buffer (IW+4), resulting in CO_2, H_2O or H_2O+CO_2 atmospheres (depending upon the case).

As a result, a planet with a reduced mantle buffer (IW-4) and low water content (cases 1 and 2) is expected to cool faster than a planet with a high water content in the atmosphere (cases 4, 5, and 6). For a moderately reduced mantle buffer (IW), the planet will cool down slowly as the OLR is the lowest for it. For a planet with an oxidized mantle buffer (IW+4), the cooling timescales will be slower than those of the IW-4, but faster than the IW case.

The initial outgassed water content along with the surface temperature and the redox state of the mantle are important factors driving planetary cooling. Figure 47 shows for lower temperature (T_s = 1650 K) and oxidized mantle (IW+4 buffer) that the OLR limit ~280 W m^{-2} (Goldblatt et al., 2013; Marcq et al., 2017) occurs only for H_2O -rich atmospheres (cases 5 and 6). However, this is not the case for a high temperature (T_s = 3300 K) and an oxidized mantle (IW+4) because at such high temperatures, the emission occurs in visible wavelengths along with infrared, and H_2O is not able to block the radiation in the visible as effectively as in infrared. Radiation is thus not able to reach the OLR limit.

Oxidized atmospheres containing heavier species such as CO_2 result in a dense atmosphere with small effective heights for transmission spectra (Fig. 48, scenarios 1.1 and 2.1) as compared to a reduced and lighter atmosphere with H_2, resulting in extended atmospheres with a large effective scale height, as shown in scenarios 1.3 and 2.3 of Fig. 48. The slope of the Rayleigh-scattering feature in the ultraviolet and visible wavelength range could provide information on the bulk atmospheric composition. However, when aerosols, thick hazes, or clouds are considered, this slope changes considerably because of the change in the wavelength dependence of the scattering (see Eq. 262), which changes the atmospheric optical depth and effective height of the atmosphere (also see Wunderlich et al., 2020).

Outgassing and escape: loss timescales. Our results suggest very different regimes in terms of outgassing of various species and escape of H_2 depending on the mantle redox state during the MO period. For the scenarios that consider the reducing and oxidizing state of the mantle, the outgassing rate of H_2 is greater than the escape rate, and there is enough interior outgassing of H_2 to form an atmosphere. A similar result was suggested by Ramirez et al. (2014) for early Earth and Mars.

Because the VMR of H_2 is high (e.g., in a reducing atmosphere), the escape of H_2 most likely occurs by energy-driven, that is, energy-limited, escape. On the other hand, if less hydrogen is present (e.g., in an oxidizing atmosphere), the diffusion of hydrogen through a heavy gas to reach the upper atmospheric regions and escape is limited. Therefore, the atmosphere would probably enter a DL configuration. Thus, depending upon the abundance of H_2 in the atmosphere, our results suggest a switch from energy-limited (EL) escape (high VMR) of H_2 to DL escape (low VMR), thus complying with Zahnle et al. (2019).

For a reduced early atmosphere with 102 bar of H_2 by the end of MO, we estimate the timescale of H_2 atmosphere removal to be $\sim$10 Myr using both DL and EL ($S = 10$) escape. On the other hand, because the H_2 mass-loss rate and the surface partial pressure of surface hydrogen are lower (2.7 bar) for an oxidized atmosphere, the mass-loss timescale is estimated to be $\sim$16 Myr assuming DL escape. Similar mass-loss timescales ($\sim 10^6$-10^7 yr) for surface pressures of 10 to 100 bar are obtained by hydrodynamic escape modeling of Pahlevan et al. (2019). The results for total hydrogen mass-loss obtained via two different parameterized escape models (this work) and hydrodynamic model (Pahlevan et al., 2019) are therefore approximately similar. Moreover, as we showed in Fig. 49, the mass loss obtained using the energy-limited (hydrodynamic) approach following Zahnle et al. (2019) (cyan shaded region) approximates the diffusion-limited mass loss at higher levels of irradiation, $S = 100$ (also see Lammer et al., 2018). Furthermore, it is worth stating that several works (e.g., Lammer et al., 2011) have noted the potential importance of EUV in driving energy-limited escape on early Earth and speculated that this quantity is not known to within a factor 100 or more times the modern-day value depending upon whether the early Sun was a fast or slow rotator.

Clouds. Clouds could be rather common features in extrasolar atmospheres, and they could have a potentially strong effect upon the atmospheric spectra, climate, and photochemistry. Spectral features can be significantly reduced depending upon the extent (layer location and thickness) and the microphysical properties (size, shape, number density distribution, and refractive index) of the clouds occurring over a wavelength range that is sensitive to the cloud diameter, for example. The general effect of clouds upon atmospheric spectra and retrieval by the James Webb Space Telescope (JWST) was discussed by Mai and Line (2019) and Fauchez et al. (2019).

In magma ocean worlds, thick water cloud layers could form (see, e.g., Lebrun et al., 2013; Marcq et al., 2017) as the outgassed steam atmospheres cool. These cloud layers could help prevent the loss of planetary infrared radiation to space, and if thick water clouds were to extend over the region sampled by transmission spectroscopy, for instance, they might significantly reduce the strength of the spectral features detected.

In Fig. 51 we show the atmospheric transit depth calculated using Eq. (264) for planet Earth orbiting an M-type star (0.4 solar radii) in the top panel and a G-type star (bottom panel) for two different redox states of the mantle, IW+4 and IW. A clear increase in transit depth is visible for the IW buffer with 50% H_2O and 0.5% H_2 because the molecular mass of the atmosphere is lower than in the pure H_2O case (IW+4 buffer). Results also suggest a substantial increase in the transit depth when observing via an M-type star because its stellar radius is smaller, thus favoring the possibility of detecting atmospheric species. We also compared the cloud-free scenarios with the cloudy simulations. With a cloud deck (see Section 3.3.3), the spectral features are weakened (depending upon the cloud cross section), as shown in Figure 51. The results of the comparison between cloud-free and cloudy scenarios ($\alpha = 0$ and enhanced scattering cross section as compared to Rayleigh) agree well with Turbet et al. (2019). The transit depths in the optically thick cloudy scenarios can be considered as maximum values (because thick clouds effectively block shortwave radiation) compared with the smaller transit depths of the clear atmosphere cases without clouds. A sensitivity study by Moran et al. (2018) that involved increasing the haze-scattering cross section also suggested a weakening in spectral features when a global layer of Rayleigh-scattering haze was added to the TRAPPIST-1 d, e, and f planets. A more involved sensitivity study including the geometry of the cloud, such as its cross section (Kitzmann et al., 2011a,b), requires the use of detailed cloud microphysics (Zsom et al., 2012) that is applicable for Earth-like exoplanets. We did not explore this here and aim to investigate it in future related studies.

Application to exoplanets. Several hundred rocky exoplanets classified as super-Earths with mass ranging between $M = 1 - 8M_{\mathrm{E}}$ and radius $R = 1 - 1.8R_{\mathrm{E}}$ are being discovered by various current space missions such as TESS[2] and will be discovered by future missions such as PLATO[3], JWST[4], and CHEOPS[5]. Atmospheric characterization of these planets via spectroscopic analysis can benefit greatly from interior geochemical models that consider outgassing during the magma ocean phase (Bower et al., 2019) and volcanic outgassing after the magma ocean phase (Ortenzi et al., 2020). Ortenzi et al. (2020) showed that

---

[2] Transiting Exoplanet Survey Satellite

[3] PLAnetary Transits and Oscillations of stars

[4] James Webb Space Telescope

[5] CHaracterising ExOPlanets Satellite

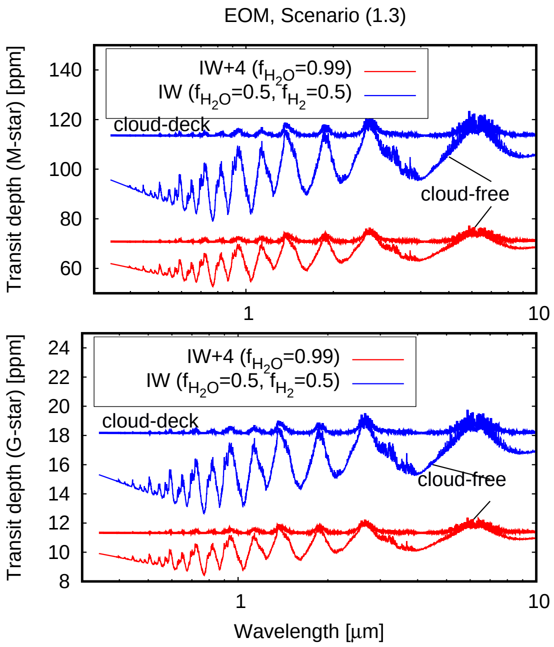

Figure 51: Atmospheric transit depth of a cloud-free planetary atmosphere around an M star (top) and G star (bottom) at the EOM phase for an atmosphere simulated from IW+4 mantle buffer (red) and IW mantle buffer (blue) is compared with the transit depth for cloudy scenarios ($\alpha = 0$ and enhanced cross-section as compared to the Rayleigh scattering).

the redox state of the mantle affects the atmospheric thickness and overall evolution, thus constraining the interior chemical state of rocky exoplanets. Puffy outgassed atmospheres for hot, molten Earth-like planets often lead to an effect known as “radius inflation” that depends upon the initial volatile inventory of H_2O and CO_2 (Bower et al., 2019) and on the irradiation that they receive from the star (Turbet et al., 2019).

Furthermore, as shown in Fig. 51, the redox state of the mantle and initial inventory of volatiles can induce strong variations in the transit depths for planets orbiting G and M stars. This would translate into changes in the planetary radius to be observed by missions such as TESS and PLATO (Rauer et al., 2014). However, the detectability of molecular spectral features may be severely affected by the presence of clouds (see e.g. Fauchez et al., 2019).

Kaltenegger et al. (2007) modeled the observable spectra of Earth-like planets about two billion years ago to a present-day atmosphere. They reported a number of constraints, such as the resolution of the telescopes for detecting the molecular species in the atmosphere. It is therefore important to characterize the atmosphere of Earth through its geological history and that our study present useful insights on this. Recent interior-atmosphere modeling studies have shown that pure steam-based atmospheres of highly irradiated exoplanets orbiting M dwarfs such as GJ 1214 b (Schaefer et al., 2016) and LHS 3844 b are subject to strong XUV of the star and could lose the outgassed atmosphere and become a bare rock (Kreidberg et al., 2019). See also Kite and Barnett (2020) for a detailed study of atmospheric loss and subsequent revival relevant for exoplanets. In all these models, the water is dissociated into hydrogen and oxygen, which escape to space, and some remaining oxygen is dissolved into the magma ocean or remains in the atmosphere (e.g., Schaefer et al., 2016).

We have provided important testable predictions to inform future space missions such as the JWST, Ariel[6] (Tinetti et al., 2018; Edwards et al., 2019), LIFE[7] (Quanz et al., 2019), and ELT[8] (Maiolino et al., 2013) that will characterize planetary atmospheres in terms of detecting species such as CO, CO_2 , and H_2O in spectral observations of Earth-sized planets.

Planets in close-in orbits around cooler stars are favored targets in exoplanetary science because of their improved contrast ratios, higher transit frequency, and increased geometric transit probability (Scalo et al., 2007; Shields et al., 2016), for example. Furthermore, the detectability of atmospheric spectral signals from MO exoplanets (Ito et al., 2015) and thick atmospheres with H_2O and CO_2 with a high sensitivity and large spectral coverage of the JWST (NIRSpec, MIRI) instruments (Ducrot et al., 2020) would bring new possibilities to constrain such atmospheres.

3.3.7 Conclusions

The main conclusions of this study are listed below.

1. The redox state of the mantle can affect not only atmospheric composition, but also the vertical temperature structure and therefore the mixing and the hydrological cycle. These interior-atmospheric couplings could be important for steam-condensation timescales and accordingly, for the formation of the Earth oceans.

2. Reduced atmospheres emit thermal radiation more strongly, which leads to faster cooling than in oxidized atmospheres because the latter feature strong absorbers such as H_2O.

3. Reduced atmospheres (CO and H_2) have much larger spectral features in transmission than oxidized atmospheres (H_2O and CO_2) because the scale heights are larger.

4. Thick optical clouds and hazes can mute or weaken the spectral signatures of molecules in the transmission spectra and enhance the transit depth because of the cloud cover. It therefore becomes difficult to probe cloudy atmospheres. On the other hand, clouds absorb much of the radiation and reduce the outgoing longwave radiation by 1-2 orders of magnitude (Marcq et al., 2017), leading to longer magma ocean cooling timescales.

---

[6] Atmospheric Remote-sensing Infrared Exoplanet Large Survey

[7] Large Interferometer for Exoplanets

[8] Extremely Large Telescope

5. The interplay between outgassing and escape suggests that outgassing of hydrogen proceeds faster than the atmospheric escape of H_2 and that enough outgassed hydrogen is available to form an atmosphere over the magma ocean duration of $\sim$1 Myr. The timescale for total H_2 mass loss, however, is estimated to be within some dozen million years. Furthermore, a more sophisticated hydrodynamical code to study the loss of H_2 and the heavy atmospheric species H_2O and CO_2 is desirable and planned for future studies.

Acknowledgements

We thank the anonymous reviewer and the editor for their valuable comments that greatly enhanced the quality of the manuscript. N.K. and G.O. acknowledge funding from the Deutsche Forschungsgemeinschaft (DFG, German Research Foundation) – Project-ID 263649064 – TRR 170. This is TRR 170 Publication No. 117. M.G. acknowledges funding from DFG - Project-ID GO 2610/1-1. F.S. acknowledges DFG project SCHR 1125/3-1.

3.3.8 Appendix

Gas constant for a mixture. When a mixture of two gases a and b, with partial pressure p_a and p_b , exists at the same volume V and temperature T, the mixture behaves like a perfect gas, and according to Dalton's law of partial pressures,

$$(p_a + p_b)V = (m_a R_a + m_b R_b)T. \tag{271}$$

Because the mixture behaves like a perfect gas, for $m = nM$ moles of a gas, the total pressure is given by

$$PV = mR_{\text{mix}}T, \tag{272}$$

where R_{mix} is the gas constant for the mixture. From Eqs. (271) and (272), $mR_{\text{mix}} = m_a R_a + m_b R_b$. Hence,

$$R_{\text{mix}} = \frac{m_a R_a + m_b R_b}{m}. \tag{273}$$

In terms of the molar volume fraction,

$$R_{\text{mix}} = \frac{n_a M_a R_a + n_b M_b R_b}{\sum_i n_i M_i}. \tag{274}$$

Because $MR = \bar{R}$, where $\bar{R}$ is the universal gas constant (= 8.31415 J kg^{-1} K^{-1}), this equation can be written as

$$R_{\text{mix}} = \frac{n_a \bar{R} + n_b \bar{R}}{n_a M_a + n_b M_b}. \tag{275}$$

For a single-component gas a, $R = \bar{R}/M_a$. For a two-component gas mixture, Eq.(275) can be written as

$$R_{\mathrm{mix}} = \bar{R}\left(\frac{n_a + n_b}{\mu}\right), \tag{276}$$

where $\mu = n_a M_a + n_b M_b$ is the mean molecular weight of the mixture. For an ith-component mixture of gases,

$$R_{\mathrm{mix}} = \bar{R}\left(\frac{\sum n_i}{\sum n_i M_i}\right). \tag{277}$$

Volatile speciation model output.

Table 17: Cases for BOM used to produce Figure 47. Cases 1, 4, and 6 are similar to scenarios 1.1, 1.2, and 1.3, respectively, which are also presented in Table 13. Columns 2 and 3 show the initial assumed mole fractions arising from H_2O and CO_2 outgassing, which is the input to the speciation model. The assumed buffer values for strongly reducing (IW-4), reducing (IW), and highly oxidizing (IW+4) have been used to study the effect of speciation under these conditions. The four columns on the right show final outgassed species from the speciation model. For these scenarios, the surface p, T setting is fixed to be $T_s = 3300$ K and $P_s = 76.7$ bar. The p_{boA} calculated from the new molecular weight of the atmosphere is also shown. The most dominant species in the atmosphere are marked in bold for each of the cases.

Case	Initial outgassing		P_s (bar)	Buffer	p_{boA} (bar)	Final outgassing			
	$f_{H_2O}^{\mathrm{init}}$	$f_{CO_2}^{\mathrm{init}}$				f_{CO_2}	f_{H_2O}	f_{H_2}	f_{CO}
1	0.05	0.95	76.7	IW-4	48	0.0018	0.0007	0.049	**0.94**
				IW	53.2	0.15	0.029	0.02	**0.79**
				IW+4	75.3	**0.90**	0.049	0.000	0.046
2	0.25	0.75	76.7	IW-4	44.14	0.0014	0.036	**0.24**	**0.75**
				IW	52.83	0.12	**0.15**	0.10	**0.62**
				IW+4	75.43	**0.71**	**0.245**	0.0016	0.036
3	0.5	0.5	76.7	IW-4	37.43	0.00	0.007	**0.49**	**0.50**
				IW	52.12	0.08	**0.30**	0.20	**0.42**
				IW+4	75.6	**0.47**	**0.29**	0.003	0.024
4	0.75	0.25	76.7	IW-4	27.1	0.000	0.01	**0.74**	**0.25**
				IW	51	0.040	**0.44**	**0.30**	**0.20**
				IW+4	75.8	**0.24**	**0.74**	0.005	0.0122
5	0.95	0.25	76.7	IW-4	14.0	0.0	0.013	**0.94**	0.0049
				IW	49.6	0.008	**0.56**	**0.38**	0.042
				IW+4	76.1	0.047	**0.94**	0.0063	0.002
6	1.0	0.00	76.7	IW-4	9.5	0.0	0.014	**0.98**	0.00
				IW	49.1	0.00	**0.60**	**0.40**	0.00
				IW+4	76.2	0.00	**0.99**	0.0069	0.00

Table 18: Same as for Table 17, but for EOM cases used to produce Figure 47. Cases 1, 4, and 6 are similar to scenarios 2.1, 2.2, and 2.3, respectively, which are also presented in Table 14. The surface p,T setting is fixed at $T_s = 1650$ K and $P_s = 395$ bar.

Case	Initial outgassing		P_s (bar)	Buffer	p_{boA} (bar)	Final outgassing			
	$f^{init}_{H_2O}$	$f^{init}_{CO_2}$				f_{CO_2}	f_{H_2O}	f_{H_2}	f_{CO}
1	0.05	0.95	395	IW-4	247.5	0.003	0.0005	0.049	**0.94**
				IW	283.7	0.22	0.025	0.025	**0.72**
				IW+4	390.4	**0.92**	0.05	0.000	0.03
2	0.25	0.95	395	IW-4	227.2	0.002	0.002	**0.25**	**0.74**
				IW	277.2	0.176	0.124	0.125	**0.57**
				IW+4	390.6	**0.72**	**0.24**	0.002	0.023
3	0.5	0.5	395	IW-4	192.4	0.0015	0.005	**0.49**	**0.49**
				IW	266	0.11	**0.25**	**0.25**	**0.38**
				IW+4	390.7	**0.48**	**0.49**	0.005	0.0157
4	0.75	0.25	395	IW-4	139	0.0007	0.007	**0.74**	**0.25**
				IW	248.9	0.058	**0.37**	**0.37**	0.19
				+4	391	**0.24**	**0.74**	0.007	0.007
5	0.95	0.25	395	IW-4	70.66	0.00	0.009	**0.94**	0.05
				IW	226.7	0.011	**0.47**	**0.47**	0.038
				IW+4	391.3	0.048	**0.94**	0.0094	0.001
6	1.0	0.0	395	IW-4	47.3	0.00	0.009	**0.99**	0.00
				IW	219	0.00	**0.50**	**0.50**	0.00
				IW+4	391.5	0.00	**0.99**	0.0099	0.00

OLR of H_2 atmospheres.

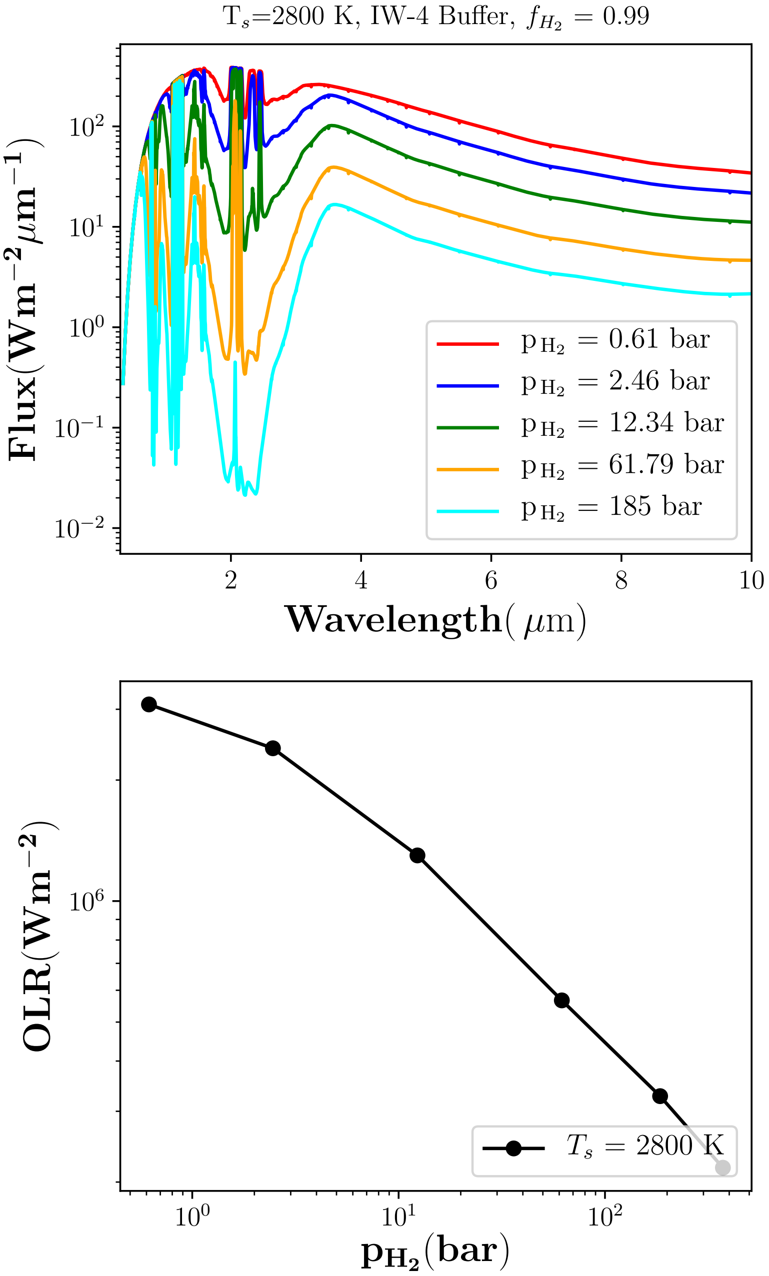

Figure 52: *T*op: Thermal emission spectra for an H_2-dominated atmosphere overlying a highly reduced mantle (IW-4) for a varying surface partial pressure of hydrogen as shown in the legend. *Bottom*: OLR plotted against p_{H_2} for a fixed surface temperature of $T_s = 2800$ K showing a decrease in OLR with increase in H_2 surface partial pressure.

3.4 Additional publications

The following research papers were developed during the PhD period but they are not directly connected to the main results of the thesis and to the application of the chemical speciation model. In Paredes-Mariño et al. (2017) (section 3.4.1) we analysed the eruption explosivity due to magma mingling of Sete Cidades Volcano (Azores, Portugal). Gaillard et al. (2021) (section 3.4.2) is a review paper on volcanic outgassing and chemical speciation of rocky planets. In Rammelkamp et al. (2021) (section 3.4.3) we analyse the spectrochemical response of handheld LIBS instrument on volcanic deposits on the island of Vulcano (Italy).

3.4.1 Enhancement of eruption explosivity by heterogeneous bubble nucleation triggered by magma mingling

Paredes-Mariño J., Dobson J.K., Ortenzi G., Kueppers U., Morgavi D., Petrelli M., Hess K.U., Laeger K., Porreca M., Pimental A. and Perugini D. *”Enhancement of eruption explosivity by heterogeneous bubble nucleation triggered by magma mingling”.* Scientific Reports 7: 16897, DOI:10.1038/s41598-017-17098-3.

The research paper analyses how the magma mingling can be a factor for triggering high explosive eruptions producing heterogeneous bubble nucleation. Samples of trachytic pumices erupted by Sete Cidades volcano (São Miguel Island, Azores) were analysed with X-ray micro tomography data acquisition, applying the fractal geometry theory and modelling the magma viscosity to investigate the magma fragmentation. The results suggest that the explosive eruption was triggered by the injection of trachibasaltic magma into a trachytic magma body. The low temperature of the trachytic body favoured the brittle fragmentation of the trachibasaltic magma increasing the discontinuity where heterogeneous bubble nucleation occurs and enhancing the explosivity of the eruption. My main contribution to the research is related to the analyses performed for my master thesis conducted during an Erasmus exchange with the Ludwig Maximilians University of Munich. I have carried out 3D image analyses on the micro tomography collected on the pumices samples. The fractal fragmentation theory was applied to explain the size distribution of the magmatic enclaves in the trachytic pumices and to support the fragmentation of the trachibasaltic magma which most likely increased the eruption explosivity.

3.4.2 The diversity of planetary ingassing/outgassing paths produced through billions of years of magmatic activities

Gaillard F., Bouhifd M.A., Furi E., Malavergne V., Marrocchi Y., Noack L., Ortenzi G., Roskocz M. and Vulpius S. *The diversity of planetary ingassing/outgassing paths produced through billions of years of* *magmatic activities*. Space Science Review. Accepted.

The manuscript is a review paper which describes the state of the art and the future direction of the ingassing/outgassing of rocky planets. The paper is focused on the C-O-H-N-S system which covers the majority of the volcanic volatile species. It gives an extended overview on the characteristics of the different volatile phases and on the outgassing at different geodynamic context on the Earth. Furthermore, it focuses on the crucial parameters that drive the outgassing on planetary rocky bodies for investigating the degassing also for extraterrestrial bodies. My personal contribution was a description of the effect of the oxygen fugacity on the gas chemical speciation for plate tectonics and stagnant lid planets. In the article are included also two figures from Ortenzi et al. (2020) to display the influence of planet sizes on the global outgassing of rocky planets and how the study of the different corresponding atmospheres can be an helpful tool for investigating rocky exoplanet atmospheres.

3.4.3 Field investigation of volcanic deposits on Vulcano, Italy using a handheld laser-induced breakdown instrument

Rammelkamp K., Schroeder S., Ortenzi G., Pisello A., Stephan K., Baqué M., Huebers H.W., Forni O., Sohl F., Thomson L., Unnithan V. *”Field investigation of volcanic deposits on Vulcano, Italy using a handheld laser-induced breakdown instrument”*. Spectrochimica acta part B: Atomic Spectroscopy. Volume 177 (March 2021) 106067. DOI https://doi.org/10.1016/j.sab.2021.106067.

The data for developing the paper were collected during the ”Fifth International Vulcano Summer School” organised by the Jacobs University of Bremen and the Institute of Planetary Research of the DLR. The study was conducted in the Vulcano island (Aeolian Islands, Italy) which represents a perfect analogue of extreme environment. The main aim of the paper was to test a commercial handheld LIBS (Laser-induced breakdown spectroscopy) instrument on the field in order to characterise the chemical composition of different lithologies. The laser-induced breakdown spectroscopy is an important investigative technique for in-situ geological analyses and also for extraterrestrial robotic exploration. The data collected during the campaign were tested with samples, collected in the field, of the same lithologies in the laboratory of the DLR Berlin to compare the possible discrepancy due to the in situ measurements with laboratory analyses. In the field campaign there were collected, on the same outcrops and lithologies, spectra also with Raman and Infrared spectroscopy handheld instruments. Thus, the wider outlook of the research is to characterise lithologies with different spectroscopic analyses to better analyse past and future data collected on the field and on extraterrestrial bodies. My personal main contribution to the research was to characterise the geology during the campaign and to identify the most interesting outcrops to test the handheld LIBS instruments. Vulcano island is characterised by a wide variety of volcanic deposits ranging from ash fall deposits to lava flows. The selection of the outcrops was central for collecting data and samples of different lithologies and minerals that are used for assessing the investigation techniques.

4 Discussion and conclusion

The thesis was part of the C5 project within the TRR-170 ”Late Accretion onto Terrestrial Planets”. The main goal was to characterise the global volcanic outgassing in different scenarios simulating the corresponding atmospheres for the early Earth evolution and for rocky planets. Following the studies of French (1966); Holloway (1981); Holland (1984); Fegley (2013); Gaillard and Scaillet (2014); Schaefer and Fegley (2017), I have developed chemical speciation models (see section 2.6) to simulate the volcanic gas species released into the atmospheres of rocky planets. I have investigated the outgassing process considering and highlighting the multidisciplinary approach to investigate the outgassing process. The volatile chemical speciation model can be considered as a tool that connects the interior of a planet to the relative outgassed atmosphere showing how the mantle redox state and volatile content influence the volatile degassing. I have simulated different chemical systems as the C-O-H and C-O-H-S considering ideal or real gas behaviour. It was necessary to test different approaches for better simulating volcanic outgassing contexts characterised by various thermodynamic conditions. For reproducing the gas chemical speciation at high pressure, I have simulated the real gas behaviour whereas, I have simulated the ideal gas behaviour for analysing the volcanic outgassing at surface with high temperature and low pressure. Almost 90% of the volcanic outgassed species are represented by the C-O-H system (Oppenheimer et al., 2014). Therefore, the first step for analysing the volcanic species and the corresponding outgassed atmospheres for rocky planets was to simulate the gas chemical speciation at the surface considering H_2O, H_2, CO_2 and CO. I have included also the methane was in some simulations but CH_4 is stable only at low temperatures or high pressures and for very reducing states (Ramirez et al., 2007; Wetzel et al., 2013). For these reasons, methane is considered to be not directly outgassed from silicate melt but it is mostly associated to hydrothermal outgassing (Chiodini, 2009). The sulphur species represent another important group of volcanic volatiles. I developed a numerical model that simulates the entire C-O-H-S system (e.g. H_2O, H_2, CO_2, CO, CH_4, H_2S and SO_2) but the range of stability, in terms of temperature and pressure, was limited. The simulations are stable only at low temperatures, approximately less than 1000 K. Most of the applications were performed with the numerical model which reproduces the volatile chemical speciation of the C-O-H system assuming an ideal gas behaviour and not considering the methane. This setup is the most stable for investigating the volcanic outgassing at surface, for low pressure (e.g. less than 300 bar) and for the typical temperature interval of silicate melt (ca. 1000 - 1500 K). The principal results of the application of the chemical speciation model are collected in three research papers, namely Ortenzi et al. (2020); Katyal et al. (2020); Guimond et al. (2021). The papers are the result of the collaboration with TRR-170 subprojects at the Freie Universitaet Berlin and the extrasolar planets and atmospheres department at the DLR and other research institutions. The research paper Ortenzi et al. (2020) (see section 3.1 for details) investigates the influences of the mantle redox states on the volcanic outgassing and on the chemical composition of the corresponding outgassed atmospheres for rocky planets. In order to simulate the volatile transition from the interior to the atmosphere, the chemical speciation model was coupled with a model that simulates the mantle convection and the volume of silicate melt produced, with a model that simulates the atmospheric thickness. The simulations were performed considering the contribution of the outgassing of silicate melts at surface for rocky planets of mass between 1 and 8 Earth masses. The main results is that the mantle redox state is the parameter which drives the volatile composition and the atmospheric thickness of the outgassed atmospheres. In reducing conditions the principal gas phases released are H_2 and only moderated gases as CO and H_2O. Whereas, in oxidising conditions the dominant outgassed volatile phases are H_2O and CO_2. The volatile composition affects the atmospheric thickness and the pressure at surface. In reducing scenarios the atmospheric thickness is larger and the pressure is lower compared to the oxidising cases. The presented atmospheric simulations can be compared with past and future observations of rocky exoplanet atmospheres. The aforementioned results are part also of the accepted review paper about the planetary ingassing/outgassing (Gaillard et al., 2021), where I participated as co-author. In Guimond et al. (2021) (see section 3.2 for details), we investigated the volcanic outgassing and the related atmosphere during the early Earth evolution considering that plate tectonics was not yet started. We coupled the chemical speciation model with a 2D numerical mantle convective model for establishing the flux of volatiles. The results confirms that the mantle redox state was the main factor that leads the volcanic outgassing at surface producing atmospheres rich in H_2O and CO_2 for the oxidised scenarios and H_2 rich with lower H_2O, CO_2 and CO for the reducing cases. Another application of the speciation model was carried out in Katyal et al. (2020) (see section 3.3). Here, we investigated the early Earth outgassing during the magma ocean period. We coupled an interior convective model with the chemical speciation model for investigating the outgassed species. The results then where inserted in a line-by-line radiative transfer model for determining the infrared emission and transmission of the planet. Even in this case, the mantle oxygen fugacity drives the composition of the outgassed volatile species. The simulated atmospheres present different characteristics in terms of atmospheric thickness and pressure at surface and consequently various emitted/transmitted spectra. In reducing conditions, the estimated atmospheres are rich in H_2, thin and they emit more radiation to the space compared to oxidising states. The results collected can be applied for investigating the interior/atmosphere interactions considering the detection of exoplanets infrared spectra.

My research period at the DLR was also characterised by the completion of the research paper Paredes-Mariño et al. (2017) (section 3.4.1). A significant portion of the results presented in the paper were collected during the research carried out for my master thesis. I performed 3D image analyses applying the fractal theory for investigating the basalt fragmentation on pumices samples from Sete Cidades (Azores, Portugal). During the PhD, I have participated also in activities that gave the opportunity to evaluate directly on the field the volcanic outgassing such as the participation to the ”Etna International Summer School: science meets practice” held in 2018. I visited the summit craters of the Etna Volcano together with experts of the INGV (National Institute of Geophysics and Volcanology) and of other research institutions in order to become familiar with some of the most common measuring techniques for investigating and sampling the volcanic gases. I have participated to three consecutive editions of the ”Vulcano International Summer School” held on the Vulcano Island (Aeolian Islands, Italy). Vulcano island was a perfect location for combining planetary science, with some terrain analogues for Mars and Moon, and Earth Sciences. Some of the most interesting results are collected in the research paper by Rammelkamp et al. (2021) (section 3.4.3). Here, we described the test of an hand-held LIBS instrument for characterising the chemical composition of different lithologies and the possible application for interpreting past and future data collected on space missions.

In conclusion, the main focus of the thesis is about the developed volatile chemical speciation model and of its wide utilization for analysing the volcanic outgassing in different contexts. The principal outcomes and implications of the chemical speciation model are:

- **Applications of the chemical speciation model.** I have presented how the chemical speciation can be applied for investigating the volatile outgassing in a wide range of scenarios including, magma ocean or rocky planets with stagnant lid convective regime. The main novelties introduced with the applications of the chemical speciation model are collected in the research papers developed during the PhD (Section 3). The principal findings of the papers show that the redox state of the mantle is a central parameter for investigating not only the outgassed atmosphere during the early Earth evolution but also the atmospheric composition of exoplanets. The results highlight how the chemical speciation model can be applied as a tool for exploring the entire volatile path considering the volatile outgassing as the connection within the interior and the atmosphere of a planet.

- **Versatility of the chemical speciation model.** One of my principal goal was to develop a speciation model for analysing several outgassing contexts and with a wide range of applications. The volatile chemical speciation for the C-O-H system (Section 2.6 for details) simulates the silicate melt degassing for the typical surface outgassing condition. It covers the entire pressure and temperature range of silicate melts at surface (i.e. considering real gas behavior < 300 bar and $800 <$ Temperature < 1500 K). In order to investigate the volcanic outgassing with a multidisciplinary approach, I have designed the volatile chemical speciation model for being easily combined with other models. Thus, I would to highlight that the chemical speciation model can be modified or adapted according to the characteristics of the outgassing scenario. The model has been already coupled with different solubility models (section 2.5) or with different parametrization for reproducing the redox state of the system. As reported in section 3, the chemical speciation model was coupled to different mantle convective regime and atmospheric models for investigating the outgassing of magma ocean or stagnant lid planets.

- **Limitations of the chemical speciation model.** In order to simulate the volcanic outgassing of different volatile species, I have developed three versions of the volatile chemical speciation model. The first one considers the ideal gas behaviour and I have designed it for investigating the C-O-H system considering as outgassed species H_2O, H_2, CO_2 and CO (see section 2.6 for details). This version of the chemical speciation model is the most stable and flexible and for these reasons was the one employed in most of the applications and in the research papers. It can be applied in a wide range of pressure and temperature for simulating volcanic outgassing at surface but, it is not designed for investigating outgassing at pressure higher than ca. 300 bar. In any case, considering the typical volatile contents of silicate melts, the majority of volatiles are not outgassed for pressure higher than 300 bar. The second variation of the chemical speciation model analyses the outgassing of the C-O-H system considering a real gas behaviour and including methane as volatile species (section 2.8 for details). Due to the presence of methane, this version can be applied for investigating a limited range of temperature and oxidation state of the system. Methane is stable only at low temperature and in very reducing conditions of the system or at very high pressure (Chiodini, 2009; Wetzel et al., 2013; Ramirez et al., 2007; Zhang and Duan, 2009; Oppenheimer et al., 2014). CH_4 is usually associated to hydrothermal outgassing and not to the active outgassing of silicate melts. Thus, this model can simulate the volcanic outgassing only for temperature lower than ca. 1000 K. The last version reproduces the degassing of the C-O-H-S system. The latter speciation model presents limitation due to the presence of methane and to the temperature range of the sulphur fugacity (Section 2.9 for details). This version of the chemical speciation model is mostly limited to the range of validity of the selected sulphur fugacity which is delimited by the interval $576 <$ Temperature $<$ 1016 K.

- **Outlook.** The flexibility of the model gives a wide range of possible future applications and improvements of the chemical speciation model. The chemical speciation model can be improved in several aspects. Specifically, the principal directions for developing the model include a better characterization of the outgassing considering high pressure and adding more volatile species (e.g. Halogens and ammonia). Another future direction is the coupling of the volatile chemical speciation model with atmospheric models that consider the kinetics of volatile reactions and the corresponding evolution of the atmospheric composition. To give some examples of future developments, I describe more in detail some possible improvements of the chemical speciation model. The range of pressure and temperature for applying the speciation model present some limitations. An extension of the pressure window of investigation can provide to the volatile chemical speciation model a broader range of application. It can be applied for analysing the passive volcanic outgassing or the outgassing at surface of planets with an high atmospheric pressure. A wider validity range for the sulphur species can provide simulations of volatile outgassing of the majority of volcanic gas phases. In Ortenzi et al. (2020); Katyal et al. (2020) and Guimond et al. (2021) the atmospheric compositions were simulated considering that the system was at the chemical equilibrium. A future development could be to take into consideration the evolution of the atmospheric composition over time considering the interactions and the stability of the volatile molecules in the atmosphere. Another interesting direction for developing the chemical speciation model is to analyse the volcanic outgassing not only directly from silicate melts but also considering the interactions in a hydrothermal context. In this case, the volcanic outgassing analysis can be used also as a tool for astrobiology applications and for the investigation of favorable conditions for the emergence of life.

Acknowledgments

I would like to thank Frank Sohl and Lena Noack for their work, guidance and support during the whole period of my PhD. Their sharing of new ideas and scientific knowledge was fundamental for my research. Thanks to the TRR-170 ”Late Accretion onto terrestrial planets” project for granting me the opportunity to carry out my research projects. I am grateful for having found a special and stimulating atmosphere at the DLR and particularly, I would thank to Doris Breuer, Heike Rauer and all the members of the Planetary Physics and Extrasolar Planets and Atmospheres departments at the German Aerospace Center. I would also thank to Nasia, Nisha, Maxime, Hugo and Mika for the great time at the DLR and for the unforgettable period in Berlin. My thanks go to Renate Schubert and to all the staff members at the DLR for their work and for being always helpful in the last four years. For the fruitful discussions during the writing of the thesis, my thanks go also to Sara Vulpius, Caroline Brachmann, Lukas Manske and Nick Wogan. A special thank to my family and my friends for always being close to me.

5 Appendix

5.1 List of figures

5.2 List of tables

*

References

Abel, M., Frommhold, L., Li, X., and Hunt, K. (2011). Collision-induced absorption by H_2 pairs: from hundreds to thousands of kelvin. *J. Phys. Chem. A*, 115:6805–6812.

Afonso, J. C., Ranalli, G., and Fernàndez, M. (2005). Thermal expansivity and elastic properties of the lithospheric mantle: results from mineral physics of composites. *Physics of the Earth and Planetary Interiors*, 149(3):279 – 306.

Albarede, F., Ballhaus, C., Blichert-Toft, J., Lee, C.-T., Marty, B., Moynier, F., and Yin, Q.-Z. (2013). Asteroidal impacts and the origin of terrestrial and lunar volatiles. *Icarus*, 222(1):44 – 52.

Albarède, F. (2009). Volatile accretion history of the terrestrial planets and dynamic implications. *Nature*, 461(7268):1227–1233.

Amundsen, H. and Neumann, E.-R. (1992). Redox control during mantle/melt interaction. *Geochimica et Cosmochimica Acta*, 56(6):2405 – 2416.

Armstrong, K., Frost, D. J., McCammon, C. A., Rubie, D. C., and Boffa Ballaran, T. (2019). Deep magma ocean formation set the oxidation state of Earth's mantle. *Science*, 365(6456):903–906.

Aulbach, S. and Stagno, V. (2016). Evidence for a reducing Archean ambient mantle and its effects on the carbon cycle. *Geology*, 44(9):751–754.

Avice, G., Marty, B., and Burgess, R. (2017). The origin and degassing history of the Earth's atmosphere revealed by archean xenon. *Nature Communications*, 8(1):15455.

Baranov, Y. I. (2018). Collision-induced absorption in the region of the $\nu_2 + \nu_3$ band of carbon dioxide. *Journal of Molecular Spectroscopy*, 345:11–16.

Barth, P., Carone, L., Barnes, R., Noack, L., Mollière, P., and Henning, T. (2020). Magma ocean evolution of the TRAPPIST-1 planets. *arXiv e-prints*, page arXiv:2008.09599.

Benneke, B. and Seager, S. (2012). Atmospheric Retrieval for Super-Earths: Uniquely Constraining the Atmospheric Composition with Transmission Spectroscopy. *The Astrophysical Journal*, 753(2):100.

Blundy, J., Cashman, K. V., Rust, A., and Witham, F. (2010). A case for CO_2-rich arc magmas. *Earth and Planetary Science Letters*, 290(3):289 – 301.

Bower, D. J., Kitzmann, D., Wolf, A. S., Sanan, P., Dorn, C., and Oza, A. V. (2019). Linking the evolution of terrestrial interiors and an early outgassed atmosphere to astrophysical observations. *Astronomy & Astrophysics*, 631:A103.

Breuer, D. (2009). 4.2.3.4 Dynamics and thermal evolution: Datasheet from Landolt-Börnstein - Group VI Astronomy and Astrophysics · Volume 4B: “Solar System” in SpringerMaterials (https://doi.org/10.1007/978-3-540-88055-4_19). Copyright 2009 Springer-Verlag Berlin Heidelberg.

Brown, S. M., Elkins-Tanton, L. T., and Walker, R. J. (2014). Effects of magma ocean crystallization and overturn on the development of 142Nd and 182W isotopic heterogeneities in the primordial mantle. *Earth and Planetary Science Letters*, 408:319–330.

Burnham, C. W. (1967). Hydrothermal fluids at the magmatic stage. *Geochemistry of hydrothermal ore deposits*, 20:34–76.

Byrne, P. K. (2020). A comparison of inner solar system volcanism. *Nature Astronomy*, 4(4):321–327.

Canil, D. (1997). Vanadium partitioning and the oxidation state of archaean komatiite magmas. *Nature*, 389:842 EP –.

Catling, D. C. and Kasting, J. F. (2017). *Atmospheric evolution on inhabited and lifeless worlds*. Cambridge University Press.

Catling, D. C. and Zahnle, K. J. (2020). The Archean atmosphere. *Science Advances*, 6(9).

Charnay, B., Hir, G. L., Fluteau, F., Forget, F., and Catling, D. C. (2017). A warm or a cold early Earth? new insights from a 3-D climate-carbon model. *Earth and Planetary Science Letters*, 474:97 – 109.

Charnay, B., Wolf, E. T., Marty, B., and Forget, F. (2020). Is the faint young Sun problem for Earth solved?

Chase, M. J. E. (1999). Tables, NIST-JANAF Thermochemical. *Journal of Physical and Chemical Reference Data*, 14(Suppl 1).

Chiodini, G. (2009). CO_2/CH_4 ratio in fumaroles a powerful tool to detect magma degassing episodes at quiescent volcanoes. *Geophysical Research Letters*, 36(2).

Cogné, J.-P. and Humler, E. (2006). Trends and rhythms in global seafloor generation rate. *Geochemistry, geophysics, geosystems*, 7(3).

Crisp, J. A. (1984). Rates of magma emplacement and volcanic output. *Journal of Volcanology and Geothermal Research*, 20(3-4):177–211.

Dasgupta, R. and Hirschmann, M. M. (2010). The deep carbon cycle and melting in Earth's interior. *Earth and Planetary Science Letters*, 298(1):1 – 13.

Dauphas, N. (2017). The isotopic nature of the Earth's accreting material through time. *Nature*, 541(7638):521–524.

de Santis, R., Breedveld, G., and Prausnitz, J. M. (1974). Thermodynamic properties of aqueous gas mixtures at advanced pressures. *Industrial & Engineering Chemistry Process Design and Development*, 13(4):374–377.

Debaille, V., O'Neill, C., Brandon, A. D., Haenecour, P., Yin, Q.-Z., Mattielli, N., and Treiman, A. H. (2013). Stagnant-lid tectonics in early Earth revealed by 142Nd variations in late Archean rocks. *Earth and Planetary Science Letters*, 373:83–92.

Delano, J. W. (2001). Redox history of the Earth's interior since $\sim$3900 Ma: Implications for prebiotic molecules. *Origins of life and evolution of the biosphere*, 31(4):311–341.

Ding, F. and Pierrehumbert, R. T. (2016). Convection in Condensible-rich Atmospheres. *The Astrophysical Journal*, 822(1):24.

Dixon, J. E., Clague, D. A., and Stolper, E. M. (1991). Degassing history of water, sulfur, and carbon in submarine lavas from Kilauea Volcano, Hawaii. *The Journal of Geology*, 99(3):371–394.

Dixon, J. E., Stolper, E. M., and Holloway, J. R. (1995). An experimental study of water and carbon dioxide solubilities in mid-ocean ridge basaltic liquids. Part i: calibration and solubility models. *Journal of Petrology*, 36(6):1607–1631.

Dorn, C. and Heng, K. (2018). Secondary Atmospheres on HD 219134 b and c. *The Astrophysical Journal*, 853(1):64.

Dorn, C., Noack, L., and Rozel, A. (2018). Outgassing on stagnant-lid super-Earths. *Astronomy & Astrophysics*, 614:A18.

Ducrot, E., Gillon, M., Delrez, L., Agol, E., Rimmer, P., Turbet, M., Günther, M., Demory, B.-O., Triaud, A., Bolmont, E., et al. (2020). TRAPPIST-1: Global results of the Spitzer Exploration Science Program Red Worlds. *Astronomy & Astrophysics*, 640:A112.

Edwards, B., Mugnai, L., Tinetti, G., Pascale, E., and Sarkar, S. (2019). An Updated Study of Potential Targets for Ariel. *The Astronomical Journal*, 157(6):242.

Elkins-Tanton, L. (2008). Linked magma ocean solidification and atmospheric growth for Earth and Mars. *Earth and Planetary Science Letters*, 271(1-4):181–191.

Elkins-Tanton, L. T. (2012). Magma Oceans in the Inner Solar System. *Annual Review of Earth and Planetary Sciences*, 40(1):113–139.

Elkins-Tanton, L. T. and Seager, S. (2008). Coreless terrestrial exoplanets. *The Astrophysical Journal*, 688(1):628.

Fauchez, T. J., Turbet, M., Villanueva, G. L., Wolf, E. T., Arney, G., Kopparapu, R. K., Lincowski, A., Mandell, A., de Wit, J., Pidhorodetska, D., Domagal-Goldman, S. D., and Stevenson, K. B. (2019). Impact of Clouds and Hazes on the Simulated JWST Transmission Spectra of Habitable Zone Planets in the TRAPPIST-1 System. *The Astrophysical Journal*, 887(2):194.

Fegley, B. (2013). Chapter 10 - Chemical Equilibria. In Fegley, B., editor, *Practical Chemical Thermodynamics for Geoscientists*, pages 423 – 508. Academic Press, Boston.

Fegley, B. and Schaefer, L. (2014). 6.3 - Chemistry of Earth's Earliest Atmosphere. In Holland, H. D. and Turekian, K. K., editors, *Treatise on Geochemistry (Second Edition)*, pages 71 – 90. Elsevier, Oxford, second edition.

Fischer-Gödde, M. and Kleine, T. (2017). Ruthenium isotopic evidence for an inner Solar System origin of the late veneer. *Nature*, 541(7638):525–527.

Flowers, G. C. (1979). Correction of Holloway's (1977) adaptation of the modified Redlich-Kwong equation of state for calculation of the fugacities of molecular species in supercritical fluids of geologic interest. *Contributions to Mineralogy and Petrology*, 69(3):315–318.

Foley, B. J. and Driscoll, P. E. (2016). Whole planet coupling between climate, mantle, and core: Implications for rocky planet evolution. *Geochemistry, Geophysics, Geosystems*, 17(5):1885–1914.

Foley, B. J. and Smye, A. J. (2018). Carbon Cycling and Habitability of Earth-Sized Stagnant Lid Planets. *Astrobiology*, 18:873–896.

Freedman, R. S., Lustig-Yaeger, J., Fortney, J. J., Lupu, R. E., Marley, M. S., and Lodders, K. (2014). Gaseous mean opacities for giant planet and ultracool dwarf atmospheres over a range of metallicities and temperatures. *The Astrophysical Journal Supplement Series*, 214(2):25.

French, B. M. (1966). Some geological implications of equilibrium between graphite and a C-H-O gas phase at high temperatures and pressures. *Reviews of Geophysics*, 4(2):223–253.

Frost, D., Mann, U., and Asahara, Y. Rubie, D. (2008). The redox state of the mantle during and just after core formation. *Philosophical Transactions of the Royal Society A: Mathematical, Physical and Engineering Sciences*, 366(1883):4315–4337.

Frost, D. J. and McCammon, C. A. (2008). The redox state of earth's mantle. *Annual Review of Earth and Planetary Sciences*, 36(1):389–420.

Gaillard, F., Bouhifd, M. A., Furi, E., Malavergne, V., Marrocchi, Y., Noack, L., Ortenzi, G., Roskocz, M., and Vulpius, S. (2021). The diverse planetary ingassing/outgassing paths produced over billions of years of magmatic activity. *Space science reviews. (Accepted).*

Gaillard, F., Pichavant, M., Mackwell, S., Champallier, R., Scaillet, B., and McCammon, C. (2003). Chemical transfer during redox exchanges between H_2 and Fe-bearing silicate melts. *American mineralogist*, 88(2-3):308–315.

Gaillard, F. and Scaillet, B. (2014). A theoretical framework for volcanic degassing chemistry in a comparative planetology perspective and implications for planetary atmospheres. *Earth and Planetary Science Letters*, 403:307–316.

Gaillard, F., Scaillet, B., and Arndt, N. T. (2011). Atmospheric oxygenation caused by a change in volcanic degassing pressure. *Nature*, 478:229–232.

Gaillard, F., Scaillet, B., Pichavant, M., and Iacono-Marziano, G. (2015). The redox geodynamics linking basalts and their mantle sources through space and time. *Chemical Geology*, 418:217–233.

Genda, H., Brasser, R., and Mojzsis, S. J. (2017). The terrestrial late veneer from core disruption of a lunar-sized impactor. *Earth and Planetary Science Letters*, 480:25–32.

Gerlach, T. (2011). Volcanic versus anthropogenic carbon dioxide. *Eos, Transactions American Geophysical Union*, 92(24):201–202.

Ghiorso, M. S. and Gualda, G. A. (2015). An H_2O – CO_2 mixed fluid saturation model compatible with rhyolite-melts. *Contributions to Mineralogy and Petrology*, 169(6):1–30.

Giordano, D., Russell, J. K., and Dingwell, D. B. (2008). Viscosity of magmatic liquids: a model. *Earth and Planetary Science Letters*, 271(1-4):123–134.

Goldblatt, C., Robinson, T. D., Zahnle, K. J., and Crisp, D. (2013). Low simulated radiation limit for runaway greenhouse climates. *Nature Geoscience*, 6(8):661–667.

Gomes, R., Levison, H. F., Tsiganis, K., and Morbidelli, A. (2005). Origin of the cataclysmic Late Heavy Bombardment period of the terrestrial planets. *Nature*, 435(7041):466–469.

Gordon, I. E., Rothman, L. S., Hill, C., Kochanov, R. V., Tan, Y., Bernath, P. F., Birk, M., Boudon, V., Campargue, A., Chance, K. V., Drouin, B. J., Flaud, J. M., Gamache, R. R., Hodges, J. T., Jacquemart, D., Perevalov, V. I., Perrin, A., Shine, K. P., Smith, M. A. H., Tennyson, J., Toon, G. C., Tran, H., Tyuterev, V. G., Barbe, A., Császár, A. G., Devi, V. M., Furtenbacher, T., Harrison, J. J., Hartmann, J. M., Jolly, A., Johnson, T. J., Karman, T., Kleiner, I., Kyuberis, A. A., Loos, J., Lyulin, O. M., Massie,

S. T., Mikhailenko, S. N., Moazzen-Ahmadi, N., Müller, H. S. P., Naumenko, O. V., Nikitin, A. V., Polyansky, O. L., Rey, M., Rotger, M., Sharpe, S. W., Sung, K., Starikova, E., Tashkun, S. A., Auwera, J. V. e., Wagner, G., Wilzewski, J., Wcisło, P., Yu, S., and Zak, E. J. (2017). The HITRAN2016 molecular spectroscopic database. *Journal of Quantitative Spectroscopy and Radiative Transfer*, 203:3–69.

Greenwood, R. C., Barrat, J. A., Miller, M. F., Anand , M., Dauphas, N., Franchi, I. A., Sillard, P., and Starkey, N. A. (2018). Oxygen Isotope Evidence for a High-Energy Moon-Forming Giant Impact and Early Delivery of Earth's Water. In *81st Annual Meeting of the Meteoritical Society*, volume 81, page 6345.

Grott, M., Morschhauser, A., Breuer, D., and Hauber, E. (2011). Volcanic outgassing of CO_2 and H_2O on Mars. *Earth and Planetary Science Letters*, 308(3-4):391–400.

Guimond, C. M., Noack, L., Ortenzi, G., and Sohl, F. (2021). The early Earth's volcanic outgassing rates from mantle convection, melting, and volatile speciation. *Physics of the Earth and Planetary Interiors. (In review).*

Hamano, K., Abe, Y., and Hidenori, G. (2013). Emergence of two types of terrestrial planet on solidification of magma ocean. *Nature*, 497:607–610.

Hamano, K., Kawahara, H., Abe, Y., Onishi, M., and Hashimoto, G. L. (2015). Lifetime and Spectral Evolution of a Magma Ocean with a Steam Atmosphere: Its Detectability by Future Direct Imaging. *The Astrophysical Journal*, 806(2):216.

Hashimoto, G. L., Abe, Y., and Sugita, S. (2007). The chemical composition of the early terrestrial atmosphere: Formation of a reducing atmosphere from CI-like material. *Journal of Geophysical Research (Planets)*, 112(E5):E05010.

Hauri, E. H., Cottrell, E., Kelley, K. A., Tucker, J. M., Shimizu, K., Voyer, M. L., Marske, J., and Saal, A. E. (2019). Carbon in the convecting mantle. In Orcutt, B. N., Daniel, I., and Dasgupta, R., editors, *Deep Carbon: Past to Present*, page 237–275. Cambridge University Press.

Hauri, E. H., Maclennan, J., McKenzie, D., Gronvold, K., Oskarsson, N., and Shimizu, N. (2017). CO_2 content beneath northern Iceland and the variability of mantle carbon. *Geology*, 46(1):55–58.

Hernlund, J. W. and Tackley, P. J. (2008). Modeling mantle convection in the spherical annulus. *Physics of the Earth and Planetary Interiors*, 171(1):48–54.

Herzberg, C., Condie, K., and Korenaga, J. (2010). Thermal history of the Earth and its petrological expression. *Earth and Planetary Science Letters*, 292(1):79 – 88.

Hessler, A. M., Lowe, D. R., Jones, R. L., and Bird, D. K. (2004). A lower limit for atmospheric carbon dioxide levels 3.2 billion years ago. *Nature*, 428(6984):736–738.

Hier-Majumder, S. and Hirschmann, M. M. (2017). The origin of volatiles in the Earth's mantle. *Geochemistry, Geophysics, Geosystems*, 18(8):3078–3092.

Hill, R. (1992). An efficient lightning energy source on the early Earth. *Origins of Life and Evolution of the Biosphere*, 22(5):277–285.

Hirschmann, M. M. (2000). Mantle solidus: Experimental constraints and the effects of peridotite composition. *Geochemistry, Geophysics, Geosystems*, 1, (10)(10).

Hirschmann, M. M. (2012). Magma ocean influence on early atmosphere mass and composition. *Earth and Planetary Science Letters*, 341:48–57.

Holland, H. D. (1984). *The chemical evolution of the atmosphere and oceans*. Princeton University Press.

Holloway, J. (1981). *Volatile Interactions in Magmas*, pages 273–293. Springer Nature Switzerland.

Holloway, J. R. (1976). Fluids in the evolution of granitic magmas: consequences of finite CO_2 solubility. *Geological Society of America Bulletin*, 87(10):1513–1518.

Holloway, J. R. (1998). Graphite-melt equilibria during mantle melting: constraints on CO_2 in MORB magmas and the carbon content of the mantle. *Chemical Geology*, 147(1-2):89–97.

Holloway, J. R. and Blank, J. G. (1994). Application of experimental results to COH species in natural melts. *Reviews in mineralogy*, 30:187–187.

Holloway, J. R., Pan, V., and Gudmundsson, G. (1992). High-pressure fluid-absent melting experiments in the presence of graphite: oxygen fugacity, ferric/ferrous ratio and dissolved CO_2. *European Journal of Mineralogy*, 4:105–114.

Höning, D., Tosi, N., and Spohn, T. (2019). Carbon cycling and interior evolution of water-covered plate tectonics and stagnant-lid planets. *Astronomy and Astrophysics*, 627:A48.

Hopp, T. and Kleine, T. (2018). Nature of late accretion to Earth inferred from mass-dependent Ru isotopic compositions of chondrites and mantle peridotites. *Earth and Planetary Science Letters*, 494:50–59.

Huang, J. (2018). A Simple Accurate Formula for Calculating Saturation Vapor Pressure of Water and Ice. *Journal of Applied Meteorology and Climatology*, 57(6):1265–1272.

Huizenga, J.-M. (2001). Thermodynamic modelling of C–O–H fluids. *Lithos*, 55(1-4):101–114.

Huizenga, J. M. (2005). COH, an excel spreadsheet for composition calculations in the COH fluid system. *Comput. Geosci.*, 31(6):797–800.

Hunten, D. M. (1973). The Escape of Light Gases from Planetary Atmospheres. *Journal of Atmospheric Sciences*, 30(8):1481–1494.

Hunten, D. M. and Donahue, T. M. (1976). Hydrogen Loss from the Terrestrial Planets. *Annual Review of Earth and Planetary Sciences*, 4:265.

Iacono-Marziano, G., Morizet, Y., Le Trong, E., and Gaillard, F. (2012). New experimental data and semi-empirical parameterization of H_2O – CO_2 solubility in mafic melts. *Geochimica et Cosmochimica Acta*, 97:1–23.

Ito, Y., Ikoma, M., Kawahara, H., Nagahara, H., Kawashima, Y., and Nakamoto, T. (2015). Theoretical Emission Spectra of Atmospheres of Hot Rocky Super-Earths. *The Astrophysical Journal*, 801(2):144.

Janle, P., Basilevsky, A. T., Kreslavsky, M. A., and Slyuta, E. N. (1992). Heat loss and tectonic style of Venus. *Earth, Moon, and Planets*, 58(1):1–29.

Jing, Z. and Karato, S. (2009). The density of volatile bearing melts in the Earth's deep mantle: The role of chemical composition. *Chemical Geology*, 262(1-2):100–107.

Johnson, A. P., Cleaves, H. J., Dworkin, J. P., Glavin, D. P., Lazcano, A., and Bada, J. L. (2008). The Miller volcanic spark discharge experiment. *Science*, 322(5900):404–404.

Johnstone, C., Güdel, M., Stökl, A., Lammer, H., Tu, L., Kislyakova, K., Lüftinger, T., Odert, P., Erkaev, N., and Dorfi, E. (2015). The evolution of stellar rotation and the hydrogen atmospheres of habitable-zone terrestrial planets. *The Astrophysical Journal Letters*, 815(1):L12.

Johnstone, C. P., Khodachenko, M. L., Lüftinger, T., Kislyakova, K. G., Lammer, H., and Güdel, M. (2019). Extreme hydrodynamic losses of Earth-like atmospheres in the habitable zones of very active stars. *Astronomy & Astrophysics*, 624:L10.

Jontof-Hutter, D. (2019). The compositional diversity of low-mass exoplanets. *Annual Review of Earth and Planetary Sciences*, 47:141–171.

Kadoya, S., Catling, D., Nicklas, R., Puchtel, I., and Anbar, A. (2020). Mantle cooling causes more reducing volcanic gases and gradual reduction of the atmosphere. *Geochem. Perspect. Lett.*, 13:25–29.

Kadoya, S. and Tajika, E. (2014). Conditions for oceans on Earth-like planets orbiting within the habitable zone: Importance of volcanic CO_2 degassing. *The Astrophysical Journal*, 790(2):107.

Kadoya, S. and Tajika, E. (2015). Evolutionary Climate Tracks of Earth-like Planets. *The Astrophysical Journal Letters*, 815(1):L7.

Kaltenegger, L. and Traub, W. A. (2009). Transits of Earth-like Planets. *The Astrophysical Journal*, 698(1):519–527.

Kaltenegger, L., Traub, W. A., and Jucks, K. W. (2007). Spectral Evolution of an Earth-like Planet. *The Astrophysical Journal*, 658(1):598–616.

Kanzaki, Y. and Murakami, T. (2018). Effects of atmospheric composition on apparent activation energy of silicate weathering: II. implications for evolution of atmospheric CO_2 in the precambrian. *Geochimica et Cosmochimica Acta*, 240:314 – 330.

Karato, S.-I. and Wu, P. (1993). Rheology of the upper mantle: A synthesis. *Science*, 260(5109):771–778.

Karman, T., Gordon, I. E., van der Avoird, A., Baranov, Y. I., Boulet, C., Drouin, B. J., Groenenboom, G. C., Gustafsson, M., Hartmann, J.-M., Kurucz, R. L., Rothman, L. S., Sun, K., Sung, K., Thalman, R., Tran, H., Wishnow, E. H., Wordsworth, R., Vigasin, A. A., Volkamer, R., and van der Zande, W. J. (2019). Update of the HITRAN collision-induced absorption section. *Icarus*, 328:160–175.

Kasting, J. F. (1988). Runaway and moist greenhouse atmospheres and the evolution of Earth and Venus. *Icarus*, 74(3):472–494.

Kasting, J. F. (1990). Bolide impacts and the oxidation state of carbon in the Earth's early atmosphere. *Origins of Life and Evolution of the Biosphere*, 20(3-4):199–231.

Kasting, J. F., Eggler, D. H., and Raeburn, S. P. (1993). Mantle redox evolution and the oxidation state of the Archean atmosphere. *The Journal of geology*, 101(2):245–257.

Katyal, N., Nikolaou, A., Godolt, M., Grenfell, J. L., Tosi, N., Schreier, F., and Rauer, H. (2019). Evolution and Spectral Response of a Steam Atmosphere for Early Earth with a Coupled Climate–Interior Model. *The Astrophysical Journal*, 875(1):31.

Katyal, N., Ortenzi, G., Grenfell, J. L., Noack, L., Sohl, F., Godolt, M., Muñoz, A. G., Schreier, F., Wunderlich, F., and Rauer, H. (2020). Effect of mantle oxidation state and escape upon the evolution of Earth's magma ocean atmosphere. *Astronomy & Astrophysics*, 643:A81.

Katz, R. F., Spiegelman, M., and Langmuir, C. H. (2003). A new parameterization of hydrous mantle melting. *Geochemistry, Geophysics, Geosystems*, 4(9).

Kegler, P., Holzheid, A., Frost, D., Rubie, D., Dohmen, R., and Palme, H. (2008). New Ni and Co metal-silicate partitioning data and their relevance for an early terrestrial magma ocean. *Earth and Planetary Science Letters*, 268(1-2):28–40.

Kite, E. S. and Barnett, M. (2020). Exoplanet secondary atmosphere loss and revival. *arXiv e-prints*, page arXiv:2006.02589.

Kite, E. S., Manga, M., and Gaidos, E. (2009). Geodynamics and rate of volcanism on massive Earth-like planets. *The Astrophysical Journal*, 700(2):1732.

Kitzmann, D., Patzer, A. B. C., von Paris, P., Godolt, M., and Rauer, H. (2011a). Clouds in the atmospheres of extrasolar planets. II. Thermal emission spectra of Earth-like planets influenced by low and high-level clouds. *Astronomy & Astrophysics*, 531:A62.

Kitzmann, D., Patzer, A. B. C., von Paris, P., Godolt, M., and Rauer, H. (2011b). Clouds in the atmospheres of extrasolar planets. III. Impact of low and high-level clouds on the reflection spectra of Earth-like planets. *Astronomy & Astrophysics*, 534:A63.

Kopparapu, R. K., Ramirez, R., Kasting, J. F., Eymet, V., Robinson, T. D., Mahadevan, S., Terrien, R. C., Domagal-Goldman, S., Meadows, V., and Deshpande, R. (2013). Habitable Zones around Main-sequence Stars: New Estimates. *The Astrophysical Journal*, 765(2):131.

Korenaga, J. (2006). Archean geodynamics and the thermal evolution of Earth. *Geophysical Monograph-American Geophysical Union*, 164:7.

Koskinen, T. T., Lavvas, P., Harris, M. J., and Yelle, R. V. (2014). Thermal escape from extrasolar giant planets. *Philosophical Transactions of the Royal Society of London Series A*, 372(2014):20130089–20130089.

Kramers, J. D. (1998). Reconciling siderophile element data in the Earth and Moon, W isotopes and the upper lunar age limit in a simple model of homogeneous accretion. *Chemical geology*, 145(3-4):461–478.

Kreidberg, L., Koll, D. D. B., Morley, C., Hu, R., Schaefer, L., Deming, D., Stevenson, K. B., Dittmann, J., Vanderburg, A., Berardo, D., Guo, X., Stassun, K., Crossfield, I., Charbonneau, D., Latham, D. W., Loeb, A., Ricker, G., Seager, S., and Vand erspek, R. (2019). Absence of a thick atmosphere on the terrestrial exoplanet LHS 3844b. *Nature*, 573(7772):87–90.

Kress, V. C. and Carmichael, I. S. (1991). The compressibility of silicate liquids containing Fe_2O_3 and the effect of composition, temperature, oxygen fugacity and pressure on their redox states. *Contributions to Mineralogy and Petrology*, 108(1-2):82–92.

Krissansen-Totton, J., Arney, G. N., and Catling, D. C. (2018). Constraining the climate and ocean pH of the early Earth with a geological carbon cycle model. *Proceedings of the National Academy of Science*, 115:4105–4110.

Krissansen-Totton, J. and Catling, D. C. (2017). Constraining climate sensitivity and continental versus seafloor weathering using an inverse geological carbon cycle model. *Nature Communications*, 8(1):1–15.

Krissansen-Totton, J. and Catling, D. C. (2020). A coupled carbon-silicon cycle model over Earth history: Reverse weathering as a possible explanation of a warm mid-Proterozoic climate. *Earth and Planetary Science Letters*, 537:116181.

Krot, A., Keil, K., Scott, E., Goodrich, C., and Weisberg, M. (2014). Classification of meteorites and their genetic relationships. *Meteorites and Cosmochemical Processes*, 1:1–63.

Kuramoto, K., Umemoto, T., and Ishiwatari, M. (2013). Effective hydrodynamic hydrogen escape from an early Earth atmosphere inferred from high-accuracy numerical simulation. *Earth and Planetary Science Letters*, 375:312–318.

Lammer, H., Kislyakova, K. G., Odert, P., Leitzinger, M., Schwarz, R., Pilat-Lohinger, E., Kulikov, Y. N., Khodachenko, M. L., Güdel, M., and Hanslmeier, A. (2011). Pathways to Earth-Like Atmospheres. Extreme Ultraviolet (EUV)-Powered Escape of Hydrogen-Rich Protoatmospheres. *Origins of Life and Evolution of the Biosphere*, 41(6):503–522.

Lammer, H., Zerkle, A. L., Gebauer, S., Tosi, N., Noack, L., Scherf, M., Pilat-Lohinger, E., Güdel, M., Grenfell, J. L., Godolt, M., and Nikolaou, A. (2018). Origin and evolution of the atmospheres of early Venus, Earth and Mars. *The Astronomy and Astrophysics Review*, 26(1):2.

Lebrun, T., Massol, H., ChassefièRe, E., Davaille, A., Marcq, E., Sarda, P., Leblanc, F., and Brandeis, G. (2013). Thermal evolution of an early magma ocean in interaction with the atmosphere. *Journal of Geophysical Research (Planets)*, 118(6):1155–1176.

Lesher, C. E. and Spera, F. J. (2015). Chapter 5 - Thermodynamic and Transport Properties of Silicate Melts and Magma. In Sigurdsson, H., editor, *The Encyclopedia of Volcanoes (Second Edition)*, pages 113 – 141. Academic Press, Amsterdam, second edition.

Lide, D. R. (2000). *CRC handbook of chemistry and physics*. CRC Press.

Lodders, K. and Fegley Jr, B. (1997). An oxygen isotope model for the composition of Mars. *Icarus*, 126(2):373–394.

Lopes-Gautier, R., Doute, S., Smythe, W., Kamp, L., Carlson, R., Davies, A., Leader, F., McEwen, A. S., Geissler, P., Kieffer, S., et al. (2000). A close-up look at Io from Galileo's Near-Infrared Mapping Spectrometer. *Science*, 288(5469):1201–1204.

Luger, R. and Barnes, R. (2015). Extreme water loss and abiotic O_2 buildup on planets throughout the habitable zones of M dwarfs. *Astrobiology*, 15(2):119–143.

Lupu, R. E., Zahnle, K., Marley, M. S., Schaefer, L., Fegley, B., Morley, C., Cahoy, K., Freedman, R., and Fortney, J. J. (2014). The Atmospheres of Earthlike Planets after Giant Impact Events. *The Astrophysical Journal*, 784(1):27.

Lusk, J. and Bray, D. M. (2002). Phase relations and the electrochemical determination of sulfur fugacity for selected reactions in the Cu–Fe–S and Fe–S systems at 1 bar and temperatures between 185 and 460 °C. *Chemical Geology*, 192(3-4):227–248.

Madhusudhan, N. (2019). Exoplanetary atmospheres: Key insights, challenges, and prospects. *Annual Review of Astronomy and Astrophysics*, 57:617–663.

Mai, C. and Line, M. R. (2019). Exploring Exoplanet Cloud Assumptions in JWST Transmission Spectra. *The Astrophysical Journal*, 883(2):144.

Maiolino, R., Haehnelt, M., Murphy, M. T., Queloz, D., Origlia, L., Alcala, J., Alibert, Y., Amado, P. J., Allende Prieto, C., Ammler-von Eiff, M., Asplund, M., Barstow, M., Becker, G., Bonfils, X., Bouchy, F., Bragaglia, A., Burleigh, M. R., Chiavassa, A., Cimatti, D. A., Cirasuolo, M., Cristiani, S., D'Odorico, V., Dravins, D., Emsellem, E., Farihi, J., Figueira, P., Fynbo, J., Gansicke, B. T., Gillon, M., Gustafsson, B., Hill, V., Israelyan, G., Korn, A., Larsen, S., De Laverny, P., Liske, J., Lovis, C., Marconi, A., Martins, C., Molaro, P., Nisini, B., Oliva, E., Petitjean, P., Pettini, M., Recio Blanco, A., Rebolo, R., Reiners, A., Rodriguez-Lopez, C., Ryde, N., Santos, N. C., Savaglio, S., Snellen, I., Strassmeier, K., Tanvir, N., Testi, L., Tolstoy, E., Triaud, A., Vanzi, L., Viel, M., and Volonteri, M. (2013). A Community Science Case for E-ELT HIRES. *arXiv e-prints*, page arXiv:1310.3163.

Mann, U., Frost, D. J., and Rubie, D. C. (2009). Evidence for high-pressure core-mantle differentiation from the metal–silicate partitioning of lithophile and weakly-siderophile elements. *Geochimica et Cosmochimica Acta*, 73(24):7360–7386.

Marcq, E., Salvador, A., Massol, H., and Davaille, A. (2017). Thermal radiation of magma ocean planets using a 1-D radiative-convective model of H_2O-CO_2 atmospheres. *Journal of Geophysical Research (Planets)*, 122(7):1539–1553.

Marrero, T. R. and Mason, E. A. (1972). Gaseous Diffusion Coefficients. *Journal of Physical and Chemical Reference Data*, 1(1):3–118.

Marty, B. (2012). The origins and concentrations of water, carbon, nitrogen and noble gases on earth. *Earth and Planetary Science Letters*, 313-314:56 – 66.

Marty, B., Zimmermann, L., Pujol, M., Burgess, R., and Philippot, P. (2013). Nitrogen Isotopic Composition and Density of the Archean Atmosphere. *Science*, 342(6154):101–104.

Maurice, M., Tosi, N., Samuel, H., Plesa, A.-C., Hüttig, C., and Breuer, D. (2017). Onset of solid-state mantle convection and mixing during magma ocean solidification. *Journal of Geophysical Research: Planets*, 122(3):577–598.

McDonough, W. F. and Sun, S.-S. (1995). The composition of the Earth. *Chemical geology*, 120(3-4):223–253.

Meech, K. and Raymond, S. N. (2019). Origin of Earth's water: sources and constraints. *arXiv e-prints*, page arXiv:1912.04361.

Michael, P. (1995). Regionally distinctive sources of depleted MORB: Evidence from trace elements and H_2O. *Earth and Planetary Science Letters*, 131(3-4):301–320.

Miller, S. L. et al. (1953). A production of amino acids under possible primitive Earth conditions. *Science*, 117(3046):528–529.

Mjelde, R., Wessel, P., and Müller, D. (2010). Global pulsations of intraplate magmatism through the Cenozoic. *Lithosphere*, 2:361–376.

Mlawer, E. J., Payne, V. H., Moncet, J.-L., Delamere, J. S., Alvarado, M. J., and Tobin, D. C. (2012). Development and recent evaluation of the MT_CKD model of continuum absorption. *Philosophical Transactions of the Royal Society A: Mathematical, Physical and Engineering Sciences*, 370(1968):2520–2556.

Moran, S. E., Hörst, S. M., Batalha, N. E., Lewis, N. K., and Wakeford, H. R. (2018). Limits on Clouds and Hazes for the TRAPPIST-1 Planets. *The Astronomical Journal*, 156(6):252.

Morizet, Y., Paris, M., Gaillard, F., and Scaillet, B. (2010). C–O–H fluid solubility in haplobasalt under reducing conditions: an experimental study. *Chemical Geology*, 279(1-2):1–16.

Moussallam, Y., Edmonds, M., Scaillet, B., Peters, N., Gennaro, E., Sides, I., and Oppenheimer, C. (2016). The impact of degassing on the oxidation state of basaltic magmas: A case study of Kīlauea volcano. *Earth and Planetary Science Letters*, 450:317 – 325.

Murphy, W. F. (1977). The Rayleigh depolarization ratio and rotational Raman spectrum of water vapor and the polarizability components for the water molecule. *The Journal of Chemical Physics*, 67(12):5877–5882.

Murthy, V. R. (1991). Early differentiation of the Earth and the problem of mantle siderophile elements: a new approach. *Science*, 253(5017):303–306.

Nakajima, S., Hayashi, Y.-Y., and Abe, Y. (1992). A study on the 'runaway greenhouse effect' with a one-dimensional radiative-convective equilibrium model. *Journal of Atmospheric Sciences*, 49(23):2256–2266.

Newman, S. and Lowenstern, J. B. (2002). Volatilecalc: a silicate melt–H_2O –CO_2 solution model written in visual basic for excel. *Computers & Geosciences*, 28(5):597–604.

Nicklas, R. W., Puchtel, I. S., and Ash, R. D. (2018). Redox state of the Archean mantle: Evidence from V partitioning in 3.5–2.4 Ga komatiites. *Geochimica et Cosmochimica Acta*, 222:447 – 466.

Nicklas, W., Puchtel, I. S., Ash, R. D., Piccoli, P. M., Hanski, E., Nisbet, E. G., Waterton, P., Pearson, D. G., and Anbar, A. D. (2019). Secular mantle oxidation across the Archean-Proterozoic boundary: Evidence from V partitioning in komatiites and picrites. *Geochimica et Cosmochimica Acta*, 250:49 – 75.

Nikolaou, A., Katyal, N., Tosi, N., Godolt, M., Grenfell, J. L., and Rauer, H. (2019). What factors affect the duration and outgassing of the terrestrial magma ocean? *The Astrophysical Journal*, 875(1):11.

Noack, L. and Breuer, D. (2013). Interior and surface dynamics of terrestrial bodies and their implications for the habitability. In *Habitability of Other Planets and Satellites*, pages 203–233. Springer.

Noack, L., Godolt, M., von Paris, P., Plesa, A., Stracke, B., Breuer, D., and Rauer, H. (2014). Can the interior structure influence the habitability of a rocky planet? *Planetary and Space Science*, 98:14–29.

Noack, L., Rivoldini, A., and Van Hoolst, T. (2016). Modeling the evolution of terrestrial and water-rich planets and moons. *International Journal On Advances in Systems and Measurements*, 9:66–76.

Noack, L., Rivoldini, A., and Van Hoolst, T. (2017). Volcanism and outgassing of stagnant-lid planets: Implications for the habitable zone. *Physics of the Earth and Planetary Interiors*, 269:40–57.

Ohtani, E., Nagata, Y., Suzuki, A., and Kato, T. (1995). Melting relations of peridotite and the density crossover in planetary mantles. *Chemical Geology*, 120(3-4):207–221.

O'Neill, C., Lenardic, A., Jellinek, A. M., and Kiefer, W. S. (2007). Melt propagation and volcanism in mantle convection simulations, with applications for martian volcanic and atmospheric evolution. *Journal of Geophysical Research: Planets*, 112(E7).

O'Neill, H. S. (1987a). Free energies of formation of NiO, CoO, Ni_2SiO_4, and Co_2SiO_4. *American Mineralogist*, 72(3-4):280–291.

O'Neill, H. S. (1987b). Quartz-fayalite-iron and quartz-fayalite-magnetite equilibria and the free energy of formation of fayalite (Fe_2SiO_4) and magnetite (Fe_3O_4). *American Mineralogist*, 72(1-2):67–75.

O'Neill, H. S. (1988). Systems Fe-O and Cu-O; thermodynamic data for the equilibria Fe-"FeO," $Fe-Fe_3O_4$,"FeO"-Fe_3O_4, Fe_3O_4-Fe_2O_3, $Cu-Cu_2O$, and Cu_2O-CuO from emf measurements. *American Mineralogist*, 73(5-6):470–486.

O'Neill, H. S., Berry, A. J., and Mallmann, G. (2018). The oxidation state of iron in mid-ocean ridge basaltic (morb) glasses: Implications for their petrogenesis and oxygen fugacities. *Earth and Planetary Science Letters*, 504:152 – 162.

O'Neill, H. S. C. (1991). The origin of the Moon and the early history of the Earth—A chemical model. part 2: The Earth. *Geochimica et Cosmochimica Acta*, 55(4):1159–1172.

Oppenheimer, C., Fischer T., P., and Scaillet, B. (2014). Volcanic degassing: Process and impact. 4.4: Treatise of geochemistry 2nd edition.

Oppenheimer, C., Scaillet, B., and Martin, R. S. (2011). Sulfur degassing from volcanoes: source conditions, surveillance, plume chemistry and earth system impacts. *Reviews in Mineralogy and Geochemistry*, 73(1):363–421.

Ortenzi, G., Noack, L., Sohl, F., Guimond, C., Grenfell, J., Dorn, C., Schmidt, J., Vulpius, S., Katyal, N., Kitzmann, D., and Rauer, H. (2020). Mantle redox state drives outgassing chemistry and atmospheric composition of rocky planets. *Scientific reports*, 10(1):1–14.

Pahlevan, K., Schaefer, L., and Hirschmann, M. M. (2019). Hydrogen isotopic evidence for early oxidation of silicate Earth. *Earth and Planetary Science Letters*, 526:115770.

Palme, H. and O'Neill, H. S. C. (2003). Cosmochemical estimates of mantle composition. *Treatise on Geochemistry 2nd Edition*, 2:568.

Papale, P., Moretti, R., and Barbato, D. (2006). The compositional dependence of the saturation surface of $H_2O+ CO_2$ fluids in silicate melts. *Chemical Geology*, 229(1-3):78–95.

Papuc, A. M. and Davies, G. F. (2008). The internal activity and thermal evolution of Earth-like planets. *Icarus*, 195(1):447–458.

Paredes-Mariño, J., Dobson, K. J., Ortenzi, G., Kueppers, U., Morgavi, D., Petrelli, M., Hess, K.-U., Laeger, K., Porreca, M., Pimentel, A., and Perugini, D. (2017). Enhancement of eruption explosivity by heterogeneous bubble nucleation triggered by magma mingling. *Scientific reports*, 7(1):1–10.

Parfitt, E. and Wilson, L. (2008). The role of volatiles. *Fundamentals of Physical Volcanology*, pages 64–76.

Parks, G. S. and Shomate, C. H. (1940). Some Heat Capacity Data for Isopropyl Alcohol Vapor. *The Journal of Chemical Physics*, 8(5):429–429.

Pawley, A. R., Holloway, J. R., and McMillan, P. F. (1992). The effect of oxygen fugacity on the solubility of carbon-oxygen fluids in basaltic melt. *Earth and Planetary Science Letters*, 110(1-4):213–225.

Petrelli, M., El Omari, K., Spina, L., Le Guer, Y., La Spina, G., and Perugini, D. (2018). Timescales of water accumulation in magmas and implications for short warning times of explosive eruptions. *Nature communications*, 9(1):1–14.

Pierrehumbert, R. and Gaidos, E. (2011). Hydrogen greenhouse planets beyond the habitable zone. *The Astrophysical Journal Letters*, 734(1):L13.

Pierrehumbert, R. T. (2010). *Principles of planetary climate*. Cambridge University Press.

Plank, T., Kelley, K. A., Zimmer, M. M., Hauri, E. H., and Wallace, P. J. (2013). Why do mafic arc magmas contain 4wt% water on average? *Earth and Planetary Science Letters*, 364(C):168–179.

Platz, T., Byrne, P., Massironi, M., and Hiesinger, H. (2015). Volcanism and tectonism across the inner solar system: an overview. *Geological Society, London, Special Publications*, 401(1):1–56.

Pluriel, W., Marcq, E., and Turbet, M. (2019). Modeling the albedo of Earth-like magma ocean planets with H_2O-CO_2 atmospheres. *Icarus*, 317:583–590.

Pyle, D. (1998). Ottonello, G. 1997. Principles of Geochemistry. xii+ 894 pp. New York: Columbia University Press. *Geological Magazine*, 135(5):723–732.

Quanz, S., Absil, O., Angerhausen, D., Benz, W., Bonfils, X., Berger, J.-P., Brogi, M., Cabrera, J., Danchi, W., Defrère, D., van Dishoeck, E., Ehrenreich, D., Ertel, S., Fortney, J., Gaudi, S., Girard, J., Glauser, A., Grenfell, J., Ireland, M., Janson, M., Kammerer, J., Kitzmann, D., Kraus, S., Krause, O., Labadie, L., Lacour, S., Lichtenberg, T., Line, M., Linz, H., Loicq, J., Mennesson, B., Meyer, M., Miguel, Y., Monnier, J., N'Diaye, M., Pallé, E., Queloz, D., Rauer, H., Ribas, I., Rugheimer, S., Selsis, F., Serabyn, G., Snellen, I., Sozzetti, A., Stapelfeldt, K., Triaud, A., Udry, S., and Wyatt, M. (2019). Atmospheric characterization of terrestrial exoplanets in the mid-infared: biosignatures, habitability & diversity. *arXiv preprint arXiv:1908.01316*.

Ramirez, I., Allende Prieto, C., and Lambert, D. (2007). Oxygen abundances in nearby stars. Clues to the formation and evolution of the Galactic disk. *A&A*, 465:271–289.

Ramirez, R. M., Kopparapu, R., Zugger, M. E., Robinson, Freedman, R., and Kasting, J. F. (2014). Warming early Mars with CO_2 and H_2. *Nature Geoscience*, 7(1):59–63.

Rammelkamp, K., Schröder, S., Ortenzi, G., Pisello, A., Stephan, K., Baqué, M., Hübers, H.-W., Forni, O., Sohl, F., Thomsen, L., and Vikram, U. (2021). Field investigation of volcanic deposits on vulcano, italy using a handheld laser-induced breakdown spectroscopy instrument. *Spectrochimica Acta Part B: Atomic Spectroscopy*, page 106067.

Rauer, H., Aerts, C., Cabrera, J., Team, P., et al. (2016). The PLATO mission. *Astronomische Nachrichten*, 337(8-9):961–963.

Rauer, H., Catala, C., Aerts, C., Appourchaux, T., Benz, W., Brandeker, A., Christensen-Dalsgaard, J., Deleuil, M., Gizon, L., Goupil, M. J., Güdel, M., Janot-Pacheco, E., Mas-Hesse, M., Pagano, I., Piotto, G., Pollacco, D., Santos, Ċ., Smith, A., Suárez, J. C., Szabó, R., Udry, S., Adibekyan, V., Alibert, Y., Almenara, J. M., Amaro-Seoane, P., Eiff, M. A.-v., Asplund, M., Antonello, E., Barnes, S., Baudin, F., Belkacem, K., Bergemann, M., Bihain, G., Birch, A. C., Bonfils, X., Boisse, I., Bonomo, A. S., Borsa, F., Brand ão, I. M., Brocato, E., Brun, S., Burleigh, M., Burston, R., Cabrera, J., Cassisi, S., Chaplin, W., Charpinet, S., Chiappini, C., Church, R. P., Csizmadia, S., Cunha, M., Damasso, M., Davies, M. B., Deeg, H. J., Díaz, R. F., Dreizler, S., Dreyer, C., Eggenberger, P., Ehrenreich, D., Eigmüller, P., Erikson, A., Farmer, R., Feltzing, S., de Oliveira Fialho, F., Figueira, P., Forveille, T., Fridlund, M., García, R. A., Giommi, P., Giuffrida, G., Godolt, M., Gomes da Silva, J., Granzer, T., Grenfell, J. L., Grotsch-Noels, A., Günther, E., Haswell, C. A., Hatzes, A. P., Hébrard, G., Hekker, S., Helled, R., Heng, K., Jenkins, J. M., Johansen, A., Khodachenko, M. L., Kislyakova, K. G., Kley, W., Kolb, U., Krivova, N., Kupka, F., Lammer, H., Lanza, A. F., Lebreton, Y., Magrin, D., Marcos-Arenal, P., Marrese, P. M., Marques, J. P., Martins, J., Mathis, S., Mathur, S., Messina, S., Miglio, A., Montalban, J., Montalto, M., Monteiro, M. J. P. F. G., Moradi, H., Moravveji, E., Mordasini, C., Morel, T., Mortier, A., Nascimbeni, V., Nelson, R. P., Nielsen, M. B., Noack, L., Norton, A. J., Ofir, A., Oshagh, M., Ouazzani, R. M., Pápics, P., Parro, V. C., Petit, P., Plez, B., Poretti, E., Quirrenbach, A., Ragazzoni, R., Raimondo, G., Rainer, M., Reese, D. R., Redmer, R., Reffert, S., Rojas-Ayala, B., Roxburgh, I. W., Salmon, S., Santerne, A., Schneider, J., Schou, J., Schuh, S., Schunker, H., Silva-Valio, A., Silvotti, R., Skillen, I., Snellen, I., Sohl, F., Sousa, S. G., Sozzetti, A., Stello, D., Strassmeier, K. G., Švanda, M., Szabó, G. M., Tkachenko, A., Valencia, D., Van Grootel, V., Vauclair, S. D., Ventura, P., Wagner, F. W., Walton, N. A., Weingrill, J., Werner, S. C., Wheatley, P. J., and Zwintz, K. (2014). The PLATO 2.0 mission. *Experimental Astronomy*, 38(1-2):249–330.

Redlich, O. and Kwong, J. N. (1949). On the Thermodynamics of Solutions, An Equation of State, Fugacities of Gaseous Solutions. *Chemical reviews*, 44(1):233–244.

Righter, K. (2011). Prediction of metal–silicate partition coefficients for siderophile elements: An update and assessment of PT conditions for metal–silicate equilibrium during accretion of the Earth. *Earth and Planetary Science Letters*, 304(1-2):158–167.

Righter, K. and Drake, M. J. (2000). Metal/silicate equilibrium in the early Earth—New constraints from the volatile moderately siderophile elements Ga, Cu, P, and Sn. *Geochimica et Cosmochimica Acta*, 64(20):3581–3597.

Righter, K. and Ghiorso, M. (2012). Redox systematics of a magma ocean with variable pressure - temperature gradients and composition. *Proceedings of the National Academy of Sciences*, 109(30):11955–11960.

Rimmer, P. and Rugheimer, S. (2019). Hydrogen cyanide in nitrogen-rich atmospheres of rocky exoplanets. *Icarus*, 329:124–131.

Ringwood, A. (1979). Composition and origin of the Earth. *The Earth: its origin, structure and evolution*, pages 1–54.

Roggensack, K., Hervig, R. L., McKnight, S. B., and Williams, S. N. (1997). Explosive basaltic volcanism from Cerro Negro volcano: influence of volatiles on eruptive style. *Science*, 277(5332):1639–1642.

Rubie, D., Nimmo, F., and Melosh, H. (2007). Formation of Earth's Core. *Treatise on geophysics*, 9:51–90.

Rubie, D. C., Frost, D. J., Mann, U., Asahara, Y., Nimmo, F., Tsuno, K., Kegler, P., Holzheid, A., and Palme, H. (2011). Heterogeneous accretion, composition and core–mantle differentiation of the Earth. *Earth and Planetary Science Letters*, 301(1-2):31–42.

Rubie, D. C., Jacobson, S. A., Morbidelli, A., O'Brien, D. P., Young, E. D., de Vries, J., Nimmo, F., Palme, H., and Frost, D. J. (2015). Accretion and differentiation of the terrestrial planets with implications for the compositions of early-formed Solar System bodies and accretion of water. *Icarus*, 248:89–108.

Rubin, A., Fegley, B., and Brett, R. (1988). Meteorites and the Early Solar System, ed. *J.F. Kerridge & MS Matthews (Tucson, AZ: Univ. Arizona Press)*, 488.

Sagan, C. and Mullen, G. (1972). Earth and Mars: Evolution of Atmospheres and Surface Temperatures. *Science*, 177(4043):52–56.

Salvador, A., Massol, H., Davaille, A., Marcq, E., Sarda, P., and Chassefière, E. (2017). The relative influence of H_2O and CO_2 on the primitive surface conditions and evolution of rocky planets. *Journal of Geophysical Research (Planets)*, 122(7):1458–1486.

Scaillet, B. and Gaillard, F. (2011). Redox state of early magmas. *Nature*, 480(7375):48–49.

Scalo, J., Kaltenegger, L., Segura, A. G., Fridlund, M., Ribas, I., Kulikov, Y. N., Grenfell, J. L., Rauer, H., Odert, P., Leitzinger, M., Selsis, F., Khodachenko, M. L., Eiroa, C., Kasting, J., and Lammer, H. (2007). M Stars as Targets for Terrestrial Exoplanet Searches And Biosignature Detection. *Astrobiology*, 7(1):85–166.

Schaefer, L. and Elkins-Tanton, L. T. (2018). Magma oceans as a critical stage in the tectonic development of rocky planets. *Philosophical Transactions of the Royal Society A: Mathematical, Physical and Engineering Sciences*, 376(2132):20180109.

Schaefer, L. and Fegley, B. (2007). Outgassing of ordinary chondritic material and some of its implications for the chemistry of asteroids, planets, and satellites. *Icarus*, 186(2):462–483.

Schaefer, L. and Fegley, B. (2010). Chemistry of atmospheres formed during accretion of the Earth and other terrestrial planets. *Icarus*, 208(1):438 – 448.

Schaefer, L. and Fegley, J. B. (2017). Redox states of initial atmospheres outgassed on rocky planets and planetesimals. *The Astrophysical Journal*, 843(2):120.

Schaefer, L., Wordsworth, R. D., Berta-Thompson, Z., and Sasselov, D. (2016). Predictions of the Atmospheric Composition of GJ 1132b. *The Astrophysical Journal*, 829(2):63.

Scheucher, M., Wunderlich, F., Grenfell, J. L., Godolt, M., Schreier, F., Kappel, D., Haus, R., Herbst, K., and Rauer, H. (2020). Consistently Simulating a Wide Range of Atmospheric Scenarios for K2-18b with a Flexible Radiative Transfer Module. *arXiv e-prints*, page arXiv:2005.02114.

Schreier, F., Gimeno García, S., Hedelt, P., Hess, M., Mendrok, J., Vasquez, M., and Xu, J. (2014). GARLIC - A general purpose atmospheric radiative transfer line-by-line infrared-microwave code: Implementation and evaluation. *Journal of Quantitative Spectroscopy and Radiative Transfer*, 137:29–50.

Schreier, F., Milz, M., Buehler, S. A., and von Clarmann, T. (2018a). Intercomparison of three microwave/infrared high resolution line-by-line radiative transfer codes. *Journal of Quantitative Spectroscopy and Radiative Transfer*, 211:64–77.

Schreier, F., Städt, S., Hedelt, P., and Godolt, M. (2018b). Transmission spectroscopy with the ACE-FTS infrared spectral atlas of Earth: A model validation and feasibility study. *Molecular Astrophysics*, 11:1–22.

Shahar, A., Driscoll, P., Weinberger, A., and Cody, G. (2019). What makes a planet habitable? *Science*, 364(6439):434–435.

Shardanand and Rao, A. D. P. (1977). *Absolute Rayleigh scattering cross sections of gases and freons of stratospheric interest in the visible and ultraviolet regions*. SAO/NASA Astrophysics Data System.

Sharp, Z. (2017). *Principles of stable isotope geochemistry*. Digital Book, digitalrepository.unm.edu.

Sharp, Z., Mccubbin, F., and Shearer, C. (2013). A hydrogen-based oxidation mechanism relevant to planetary formation. *Earth and Planetary Science Letters*, 380:88–97.

Shi, P. and Saxena, S. (1992). Thermodynamic modeling of the CHOS fluid system. *American Mineralogist*, 77(9-10):1038–1049.

Shields, A. L., Ballard, S., and Johnson, J. A. (2016). The habitability of planets orbiting M-dwarf stars. *Physics Reports*, 663:1.

Shinohara, H. (2008). Excess degassing from volcanoes and its role on eruptive and intrusive activity. *Reviews of Geophysics*, 46(4).

Shorttle, O., Moussallam, Y., Hartley, M. E., Maclennan, J., Edmonds, M., and Murton, B. J. (2015). Fe-XANES analyses of Reykjanes Ridge basalts: Implications for oceanic crust's role in the solid Earth oxygen cycle. *Earth and Planetary Science Letters*, 427:272 – 285.

Sigurdsson, H., Houghton, B., McNutt, S., Rymer, H., and Stix, J. (2015). *The encyclopedia of volcanoes*. Elsevier.

Sleep, N. H. and Zahnle, K. (2001). Carbon dioxide cycling and implications for climate on ancient Earth. *Journal of Geophysical Research*, 106:1373–1400.

Smart, K. A., Tappe, S., Stern, R. A., Webb, S. J., and Ashwal, L. D. (2016). Early Archaean tectonics and mantle redox recorded in Witwatersrand diamonds. *Nature Geoscience*, 9(3):255–259.

Smrekar, S. E., Stofan, E. R., Mueller, N., Treiman, A., Elkins-Tanton, L., Helbert, J., Piccioni, G., and Drossart, P. (2010). Recent Hotspot Volcanism on Venus from VIRTIS Emissivity Data. *Science*, 328(5978):605–608.

Sneep, M. and Ubachs, W. (2005). Direct measurement of the Rayleigh scattering cross section in various gases. *Journal of Quantitative Spectroscopy and Radiative Transfer*, 92(3):293–310.

Spohn, T., Breuer, D., and Johnson, T. (2014). *Encyclopedia of the solar system.* Elsevier.

Stagno, V. (2019). Carbon, carbides, carbonates and carbonatitic melts in the Earth's interior. *Journal of the Geological Society*, 176(2):375–387.

Stevenson, D. (1988). Fluid dynamics of core formation. In *Topical Conference Origin of the Earth*, volume 681, page 87.

Stevenson, D. J. (1983). *The nature of the earth prior to the oldest known rock record - The Hadean earth.* Princeton.

Symonds, R. B. and Reed, M. H. (1993). Calculation of multicomponent chemical equilibria in gas-solid-liquid systems: Calculation methods, thermochemical data, and applications to studies of high-temperature volcanic gases with examples from Mt. St. Helens. *American Journal of Science;(United States)*, 293(8).

Tackley, P. J., Ammann, M., Brodholt, J. P., Dobson, D. P., and Valencia, D. (2013). Mantle dynamics in super-Earths: Post-perovskite rheology and self-regulation of viscosity. *Icarus*, 225(1):50–61.

Tetens, O. (1930). Über einige meteorologische Begriffe (On some meteorological terms). *Z. Geophys.*, 6(6):207–309.

Tian, F. (2015). Atmospheric Escape from Solar System Terrestrial Planets and Exoplanets. *Annual Review of Earth and Planetary Sciences*, 43:459–476.

Tian, F. and Ida, S. (2015). Water contents of Earth-mass planets around M dwarfs. *Nature Geoscience*, 8(3):177–180.

Tian, F., Toon, O. B., Pavlov, A. A., and De Sterck, H. (2005). A Hydrogen-Rich Early Earth Atmosphere. *Science*, 308(5724):1014–1017.

Tinetti, G., Drossart, P., Eccleston, P., Hartogh, P., Heske, A., Leconte, J., Micela, G., Ollivier, M., Pilbratt, G., Puig, L., Turrini, D., Vandenbussche, B., Wolkenberg, P., Beaulieu, J.-P., Buchave, L. A., Ferus, M., Griffin, M., Guedel, M., Justtanont, K., Lagage, P.-O., Machado, P., Malaguti, G., Min, M., Nørgaard-Nielsen, H. U., Rataj, M., Ray, T., Ribas, I., Swain, M., Szabo, R., Werner, S., Barstow, J., Burleigh, M., Cho, J., du Foresto, V. C., Coustenis, A., Decin, L., Encrenaz, T., Galand, M., Gillon, M., Helled, R., Morales, J. C., Muñoz, A. G., Moneti, A., Pagano, I., Pascale, E., Piccioni, G., Pinfield, D., Sarkar, S., Selsis, F., Tennyson, J., Triaud, A., Venot, O., Waldmann, I., Waltham, D., Wright, G., Amiaux, J., Auguères, J.-L., Berthé, M., Bezawada, N., Bishop, G., Bowles, N., Coffey, D., Colomé, J., Crook, M., Crouzet, P.-E., Da Peppo, V., Sanz, I. E., Focardi, M., Frericks, M., Hunt, T., Kohley, R., Middleton, K., Morgante, G., Ottensamer, R., Pace, E., Pearson, C., Stamper, R., Symonds, K., Rengel, M., Renotte, E., Ade, P., Affer, L., Alard, C., Allard, N., Altieri, F., André, Y., Arena, C., Argyriou, I., Aylward, A., Baccani, C., Bakos, G., Banaszkiewicz, M., Barlow, M., Batista, V., Bellucci, G., Benatti, S., Bernardi, P., Bézard, B., Blecka, M., Bolmont, E., Bonfond, B., Bonito, R., Bonomo, A. S., Brucato, J. R., Brun, A. S., Bryson, I., Bujwan, W., Casewell, S., Charnay, B., Pestellini, C. C., Chen, G., Ciaravella, A., Claudi, R., Clédassou, R., Damasso, M., Damiano, M., Danielski, C., Deroo, P., Di Giorgio, A. M., Dominik, C., Doublier, V., Doyle, S., Doyon, R., Drummond, B., Duong, B., Eales, S., Edwards, B., Farina, M., Flaccomio, E., Fletcher, L., Forget, F., Fossey, S., Fränz, M., Fujii, Y., García-Piquer, Á., Gear, W., Geoffray, H., Gérard, J. C., Gesa, L., Gomez, H., Graczyk, R., Griffith, C., Grodent, D., Guarcello, M. G., Gustin, J., Hamano, K., Hargrave, P., Hello, Y., Heng, K., Herrero, E., Hornstrup, A., Hubert, B., Ida, S., Ikoma, M., Iro, N., Irwin, P., Jarchow, C., Jaubert, J., Jones, H., Julien, Q., Kameda, S., Kerschbaum, F., Kervella, P., Koskinen, T., Krijger, M., Krupp, N., Lafarga, M., Landini, F., Lellouch, E., Leto, G., Luntzer, A., Rank-Lüftinger, T., Maggio, A., Maldonado, J., Maillard, J.-P., Mall, U., Marquette, J.-B., Mathis, S., Maxted, P., Matsuo, T., Medvedev, A., Miguel, Y., Minier, V., Morello, G., Mura, A., Narita, N., Nascimbeni, V., Nguyen Tong, N., Noce, V., Oliva, F., Palle, E., Palmer, P., Pancrazzi, M., Papageorgiou, A., Parmentier, V., Perger, M., Petralia, A., Pezzuto, S., Pierrehumbert, R., Pillitteri, I., Piotto, G., Pisano, G., Prisinzano, L., Radioti, A., Réess, J.-M., Rezac, L., Rocchetto, M., Rosich, A., Sanna, N., Santerne, A., Savini, G., Scandariato, G., Sicardy, B., Sierra, C., Sindoni, G., Skup, K., Snellen, I., Sobiecki, M., Soret, L., Sozzetti, A., Stiepen, A., Strugarek, A., Taylor, J., Taylor, W., Terenzi, L., Tessenyi, M., Tsiaras, A., Tucker, C., Valencia, D., Vasisht, G., Vazan, A., Vilardell, F., Vinatier, S., Viti, S., Waters, R., Wawer, P., Wawrzaszek, A., Whitworth, A., Yung, Y. L., Yurchenko, S. N., Osorio, M. R. Z., Zellem, R., Zingales, T., and Zwart, F. (2018). A chemical survey of exoplanets with ARIEL. *Experimental Astronomy*, 46(1):135–209.

Tosi, N., Godolt, M., Stracke, B., Ruedas, T., Grenfell, J. L., Höning, D., Nikolaou, A., Plesa, A., Breuer, D., and Spohn, T. (2017). The habitability of a stagnant-lid Earth. *Astronomy & Astrophysics*, 605:A71.

Trail, D., Watson, E. B., and Tailby, N. D. (2011). The oxidation state of Hadean magmas and implications for early Earth's atmosphere. *Nature*, 480:79 EP –.

Tu, L., Johnstone, C. P., Güdel, M., and Lammer, H. (2015). The extreme ultraviolet and X-ray Sun in Time: High-energy evolutionary tracks of a solar-like star. *Astronomy & Astrophysics*, 577:L3.

Tucker, J. M., Hauri, E. H., Pietruszka, A. J., Garcia, M. O., Marske, J. P., and Trusdell, F. A. (2019). A high carbon content of the hawaiian mantle from olivine-hosted melt inclusions. *Geochimica et Cosmochimica Acta*, 254:156 – 172.

Turbet, M., Ehrenreich, D., Lovis, C., Bolmont, E., and Fauchez, T. (2019). The runaway greenhouse radius inflation effect. An observational diagnostic to probe water on Earth-sized planets and test the habitable zone concept. *arXiv:1906.03527*, 628:A12.

Turcotte, D. (1980). On the thermal evolution of the Earth. *Earth and Planetary Science Letters*, 48(1):53 – 58.

Valley, J., Peck, W., M. King, E., and Wilde, S. (2002). A cool early Earth. *Geology*, 30:351–.

Valley, J. W., Cavosie, A. J., Ushikubo, T., Reinhard, D. A., Lawrence, D. F., Larson, D. J., Clifton, P. H., Kelly, T. F., Wilde, S. A., Moser, D. E., and Spicuzza, M. J. (2014). Hadean age for a post-magma-ocean zircon confirmed by atom-probe tomography. *Nature Geoscience*, 7:219 EP –.

Van Hoolst, T., Noack, L., and Rivoldini, A. (2019). Exoplanet interiors and habitability. *Advances in Physics: X*, 4(1):1630316.

Wade, J. and Wood, B. (2005). Core formation and the oxidation state of the Earth. *Earth and Planetary Science Letters*, 236(1-2):78–95.

Wagner, W. and Pruß, A. (2002). The IAPWS Formulation 1995 for the Thermodynamic Properties of Ordinary Water Substance for General and Scientific Use. *Journal of Physical and Chemical Reference Data*, 31(2):387–535.

Walker, J. C. G., Hays, P. B., and Kasting, J. F. (1981). A negative feedback mechanism for the long-term stabilization of the Earth's surface temperature. *Journal of Geophysical Research*, 86:9776–9782.

Wallace, P. (2001). Volcanic SO_2 emissions and the abundance and distribution of exsolved gas in magma bodies. *Journal of Volcanology and Geothermal Research*, 108(1-4):85–106.

Wallace, P. J. (1998). Water and partial melting in mantle plumes: Inferences from the dissolved H_2O concentrations of Hawaiian basaltic magmas. *Geophysical Research Letters*, 25(19):3639–3642.

Wallace, P. J. (2005). Volatiles in subduction zone magmas: concentrations and fluxes based on melt inclusion and volcanic gas data. *Journal of Volcanology and Geothermal Research*, 140(1):217 – 240. Energy and Mass Fluxes in Volcanic Arcs.

Wallace, P. J., Anderson, A. T. J., and Davis, A. M. (1995). Quantification of pre-eruptive exsolved gas contents in silicic magmas. *Nature*, 377(6550):612.

Wallace, P. J. and Anderson, Alfred T., J. (1998). Effects of eruption and lava drainback on the H_2O contents of basaltic magmas at Kilauea Volcano. *Bulletin of Volcanology*, 59(5):327–344.

Wallace, P. J., Plank, T., Edmonds, M., and Hauri, E. H. (2015). Volatiles in magmas. In *The encyclopedia of volcanoes*, pages 163–183. Elsevier.

Walsh, K. J., Morbidelli, A., Raymond, S. N., O'brien, D., and Mandell, A. (2012). Populating the asteroid belt from two parent source regions due to the migration of giant planets—"The Grand Tack". *Meteoritics & Planetary Science*, 47(12):1941–1947.

Wang, Z. and Becker, H. (2013). Ratios of S, Se and Te in the silicate Earth require a volatile-rich late veneer. *Nature*, 499:1476–4687.

Wänke, H. (1981). Constitution of terrestrial planets. *Philosophical Transactions of the Royal Society of London. Series A, Mathematical and Physical Sciences*, 303(1477):287–302.

Wänke, H. and Dreibus, G. (1988). Chemical composition and accretion history of terrestrial planets. *Philosophical Transactions of the Royal Society of London. Series A, Mathematical and Physical Sciences*, 325(1587):545–557.

Watson, A. J., Donahue, T. M., and Walker, J. C. (1981). The dynamics of a rapidly escaping atmosphere: applications to the evolution of Earth and Venus. *Icarus*, 48:150–166.

Wetzel, D. T., Rutherford, M. J., Jacobsen, S. D., Hauri, E. H., and Saal, A. E. (2013). Degassing of reduced carbon from planetary basalts. *Proceedings of the National Academy of Sciences*, 110(20):8010–8013.

Wilde, S. A., Valley, J. W., Peck, W. H., and Graham, C. M. (2001). Evidence from detrital zircons for the existence of continental crust and oceans on the Earth 4.4 Gyr ago. *Nature*, 409:175 EP –.

Wilson, L. (2009). Volcanism in the solar system. *Nature Geoscience*, 2(6):389–397.

Wolf, E. and Toon, O. (2014). Controls on the archean climate system investigated with a global climate model. *Astrobiology*, 14(3):241–253. PMID: 24621308.

Wood, B. J., Bryndzia, L. T., and Johnson, K. E. (1990). Mantle oxidation state and its relationship to tectonic environment and fluid speciation. *Science*, 248(4953):337–345.

Wood, B. J., Walter, M. J., and Wade, J. (2006). Accretion of the Earth and segregation of its core. *Nature*, 441(7095):825.

Wordsworth, R. and Pierrehumbert, R. (2013). Hydrogen-Nitrogen Greenhouse Warming in Earth's Early Atmosphere. *Science*, 339(6115):64–67.

Wordsworth, R. and Pierrehumbert, R. (2014). Abiotic oxygen-dominated atmospheres on terrestrial habitable zone planets. *The Astrophysical Journal Letters*, 785(2):L20.

Wordsworth, R. D., Schaefer, L. K., and Fischer, R. A. (2018). Redox Evolution via Gravitational Differentiation on Low-mass Planets: Implications for Abiotic Oxygen, Water Loss, and Habitability. *The Astronomical Journal*, 155(5):195.

Wunderlich, F., Scheucher, M., Godolt, M., Grenfell, J. L., Schreier, F., Schneider, P. C., Wilson, D. J., Sánchez López, A., López Puertas, M., and Rauer, H. (2020). Distinguishing between wet and dry atmospheres of TRAPPIST-1 e and f. *arXiv e-prints*, page arXiv:2006.11349.

Yan, F., Fosbury, R. A., Petr-Gotzens, M. G., Zhao, G., Wang, W., Wang, L., Liu, Y., and Pallé, E. (2015). High-resolution transmission spectrum of the earth's atmosphere-seeing earth as an exoplanet using a lunar eclipse. *International Journal of Astrobiology*, 14(2):255–266.

Zahnle, K. J. and Catling, D. C. (2017). The Cosmic Shoreline: The Evidence that Escape Determines which Planets Have Atmospheres, and what this May Mean for Proxima Centauri B. *The Astrophysical Journal*, 843(2):122.

Zahnle, K. J., Gacesa, M., and Catling, D. C. (2019). Strange messenger: A new history of hydrogen on Earth, as told by Xenon. *Geochimica et Cosmochimica Acta*, 244:56 – 85.

Zahnle, K. J., Lupu, R., Catling, D. C., and Wogan, N. (2020). Creation and Evolution of Impact-generated Reduced Atmospheres of Early Earth. *The Planetary Science Journal*, 1(1):11.

Zhang, C. and Duan, Z. (2009). A model for C–O–H fluid in the Earth's mantle. *Geochimica et Cosmochimica Acta*, 73(7):2089–2102.

Zhang, X. (2020). Atmospheric Regimes and Trends on Exoplanets and Brown Dwarfs. *arXiv e-prints*, page arXiv:2006.13384.

Zhang, Y., Xu, Z., Zhu, M., and Wang, H. (2007). Silicate melt properties and volcanic eruptions. *Reviews of Geophysics*, 45(4).

Zolotov, M. Y. and Fegley Jr, B. (1999). Oxidation state of volcanic gases and the interior of Io. *Icarus*, 141(1):40–52.

Zsom, A., Kaltenegger, L., and Goldblatt, C. (2012). A 1D microphysical cloud model for Earth, and Earth-like exoplanets: Liquid water and water ice clouds in the convective troposphere. *Icarus*, 221(2):603–616.